

PLASMONIC PLATFORM FOR SUPER-RESOLUTION IMAGING AND
APPLICATIONS IN BIOLOGICAL AND NANOENERGETIC SYSTEMS

A Dissertation
presented to
the Faculty of the Graduate School
at the University of Missouri

In Partial Fulfillment
of the Requirements for the Degree
Doctor of Philosophy

by
BIYAN CHEN
Dr. Shubhra Gangopadhyay, Dr. Matthew R. Maschmann

Dissertation Supervisors

DECEMBER 2017

The undersigned, appointed by the dean of Graduate School, have examined the dissertation entitled

PLASMONIC PLATFORM FOR SUPER-RESOLUTION IMAGING AND APPLICATIONS IN BIOLOGICAL AND NANOENERGETIC SYSTEMS

presented by Biyan Chen,

a candidate for the degree of doctor of philosophy

and hereby certify that, in their opinion, it is worthy of acceptance.

SHUBHRA GANGOPADHYAY

MATTHEW R. MASCHMANN

SCOTT KOVALESKI

CLAY STALEY

SHEILA GRANT

DEDICATION

I wish to dedicate this work to my loving parents, my brother and sister, and my husband Haisheng Zheng. Their love and company has always been my motivation and support for the exploration of life and science. I would also like to thank our former Business Support Specialist, Jami D. Thompson, who helped us to take care of all stuffs in our research group. Thank you.

ACKNOWLEDGEMENTS

I sincerely thank my doctoral committee chair and research co-supervisor, Dr. Shubhra Gangopadhyay, for giving me the opportunities to work in her research group on these very interesting projects and for providing excellent guidance and advice throughout my time in her group. Throughout my doctoral study, she's the one who motivates me to see the beauty of science, teaches me how to think out of the box and work in a team. Most importantly, I owe gratitude to my supervisor for gaining self-esteem, self-confidence and professionalism due to my association with her for the last four and a half years. I would like to thank my co-supervisor, Dr. Matthew R. Maschmann, for providing dedicated guidance on teaching me the theory and helping us to write papers. His great personality treating us like friends motivates us to discuss the science and data openly and freely. Our work would not have been possible without the collaboration between my co-supervisors and their support. I also graciously thank my other doctoral committee members, Dr. Scott Kovaleski, Dr. Sheila Grant, and Dr. Clay Staley for their guidance and helpful discussions.

It would have been nearly impossible for me to reach this point without the help and support provided by my current and previous mentors and group members: Dr. Keshab Gangopadhyay, Dr. Jacob A. McFarland, Dr. Bok Sangho, Dr. Mathai C. Joseph, Dr. Syed Barizuddin, Dr. Rajagopala Thiruvengadathan, Dr. Peter V. Cornish, Dr. Sagnik Basuray, Dr. Raghuraman Kannan, Dr. Haisheng Zheng, Dr. Aaron Wood, Dr. Charles Darr, Dr. Mukjee Somik, Dr. Steven Hamm, Naadaa Zakiyyan, Matthew E. Riehn, Anqi Wang, Avinash Pathak, Arnab Ghosh, Junsang Yoon, Connor D. Wolenski, Francisco Cortalezzi,

Samiullah Pathan, Ximeng Jia, Mu Li, Brandon Smith, Octavio Sosa and all my other colleagues.

TABLE OF CONTENTS

LIST OF FIGURES.....	viii
LIST OF TABLES.....	xxx
Chapter 1. Introduction	1
1.1 Plasmonics	1
1.2 Super-resolution Imaging.....	3
1.3 Nanoenergetic.....	4
1.3.1 Al/fluoropolymer nanoenergetic system	4
1.3.2 Photothermal heating of nanoenergetics	5
1.3.3 Reaction Processes of Al/fluoropolymer nanoenergetics	6
1.3.4 Diffusive oxidation mechanism vs. melt dispersion mechanism	8
1.3.5 Characterization tools	9
1.4 Scope of This Dissertation.....	10
Chapter 2. Theory for Plasmonic and Super-Resolution Imaging.....	13
2.1 Design of Plasmonic Gratings.....	13
2.1.1 Dispersion relation of Surface Plasmons.....	13
2.1.2 Surface Plasmon Resonance	18
2.1.3 FDTD simulations and experiment studies on surface plasmon resonance (SPR) dispersion curve for grating microchips.....	22
2.1.4 FDTD Simulations for the design of grating microchip configuration.....	25
2.2 Super-Resolution Imaging by Plasmonic Grating.....	28
2.2.1 Design of Plasmonic Grating Superlens for Far Field Imaging	28
2.2.2 Combination of Plasmonic Grating with Localization Microscopy.....	35
2.3 Fluorescence Beads for Experimental Point Spread Function (PSF) Studies	36
2.3.1 Theory of PSF, Convolution, and Deconvolution	36
2.3.2 Selection Rules for Fluorescent Bead for PSF Measurement.....	38
2.3.3 Preparation of Samples for PSF Measurement	40
2.3.4 Fluorescence Measurement for PSF Studies	41
2.4 Future Work.....	44
Chapter 3. Plasmonic Gratings with Nano-protrusions Made by Glancing Angle Deposition for Single-Molecule Super-Resolution Imaging	46

3.1	Introduction	46
3.2	Experiment.....	49
3.2.1	<i>Fabrication of Plasmonic Silver Gratings by GLAD</i>	49
3.2.2	<i>GLAD Grating Characterization</i>	50
3.2.3	<i>Fluorescence Image Collection</i>	51
3.2.4	<i>Single-molecule Image and Super-Resolution Analysis</i>	51
3.3	Discussion.....	52
3.3.1	<i>Design and Fabrication of GLAD Gratings</i>	52
3.3.2	<i>Experimental and Simulated Optical Properties</i>	58
3.3.3	<i>Single-molecule Imaging</i>	75
3.3.4	<i>Beating the Diffraction Limit</i>	78
3.3.5	<i>Localization Microscopy for Super-resolution Imaging</i>	80
3.4	Future Work.....	86
Chapter 4. Super-resolution Imaging on Nanostructures on Plasmonic Grating Superlens		88
4.1	Introduction	88
4.2	Experiment.....	88
4.3	Discussion.....	89
4.3.1	<i>Ground state depletion (GSD) microscopy</i>	90
4.3.2	<i>Localization Microscopy using Plasmonic Grating under epi-fluorescence microscope</i>	91
4.3.3	<i>Airyscanning Microscopy Combining with Plasmonic Grating</i>	94
4.3.4	<i>Combining Plasmonic Grating with Smartphone Imaging</i>	95
4.4	Future Work.....	97
Chapter 5. Theory for Photothermal Heating.....		98
5.1	Design of Plasmonic Gratings.....	98
5.1.1	<i>FDTD simulation for grating microchips with Al nanoparticles</i>	98
5.2	COMSOL modeling absorption and electric field of Al-polymer nanoenergetic systems 103	
5.2.1	<i>Scattering and absorption of Al nanoparticle in different oxidizers</i>	104
5.2.2	<i>Electric field of Al nanoparticle in different oxidizers</i>	108
5.2.3	<i>Temperature of Al nanoparticles by photothermal heating</i>	110
5.3	Combining FDTD simulation and COMSOL modeling for thermal characteristics of Al-polymer nanoenergetic systems under laser excitation.....	113
5.3.1	<i>FDTD simulations of electric field on gratings</i>	113

5.3.2	<i>COMSOL modeling for temperature of Al/THV under laser excitation</i>	115
5.4	Future Work	118
Chapter 6. Plasmonic Grating Enhanced Fluorescence-Based Temperature Sensor for <i>In-Situ</i> Imaging Local Temperature of Aluminum Nanoparticles		
6.1	Abstract	119
6.2	Introduction	120
6.3	Experiment	123
6.3.1	<i>Fabrication of Plasmonic Gratings</i>	123
6.3.2	<i>Prepare Al/THV nanoenergetics films with temperature sensitive dyes</i>	123
6.3.3	<i>Temperature-fluorescence calibration curve for Al/THV/R6G systems</i>	124
6.3.4	<i>Develop and characterize tunable laser heating setup in microscope for in-situ heating and imaging</i>	126
6.4	Results and Discussion	128
6.4.1	<i>Temperature-dependent spectra and reversible response</i>	128
6.4.2	<i>Temperature calibration curve and effects of photobleaching</i>	130
6.4.3	<i>Enhancement of Plasmonic Gratings and Al Nanoparticles on Laser Heating</i>	131
6.4.4	<i>Effects of laser power on heating</i>	134
6.4.5	<i>Nanoscale local temperature comparison between Al NPs and THV</i>	136
6.4.6	<i>Movement of Al NPs</i>	139
6.4.7	<i>Simulation for electric field enhancement and temperature change</i>	143
6.5	Effect of Laser Wavelengths on Heating (Blue vs IR Laser)	146
6.6	Conclusion	148
6.7	Future Work	149
Chapter 7. <i>In-Situ</i> Characterization of Photothermal Nanoenergetic Combustion on a Plasmonic Microchip		
7.1	Abstract	151
7.2	Introduction	151
7.3	Materials and Methods	153
7.3.1	<i>Plasmonic Grating Fabrication</i>	153
7.3.2	<i>Preparation of Al/THV Nanoenergetic Films</i>	154
7.3.3	<i>Characterization</i>	155
7.3.4	<i>Laser Control</i>	155
7.4	Results and Discussion	156
7.4.1	<i>Imaging Methodologies</i>	156

7.4.2	<i>Photothermal Heating Experiments</i>	159
7.4.3	<i>Time-evolving Combustion Behavior</i>	163
7.4.4	<i>In-Situ Optical Pyrometry</i>	169
7.4.5	<i>Electromagnetic Simulation</i>	172
7.4.6	<i>Thermal Model</i>	174
7.4.7	<i>Optical Scattering</i>	177
7.4.8	<i>Effects of Temperature on Properties and Coupling</i>	180
7.4.9	<i>Melt and Vaporize Al</i>	182
7.5	<i>Two-Color Pyrometry</i>	183
7.5.1	<i>Theory</i>	183
7.5.2	<i>Temperature calibration by both fast camera and spectrometer</i>	185
7.5.3	<i>Calibration Curves for New Setup through Eyepiece Port</i>	187
7.5.4	<i>Spectrum Measurement and Fitting for Laser Ignition Study</i>	189
7.5.5	<i>Comparison between Grating and Flat Silver under Laser Ignition.</i>	194
7.5.6	<i>Temperature Map Reconstruction for Grating under Laser Ignition.</i>	195
7.6	<i>Conclusion</i>	198
7.7	<i>Future Work</i>	199
	REFERENCES.....	201
	LIST OF PUBLICATIONS.....	209
	VITA.....	212

LIST OF FIGURES

Figure 2-1 Illustration of a photon incident on a metal/dielectric interface, and the photon
 18

Figure 2-2 Prism-based SPR excitation: (a) Otto and (b) Kretschmann configurations, (c)
 photon and SPR wavevector matching conditions..... 20

Figure 2-3 Grating-based SPR excitation: (a) grating configurations, (b) photon and SPR
 wavevector matching conditions..... 21

Figure 2-4 AFM and SPR dispersion curves for (a-d) HD-DVD and (e-h) Bluray
 gratings. The dispersion curve is based on coupling peak location from reflectivity data
 for 100 nm silver gratings with 10 nm alumina coating. (Left) AFM for PMSSQ gratings
 without metal coating; (Middle) experimental dispersion curve measured by ellipsometry:
 (b, f) the incident angles in air, (c, g) incident angles corrected by Snell’s law for the
 mediums; (Right) simulated dispersion curve. 25

Figure 2-5 FDTD simulated (a) reflectance and (b) maximum E-field strength (E_z
 $_{max}/E_{z,0}$) and SPR wavelengths varying with different silver thickness from 20 nm to 120
 nm, under normal incidence (0°) of light in oil (or nitrocellulose) environment. (c) E-field
 distribution of for grating microchips The E-field ($E_z/E_{z,0}$) scale is normalized to 0~5.
 The scale bar is 200 nm. 27

Figure 2-6 (a) Ideal OTF for FSL that enhances incident evanescent waves within
 wavevector bands. (b) 2D Fourier space for HDDVD gratings. (c) Spatial resolution for
 diffraction limit condition and with HDDVD grating wavevector modulation..... 32

Figure 2-7 (a-e) COMSOL simulation for HDDVD silver gratings (a) 0 order reflectance (R_0), (b) -1 order reflectance (R_{-1}), (c) the ratio of R_{-1}/R_0 ; (d) E-field profile at 0° angle of incidence at 656 nm, (e) E-field profile at the maximum R_{-1} at different angles of incidence from 0° to 30° . Normalized intensity for (f) Xenon lamp and (g) Illumination angle for $100\times$ oil objective used in the experiment. 35

Figure 2-8 The process of convolution and deconvolution between object and image through PSF. 38

Figure 2-9 Comparison of 100 nm fluorescence beads imaging on different substrates including glass, flat silver and silver gratings, under FTIC filter. 43

Figure 2-10 100 nm fluorescence beads imaging on silver gratings, under the CY5 filter. 43

Figure 2-11 PSF for 100 nm fluorescence beads imaging on the glass, under FTIC filter. 44

Figure 3-1 Schematic of a silver plasmonic grating on the fluorescence-based application: (a) regular grating and (b) GLAD grating, (c) zoom in to show the GLAD morphology with nano-protrusions and nanogaps. The brighter yellow color of the fluorophore indicates the higher fluorescent intensity when nearby a nano-protrusion. The platform can be coated with any medium to suit the needs of the application. For example, it is important to have a stable surface with sufficient binding sites for biological studies, and hence, the GLAD grating can be coated with SiO_2 or gold to functionalize the surface; the GLAD grating can also be coated with a PMSSQ matrix with dye for fluorescence studies..... 49

Figure 3-2 Illustration of the GLAD growth process showing the oblique arrival of silver vapor to the PMSSQ gratings: (a) step #1. Deposition of the thin chromium adhesion layer; (b) step #2. Rapid silver deposition encourages vertical growth that results in plenty of nano-protrusions, and clear nanogaps. Comparison between rapid and stepped-deposition: (c) deposition rates and silver thicknesses over time, (d) AFM 2D profiles. AFM 3D contour maps: (e) regular grating at a normal deposition angle ($\alpha = 0^\circ$) showing few typical surface features; (f) GLAD grating with rapid silver deposition rates at an oblique deposition angle ($\alpha = 60^\circ$), showing controlled nanogaps, and nano-protrusions (hot spots)..... 53

Figure 3-3 2D AFM images and profiles of silver GLAD gratings with rapid silver deposition rates at different deposition angles (a) $\alpha = 0^\circ$, (b) $\alpha = 30^\circ$, (c) $\alpha = 60^\circ$, (d) $\alpha = 70^\circ$ 55

Figure 3-4 (a) Nano-protrusion height above the grating ridge histograms and (b) nano-protrusion base diameter histograms at $\alpha = 30^\circ$, $\alpha = 60^\circ$, and $\alpha = 70^\circ$ deposition angles. Histograms obtained from a sample of 100 nano-protrusions from AFM topography scan with a ~ 1 nm radius tip. GLAD samples were deposited over an 8 month period and found to be very consistent in surface structure and reflectance. 56

Figure 3-5 $1 \times 1 \mu\text{m}$ AFM scans and height histograms of silver GLAD gratings ($\alpha = 60^\circ$) with the (a) entire scan or (b,c,d) regions of interest highlighted. Highlighted portion of the GLAD grating containing the (b) nanogap region, (c) nano-protrusions in the deposition shadow region, and (d) Nano-protrusion region on top of the grating ridge. . 57

Figure 3-6 Enhancement factors (with respect to glass and flat silver) with spun-coated Cy5 (in PMSSQ + ethanol solution) on 40 nm silver HDDVD GLAD gratings at different deposition angles (a) $\alpha = 30^\circ$, (b) $\alpha = 60^\circ$, (c) $\alpha = 70^\circ$. The images were taken with $60\times$ water-immersion objective and with 400 ms and 700 ms exposure times. The samples were illuminated by Xenon light source with broad spectra filtered by Cy5 filter cubes. 58

Figure 3-7 Experimental frequency vs. wave vector plot for a silver GLAD grating in air calculated by the SPR peak location from the reflectance. Inset: Illustration of the wave vector matching between incident EM radiation (transverse-magnetic (TM) light) on a grating and a propagating surface plasmon polariton. 60

Figure 3-8 800×800 nm AFM scans of (a) 60° GLAD Grating and (b) silver grown on flat glass deposited at 60° GLAD with the same height scale as Fig. S2 (0 – 90 nm). Scanned with a ~ 1 nm AFM tip. The roughness of the flat silver film and its granular structure provides a substantial increase in surface area as compared to, for example, glass surfaces. The calculated surface area via Gwiddyon © AFM analysis software of (a) is $782.475\times 10^{-15}\text{m}^2$ with a projected flat area of $640.0\times 10^{-15}\text{m}^2$. (b) has a calculated surface area via via Gwiddyon © of $782.173\times 10^{-15}\text{m}^2$ and a projected flat area of flat area of $640.0\times 10^{-15}\text{m}^2$ 61

Figure 3-9 Optical properties of 40 nm Ag GLAD gratings (deposited at $\alpha = 60^\circ$): (a) experimental and simulated TM-polarized light reflection spectra taken at 15° incidence of light in air; (b) experimental transmission taken at 0 - 15° incidence of light in water; (c) experimental transmission, reflection, and absorption taken at 15° incidence of light in water, where absorption (pA) = 1-transmission (pT)-reflection (pR). The color bars in (b-c) indicate the excitation and emission wavelengths range for Cy3 and Cy5; the arrows

point out the upper and lower resonance mode at 15 °incidence for GLAD gratings. (d) Normalized fluorescence intensities vs excitation angle for different Cy5 spin-coated on the surface of Ag GLAD gratings (10 μM concentration, and thickness of 30 nm in a PMSSQ matrix using a 60× water-immersion objective by epifluorescence microscope; the power of 642 nm laser for Cy5 is 50 mW) and simulated normalized E-field intensity ($|E_z/E_{z,0}|^2$) under Cy5 excitation wavelength (642 nm). (e) Simulated maximum $E_z/E_{z,0}$ at nano-protrusion vs. incident angle for 40 nm Ag GLAD gratings coated with 30 nm PMSSQ in water environment at excitation and emission wavelength of Cy5; maximum $E_z/E_{z,0}$ at regular grating and nano-protrusion on 40 nm flat Ag under the same condition as comparisons. 63

Figure 3-10 Design of simulated geometry for 40 nm Ag HD-DVD GLAD gratings: refractive index (RI) profile and E-field ($E_z/E_{z,0}$) at 40 °incident angle at resonance wavelength in air; intensity bar is 0-10, and scale bar is 100 nm. 64

Figure 3-11 Experimental and simulated p-polarized light reflectance spectra taken at 40 °incidence of 40 nm Ag gratings deposited at $\alpha = 0^\circ$ (regular) and $\alpha = 60^\circ$ (GLAD) in air; (#1-#3) FDTD-simulated E-field ($E_z/E_{z,0}$) for one period of GLAD structure showing E-field concentration at hot spots for different incident wavelengths; intensity bar is 0-10, and scale bar is 50 nm. 65

Figure 3-12 Experimental reflectance taken by ellipsometry for 40 nm silver HDDVD gratings: (a) regular grating ($\alpha = 0^\circ$) in the air, (b) GLAD grating ($\alpha = 60^\circ$) in the air. The blue arrows point out the additional peak from GLAD gratings compared with regular gratings. 66

Figure 3-13 Simulated E-field ($|E_z/E_{z,0}|$) distribution for 40 nm Ag regular (left) and GLAD (right) gratings coated with 30 nm PMSSQ in water environment at excitation and emission wavelength of Cy5: (a, b) Cy5 excitation ($\lambda = 642$ nm, $\theta = 0^\circ$); (c, d) Cy5 emission ($\lambda = 670$ nm, $\theta = 12.2^\circ$). (e) E-field distribution for Cy5 emission ($\lambda = 670$ nm, $\theta = 0^\circ$) and (f) corresponding E-field profile in the z-direction at nano-protrusion and nanogap region, and grating (10 nm apart from nano-protrusion). Intensity bar is 0-5, and scale bar is 50 nm..... 69

Figure 3-14 Simulated E-field ($|E_z/E_{z,0}|$) distribution for 40 nm Ag regular (left) and GLAD (right) gratings coated with 30 nm PMSSQ in water environment at excitation and emission wavelength of Cy3: (a, b) Cy3 excitation ($\lambda = 532$ nm, $\theta = 0.2^\circ$); (c, d) Cy3 emission ($\lambda = 570$ nm, $\theta = 2.6^\circ$). Intensity bar is 0-5, and the scale bar is 50 nm. (e) Simulated maximum $E_z/E_{z,0}$ at hot spots vs. incident angle for 40 nm Ag GLAD gratings coated with 30 nm PMSSQ in water environment at excitation and emission wavelength of Cy3 and Cy5. The angles with the maximum $E_z/E_{z,0}$ are as indicated. 71

Figure 3-15 Effect of Au coating on E-field and fluorescence. Simulated E-field distribution for 30 nm Ag GLAD grating with additional (a, b) 10 nm Ag and (c, d) 10 nm Au coating at excitation and emission wavelength of Cy5 taken at 0° incidence in water. E-field strength is plotted from 0 to 10. Note: Cy5 excitation wavelength = 642 nm, Cy5 emission wavelength = 670 nm. Fluorescence images (false-color) for (e) 40 nm Ag and (f) 30 nm Ag + 10 nm Au GLAD grating ($\alpha = 60^\circ$) with 10 μ M Cy5 in 30 nm PMSSQ coating; (g) corresponding mean and maximum enhancement factors with respect to the glass with 700 ms exposure time..... 74

Figure 3-16 Fluorescence and bright field images for 30 nm Ag GLAD grating ($\alpha = 60^\circ$) capped with different thickness of gold (a-c) 5 nm and (d-g) 10 nm, with 10 μM Cy5 in 30 nm PMSSQ coating. Bright field images: (b, e) before and (c, f) after T50 buffer solution overnight test. The scale bar for all images is 10 μm . (g) Corresponding mean and maximum enhancement factors with respect to the glass with 700 ms exposure time. 74

Figure 3-17 (a-e) A wide range of dye concentration for SM imaging on silver GLAD gratings ($\alpha = 60^\circ$): (a) the structure of Cy3/Cy5-labeled DNA-RNA duplex (excited Cy5 only with 642 nm red laser); (b) 50 pM and (c) 100 pM DNA/RNA duplex labelled with Cy3/Cy5, (d) 1 μM and (e) 10 μM Cy5 in PMSSQ matrix. Scale bar is 5 μm for all images. Representative time traces for 1 μM Cy5 at hot spots with single/double/multiple step bleaching behavior: (f-h) high-intensity levels (i-k) low-intensity levels, using 550 μW 642 nm laser taken with 60 \times objective in epifluorescence mode. (l-m) Representative time traces for 100 pM Cy3/Cy5-labeled DNA/RNA duplex at hot spots: (l) high-intensity levels (m) low-intensity levels. 76

Figure 3-18 Comparison of hot spot density between (a) AFM image using masking regions to expose protruding grains and (b) fluorescence image (false-color) of 10 μM Rhodamine 6G dye in a PMSSQ matrix using 60 \times water-immersive objective (NA=1.2) after background subtraction; (c) intensity vs. distance plot from fluorescence image; the inset image shows two analyzed hot spots and the cutting curve for profile analysis. The fluorescence images were taken by ORCA-Flash 2.8 CMOS camera. 78

Figure 3-19 Single molecules images to show the size and separation of nanostructures: Representative fluorescence image (a) one time frame fluorescence raw image before

super-resolution analysis and (b) super-resolution image after localization microscopy analysis (zoom in), and (c) corresponding 3D intensity map of nano-protrusions and (d) corresponding time trace to resolve nanostructures at different positions; (e) intensity vs. distance plot to show the size obtained from super-resolution fluorescence image; (f) height vs. distance plot of AFM image to show the size of nano-protrusions. Insets are corresponding fluorescence and AFM images with the cutting curve for profile analysis, and full width at half maximum (FWHM) for each fitting peaks. The fluorescence movies were taken by Andor iXon⁺ EMCCD camera..... 83

Figure 3-20 Statistical analysis for (a-d) AFM scan over large areas (30 μm×30 μm) of GLAD gratings and (e-g) super-resolution fluorescence image for GLAD grating coated with 1 μM Cy5: (a) AFM 2D profile to show how the nano-protrusion size, distribution and density changes with height (vertically cutting), and the red regions are selected for analysis; (b) representative AFM height vs. distance profile to show grain sizes by increasing the cutting height; (c) mean grain size and (d) grain density for AFM image (inset: masking the structures below height of 58 nm to show the nano-protrusion distribution); (e) representative intensity vs. distance profile to show spot sizes by increasing the cutting intensity, and the inset is corresponding 3D fluorescence profile; (f) mean spot size and (g) spot density for super-resolution fluorescence image (inset: showing hot spots distribution in a small area). Histogram of (h) nano-protrusion height obtained from AFM image and (i) fluorescence intensity of hot spots obtained from fluorescence image before localization microscopy analysis (Fig. 6c). 85

Figure 4-1 (a) Schematic of nanoparticles (nanoprisms/nanopyramids and cubical nanocages) on silver plasmonic gratings platform with dye coating, the brighter color of

fluorophores indicates that the fluorescence is enhanced by nanoparticles. (b-c) TEM images of silver nanoparticles: (b) large area image shows 50% yield of triangle structures, (c) higher resolution TEM image to show the triangle structure and (d) corresponding super-resolution fluorescence image by blinking localization microscopy. (e-f) 3D ground state depletion (GSD) microscopy on silver nanoparticles coated with 1 nM R6G on the grating platform: (e) fluorescence blinking time trace; (f) 3D reconstructed structures show nanoprism/nanopyramid structures. (g-j) Epi-fluorescence microscopy images: super-impose bright field (BF, false-color of orange hot) and fluorescence (FL, false-color of green) images for nanoparticles on (g) glass and (h) grating, the arrows point out the fluorescence showing up and enhanced by nanoparticle at this fluorescence time frame, and the triangle and circle shows the shape of nanoparticles seen from bright field; (i) representation bright field and fluorescence image (false-color: cyan hot) after localization blinking super-resolution microscope for one nanoprism on grating..... 93

Figure 4-2 (a) AFM 3D profile for thermally deposited silver gratings with 10 nm capping layer, the length and width are 3 μm . TEM of Nanoparticles with different scale bars (b) 100 nm and (c) 50 nm..... 94

Figure 4-3 (a) AFM 3D profile for thermally deposited silver gratings with 10 nm capping layer, the length and width are 3 μm . TEM of Nanoparticles with different scale bars (b) 100 nm and (c) 50 nm..... 94

Figure 4-4 (a-c) Airyscan microscopy: (a) fluorescence image for silver nanoparticles coated with 1 nM R6G on grating platform, (b) change the contrast of the fluorescence image to highlight the regions selected for spectra analysis, and (c) corresponding

emission spectra for nanoparticles, the arrows point out the fluorescence from R6G dye or silver nanoparticle based on the spectra. (d-g) Smartphone imaging for the silver nanoparticles samples through the eyepiece of epi-fluorescence microscope: (d) a demo to show the smartphone imaging platform; fluorescence images were taken by (e) 10×, (f) 40× and (g) 100× objectives. 96

Figure 4-5 smartphone imaging platform: fluorescence images taken by 100× objectives. 97

Figure 5-1 FDTD simulated E-field distribution of 80 nm Al nanoparticles (NPs) on different substrates: (a-c) flat silver, (d-f) silver gratings, (d) plain glass and (h) aluminum gratings, with different laser wavelengths including 408 nm, 532 nm and 650 nm under normal incidence (0 °) of light in oil (or nitrocellulose) environment. The E-field ($E_z/E_{z,0}$) scale is normalized to 0~5. Each condition shows a 3D view of E-field distribution (left) and the corresponding 2D view of the x-z plane (right). The scale bar in x-z plane is 200 nm. 100

Figure 5-2 FDTD simulated E-field distribution of Al nanoparticles with different sizes: (a) 50 nm, (b) 80 nm, (c) 120 nm, with 650 nm laser under normal incidence (0 °) of light in oil (or nitrocellulose) environment. The E-field ($E_z/E_{z,0}$) scale is normalized to 0~5. Each condition shows a 3D view of E-field distribution (left) and the corresponding 2D view of the x-z plane (right). The scale bar in x-z plane is 200 nm..... 101

Figure 5-3 FDTD simulated E-field distribution of two adjacent 80 nm Al nanoparticles with different arrangement on silver gratings: (a) align vertically to grating lines and (b) align parallel to grating lines, with laser wavelength of 650 nm under normal incidence

(0°) of light in oil (or nitrocellulose) environment. The E-field ($E_z/E_{z,0}$) scale is normalized to 0~5. Each condition shows a 3D view of E-field distribution (left) and the corresponding 2D view of the x-z plane, y-z plane and x-y plane (right). The scale bar in 2D view is 200 nm. The y-z plane view is a cross section with maximum E-field strength ($E_{z,max}/E_{z,0}$). 103

Figure 5-4 (a-c) Absorption and (d-f) scattering cross section of a single sphere aluminum nanoparticle with different aluminum radius ($r=25$ nm, 40 nm, 60 nm) in different medium: (a) air, (b) THV, (c) Nitrocellulose (NC). The thickness of the alumina shell is 2 nm for all models. 107

Figure 5-5 (a-c) Absorption and (d-f) scattering efficiency of a single sphere aluminum nanoparticle with different aluminum radius ($r=25$ nm, 40 nm, 60 nm) in different medium: (a) air, (b) THV, (c) Nitrocellulose (NC). The thickness of the alumina shell is 2 nm for all models. 108

Figure 5-6 Electric field strength (E/E_0) distribution of a single sphere aluminum nanoparticle with aluminum radius ($r=40$ nm) in THV at different peak wavelengths of 250 nm (quadrupole), 378 nm (dipole) and 810 nm. The thickness of the alumina shell is 2 nm for all models. 109

Figure 5-7 Electric field strength (E/E_0) distribution of a single sphere aluminum nanoparticle with aluminum radius ($r=40$ nm) in nitrocellulose (NC) at different peak wavelengths of 266 nm (quadrupole), 414 nm (dipole) and 810 nm. The thickness of the alumina shell is 2 nm for all models. 110

Figure 5-7 Schematic diagrams of 3D FDTD simulated silver plasmonic gratings with Al NPs. (a) x-z plane (side) and (b) y-z plane (front) and (c) x-y plane (top-down) views with color code: red = aluminum, yellow = Al₂O₃, gray = silver, and turquoise = THV. The orange horizontal bar represents the angled light source and the green one represents the photodetector, and the open purple box represents the simulation window. The open triangle indicates angle with respect to the axis view. The incident angle is calculated based on Snell's law, 70° incident from the air ($n=1$) corresponds to 43.7° in THV ($n=1.36$). (d) 3D schematic of six Al NPs on silver plasmonic gratings showing the arrangement of Al NPs..... 114

Figure 5-7 FDTD simulated E-field distribution of six 80 nm Al NPs on plasmonic silver gratings under laser wavelengths of 446 nm in THV matrix: (a) 3D side view and (b) 3D top view of E-field distribution and (c) the corresponding 2D view of the x-y plane. The scale bar in x-z plane is 200 nm. The relative z-component of E-field ($E_z/E_{z,0}$) scale is normalized to 0~2. The incident angle is calculated based on Snell's law, 70° incident from the air ($n=1$) corresponds to 43.7° in THV ($n=1.36$). 115

Figure 5-7 (A) Geometric Model. Anisotropic properties in (B) X direction (C) Y direction. The faces indicated in blue were joined with altered “effective” properties.. 116

Figure 6-1 (a) A schematic of the *in situ* fluorescence imaging platform to study photothermal heating of nanoenergetic thin film. The system consists of a plasmonic grating, microscope objective, fast camera, and external laser. (b) A schematic of the imaging setup for *in-situ* in fluorescence mode with a band-pass emission filter to block the excitation light and the laser. (c-d) Fluorescence images for Al/THV/R6G films on

gratings (c) before and (d) after 808 nm laser heating (200 mW, 4 s continuous wave (CW) exposure) with magenta laser spot superimposed.....	122
Figure 6-2 Al/THV/R6G film preparation on plasmonic grating and glass substrate. ..	124
Figure 6-3 Setup for microscope equipped with a heating stage for temperature calibration.	125
Figure 6-4 Schematic of the laser heating setup.	127
Figure 6-5 The 808 nm laser beam calibrated by CMOS camera with 20 °illumination (incident angle w.r.t. the sample surface). It shows a Gaussian distribution of laser power density over the area.	128
Figure 6-6 Temperature dependency of R6G spectra: (a) excitation and (b) emission spectra of the sample of THV-220V/R6G (1 μM)/Al films on grating heated from 30 °C to 65 °C in a microplate reader. Spectra recovery: excitation and emission spectra at 30 °C before and after one heating cycle on the sample (heated from 30 °C to 65 °C, and then cooled back to 30 °C). Data (a-c) were taken by microplate reader with built-in temperature control and normalized to maximum intensity at 30 °C. Fluorescence-temperature curve for THV-220V/R6G (1 μM)/Al films on gratings: (d) mean intensity and (e) normalized mean intensity with respect to the room temperature (RT), for analysis of Al and THV regions. (f) Photobleaching measurement by the background excitation light over time with and without 25% and 6% neutral density (ND) filters. Data (d-f) are taken by 40× air objective in an epi-fluorescence microscope equipped with a heating stage.	129

Figure 6-7 Effect of plasmonic gratings and Al NPs on laser heating. Fluorescence images for THV/R6G films (a) with and (b) without Al NPs on gratings, before and after 808 nm laser heating (60 mW, 4 s exposure) and the corresponding fluorescence difference. (c) Mean intensity, (d) temperature change and temperature, (e) heating rate under 808 nm laser heating (60 mW, 4 s exposure). All data were taken by 40× air objective in the epi-fluorescence microscope. The mean value is obtained by analysis in the large area indicated as a black rectangular box in a..... 131

Figure 6-8 Comparison between the low power (33 mW) and high power (200 mW) of laser input for *in-situ* fluorescence and temperature monitoring for Al/THV/R6G films on gratings with exposure to 808 nm laser for 4 s. Dynamic temperature map for different laser input power (a) 33 mW and (b) 200 mW over time. All images are false-color images. (c) Mean fluorescence intensity and corresponding temperature over time; (d) Heating rate calculated by the first derivative of temperature change over time; (e) Heating rate vs. The temperature for different powers and substrates. All data are taken by 40× air objective in the epi-fluorescence microscope. The mean value is obtained by analysis in the large area indicated as a green rectangular box in a-b. 134

Figure 6-9 *In-situ* fluorescence and temperature monitoring for Al/THV/R6G films on gratings with exposure to 200 mW 808 nm laser for 4 s: (a) Laser scattering to show the laser power intensity distribution; (b) Start (initial fluorescence, $I_0=I_{RT}$); (c) During laser on (I_{on}): the frame shown is right at 4 s radiation before laser off; (d) After laser off (I_{off}): after exposure to 808 nm laser for 4 s; (d) Intensity difference (=initial fluorescence – fluorescence during laser on, i.e. $\Delta I= I_{on} - I_0$). All images are false-color images, taken by 40× air objective in the epi-fluorescence microscope. The circles point out the Al NPs

and THV, and the rectangle points out the large area with laser heating. Temperature monitoring over time: (f) Comparison among Al NPs in the high and low power density regions; (g) Comparison among Al NP, THV and a large area in the high power density region. 138

Figure 6-10 Al NPs *in-situ* movement monitored by fluorescence images of Al/THV/R6G films on gratings with exposure to 200 mW 808 nm laser for 4 s. (a) Laser scattering to show the laser power intensity distribution; (b) fluorescence induced by the laser; (c) fluorescence intensity change over time. All images are false-color images, taken by 40× air objective in the epi-fluorescence microscope. 139

Figure 6-11 Al NPs *ex-situ* movement monitored by bright field and fluorescence images of Al/THV/R6G films on gratings after exposure to 200 mW 808 nm laser for 4 s. (a) Bright field images (gray color) before and after 200 mW laser irradiation to show the movement direction for Al NPs at different locations indicated by red arrows. The image at the back superimposes fluorescence (green) after 200 mW laser irradiation and laser spot (magenta). The yellow rectangular boxes mark down important interesting areas (#1-#6). (b-c) Comparison between the bright field (gray color) and fluorescence image (green color) before laser heating, and after exposure to 33 mW and 200 mW lasers for 4 s for the data of #2 Al aggregates. Deconvolution imaging processing was applied to increase the contrast of the image. The scale bar for b-c is 5 μm. All images are false-color images, taken by 40× air objective in the epi-fluorescence microscope. All bright field and fluorescence images before, after exposure to 33 mW and 200 mW lasers were outlined by dark blue, green, and orange, respectively. 141

Figure 6-12 Comparison between (a) bright field and (b) fluorescence image for Al/THV/R6G films on gratings after exposure to 808 nm laser heating (200 mW, 20 ° incidence with respect to the horizontal line) for 4 s. All images are false-color images, taken by 40× air objective in the epi-fluorescence microscope. The scale bar is 20 μm. The red rectangular boxes mark down important interesting areas for further analysis. 142

Figure 6-13 Comparison between bright field (gray color) and fluorescence image (green color) for Al/THV/R6G films on gratings (1) before laser heating, and after exposure to 808 nm laser heating (20 ° incidence with respect to horizontal line) for 4 s with different powers (2) 33 mW and (3) 200 mW. All images are false-color images, taken by 40× air objective in the epi-fluorescence microscope. The scale bar is 5 μm. The interesting areas #1-6 in this analysis are marked as the red rectangular boxes in **Figure 6-12**. 143

Figure 6-14 (a-b) FDTD simulated E-field distribution of 80 nm Al NP on different substrates: (a) plain glass (b) silver gratings under laser wavelengths of 808 nm in THV matrix. The relative z-component of E-field ($E_z/E_{z,0}$) scale is normalized to 0~2. Each condition shows a 3D view of E-field distribution (left) and the corresponding 2D view of the x-z plane (right). The scale bar in x-z plane is 200 nm. The incident angle is calculated based on Snell’s law, 70° incident from the air ($n=1$) corresponds to 43.7 ° in THV ($n=1.36$). (c) Comparison of the maximum temperature change (ΔT_{max}) vs. laser power between the COMSOL simulated value and experimental value on the plasmonic silver grating and the glass substrate. 144

Figure 6-15 *In-situ* measurement of 446 nm blue laser heating of the Al/THV/R6G films on (a,c) gratings and (b,d) glass. All data were taken by 40× air objective with the 2.5× adaptor in epi-fluorescence microscope..... 147

Figure 6-16 Fluorescence of the THV/R6G films (a,b) with and (c,d) without Al NPs on gratings (a,c) before and (b,d) after blue laser heating. All data were taken by 20× air objective with the 2.5× adaptor in the epi-fluorescence microscope..... 148

Figure 7-1 A schematic of the *in situ* analysis platform to study nanoenergetic thin film morphology and combustion. The system consists of a plasmonic grating microchip, microscope objective, fast camera, and external laser. 153

Figure 7-2 The preparation of THV, namely, poly(TFE-co-HFP-co-VDF). 154

Figure 7-3 A schematic of the imaging setup for *in-situ* and *ex-situ* imaging. (a) *In-situ* imaging setup using the bright field in reflection mode with background light, and with a long-pass filter to block the laser. (b) Profile of laser beam directly measured by CMOS at an incident angle of 70 °, (c) laser scattering from the sample after aligning and focusing on the Al NPs of interest, (d) bright field image of Al/THV film on plasmonic grating, (e) superimposed image of laser and bright field to match laser location and Al NPs, (f) the grating lines imaged under 40× objective by blue laser. All images were taken by the fast color camera. (g) *Ex-situ* imaging setup using polarization microscopy for scattering imaging by blocking the incident light with a combination of polarizer and analyzer. Images of single Al NP on a plasmonic grating microchip: (h) SEM, (i) scattering, (j) bright field. The scattering and bright field images were taken under 100× oil-immersive objective by the black and white camera; both images were false color images. 158

Figure 7-4 (a) Summary of the relationship between power (and peak energy flux) and phenomena for both silver grating microchip and flat silver platform. Comparison

between (b-c) silver gratings and (d-e) flat silver for laser ignition. All data were taken by a fast camera in an epi-fluorescence microscope equipped with a 40× air objective with the 2.5× adaptor under modified FITC filter. 160

Figure 7-5 DSC/TGA measurement for (a) THV and (b) Al/THV(30/70) composites. 163

Figure 7-6 *In-situ* imaging (0-400 μs) of 446 nm blue laser ignition for Al/THV film on plasmonic silver gratings with different laser powers of (a) 255 mW (0.32 mW/μm² peak), (b) 1080 mW (1.35 mW/μm² peak), and (c) 1500 mW (1.88 mW/μm² peak). All data were taken by a fast speed camera in an epi-fluorescence microscope equipped with a 40× air objective with the 2.5× adaptor under modified FITC filter. Red arrows indicate flames in excess of 1 μm in size, while white arrows indicate sub-micron nano-flames. The red dashed circles indicate the solid to the liquid melting front, and the blue dotted circles indicate the location of vapor-liquid boundaries. The extended dashed profile in (a-b) indicates the spatial envelope of thermal diffusion with time. Solid lines at 350 μs in (b) indicate aligned mobile Al NPs being carried by merging melting fronts..... 165

Figure 7-7 Phase change of THV before, during and after 446 nm blue laser ignition for Al/THV film on plasmonic silver gratings with a laser power of 1080 mW. (a) 2D x-y image sequences for the first pulse with 1 ms laser on and 30 ms laser off, and the image with THV re-solidification by removing the laser after 20 pulses. (b) Time (t , μs) vs distance (x , μm) plot by reconstructing the x-axis in the middle of the whole image sequences for the first three pulses out of 20 pulses. The red dashed curves indicate the trend of phase change region when the laser was on and off; the white arrows indicate some of the flames during laser exposure; the pink arrows indicate the fluctuation of phase change. All data were taken by a fast speed camera in an epi-fluorescence

microscope equipped with a 40× air objective with the 2.5× adaptor under modified FITC filter..... 168

Figure 7-8 Two-color pyrometry analysis. (a) Before and (b) *In-situ* ignition imaging of Al/THV film on plasmonic silver gratings with laser powers of 1080 mW. *In-situ* images were taken by a high-speed camera in an epi-fluorescence microscope equipped with a 40× air objective with the 2.5× adaptor under modified FTIR filter without background light. The white numbers indicate isolated combustion events. (c) Comparison of bright field, *in-situ* flame image, and corresponding temperature maps. (d) The temperature profile of single nano-flame from position F1, with FWHM of 600 nm. (e) Histogram of all flame temperatures observed in 1 ms pulse. 171

Figure 7-9 (a) Simulated absorption efficiency of a single Al NP embedded in fluoropolymer oxidizer THV; the inset is the E-field distribution at 446 nm and 808 nm for 80 nm Al NP with normalized E-field scale of 0-5. FDTD simulated E-field distribution of 80 nm Al NPs on different substrates: (b) plain glass (c) flat silver, (d-g) silver gratings under laser wavelengths of 446 nm in THV matrix. The relative z-component of E-field ($E_z/E_{z,0}$) scale is normalized to 0~2. Each condition shows a 3D view of E-field distribution (left) and the corresponding 2D view of the x-z plane (right). The scale bar in x-z plane is 200 nm. The incident angle is calculated based on Snell's law, 70° incident from the air ($n=1$) corresponds to 43.7° in THV ($n=1.36$). 172

Figure 7-10 (a-b) Comparison of theoretical threshold fluence (J_{th}) for Al/THV energetic system (solid lines) and experimental laser fluence (J_c) with laser powers of 255 mW, 1080 mW and 1500 mW (dashed lines). (c) Maximum Al NP temperature at the end of the laser pulse as a function of laser power for different numbers (N) of Al NPs..... 177

Figure 7-11 Optical scattering before and after laser ignition for Al/THV films on plasmonic silver gratings. Low-resolution images: bright field (a) before and (b) after laser ignition; scattering (c) before and (d) after laser ignition. The data were taken by 40× air objective with the 2.5× adaptor in the epi-fluorescence microscope by the fast camera. The red and white arrows indicate the reacted and unreacted spots, respectively. High-resolution images: scattering (e) before and (f) after laser ignition. The data were taken by 100× oil objective with the 2.5× adaptor in the epi-fluorescence microscope by the black and white camera. (g) *In-situ* imaging of 446 nm laser ignition for Al/THV film on silver gratings and the red arrows show the flame propagation. (h) *Ex-situ* imaging of scattering before ignition for identification of the combustion sites. 178

Figure 7-12 The minimum laser pulse time required to (a) melt solid Al and (b) vaporize solid Al with different E-field enhancement..... 182

Figure 7-13 Schematics showing the heat map reconstruction using Two-color Pyrometry..... 185

Figure 7-14 Designing of adaptor using OpenSCAD 186

Figure 7-15 Illustration showing the optical setup for taking the flame spectrum using a USB-4000 spectrometer and flame imaging using the Phantom V7.3 fast camera simultaneously. 187

Figure 7-16 Temperature vs. G/R channels gray intensity ratio of our optical system with the V7.3 Phantom fast camera through camera port..... 188

Figure 7-17 Temperature vs. G/R channels gray intensity ratio of our optical system with the V7.3 Phantom fast camera. The curves were calibrated through camera port and eyepiece port, respectively..... 189

Figure 7-18 Spectrum of the laser with and without filtering the main laser peak. Al/THV on gratings exposed to 90 mW 466nm pulse laser (10 ms on) without background light. With filter was measured under FITC, and without the filter was measured under DAPI..... 190

Figure 7-19 (left) Spectrum and (right) after system response calibration and fitted with the blackbody emission model for laser ignition study. Al/THV on gratings exposed to 1080 mW 466nm pulse laser (1 ms on and 49 ms off, 30 pulses) without background light, under FITC emission filter. 192

Figure 7-20 Spectra for FITC filter set including excitation, dichroic and emission filters. 192

Figure 7-21 Fitted temperature (K) vs. pulse number (#). Al/THV on gratings exposed to 1080 mW 466nm pulse laser (1 ms on and 49 ms off, 30 pulses) without background light, under FITC emission filter. 193

Figure 7-22 Calibrated and fitted spectra for laser ignition study over multiple pulses. Al/THV on gratings exposed to 1080 mW 466nm pulse laser (1 ms on and 49 ms off, 30 pulses) without background light, under FITC emission filter. The figure (top) shows the calibrated spectrum at the 28th pulse, and the figure (right) shows the intensity dependency at 615.9nm over time. 193

Figure 7-23 Spectrum for laser ignition study on the flat silver region (two different areas). Al/THV on flat silver exposed to 1080 mW 466nm pulse laser (1 ms on and 49 ms off, 30 pulses) without background light, under FITC emission filter. 194

Figure 7-24 Temperature map reconstruction of the flame or “hot carbon”. Al/THV on gratings exposed to 1080 mW 466nm pulse laser (1 ms on and 49 ms off, the 30th pulse in 30 pulses) without background light, under FITC emission filter. 196

Figure 7-25 (Left) Green and (Right) red channel images with different intensity bar to show different visible structures. Al/THV on gratings exposed to 1080 mW 466nm pulse laser (1 ms on and 49 ms off, the 30th pulse in 30 pulses) without background light, under FITC emission filter. 197

Figure 7-26 The statistical analysis for frequency vs. temperature (right) of the flame in all frames (0-1 ms). Al/THV on gratings exposed to 1080 mW 466nm pulse laser (1 ms on and 49 ms off, the 30th pulse in 30 pulses) without background light, under FITC emission filter. 198

Figure 7-27 Temperature map reconstruction of the small local flame. Al/THV on gratings exposed to 1080 mW 466nm pulse laser (1 ms on and 49 ms off, 350 μ s in the 1st pulse of 30 pulses) without background light, under FITC emission filter. 198

LIST OF TABLES

Table 2-1 Maxwell equations.....	14
Table 2-2 The specification of different fluorescence filter sets in the experiment (black), and excitation and emission peaks for fluorescence bead under different filter set (red). Unit: nm	40
Table 3-1 Average grating pitch, height, and nano-protrusion height above the ridge and nanogap width obtained by AFM.	57
Table 3-2 The Rayleigh diffraction limit (in nanometers) given different wavelengths and different objective lenses.	80
Table 7-1 Thermal expansion of Al and Al ₂ O ₃	181

Chapter 1. Introduction

1.1 Plasmonics

Plasmonics studies the coupling of photons to the oscillation of free electrons in metals.[1]–[3] The electric component of incident light can excite conduction electrons to collective oscillations at the interface between a negative and positive permittivity material under resonant condition.[1], [2] This phenomenon is known as “surface plasmon resonance (SPR)”. The wave nature of electromagnetic wave leads to the diffraction limit which is around half of the wavelength. Nevertheless, in the case of SPR, the strong confinement and enhancement of electromagnetic field localized near the metal surface enable the applications such as fluorescence enhancement[4]–[6], surface-enhanced spectroscopy (SERS)[7], [8], optoelectronic circuits, and subwavelength optics[2]. Therefore, the plasmonic nanostructures are very promising for super-resolution imaging.[9] Due to the electromagnetic resonances highly relying on the details of the nanostructure, SPR is perspective in controlling light confinement on the nanoscale.[3] During the plasmon oscillation, there is inevitable energy loss owing to the Ohmic loss [1] and electron-core interactions in the metal. Generally, this is considered to be detrimental to most plasmonic devices by limiting their performance due to the nonradiative surface plasmon relaxation [10], especially for high-loss metal like aluminum (Al). However, the heat generated by the loss (i.e. absorption) in the metal can contribute to photothermal heating, opening up the opportunity for application in light-induced nanoenergetic heating and combustion.[11]

A variety of plasmonic nanostructures has been developed and fabricated, such as nano-sphere, nano-rod, nano-cube, nano-prism, and nano-gratings. Different from the localized surface plasmon resonance (LSPR) generated by separated nanoparticles, plasmonic gratings create propagating surface plasmon (PSP) that can travel on the metal surface. Metallic gratings are typically fabricated by expensive fabrication techniques traditionally used for nanoscale patterning such as e-beam lithography. Our group has developed a proprietary low-cost method for fabricating tunable nanostructured plasmonic gratings using CDs, DVDs, HD-DVDs, and Blu-rays as master grating molds [4], [5], [7], [9], [12]–[22]. Plasmonic gratings are fabricated as hybrid soft/hard nanostructures by first imprinting polymethylsilsesquioxane (PMSSQ) as a polymer ink using the intrinsic periodic grating structures of HD-DVDs followed by deposition of a thin plasmonic layer such as Ag, Au, and Al.[23]–[27]

In our previous studies, the nanogap-embedded gratings were utilized for single molecule (SM) studies using epifluorescence microscope. DNA/RNA duplex molecules tagged with Cyanine 3 (Cy3) and Cyanine 5 (Cy5) fluorophores were immobilized on SiO₂-capped gratings. The SM fluorescence intensity of fluorophores on nanogaps showed approximately 100-fold mean enhancement with respect to fluorophores observed on quartz slides in epifluorescence mode.[6] Not only are single molecules identifiable by single-step photobleaching, but intermediate fluorescence dynamics was observed with the unprecedented scale at the intersection of nanogaps with the plasmonic gratings. The results show that molecules located deep within the nanogaps exhibit sub-1 Hz fluorescence intensity oscillations with a strong dependence on magnesium chloride concentration.[13] However, Förster resonance energy transfer (FRET) for Cy3/Cy5-

labeled DNA/RNA duplex molecules cannot be detected with this extant plasmonic grating due to directed surface plasmon-coupled emission (SPCE), which results in low capture efficiency of Cy5 emission.

1.2 Super-resolution Imaging

Optical microscopy is a popular imaging method in biological research, due in part to its ease of use in visualizing complex microstructures and relatively non-invasive nature.[28], [29] However, the spatial resolution of conventional optical microscopy is limited by approximately half the wavelength of light used (~200-400 nm). This resolution is substantially larger than the typical molecule length scale, restricting it from many applications in nanoscience and nanotechnology.[30] Super-resolution microscopy can overcome this fundamental diffraction limit to achieve spatial resolutions of only a few nanometers.[28]–[33] Super-resolution techniques can be divided into two categories: (1) “true” and (2) “functional” super-resolution. True super-resolution techniques involve the capture of the high spatial frequency information contained in evanescent waves[34]–[39], such as near-field scanning optical microscopy (NSOM), or by converting evanescent waves into a propagating wave that can be imaged in far-field using a superlens.[40] Functional super-resolution techniques reconstruct super-resolution images using known system limitations, series of diffraction-limited images, and mathematical models. These techniques include photo-activated localization microscopy (PALM or FPALM)[41], [42], stochastic optical reconstruction microscopy (STORM)[43], [44], and stimulated emission depletion (STED) microscopy.[45]

These various super-resolution techniques have facilitated numerous research

breakthroughs but are still limited by technique-specific restrictions and resolution limits. For example, NSOM and other probe-based techniques utilize a sharp probe in the near field to collect evanescent wave information.[46] Tip-based techniques are generally limited to scanning hard surfaces and require lengthy scan times, which greatly limits their application in live imaging biological systems, such as cells.[39] Unlike probe scanning techniques, PALM and STORM are techniques that utilize photo-switchable fluorophores to separate the spatially overlapping single molecules in each image, enabling the construction of high-resolution images. These techniques typically require high fluorophore labeling density and sometimes require the use of a total internal reflection fluorescence microscopy (TIRFM) or a confocal microscope for best results.[31] Overall, most super-resolution techniques require expensive and complex instrumentation, highly trained operators, and lengthy imaging periods. Therefore, it is important to develop novel super-resolution approaches that are cost-effective, easy to operate and rapid data acquisition.

1.3 Nanoenergetic

1.3.1 Al/fluoropolymer nanoenergetic system

Improved synthesis and metrology capabilities continue to advance nanoenergetics[47]–[53] towards applications in chemical propellant microthrusters[54], [55], explosive devices[56], [57], medical therapeutic devices[58]–[60], bio-film neutralizers[61], and micro-fluidic actuators[62]. Nanothermites typically consist of a heterogeneous mixture of nanoscale particulate fuels (for example, aluminum, silicon, and lithium) and oxidizers (for example, metal oxides including bismuth trioxide, copper oxide,

and molybdenum oxide; polymer oxidizer including Teflon, and nitrocellulose).[52], [54]–[56], [58], [63] In general, the rate of reaction for the thermites is restricted by heat and mass transfer.[64] When compared to conventional thermites, nanothermites significantly reduce heat and mass diffusion lengths of the reactants while increasing the packing density of constituent materials, resulting in substantially higher energy densities[64], [65].

Aluminum and polymer energetic systems are of particular interest for various energetic materials applications due to high volumetric energy capacity, ease of film processing, and multi-functionality as both a structural element and an explosive element[61], [64], [66], [67]. For example, Al/Teflon has a theoretical heat of combustion of 21 kJ/cm^3 , approximately 3 times of the value of trinitrotoluene (TNT)[67]. Fluorine-containing oxidizers in Al-based thermite reactions achieve higher peak pressure and more gas production than oxygen-containing oxidizing agents.[68] The current study utilized aluminum nanoparticles (Al NPs) as fuel with fluoropolymer oxidizers made of a terpolymer of tetrafluoroethylene, hexafluoropropylene, and vinylidene fluoride (THV). THV shares similar composition with Teflon, but its mild combustion characteristics facilitates the use of Al/THV for biological application without damaging the underlying specimen or substrate[61]. Additionally, the excellent optical clarity, high optical transmission, and low absorption of THV are beneficial for efficient photothermal heating of Al NPs from external stimuli.

1.3.2 Photothermal heating of nanoenergetics

Photothermal heating of nanoenergetic materials provides a non-contact, non-invasive, localized, and rapid heat generation mechanism. Numerous researchers have

utilized near-infrared (NIR) lasers to heat Al NPs by activating the Al dielectric loss. Examples include 1053 nm wavelength pulses from a Nd : YLF(yttrium lithium fluoride) laser[66], [67], [69], [70],1064 nm wavelength pulses from Nd : YAG(yttrium-aluminum-garnet) laser [71], [72], 800 nm wavelength pulses from a Ti : sapphire laser[73]. The plasmonic photothermal heating of Al NPs at visible wavelengths, however, has been sparsely explored for energetic applications. The localized surface plasmon resonance (LSPR) of Al NPs for improvement of photothermal effect was only studied by a xenon flash lamp with broad spectra.[74] The threshold ignition energy fluence for embedded Al NPs is a strong function of laser pulse duration, mainly due to time-dependent diffusive losses to the particle surroundings.[75] Correspondingly, short-pulse nanosecond or picosecond lasers with a high flux in order of magnitude of 10^4 - 10^5 mW/ μm^2 are often required for photothermal ignition of nanothermite systems.[66], [67], [69], [71]–[73], [76] Methods to locally enhance the electric field around Al NPs could significantly reduce the threshold fluence, providing a potential means of igniting nanothermites with less expensive and more commercially available low power lasers.

1.3.3 Reaction Processes of Al/fluoropolymer nanoenergetics

The reaction processes of Al/THV nanoenergetic system include depassivation, initiation, ignition, and combustion.[67], [69] **Depassivation** refers to the active Al fuel released from its passivating Al_2O_3 shell so that the oxidizers can contact and react with the fuel. There are several possible ways of depassivation: (1) the perforation of the oxide shell allows external oxidizers to enter and react with Al core, which was proved by multimillion atom simulations for flash-heated Al/ Al_2O_3 core–shell nanoparticles with O_2

oxidizer[77]–[79]; (2) the mechanically-induced spallation of core–shell nanoparticles disperse the Al fuel out to the surrounding oxidizer under fast heating, whose theory was proposed by Levitas et al [80]–[82]; (3) the Al_2O_3 is melted and the Al core is almost vaporized when it reaches the threshold energy density of a laser flash-heating, which was demonstrated by ultrafast emission spectroscopy showing vapor Al/Teflon reactions exhibit the rate of energy release with a ~ 100 ps lifetime[83]; (4) the fluorination of Al_2O_3 shell to expose Al core to the oxidizers, and this pre-ignition reaction (PIR) between Al_2O_3 /fluoropolymer is only significant in nanoenergetics of Al fuels in nanosize rather than those in microsize[84]. The onset temperature for PIR occurs from 371.7 °C to 418.2 °C as the Al_2O_3 diameter decreasing from 50 nm to 15 nm[84]. **Initiation** refers to the onset of chemical reactions in energetic materials.[67], [69] In the initiation process for Al/fluoropolymer, Al strips fluorine from polymer chains requiring input energy to break C–F bonds, which is an endothermic process. Time-resolved infrared absorption spectroscopy indicates two phases of reaction occurring on the 50 and 700 ps for flash-heating initiation of Al/Teflon.[73] **Ignition** refers to the onset of Al-oxidizer chemical reactions that produce large amounts of heat and light when the nascent products are formed, such as aluminum fluorides (e.g., AlF) generated in electronically and vibrationally excited states, whose excess energy is released into the surroundings.[67] **Combustion** involves the phenomena of local hot spot formation, propagation, and energy release after ignition.[69] The material structures of Al NPs and oxidizer break down due to the chemical reaction. The exothermic process of the phase transition of the reaction product AlF_3 from β to α phase happens at roughly 550 °C.

The combustion temperatures (>2000 °C) are sufficient to melt and sublime the

reaction product AlF_3 ($T_m = 1291\text{ }^\circ\text{C}$), which may then degrade or remove the diffusion barrier between remaining reactant species.[85] Therefore, the formation of AlF_3 as a product accelerates the reaction for Al/THV compared to the formation of Al_2O_3 for oxygen-containing oxidizers. Additionally, the high combustion temperature can also help to depassivate Al NPs nearby the reaction center through the reaction between the fluoropolymer and the oxide shell. The Al_2O_3 shell (melting point of $2072\text{ }^\circ\text{C}$) can be etched or removed at a much lower temperature due to the conversion into AlF_3 gas. Even though the solid phase of AlF_3 is formed or left on the nanocomposites, the melting point of the shell layer is still reduced compared to Al_2O_3 . The fluorination of the Al_2O_3 shell passivating the Al particles can cause unique pre-ignition reaction and reduces the onset temperature of Al ignition[84]. Overall, THV and Al_2O_3 can form AlF_3 and CO_2 gaseous products.

1.3.4 Diffusive oxidation mechanism vs. melt dispersion mechanism

For diffusive oxidation mechanism, outward diffusion of Al through the oxide shell is possible before and after the melting of Al, but the diffusion of Al is a very slow process in the timescale of several seconds. Above the melting temperature of Al, outward diffusion of Al ions through the oxide shell predominates, and the reaction interface is located at the external surface.[86] However, the growth of Al out of the oxide shell due to diffusion of Al ions is only several nanometers in thickness attached to the shell[86], which is much less than microns usually shown in the bursting flame by microscope, so this mechanism is not suitable for explaining the above phenomena. One possibility is the diffusion of hot Al atoms generated by the vaporization of Al ($>2470\text{ }^\circ\text{C}$) due to fast laser heating, which

is even able to diffuse through the solid state of THV without the necessary of phase change of THV. Therefore, the atomic diffusion of vaporized Al plasma[83] is possible to travel several micrometers and then start the atomic reaction of Al with THV.

For melt dispersion mechanism, Levitas et al[47], [68], [80], [82] predicted in theory and confirmed by experiment that this model is suitable for fast reaction of Al NPs with the heating rate at 10^6 - 10^8 K/s. The melt dispersion mechanism postulates that the fast melting of the Al core of the nanoparticles creates high internal pressure in the order of 1-3 GPa inside the Al_2O_3 shells due to the volume expansion until dynamic spallation occurs when the hoop stresses exceed the ultimate strength of Al_2O_3 . The spallation generated by such a high pressure releases a radial dispersion of molten Al at high velocities (100-250 m/s)[68], which is possible to happen even when the fluoropolymer is in the solid state. The time required to fly dispersed molten Al over a distance of 1 μ m is 4-10 ns within one imaging frame of 50 μ s that will be discussed in **Chapter 7**. Subsequently, the smaller pieces of Al after spallation is free to react with the adjacent THV. Since it took less than 50 μ s to melt Al (>663 °C), the heating rate is estimated above 10^7 K/s. The entire process including photothermal heating of Al until melting, spallation of Al, and reaction with THV to generate flame, finishes within 50 μ s captured by the fast camera.

1.3.5 Characterization tools

In situ characterization of nanoenergetic systems is key for understanding the reaction kinetics of these systems. The large-scale combustion performance of large amounts of nanoenergetic materials is traditionally measured using photodiodes, pressure transducers, and spectrometers.[57], [63], [65] While this data provides critical information

regarding the bulk combustion properties and pressure generation rate of relatively large quantities of material, investigating the behavior of individual nanoenergetic material grains traditionally requires scanning electron microscopy (SEM) or transmission electron microscopy (TEM) interrogation. Dynamic transmission electron microscopy (DTEM) has recently been utilized by Zachariah et al.[72] to observe Al NPs *in-situ* reactions. Particle morphology variations were initiated within 15 ns and were completed in less than 50 ns when heated by a 1064 nm wavelength pulsed laser producing rapid heating (10^6 – 10^{11} K/s).[72] While *in-situ* DTEM diagnostic is powerful, it is not readily available, specimens must be ultra-thin, and a small field of view facilitates observation of only a few particle interactions. Two-color pyrometric methods are another important *in-situ* techniques that have been widely used in noncontact temperature measurement, due to the non-invasive nature and real-time imaging capability.[87] Accurate, reliable measurements of 3D flame temperature distributions are highly desirable to achieve an in-depth understanding of combustion and reactant formation processes. Due to the thermal and dynamic nature of the flame, an effective means for the spatial and temporal measurement of the flame temperature of individual Al NP combustion events remains a challenge for combustion and measurement researchers.

1.4 Scope of This Dissertation

This dissertation is divided into 7 chapters for plasmonic platforms for super-resolution imaging and photothermal heating as well as applications for biological materials and combustion diagnostics of Al-polymer nanoenergetic systems. **Chapter 1** introduces the background for plasmonics, super-resolution imaging, and nanoenergetics.

Chapter 2 first describes the basic theory of plasmonic gratings, and the design of grating structures and coupling condition for different applications were simulated by finite-difference time-domain (FDTD) algorithm to study the electric field and optical response. Second, the theory of super-resolution imaging techniques including localization microscopy and superlens were discussed, and then the combination of these techniques with plasmonic grating platforms was demonstrated.

Chapter 3 and **Chapter 4** describes the application of super-resolution imaging using plasmonic grating platforms. **Chapter 3** reports a glancing angle deposition (GLAD) technique to fabricate plasmonic nanostructures combining periodic gratings with nano-protrusion for single molecule super-resolution imaging. We studied the single-molecule behavior of Cy3/Cy5-labeled DNA/RNA duplex and dye-doped polymer films. The GLAD platform allows simultaneous imaging of a large area of single Cyanine-5 molecules in wide dye concentrations ranging from 50 pM to 10 μ M under an epifluorescence microscope. The combination of the near-field plasmonic nano-protrusion probes and localization microscopy can resolve grain sizes down to 65 nm. **Chapter 4** discusses subwavelength nanoparticles with various shapes were investigated on the plasmonic grating platforms in both fluorescence and bright field mode. We first utilized current super-resolution approaches including ground state depletion (GSD) microscopy and Airyscan microscopy to confirm the structure of nanoparticles, and then we reconstructed the size and shape of nanoparticle on our platforms by localization microscopy.

Chapter 5 describes the basic theory of plasmonic photothermal heating, and calculates the electric field of combining the plasmonic grating and Al NPs by FDTD simulation. COMSOL models photon to phonon conversion and thermal characteristics of

Al-polymer nanoenergetic. We investigate the scattering, absorption and electric field of Al NPs in different polymer oxidizers, and predict the photothermal heating for our systems.

Chapter 6 and **Chapter 7** demonstrate the plasmonic grating microchips for enhancing and diagnosing the laser-induced photothermal heating and combustion of Al-THV nanoenergetic films. **Chapter 6** reports a dynamic thermal mapping with temperature sensitive dyes to study the early stages of Al NPs heating behavior pre-ignition. The temperature map shows that Al NPs is key for photothermal heating in the Al-THV system. The plasmonic gratings enhance the photothermal heating of nanoenergetic system further due to the light coupling. **Chapter 7** describes the laser-induced combustion behavior of Al/THV films investigated by simultaneously using emission spectroscopy and *in-situ* high-speed microscopic imaging. The flame temperatures are recorded using calibrated two-color pyrometry from color imagery. The phase change of THV due to the photothermal heating of Al and exothermic reaction, reactive sintering, and flame propagation properties was investigated using the setup.

Chapter 2. Theory for Plasmonic and Super-Resolution Imaging

2.1 Design of Plasmonic Gratings

FullWAVE software (RSoft, Inc.) was used to simulate the theoretical reflectance, electromagnetic (EM) field distribution, and EM field enhancement resulting from the light interaction of plasmonic grating platform to guide the different application. FullWAVE employs the Full-vector, Finite-difference Time-domain (FDTD) algorithm to provide solutions to Maxwell's equations by discretizing time and space domains. First, we simulated surface plasmon resonance (SPR) dispersion curve for the grating with different grating pitches and heights including HD-DVD and Bluray and in different environments, such as air, water and oil. The SPR dispersion curve was then compared with experimental values. Second, we designed the grating microchip configuration by varying the metallic layer thickness of the device. Finally, we discuss the basic theory of super-resolution imaging, especially for the grating structures, and then the incorporate it for fluorescence imaging, and points spread function studies.

2.1.1 Dispersion relation of Surface Plasmons

Surface plasmons (SPs) are coherent free electron oscillations at the metal-dielectric interface. [9], [15], [20], [22] Surface plasmon polaritons (SPPs) represent waves involving both free electron motion travelling at the metal surface termed as "SPs" and electromagnetic waves in dielectric termed as "polariton". The electromagnetic behavior of SPs can be explained by deriving the four basic Maxwell equations, whose differential

forms and corresponding laws are given below:

Table 2-1 Maxwell equations

Name	Differential equations
Gauss's law	$\nabla \cdot \mathbf{E} = \frac{\rho}{\epsilon_0}$
Gauss's law for magnetism	$\nabla \cdot \mathbf{B} = 0$
Faraday's law of induction	$\nabla \times \mathbf{E} = -\frac{\partial \mathbf{B}}{\partial t}$
Ampère's circuital law	$\nabla \times \mathbf{B} = \mu_0(\mathbf{J} + \epsilon_0 \frac{\partial \mathbf{E}}{\partial t})$

In addition, the electric and magnetic quantities follow the material equations:

$$\mathbf{D} = \epsilon_0 \epsilon(\omega) \mathbf{E} \quad (2.1)$$

$$\mathbf{B} = \mu_0 \mu(\omega) \mathbf{H} \quad (2.2)$$

where \mathbf{E} is the electric field (V/m), and \mathbf{H} is the magnetic field (A/m), \mathbf{D} is the electric field displacement (C/m²), \mathbf{B} is the magnetic field strength (N/A/m), t is the time (s), ρ is the charge (C), \mathbf{J} is the current (A/m), ϵ_0 is the electric permittivity of free space, μ_0 is the magnetic permeability of free space, $\epsilon(\omega)$ is the dielectric constant, and $\mu(\omega)$ is the relative permeability, ω is the angular frequency. Assuming that both metal and dielectric are isotropic and homogeneous materials, both $\epsilon(\omega)$ and $\mu(\omega)$ can be considered as functions of the variables ω of the external electric field. In a region with no charges ($\rho = 0$) and no currents ($\mathbf{J} = \mathbf{0}$), the Maxwell's equations can be simplified as:

$$\nabla \cdot \mathbf{D} = 0 \quad (2.3)$$

$$\nabla \cdot \mathbf{B} = 0 \quad (2.4)$$

$$\nabla \times \mathbf{E} = -\frac{\partial \mathbf{B}}{\partial t} \quad (2.5)$$

$$\nabla \times \mathbf{H} = -\frac{\partial \mathbf{D}}{\partial t} \quad (2.6)$$

A plane wave is considered as the incident light to solve the Maxwell's equations as given below:

$$\mathbf{E}(\mathbf{r}, t) = \mathbf{E}_0 e^{i(\mathbf{k} \cdot \mathbf{r} - \omega t)} \quad (2.7)$$

Where \mathbf{E}_0 is the electric field amplitude, \mathbf{r} is the position vector in space, and \mathbf{k} is the wavevector. Equation (2.8) represents the photonic dispersion relation to correlate \mathbf{k} and ω :

$$\frac{\omega^2}{|\mathbf{k}|^2} = \frac{1}{\mu_0 \mu(\omega) \epsilon_0 \epsilon(\omega)} \quad (2.8)$$

The identity of the speed of light (c) in a vacuum relates to the free space permittivity and permeability:

$$c = \frac{1}{\sqrt{\mu_0 \epsilon_0}} \quad (2.9)$$

For a nonmagnetic media with properties of $\mu(\omega) = 1$, Equation (2.8) can be simplified to:

$$|\mathbf{k}| = \omega \sqrt{\mu_0 \epsilon_0 \epsilon(\omega)} = \frac{\omega}{c} \sqrt{\epsilon(\omega)} \quad (2.10)$$

Note that only the transverse magnetic (TM) polarized light with electric field component in z-direction can excite SPR, due to the discontinuity at the interface of two materials ($z=0$). However, a transverse electric (TE) polarized light with electric field component only in x-y plane would not generate a charge oscillation due to no discontinuity in this plane. The electric and magnetic fields in two different mediums separated by a boundary ($z=0$) can be represented by:

$$\mathbf{E}_1 = \begin{bmatrix} E_{x1} \\ 0 \\ E_{z1} \end{bmatrix} e^{i(k_{x1}x + k_{z1}z - \omega_1 t)}; \quad z > 0 \quad (2.11)$$

$$\mathbf{H}_1 = \begin{bmatrix} 0 \\ H_{y1} \\ 0 \end{bmatrix} e^{i(k_{x1}x + k_{z1}z - \omega_1 t)}; \quad z > 0 \quad (2.12)$$

$$\mathbf{E}_2 = \begin{bmatrix} E_{x2} \\ 0 \\ E_{z2} \end{bmatrix} e^{i(k_{x2}x + k_{z2}z - \omega_2 t)}; \quad z < 0 \quad (2.13)$$

$$\mathbf{H}_2 = \begin{bmatrix} 0 \\ H_{y2} \\ 0 \end{bmatrix} e^{i(k_{x2}x + k_{z2}z - \omega_2 t)}; \quad z < 0 \quad (2.14)$$

Where $z > 0$ represents medium 1, and $z < 0$ represents medium 2; the angular frequency in medium 1 and medium 2 is the same, *i.e.* $\omega_1 = \omega_2 = \omega$; the complex wavevector component in z direction for both media are perpendicular to the interface: $k_{z1} = k_{z1}' + ik_{z1}''$, and $k_{z2} = k_{z2}' + ik_{z2}''$; similarly, the complex wavevector component in x direction are parallel to the interface: $k_{x1} = k_{x1}' + ik_{x1}''$, and $k_{x2} = k_{x2}' + ik_{x2}''$, where k' is the real part and k'' is the imaginary part. Applying the field continuity conditions for \mathbf{E} and \mathbf{H} parallel to the interface:

$$E_{x1} = E_{x2} = E_x \quad (2.15)$$

$$H_{y1} = H_{y2} = H_y \quad (2.16)$$

$$k_{x1} = k_{x2} = k_x \quad (2.17)$$

Inserting Equations (2.11-2.14) into the Maxwell's Equations (2.3-2.6), the following relations are obtained:

$$k_{z1}H_{y1} = \frac{\omega}{c} \varepsilon_1 E_{x1} \quad (2.18)$$

$$k_{z2}H_{y1} = \frac{\omega}{c} \varepsilon_2 E_{x2} \quad (2.19)$$

By dividing Equation (2.18) by Equation (2.19), the relationship between

wavevectors and the permittivities are obtained:

$$\frac{k_{z1}}{k_{z2}} = -\frac{\varepsilon_1}{\varepsilon_2} \quad (2.20)$$

According to Equation (2.20), since the left side is always positive, the only condition to satisfy the surface plasmon solutions is that ε_1 and ε_2 are of opposite signs. Therefore, the surface plasmon can only exist at the interface between any two media where the real part of the dielectric function changes sign across the interface, for example, a metal with negative permittivity ($\varepsilon_m < 0$) and a dielectric with positive permittivity ($\varepsilon_d > 0$). The wavevector components k_z and k_x can be related by the total wavevector \mathbf{k}_i in each medium via Equation (2.10):

$$k_{zi}^2 = |\mathbf{k}_i|^2 - k_{xi}^2 = \left(\frac{\omega}{c}\right)^2 \varepsilon_i - k_{xi}^2 \quad (2.21)$$

Due to the x-components are equal in both media, $k_{x1} = k_{x2} = k_x$, and inserting Equation (2.20) into Equation (2.21), we get:

$$\left(\frac{\omega}{c}\right)^2 \varepsilon_1 - k_x^2 = \left(\frac{\varepsilon_1}{\varepsilon_2}\right)^2 \left[\left(\frac{\omega}{c}\right)^2 \varepsilon_2 - k_x^2\right] \quad (2.22)$$

Solving for k_x based on Equation (2.22), the SPPs propagating along the interface of two media obey the following dispersion relation:

$$k_x = \frac{\omega}{c} \sqrt{\frac{\varepsilon_1 \varepsilon_2}{\varepsilon_1 + \varepsilon_2}} \quad (2.23)$$

To investigate the properties of k_z , now consider a metal-dielectric interface ($\varepsilon_1 = \varepsilon_d$ and $\varepsilon_2 = \varepsilon_m$) with complex wavevectors k_x and k_z . The z-component of the electromagnetic fields in Equations (2.11-2.14) for the complex term $k_z = k_z' + ik_z''$ is:

$$e^{i((k_z' + ik_z'')z - \omega t)} = e^{i(k_z'z - \omega t)} e^{-k_z''z} \quad (2.24)$$

This indicates that the SPP is an evanescent wave decaying exponentially in the z

direction, with a decay length of $d = 1/k_z''$. And the E_x and H_y show similar evanescent behaviors. Therefore, the SPPs are non-radiative electromagnetic surface waves propagating in the x-direction bound to the surface, with propagating lengths of several microns under most conditions.

2.1.2 Surface Plasmon Resonance

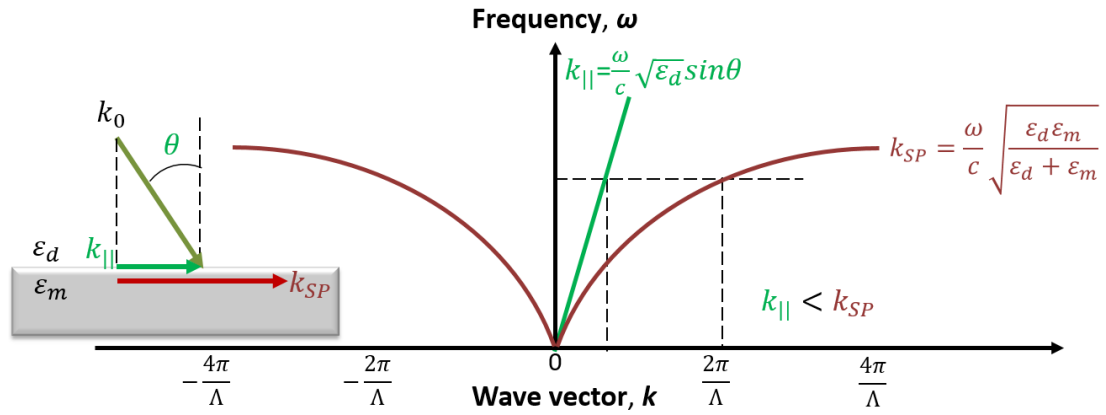


Figure 2-1 Illustration of a photon incident on a metal/dielectric interface, and the photon dispersion vs. the plasmonic dispersion.

To generate surface plasmon resonance (SPR), one can utilize electron bombardment or incident light beam. In the case of a photon to excite an SPP, it should satisfy the frequency (ω) and momentum ($p = \hbar k$) matching conditions. Generally, we investigate the wavevector ($k = p/\hbar$) to represent the momentum matching condition. Let us consider an photon impinging on a metal surface at an incident angle of θ to the normal (**Figure 2-1**), with a specific frequency ω propagating through a dielectric with refractive index (RI) of $n = \sqrt{\epsilon_d}$. The in-plane wavevector parallel to the surface in x-direction is given by:

$$k_{||} = \frac{\omega}{c} \sqrt{\epsilon_d} \sin\theta = \frac{\omega}{c} n \sin\theta \quad (2.25)$$

The dielectric permittivity of the metal is $\epsilon_m = \epsilon_m' + i\epsilon_m''$, and most noble metals are low loss in the visible range, *i.e.* $|\epsilon_m''| \ll |\epsilon_m'|$. Resonance only occurs when momentum of the incident light matched SPR momentum, however, as shown in **Figure 2-1**, the photon wavevector ($k_{||}$) in a certain dielectric is always less than the surface plasmon wavevector (k_{SP}):

$$k_{SP} = \frac{\omega}{c} \sqrt{\frac{\epsilon_d \epsilon_m}{\epsilon_d + \epsilon_m}} > \frac{\omega}{c} \sqrt{\epsilon_d} \sin\theta = k_{||} \quad (2.26)$$

The above inequality indicates that one cannot use flat metal surface directly to couple free photons to the surface plasmons in natural conditions. In order to couple between surface plasmons and photons, one needs to provide additional optical momentum at a particular angular frequency to match both energy and optical momentum conditions.

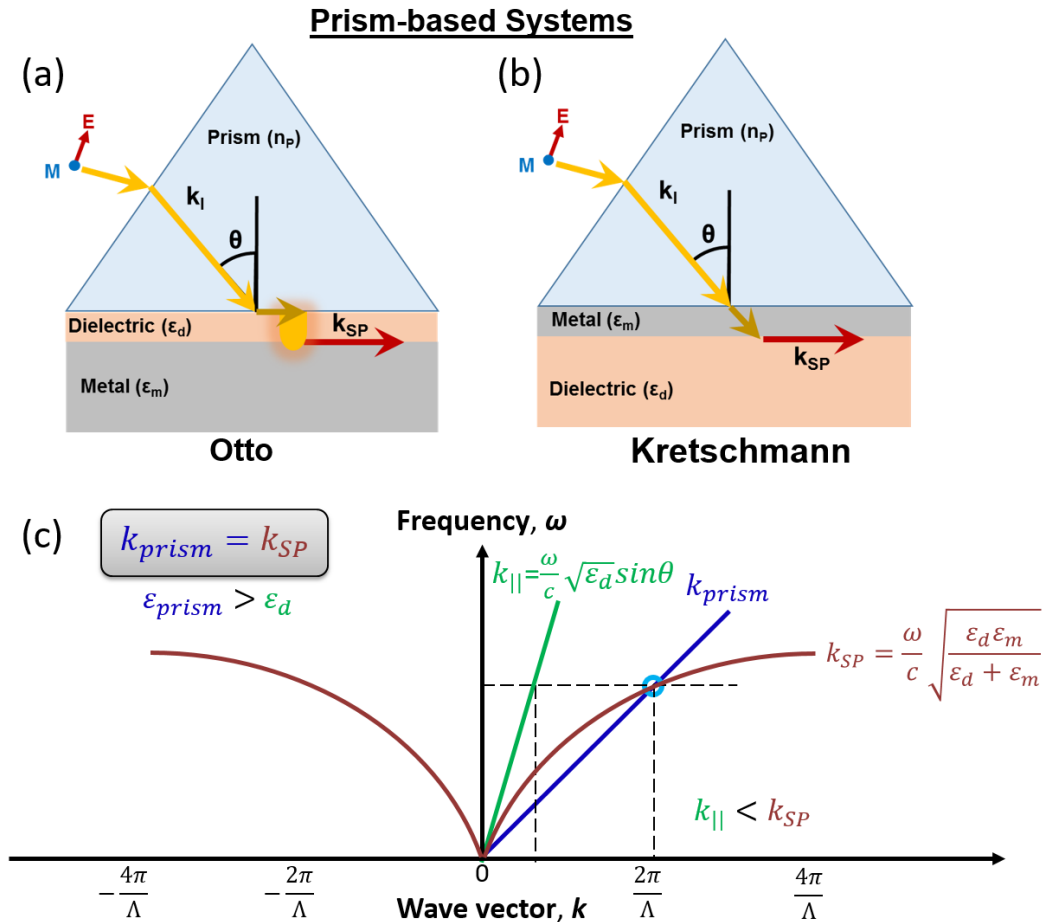


Figure 2-2 Prism-based SPR excitation: (a) Otto and (b) Kretschmann configurations, (c) photon and SPR wavevector matching conditions.

Generally, two methods are commonly used to excite surface plasmons on a metal surface by photons: 1) prism-based systems and 2) grating-based systems. The prism-based setups include two configurations: 1) the Otto configuration (**Figure 2-2a**), with a prism on a thin dielectric film and a then thick metal film; 2) the Kretschmann configuration (**Figure 2-2b**) essentially switches the positions of the metal and dielectric layers of the Otto configuration. Take Kretschmann configuration as an example. The incident light beams imping through a high refractive index prism ($n_{prism} > n_d, \epsilon_{prism} > \epsilon_d$) on a thin metal film. The increase of refractive index by introducing prism increases the photon wavevector at a specific angle of incidence, and therefore, the x-component of the photon wavevector is possible to match the surface plasmon as shown in **Figure 2-2c**:

$$k_{sp} = \frac{\omega}{c} \sqrt{\frac{\epsilon_d \epsilon_m}{\epsilon_d + \epsilon_m}} = \frac{\omega}{c} n_{prism} \sin \theta_{SPR} = k_{prism} \quad (2.27)$$

where, θ_{SPR} is the surface plasmon resonance angle for a specific wavelength to achieve surface plasmon resonance. There are some limitations with these methods: 1) the prism would bulky for some setups to incorporate and more expensive to operate; 2) the metal or dielectric layer thicknesses are very critical for prism-based systems to function properly; 3) the coupling are extremely sensitive to angle and wavelengths in a narrow range; 4) the prism cannot be used for the dielectrics with higher refractive index.

Grating-based Systems

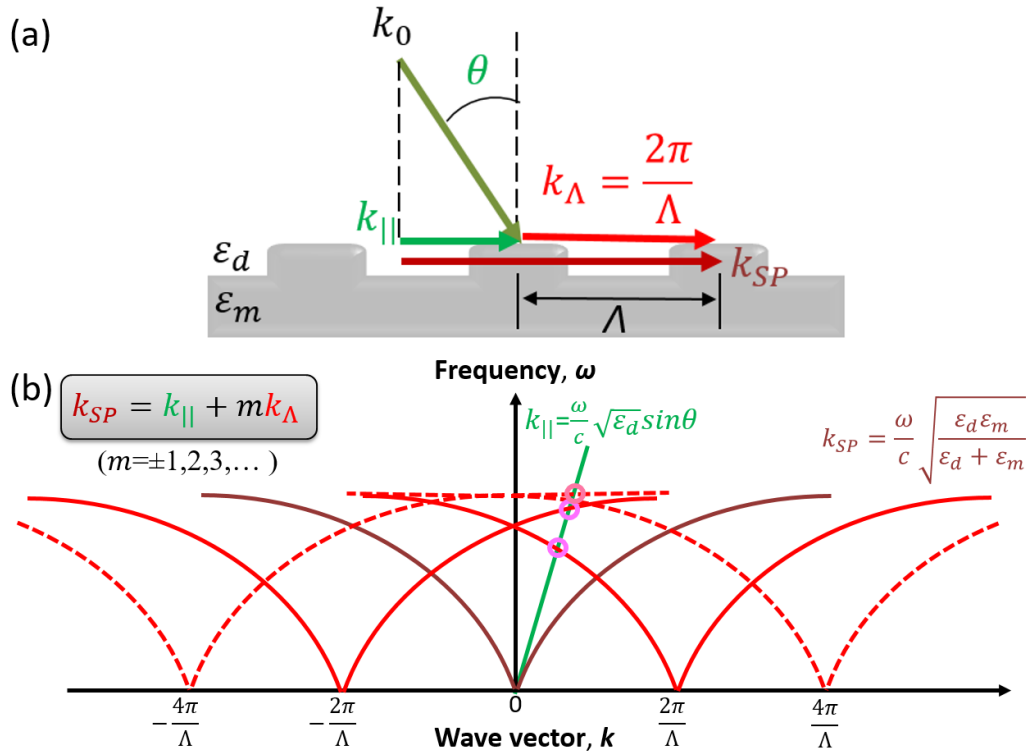


Figure 2-3 Grating-based SPR excitation: (a) grating configurations, (b) photon and SPR wavevector matching conditions.

An alternative way to the prism-based system for generating SPR is in the use of metallic gratings with one-dimensional periodic grooves and ridges to provide additional optical momentum (**Figure 2-3a**). The characteristics of grating structures include the grating pitch (Λ) that is the distance from peak to peak in the periodic pattern, and the grating height (h) that is the distance from the bottom to the top of the structure. The photons impinging on a metal grating are diffracted due to the periodic pattern, which enhances the total field by constructive interference based on the individual scattered waves, which form multiple diffraction orders. The surface plasmons on the metal surfaces are possible to be matched by the in-plane component of the m^{th} diffraction order of the incoming light to couple the SPR (**Figure 2-3b**). The grating vector k_{Λ} for periodic metal

gratings based on the grating pitch can be defined as:

$$\mathbf{k}_\Lambda = \frac{2\pi}{\Lambda} \quad (2.28)$$

The grating vector in the x-direction is perpendicular to the grating grooves. Multiples m of the grating vector will be incorporated to the reflected light to provide additional optical momentum to the incoming photon, and therefore, the light beam can excite the surface plasmons by introducing the metallic grating surface:

$$k_{SP} = \frac{\omega}{c} \sqrt{\frac{\epsilon_m \epsilon_d}{\epsilon_m + \epsilon_d}} = k_x + m k_\Lambda = \frac{\omega}{c} \sqrt{\epsilon_d} \sin \theta_{SPR} + m \frac{2\pi}{\Lambda} \quad (m = \pm 1, 2, 3, \dots) \quad (2.29)$$

The resonance condition will be achieved at a particular incidence angle, θ_{SPR} at specific wavelength. The photon-plasmon coupling is only possible for p-polarized light because of the transverse magnetic nature of the surface plasmons. This plasmonic grating platform shows advantages, such as wide angle/wavelength coupling range, without bulky prism system, and tunable for wide range of dielectrics.

2.1.3 FDTD simulations and experiment studies on surface plasmon

resonance (SPR) dispersion curve for grating microchips

We utilized grating microchips to couple incident optical energy at the grating surface by surface plasmon resonance (SPR), which can result in enhanced photothermal heating of nanoenergetic systems. SPR coupling only occurs if the incoming momentum (P) matches that of a surface plasmon polariton (SPP). The tunability of the plasmonic grating microchip system enables E-field enhancement within the visible and near-infrared (NIR) spectrums. To obtain the optimal conditions for nanoenergetic studies, we can tune the grating configuration and the experimental conditions, such as refractive index of

medium, wavelength and incident angle of light.

Our group already developed a soft lithography fabrication process to prepare these grating nanostructures with the capability of significant electromagnetic field enhancement. We have fabricated grating microchip using HD-DVD and Bluray as a template, which has different grating pitches and grating heights. The grating surface structure was characterized with atomic force microscopy (AFM) and analyzed using Gwyddion software to obtain the grating pitch, height, root mean square (RMS) roughness, duty cycle, and grain diameter, etc. As shown in **Figure 2-4(a,d)**, HD-DVD gratings have a pitch of 400 nm and height of 52 nm in average; while, Bluray gratings have a pitch of 320 nm and height of 32.5 nm in average.

We simulated and measured experimentally 100 nm silver gratings with 10 nm alumina coating directly in the air as well as immersed in water or oil. The resulting SPR dispersion curves have been provided in **Figure 2-4 (b-c)** for silver HD-DVD gratings and **Figure 2-4 (e-f)** for silver bluray gratings. We employed two-dimensional (2D) FDTD simulation to get the dispersion curve of the periodic plasmonic grating structure. P-polarized light reflectance measured by Ellipsometer (VASE, J. A. Woollam) was used to obtain the experimental dispersion curve. For *in-situ* imaging study and plasmonic heating for nanoenergetic system, it is important to note that the Al nanoparticle extinction and scattering spectra or the fluorophore excitation and emission spectra (fluorescent dyes were used to obtain the local temperature mapping in **Chapter 6**) should be as close as possible to the 0° coupling angles in order to obtain optimal plasmonic excitation that matches with the coupling wavelengths within the acceptance angles in common imaging systems such as epi-fluorescence and absorption microscopes. This is necessary for two reasons: 1) The

inherently larger illumination intensity at or near 0° from such imaging systems and 2) To ensure that the angular fluorescence emission from the plasmonic gratings will be near 0° such that it can be collected by the imaging system. Both simulated and experimental dispersion curves show that the SPR dispersion shifts to longer wavelengths as the refractive index of the medium (air, water and oil) increases. For example, the resonance wavelength in oil at normal incidence (0°) for HD-DVD and Bluray is approximately 640 nm and 545 nm, respectively, according to both simulation and experiment. In order to effectively enhance photothermal heating Al nanoparticles, the SPR wavelengths should match with the absorption of the Al nanoparticles which can be tuned from UV to NIR based on the size and configuration of Al nanoparticles. To satisfy this large range of absorption wavelengths that are possible under different experimental conditions, the tunability of SPR wavelengths in such a large range can be achieved by combining HD-DVD and Bluray silver grating immersed in a different medium and illuminated by different angles. In particular, we are interested in *in-situ* imaging using high refractive index oil-immersed lens with large numerical aperture (NA) lens which can enhance the imaging resolution significantly compared with water and air medium. For example, we can use HD-DVD gratings in oil in the case of absorption spectra of Al nanoparticles between 600 - 700 nm. Due to the smaller grating pitch of Blu-rays, the SPR dispersion is shifted towards shorter wavelengths as compared to HD-DVD gratings. In contrast to the previous example with HD-DVDs, Bluray gratings in oil would optimally enhance spectrums between 500 - 600 nm.

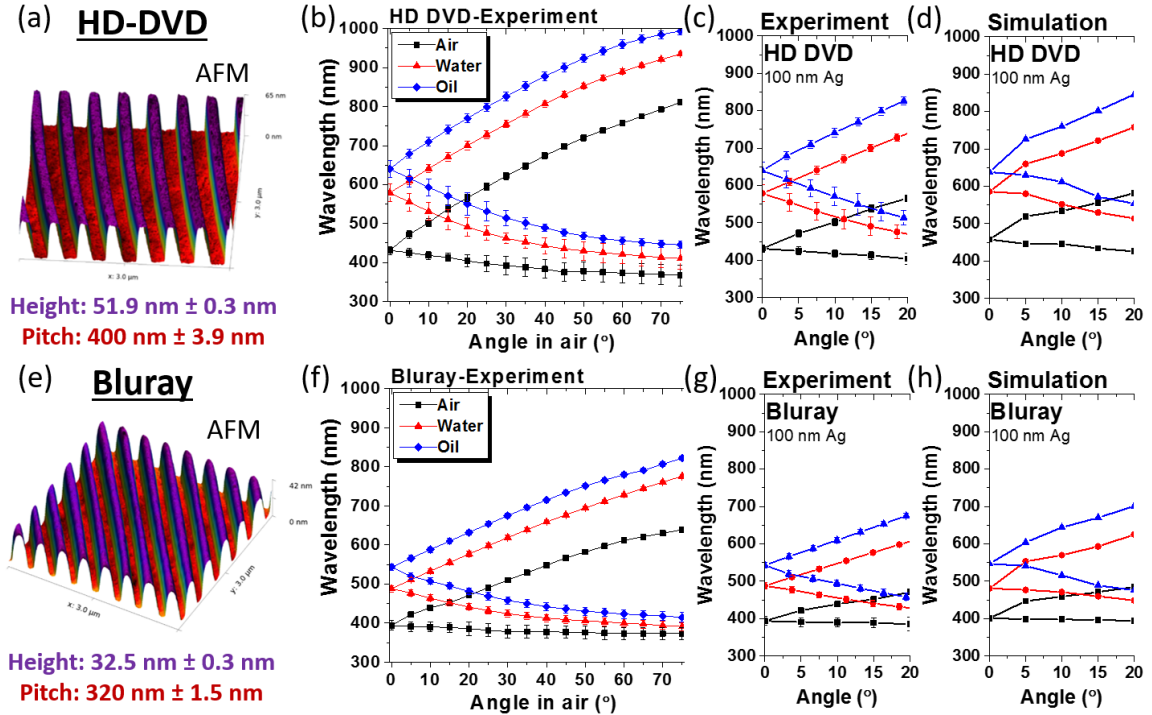


Figure 2-4 AFM and SPR dispersion curves for (a-d) HD-DVD and (e-h) Bluray gratings. The dispersion curve is based on coupling peak location from reflectivity data for 100 nm silver gratings with 10 nm alumina coating. (Left) AFM for PMSSQ gratings without metal coating; (Middle) experimental dispersion curve measured by ellipsometry: (b, f) the incident angles in air, (c, g) incident angles corrected by Snell’s law for the mediums; (Right) simulated dispersion curve.

2.1.4 FDTD Simulations for the design of grating microchip configuration

To construct a grating microchip configuration, the effect of geometrical parameters must be considered. The thickness of metallic layers is a physical parameter of microchip structures and can be adjusted to improve the E-field. We simulated different silver grating configurations with various silver thicknesses from 20 nm to 120 nm under normal incidence (0 °) of light in oil (or nitrocellulose) environment, as shown in **Figure**

2-5. We first chose these simulation parameters because the targeted *in-situ* imaging of nanoenergetic reaction with an epi-fluorescence microscope was carried out with high magnification oil-immersed lens, and a large portion of light was illuminated on the samples under normal incidence. The reflective index of oil (RI=1.515) matches that of nitrocellulose (RI=1.5), which can also be used to estimate the properties of grating microchips coated with polymers (nitrocellulose).

The calculated optical properties of grating-based SPR spectra were significantly affected by metal thickness. Based on the reflectance dips, several parameters can be evaluated to compare the coupling properties of gratings, such as full width at half maximum (FWHM), coupling strength (σ), and peak wavelength (λ), quality factor ($QF = \frac{\lambda}{FWHM}$) and Gamma ($\gamma = \frac{\sigma}{FWHM}$). **Figure 2-5(a)** shows the reflectance of silver HD-DVD grating with 10 nm Al₂O₃ on top by varying the silver thickness under normal incidence of light in oil (or nitrocellulose) environment. There are two resonance peaks at 510 nm and 640 nm, and we focus on the main resonance peak at 640 nm which exhibits higher E-field enhancement for this study. The broad peak shown in reflectance curve enables a large range of wavelength coupling, which is beneficial to the Al nanoparticles with broad excitation spectra.

The FDTD simulated maximum E-field strength ($E_{z \text{ max}}/E_{z,0}$) increases with increasing the silver thickness (**Figure 2-5(b)**). From 20 nm to 60 nm, the E-field changes significantly, while E-field increases slowly when the thickness is thicker than 60 nm, and it does not change with thickness more than 100 nm. Therefore, we chose 100 nm as silver thickness for our preliminary FDTD simulation study when integrating with Al nanoparticles in the following chapters. We are also interested in thinner silver films since

the transparency enables the use of illumination from the bottom of gratings. As shown in **Figure 2-5(c)**, there is a large portion of E-field penetrates to the other side of the grating with a silver thickness less than 60 nm. We will simulate these grating structures in our future study. The SPR wavelength is another important parameter which should be considered to get the maximum enhancement, influencing the coupling with Al nanoparticles and selection of the laser with a specific wavelength. The SPR wavelength changes within 4 nm when using different silver thickness, which will facilitate the optimization of silver thickness for different application without changing the lasers. The FWHM increases and coupling strength decrease as the Ag thickness decrease from 60 nm to 20 nm, which results in lower quality factor and Gamma value. Therefore, by considering both transmittance and coupling properties for the transparent gratings, 40 nm Ag grating is ideal for future study.

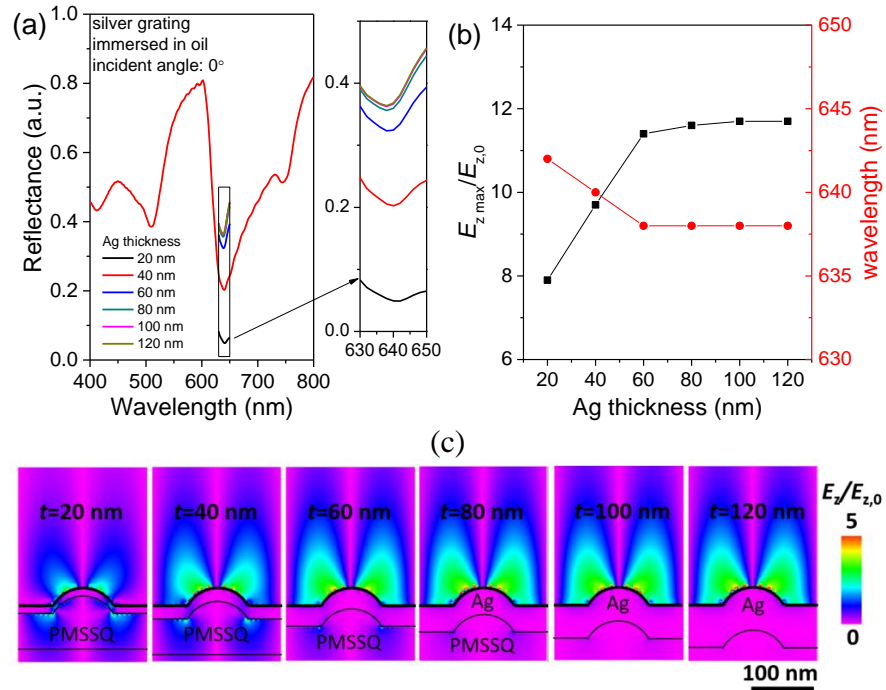


Figure 2-5 FDTD simulated (a) reflectance and (b) maximum E-field strength ($E_{z,max}/E_{z,0}$)

and SPR wavelengths varying with different silver thickness from 20 nm to 120 nm, under normal incidence (0°) of light in oil (or nitrocellulose) environment. (c) E-field distribution of for grating microchips The E-field ($E_z/E_{z,0}$) scale is normalized to 0~5. The scale bar is 200 nm.

2.2 Super-Resolution Imaging by Plasmonic Grating

2.2.1 Design of Plasmonic Grating Superlens for Far Field Imaging

In a three-dimensional (3D) system, a monochromatic plane wave U in free space with a refractive index n can be written as:

$$U = U_0 e^{-i(k_x x + k_y y + k_z z - n 2\pi c t / \lambda_0)} \quad (2.30)$$

where λ_0 is the average observed wavelength in free space, c is the speed of light in vacuum, the wave's angular frequency $\omega = 2\pi n c / \lambda_0$, k_x and k_y are the transverse wavenumbers, k_z are the longitudinal wavenumbers, and wave vector $\mathbf{k} = (k_x, k_y, k_z)$, in the (x, y, z) Cartesian axis.

If we consider imaging under a microscope with objectives, based on Maxwell's equations, transverse and longitudinal wavenumbers must satisfy:

$$\mathbf{k}^2 = k_x^2 + k_y^2 + k_z^2 = k_{obs}^2 \quad (2.31)$$

Where $k_{obs} = NA k_0$ is the maximum observable spatial frequency, and $NA = n \sin \alpha$ is the numerical aperture of the objective lens, n is the refractive index of imaging medium, and α is the maximal half-angle of the cone of light that can enter (illumination angle) or exit (acceptance angle) the lens, and $k_0 = \frac{2\pi}{\lambda_0}$ is the wavevector in free space.

To obtain propagating waves, we should let k_z be a purely real number, so the wavenumbers should satisfy $|k_x^2 + k_y^2| \leq k_{obs}$, and the lower spatial frequencies carry diffraction-limited information to represent coarse details. To obtain evanescent waves, we should let k_z be a purely imaginary number, so the wavenumbers should satisfy $|k_x^2 + k_y^2| > k_{obs}$, and the higher spatial frequencies carry super-resolution information to represent fine object details. However, the intensity of evanescent waves decays exponentially with distance in near-field, which cannot be detected in far-field.

One method to acquire super-resolution information in far field is to extend the maximum observable spatial frequency k_{obs} . The periodic gratings can convert near-field into far-field by modulating the wavevector of evanescent waves through incorporating the grating vector ($\mathbf{k}_\Lambda = \frac{2\pi}{\Lambda}$, where Λ is the grating period). Here, take HDDVD gratings for imaging fluorescent dye R6G under an oil immersive objective as an example. As shown in **Figure 2-6b**, the emission wavelength of R6G is $\lambda_0 = 550$ nm, HDDVD gratings period is $\Lambda = 400$ nm, the numerical aperture of the objective is $NA = 1.49$, and hence, the grating vector is $k_{\Lambda-HDDVD} = 1.38k_0$, the maximum observable wavenumber is $k_{obs} = 1.49k_0$. The subwavelength gratings can shift the incident wavevector (\mathbf{k}) into different diffraction orders m , so that it can satisfy propagating waves condition: $|\mathbf{k} \pm m\mathbf{k}_\Lambda| \leq k_{obs}$. Therefore, the highest observable spatial frequency k_{max} in Fourier space is extended from k_{obs} to $k_{obs} \pm mk_\Lambda$. It has been demonstrated by researchers that grating-based nanostructures can be used for superlensing to obtain super-resolution images. For microscopic imaging, the resolution can be defined to distinguish a phase difference of π for two sinusoidal waves in frequency domain, that is to say, the spatial resolution $r =$

π/k_{max} . Therefore, the diffraction limit is $r_{DL} = \frac{\lambda_0}{2NA}$, and the improved resolution by the grating superlens can be derived as below:

$$r_{GS} = 1/2\left(\frac{NA}{\lambda_0} \pm \frac{m}{\Lambda}\right) \quad (2.32)$$

It indicates that smaller grating period (Λ) and higher effective diffraction order (m) can lead to better spatial resolution for grating superlens. For example, when the diffraction order is $m = \pm 1$, the spatial resolution can be improved from 185 nm to 95 nm by HDDVD grating for the light with wavelength of 550 nm (**Figure 2-6c**).

For metal gratings, in addition to the diffraction due to grating structure, one should consider the surface plasmons (SP) at the metal/dielectric interface due to the collective oscillation of free electrons on metal. The wavenumber of SP (k_{SP}) is higher than the wavenumber of the incident light in free space (k_0) as shown below:

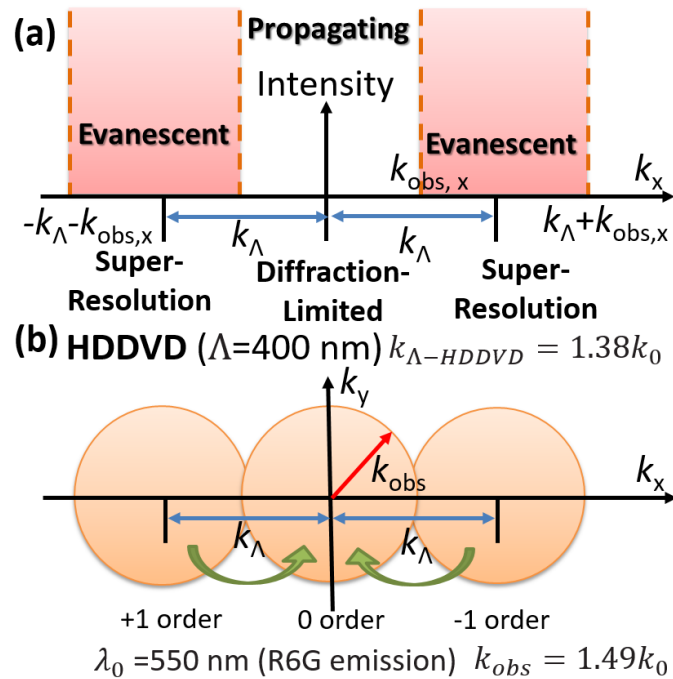
$$k_{SP} = k_0 \sqrt{\frac{\epsilon_m \epsilon_d}{\epsilon_m + \epsilon_d}} = \frac{\omega}{c} \sqrt{\frac{\epsilon_m \epsilon_d}{\epsilon_m + \epsilon_d}} \quad (2.33)$$

where ω is the frequency of the incident light, c is the speed of light in free space, ϵ_m and ϵ_d are the dielectric constant of the metal and the surrounding dielectric medium, respectively. The grating can provide additional wave number to the transverse wavenumber ($k_{||}$) of incident light to satisfy the momentum matching condition:

$$k_{SP} = k_{||} = nk_0 \sin\theta \pm mk_{\Lambda} = \frac{\omega}{c} \sqrt{\epsilon_d} \sin\theta \pm m \frac{2\pi}{\Lambda} \quad (m = \pm 1, 2, 3, \dots) \quad (2.34)$$

where θ is the incident angle of the light. This phenomena is called surface plasmon resonance (SPR). The coupling can happen at both excitation and emission process, and

the surface plasmon-coupled emission (SPCE) is the inverse process of the surface plasmon resonance absorption. These two phenomena during the processes of excitation and emission are independent. In another word, the SPCE phenomenon can occur, regardless of whether the surface-plasmon excitation happens or not. For the application with fluorescent dye, the excited fluorophores in the vicinity of a metal film surface (0–250 nm) can non-radiatively transfer energy to the metal to form a radiative or non-radiative surface plasmon. The radiative surface plasmon emitting at the resonance angle provides the highly directional properties of SPCE process.



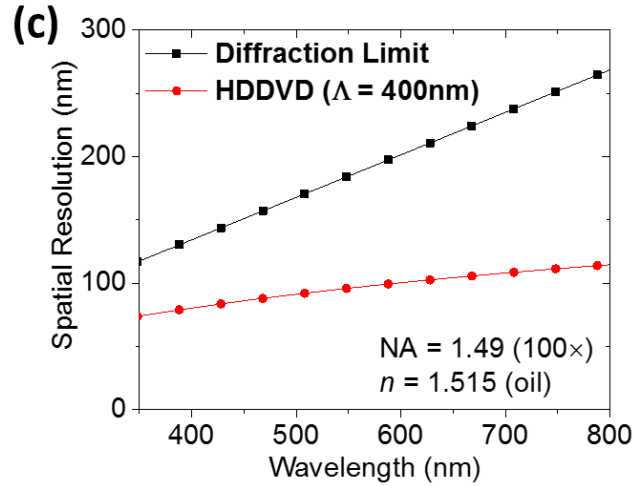


Figure 2-6 (a) Ideal OTF for FSL that enhances incident evanescent waves within wavevector bands. (b) 2D Fourier space for HDDVD gratings. (c) Spatial resolution for diffraction limit condition and with HDDVD grating wavevector modulation.

Although the periodic gratings can transfer evanescent waves into propagation waves, however, the far-field information contains the mixture of different diffraction orders (*e.g.* -1, 0, +1). To retrieve “one-to-one” object information by only reconstructing the original evanescent super-resolution information, one needs to solve wavevector mixing issue. There are two methods to separate the mixed information for grating systems. One method is to separate different orders in Fourier space with the help of the second dimension by moiré effect, where the sets differ in relative size, angle, or spacing. Without the translation process, another method is to distinguish different orders by controlling the ratio of different orders, so that a far-field superlens with the specific wavevector dependent optical transfer function (OTF) to suppress 0 order and enhance ± 1 orders.

The plasmonic metal gratings play roles in both excitation (absorption) and emission processes. When imaging fluorescence in the far-field, the mechanism is: (1) the

absorption of light by fluorophores is enhanced by coupling the excitation light, and then (2) the emission from the fluorophores near the surface of the grating re-coupled to the plasmonic grating is enhanced and emitted at the SPCE angle. The excitation light is filtered out by fluorescence filter cubes, and only the fluorescence re-coupled at a certain diffraction order m of the plasmonic grating can propagate into the far field due to SPCE.[9] Therefore, the SPCE containing higher order information other than 0 order diffraction limited information can be retrieved to obtain super-resolution imaging.

Furthermore, there are still lots of application without fluorescence properties, so it is also interesting to consider imaging under bright field mode without any fluorescent filter sets. Since the 100 nm-thick silver gratings are reflective gratings, the COMSOL simulation was utilized to simulate different reflection orders under the imaging condition with oil immersion. **Figure 2-7** shows the 0 order reflectance (R_0) and -1 order reflectance (R_{-1}), as well as the ratio of R_{-1}/R_0 for HDDVD silver gratings illuminated with different wavelengths of p-polarized light at different angles of incidence from 0° to 30° . As shown in **Figure 2-7b**, -1 order reflectance is high in the wavelength range from ~470 nm to ~620 nm at different angles of incidence. In addition, the ratio of R_{-1}/R_0 is high in the wavelength range from ~470 nm to ~570 nm as well, which is able to distinguish signal coming from the -1 order reflection out of that coming from the 0 order reflection. The 0 order reflectance dip at 656 nm under 0° illumination (**Figure 2-7a**) indicates the highly enhanced electric field in near field (**Figure 2-7d**) with much weaker electric field propagating into the far field. When $\theta = 0^\circ$, $k_{SP} = \frac{\omega}{c} \sqrt{\frac{\epsilon_m \epsilon_d}{\epsilon_m + \epsilon_d}} = \pm m \frac{2\pi}{\Lambda}$, the resonance frequency (ω) only depends on imaging medium (ϵ_d) if the plasmonic grating superlens is already provided with a fixed metal (ϵ_m) and grating structure (Λ). **Figure 2-7e** shows the

electric field profile at the maximum of -1 order reflection at different angles of incidence from 0° to 30° (**Figure 2-7b**). Under these conditions, the electric field propagating into far field is more comparable to the electric field localized on the grating surfaces. In this experiment, a xenon lamp with broad spectra from ~ 380 nm to ~ 700 nm (**Figure 2-7f**) was used for bright field imaging, and the $100\times$ oil immersive objective (NA=1.49) with broad convergence angle (79.62°) was selected (**Figure 2-7g**).

In sum, for the design of plasmonic grating superlens, the imaging resolution depends on how many and how high orders effectively utilized to couple evanescent waves into propagating ones. The ± 1 orders are mainly considered because the amplitude of higher orders is negligible in this experiment, but it is not limited to further modification of design for higher resolution application. The contrast relies on how good the separation of the original propagation waves and the converted evanescent waves, and how well the intensity enhanced by the plasmonic gratings.

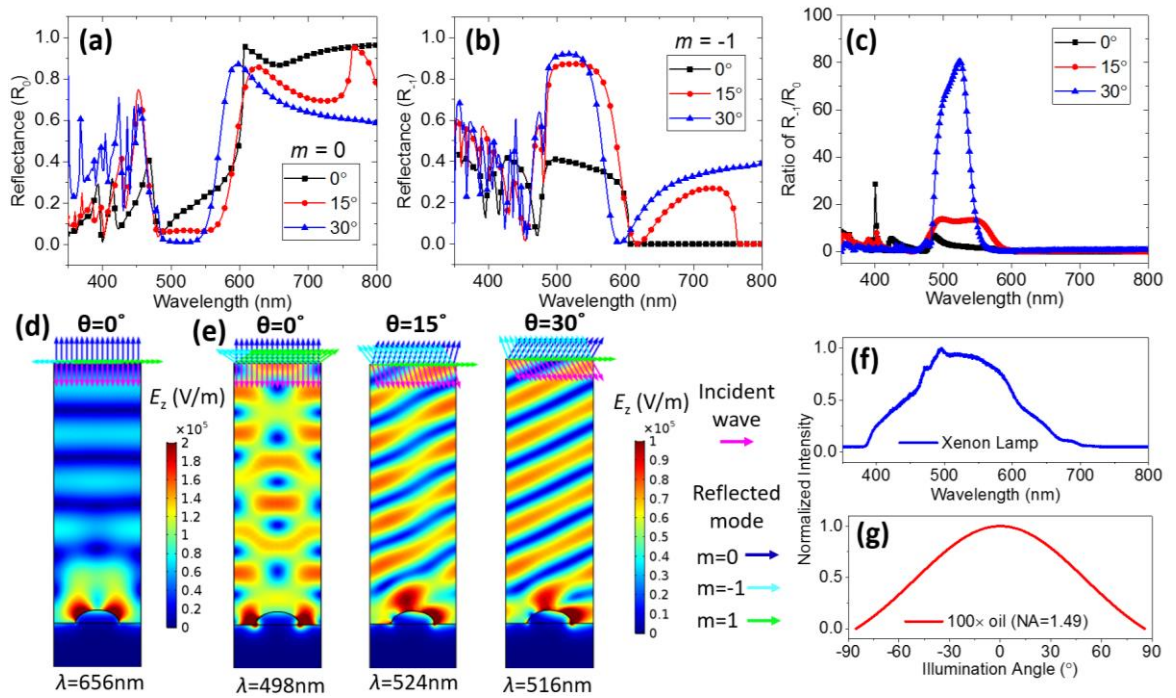


Figure 2-7 (a-e) COMSOL simulation for HDDVD silver gratings (a) 0 order reflectance (R_0), (b) -1 order reflectance (R_{-1}), (c) the ratio of R_{-1}/R_0 ; (d) E-field profile at 0° angle of incidence at 656 nm, (e) E-field profile at the maximum R_{-1} at different angles of incidence from 0° to 30° . Normalized intensity for (f) Xenon lamp and (g) Illumination angle for $100\times$ oil objective used in the experiment.

2.2.2 Combination of Plasmonic Grating with Localization Microscopy

The resolution improvement of localization microscopy by combining with plasmonic grating superlens depends on two aspects: (1) Pre-processing (raw imaging data): plasmonic grating superlens can provide evanescent information (high spatial frequencies) in the far-field to improve the spatial resolution of original image sequences as discussed above; (2) In-processing (reconstructed image by pointillism): plasmonic nanostructures can improve localization precision by increasing the number of collected photons.

The localization precision σ can be calculated on the basis of the following formula:

$$\sigma = \sqrt{\left(\frac{s_i^2 + \frac{a^2}{12}}{N}\right) \cdot \left(\frac{16}{9} + \frac{4\tau s_i^2 b^2}{Na^2}\right)} \quad (2.35)$$

where N is the number of collected photons, a is the pixel size of the imaging detector, b^2 is the average background signal, and s_i is the standard deviation of the point spread function. In order to maximize localization precision, it requires an enhanced signal-to-noise ratio (SNR). This is the reason why STORM/PALM is frequently combined with widefield fluorescence microscopes with the capability of optical sectioning, for example,

TIRFM. Therefore, the fluorescence enhancement due to plasmonic nanostructures leads to the increment of the total number of detected photons (N), which is beneficial to improve the localization precision. Compared with STORM/PALM, the enhanced SNR enables imaging larger range of fluorophores concentration in epi-fluorescence mode rather than TIRFM.

2.3 Fluorescence Beads for Experimental Point Spread Function (PSF) Studies

2.3.1 Theory of PSF, Convolution, and Deconvolution

Point spread function (PSF) is the response of an imaging system to an infinitely small point source. In general, due to the limitation of diffraction of light, the ideal PSF describes a 3D diffraction pattern of the emitted light from a point object, which appears as an Airy disk formed under a perfect lens with a circular aperture.[31] In the experiment, other than the objective lens, the entire emission light path and the camera system would affect the PSF, which would bring more noise and loss of resolution to make it less resolved than the ideal PSF. The PSF plays a very important role in determining the resolution of imaging, that is to say, the resolution can be improved by modifying the PSF. The method of modification of PSF includes some of the most important and advanced super-resolution techniques, such as stimulated emission depletion (STED), saturated structured illumination microscopy (SSIM), and ground state depletion (GSD).[28], [30] The process of painting with PSF for the object is a “convolution” operation to form the image, and the reverse process of reconstructing the object from the image by PSF is called “deconvolution” (**Figure 2-8**). The convolution operation can be symbolical as shown

below:

$$\text{Image}(r) = \text{Object}(r) \otimes \text{PSF}(r) \quad (2.36)$$

where \otimes is convolution operation symbol; the image, object, and PSF are represented as functions of position (r) or an x , y , z , and t (time) coordinate. Mathematically, the object plane field is a sum over weighted impulse functions with the sifting property of 2D delta functions, so we can express the object plane field $O(x_0, y_0)$ by the object transmittance function as follows [88]:

$$O(x_0, y_0) = \iint O(u, v) \delta(x_0 - u, y_0 - v) dudv \quad (2.37)$$

Therefore, we can calculate the image plane field by superimposing the images of each of the individual impulse functions over weighted PSF in the image plane using the same weighting function as in the object plane, taking the advantages of the linearity property of optical imaging systems. The image $I(x_i, y_i)$ is mathematically represented as:

$$I(x_i, y_i) = \iint O(u, v) \text{PSF}(x_i/M - u, y_i/M - v) dudv \quad (2.38)$$

where $\text{PSF}(x_i/M - u, y_i/M - v)$ is the image of the impulse function $\delta(x_0 - u, y_0 - v)$. Similarly, we can retrieve the real structure and size of object by inversed calculation from the image plane field. This is the way to improve the contrast of the images.

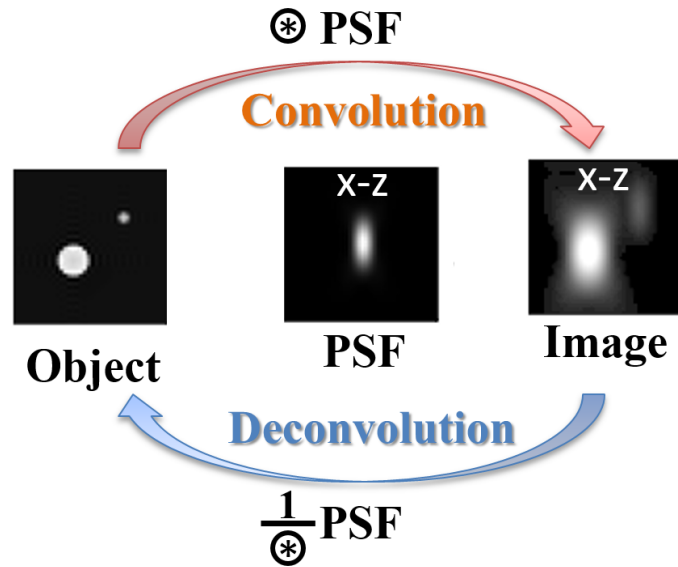


Figure 2-8 The process of convolution and deconvolution between object and image through PSF.

2.3.2 Selection Rules for Fluorescent Bead for PSF Measurement

Although we can theoretically predict the ideal PSF, it is still very important to measure PSF experimentally, not only to include the effects of the instrument response and imaging conditions but also to consider the change of the light propagation behavior due to light coupling, for example, plasmonic grating platform. Based on the experimental PSF, we can obtain the resolution of our system to learn what level of detail that can be expected from the image. Further, it can facilitate the comparison of resolution among different instruments and imaging platforms. The influences from the entire imaging path can be corrected, which makes an accurate assessment of the PSF for post-processing, for example, deconvolution. Diffraction-limited fluorescence beads were usually applied for experimental PSF measurement, and there are some rules for selecting fluorescent bead, including:

(1) small size to provide sufficient high spatial frequency components:

A small bead has a higher surface/volume ratio than a large bead. Therefore it has enhanced “edge energy” per unit of total signal strength.

(2) sufficient signal strength for the precision of alignment procedure:

Low signal strength can limit the precision of the alignment procedure. Very small beads (<25 nm) have an ideal spectral content with very high spatial frequency component, however, up to now, such small objects have lacked signal strength. Lots of papers and materials show good results obtained with ~100 nm beads. If we would like to reduce the optimal size of fluorescence bead, we can increase the fluorescence yield of beads by better dyes or better anti-bleaching agents, for example, using quantum dots. It is possible to use metal nanoparticles to enhance the fluorescence signal for PSF measurement.

(3) Homogeneously stained to provide correct PSF:

Large beads (for example, 1 μm) are often not stained homogeneously and are likely to distort the PSF due to their high refractive index. So 1 μm beads are unsuitable for PSF measurement.

Based on the above rules, we chose the 0.1 μm fluorescent beads (TetraSpeck™ Microspheres, fluorescent blue/green/orange/dark red). This product is suggested beads for widefield (like our epi-fluorescence microscope) PSF acquisition. The 0.1 μm TetraSpeck™ microspheres are stained throughout with four different fluorescent dyes, yielding beads that each display four well-separated excitation/emission peaks - 360/430 nm (blue), 505/515 nm (green), 560/580 nm (orange) and 660/680 nm (dark red). The 0.1 μm and 0.2 μm TetraSpeck™ beads are ideal as sub-resolution fluorescent sources for calibrating instrument optics, especially in three-dimensional applications. This kind of

multicolor beads is very useful to calibrate also the Color Shift. It would be helpful for us to test the PSF difference for different wavelength in the different medium on our grating platform.

Table 2-2 The specification of different fluorescence filter sets in the experiment (black), and excitation and emission peaks for fluorescence bead under different filter set (red).

Unit: nm

FILTER SETS	EXCITATION	EXCITATION PEAK	MIDLINE OF DICHROIC	LONG-PASS EMISSION MINIMUM	EMISSION PEAK
DAPI	305-385	360	400	430	430
FITC	460-490	505	502	517	515
R6G	508-528	505	538	542	515
TRITC	528-555	560	566	602	580
CY5	630-647	660	655	665	680

Note: Cy5's emission filter is bandpass filter of 692/40nm; excitation: 628/40nm

2.3.3 Preparation of Samples for PSF Measurement

We prepared fluorescence beads on different substrates including plasmonic silver gratings, and flat silver and glass as a control for PSF measurement. First, substrates were properly cleaned before depositing fluorescence beads: glass microscope slides were cleaned by Piranha method; the 100 nm sputtered silver HDDVD gratings (10 nm Al₂O₃ coating) and flat silver substrates were cleaned by AMD wash. Second, the beads in suspension were diluted 1, 10, and 50 times with DI water before use. Before sampling, the beads were uniformly suspended by mixing and dispersing with a vortex mixer and sonicator. After checking different dilutions under 100× oil objective, 10-time dilution provides most suitable imaging condition. 5 μL of the TetraSpeck™ bead suspension was

applied to the surface of the substrates. After the droplet had been dried, the mounting medium (ProLong® Diamond Antifade Mountant) were applied to the dry sample of beads. The samples were then covered with a glass coverslip. Finally, the samples for PSF measurement were ready after the mounting medium cured for 24 h.

2.3.4 Fluorescence Measurement for PSF Studies

Fluorescence images for PSF measurement were taken by an Olympus BX51W1 epi-fluorescence microscope with a Hamamatsu ORCA-Flash 2.8 CMOS camera. The light source was a xenon lamp with a broad spectral range from 260 – 700 nm range without neutral density (ND) filter. Different fluorescence filter sets including DAPI, FITC, R6G, TRITC, and CY5, were used to study the PSF for different wavelengths. The images were characterized under 100× oil-immersed objective (NA=1.49) with a 2.5×adaptor. We first take the analysis for different substrates under FTIC filter as an example because we used FTIC filter for lots of our works, and the fluorescence exposure time was set to be 1 s or 2 s under this imaging condition.

Figure 2-9 shows the comparison of 100 nm fluorescence beads imaging on different substrates including glass, flat silver, and silver gratings, under FTIC filter. On both glass and flat silver, the fluorescence patterns follow the regular Airy disk diffraction pattern with a circular bright spot in the center and different diffraction order rings around it. However, the silver plasmonic grating substrates showed both Airy disk pattern and directed surface plasmon-coupled emission (SPCE) pattern. The directional emission perpendicular to the grating lines appears as a pair of spots, which make the shape in focus look like an ellipse when combining the circular bright spot. When the fluorescence bead

is out of focus, 1st diffraction order starts to become clear for all different substrates. It is still interesting to observe that the SPCE 1st order and 2nd order can be distinguished easier than the focus image due to the anisotropic directional emission. Based on the ratio of Airy disc and SPCE, we can determine how much emission is coupled back to the gratings. The fluorophores in a “large” 100 nm fluorescence bead are located at a different position with respect to the gratings, which leads to different coupling efficiency, resulting in the combination effect of Airy disc and SPCE on the plasmonic grating. This demonstrates that the plasmonic gratings can resolve the tiny difference at the nanoscale, by examining the fluorescence pattern and intensity.

In **Figure 2-10**, since CY5 filter matches better with the HDDVD silver grating dispersion curve in oil, the sub-diffraction limited information due to SPCE is more clear than Airy disk rings in the slightly defocus image, although the diffraction limited information overlay with the SPCE information in the focus image. We reconstructed 100 nm fluorescence bead using the experimental measured PSF, as shown in **Figure 2-11**. Since we would like to confirm the measured PSF, so we started with the simplest case on the glass which has the closest PSF compared to the theoretical PSF. The initial results show that reconstructed beads have the similar size for both experimental and theoretical PSF. The slightly larger size of experimental PSF compared with theoretical is probably due to the loss of resolution in the emission path.

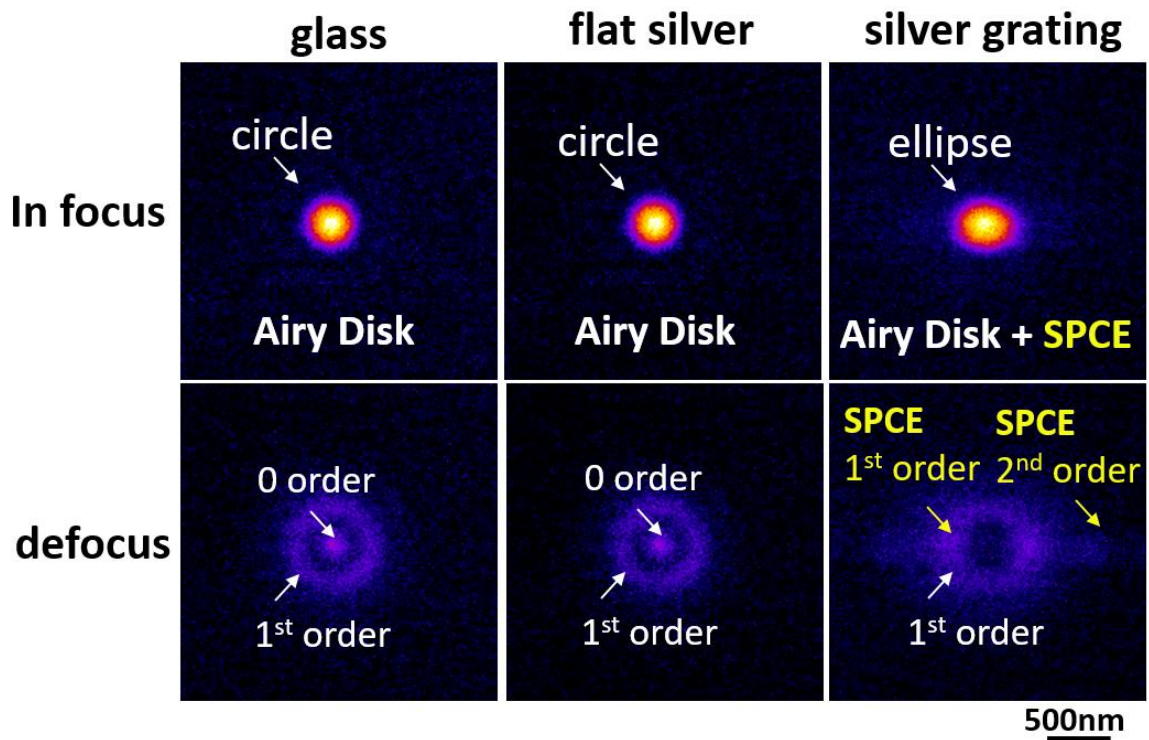


Figure 2-9 Comparison of 100 nm fluorescence beads imaging on different substrates including glass, flat silver and silver gratings, under FTIC filter.

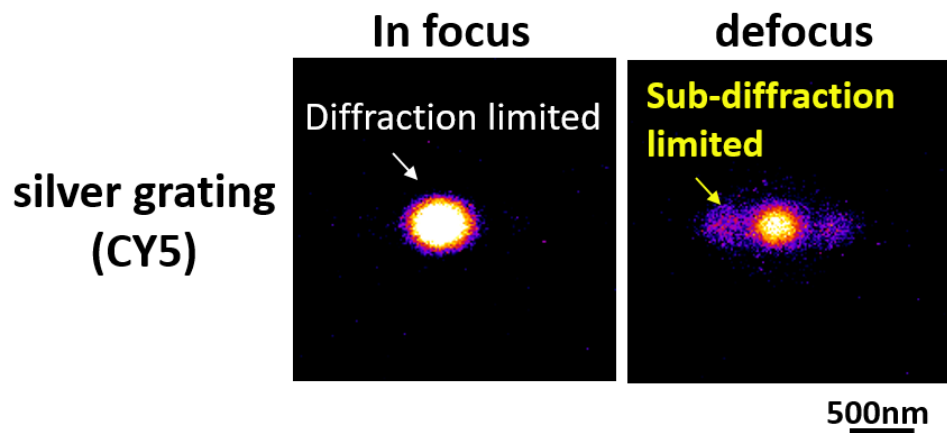


Figure 2-10 100 nm fluorescence beads imaging on silver gratings, under the CY5 filter.

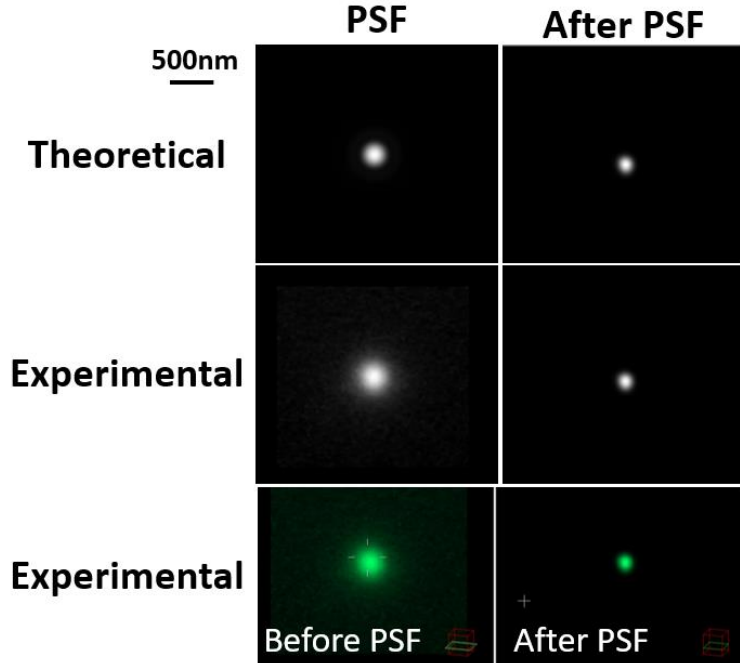


Figure 2-11 PSF for 100 nm fluorescence beads imaging on the glass, under FTIC filter.

2.4 Future Work

First, we will continue to add the effects of the plasmonic grating configuration by simulating different grating height, grating width, grating shape, metallic thickness, metallic or dielectric coating, etc. Moreover, we will describe how to optimize this conditions for different application. Second, we will explore the best grating configuration for the top and bottom illumination. We will utilize the superlensing theory for our gratings in this chapter to explain the enhanced resolution of the bright field imaging of different nanoparticles including aluminum nanoparticles, gold nanorods, silver nanoprisms, and so on. We need to match the coupling information for different structures and materials. Finally, we will calculate the PSF for gratings based on the fluorescence bead data including different fluorescence filters, polarizer, and analyzer. We will then apply it for the deconvolution of fluorescence images to improve the resolution. We will expand the

PSF studies to the super-resolution imaging of different nanostructures as well. We will come up with a more comprehensive theory for grating super-resolution images.

Chapter 3. Plasmonic Gratings with Nano-protrusions Made by Glancing Angle Deposition for Single-Molecule Super-Resolution Imaging

Super-resolution imaging has been advantageous in studying biological and chemical systems, but the required equipment and platforms are expensive and unable to observe single-molecules at the high (μM) fluorophore concentrations required to study protein interaction and enzymatic activity. Here, a plasmonic platform was designed that utilized an inexpensively fabricated plasmonic grating in combination with a scalable glancing angle deposition (GLAD) technique using physical vapor deposition. The GLAD creates an abundance of plasmonic nano-protrusion probes that combine the surface plasmon resonance (SPR) from the periodic gratings with the localized SPR of these nano-protrusions. The resulting platform enables simultaneous imaging of a large area without point-by-point scanning or bulk averaging for the detection of single Cyanine-5 (Cy5) molecules in dye concentrations ranging from 50 pM to 10 μM using epifluorescence microscopy for dye-doped polymer film and Cy3/Cy5-labeled DNA-RNA duplex. Combining the near-field plasmonic nano-protrusion probes and super-resolution technique using localization microscopy, we demonstrate the ability to resolve grain sizes down to 65 nm. This plasmonic GLAD grating is a cost-effective super-resolution imaging substrate with potential applications in high-speed biomedical imaging over a wide range of fluorescent concentrations.

3.1 Introduction

Due largely in part to the advances made over the past ten years, super-resolution

imaging has been used for single-molecule (SM) studies that have revolutionized *in-situ* investigation of chemical and biological systems.[89]–[91] Generally, SM imaging is only feasible within a limited fluorophore concentration range (from roughly 1 pM to 10 nM) in most diffraction-limited imaging techniques.[92] Unfortunately, protein interactions and enzymatic activity experiments often require much larger fluorophore concentrations (>1 μ M). This renders the observation of single-molecule fluorescence impossible in many imaging systems. Many promising strategies are in development to beat the high concentration imaging limit with reasonable success.[92] A prominent example of which is the combination of zero-mode waveguides (ZMWs) and nano-antennas termed “nano-antenna-in-box”. Fluorescence correlation spectroscopy (FCS) measurements revealed that single molecules can be detected at concentrations higher than 15 μ M at the hot spot formed by the nanoantenna-in-box.[93] While convenient for FCS measurements, it is still challenging to immobilize molecules at the precise location of the hot spots formed by these nanoantennas or at a determined position within the ZMWs.[92]

To compensate for the inability to immobilize molecules at precise locations, the density of hot spots should be increased such that the probability that a randomly immobilized molecule located within the proximity of a hot spot is much higher. In this chapter, we developed a straightforward method for fabricating a fluorescence enhancing substrate that combines the surface plasmon resonance (SPR) created by periodic gratings with the localized SPR (LSPR) formed by nano-protrusions grown on top of the grating ridges and nanogaps formed between the grating ridges. In previously published literature, we developed a method of fabricating plasmonic gratings (**Figure 3-1a**) with random nanogaps for SM fluorescence intensity enhancement[6] as well as visualization of DNA

oscillation intensity.[94] To greatly improve SM fluorescence enhancement, we utilized a glancing angle deposition (GLAD) technique to control the silver film growth on the polymethylsilsesquioxane (PMSSQ) polymer gratings replicated from HD DVD grating molds. Depositing silver at a specific angle relative to the surface can create a high density of silver nano-protrusions on the grating surface and ordered nanogaps in the shadowed region of the grating, as shown in **Figure 3-1b-c**. The high density of nano-protrusions and nanogaps, which behave as plasmonic hot spots, enables simultaneous imaging of the entire sample without requiring point-by-point scanning as in NSOM or precise molecule immobilization regions as needed in ZMWs.

GLAD silver gratings were deposited at $\alpha=60^\circ$ using thermal evaporation and characterized using atomic force microscopy (AFM) as well as variable angle spectroscopic ellipsometry (VASE) to determine the structure and SPR generation characteristics. Using this information, finite-difference time-domain (FDTD) simulations were made to study where electromagnetic (EM) fields are concentrated in the unique nanostructures of a GLAD grating. SM fluorescence images were taken using the GLAD gratings over a wide range of concentrations of either a DNA/RNA duplex with Cyanine-3 (Cy3) and Cyanine-5 (Cy5) dye labels or with Cy5 dye molecules immobilized in a 30 nm thick PMSSQ matrix spin-coated onto the grating. Combining the “true” super-resolution approach (near-field plasmonic probes from GLAD gratings with incorporated nano-protrusions) and “functional” super-resolution analysis of localization microscopy, it enables rapid imaging of nanostructures with a high density of fluorophores.

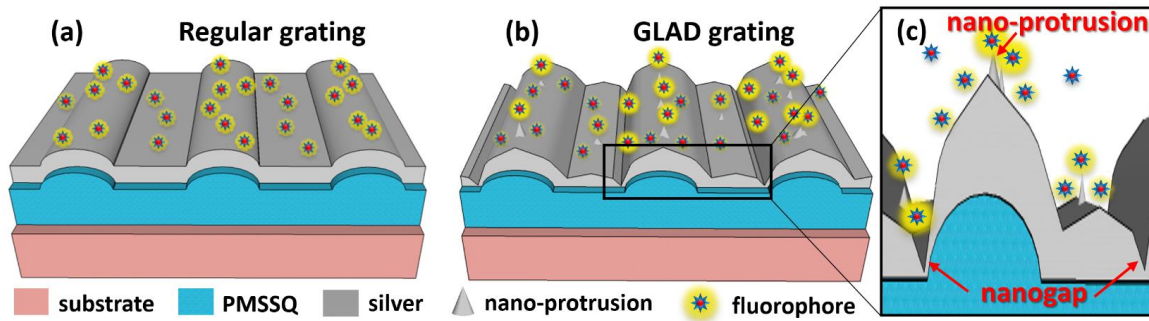


Figure 3-1 Schematic of a silver plasmonic grating on the fluorescence-based application: (a) regular grating and (b) GLAD grating, (c) zoom in to show the GLAD morphology with nano-protrusions and nanogaps. The brighter yellow color of the fluorophore indicates the higher fluorescent intensity when nearby a nano-protrusion. The platform can be coated with any medium to suit the needs of the application. For example, it is important to have a stable surface with sufficient binding sites for biological studies, and hence, the GLAD grating can be coated with SiO₂ or gold to functionalize the surface; the GLAD grating can also be coated with a PMSSQ matrix with dye for fluorescence studies.

3.2 Experiment

3.2.1 Fabrication of Plasmonic Silver Gratings by GLAD

PMSSQ gratings were formed using a 3 wt% PMSSQ and 1 wt% (3-aminopropyl)triethoxysilane (APTES) in 100% ethanol. Following stamping, gratings were heated at 60 °C for 20 min to crosslink further the PMSSQ/APTES gratings. Metallic gratings were fabricated with a variety of angles (from 30 ° to 70 °) and at varying deposition thicknesses to find the best nano-protrusion density and nanogap widths as well as grating profiles necessary for enhancements. Ultimately $\alpha=60^\circ$ was selected as it produced the largest number of nano-protrusions and most uniform nanogaps of any of the tested angles.

The silver was deposited using a Nano 38, Kurt J Lesker thermal evaporator with a deposition rate of 0.55 \AA/s , a working vacuum of 5×10^{-8} Torr at room temperature. A 2 nm adhesion layer of chromium was deposited before the 30 to 40 nm thick silver layer and lastly the 10 nm thick gold layer. It was seen that for thicker metal layers (*e.g.* 100 nm silver), the nano-protrusions and nanogaps start to coalesce with surrounding films leading to a reduction in the overall localized enhancement characteristics. In contrast, a thinner deposition of metal (*e.g.* 40 nm silver) leads to a better controllability of the hot spot regions. Unfortunately, the downside of thinner films is that at very low metal thicknesses the overall grating structure is optically lossy due to transmission.

3.2.2 *GLAD Grating Characterization*

The GLAD gratings were characterized using a J. A. Woollam Variable Angle Spectroscopic Ellipsometer (VASE) in the reflectance and transmittance mode with a TM-polarized light incident on the gratings at different angles and wavelengths. This setup comprises of a Xenon broadband source that directs light through a monochromator via an optical fiber. The light is made incident on the silver grating sample with the gratings aligned perpendicular to the plane of incidence for optimum excitation of the surface plasmons on the silver grating. Surface topography was measured using a Bruker © Innova AFM equipped with an open-loop, small area scanner, and AppNano ACTA silicon SPM tips (k: 40 N/m, f: 295 kHz, tip radius: ~6 nm). As the spatial resolution of AFM is closely tied to the tip radius, the SPM tips were used to provide the necessary resolution to obtain accurate nano-protrusion size above 6 nm.[95] All AFM measurements were completed within 2 hours of metal deposition. All fluorescent dye measurements taken within 4 hours

of metal deposition and DNA/RNA imaging was taken within 24 hours of metal deposition. No visible degradation was observed during microscope imaging. 30 glancing angle depositions were run over an 8 month period and found to be consistent in surface structure.

3.2.3 Fluorescence Image Collection

Fluorescence images were collected using an Olympus BX51W1 epi-fluorescence microscope equipped with a Hamamatsu ORCA-Flash 2.8 CMOS camera and a xenon white light source with a broad spectral range from 260 – 700 nm range. Rhodamine 6G dye films were imaged with a 518 ± 8 nm bandpass excitation filter, 540 nm dichroic mirror, and 542 nm long pass emission filter. Cy5 fluorescence was observed with a 627 ± 21 nm bandpass excitation filter, 665 nm dichroic mirror, and 672 nm long pass emission filter.

3.2.4 Single-molecule Image and Super-Resolution Analysis

SM images were taken with an Olympus IX-71 inverted epifluorescence microscope with tunable excitation angle. The excitation source for Cy5 and the DNA/RNA duplex was a 100 mW 642 nm diode-pumped solid-state lasers (Spectra-Physics, Excelsior One.) Fluorescence was collected using a UPlanSApo 60 \times water-immersion objective (Olympus, NA = 1.20) and imaged with an Andor iXon⁺ EMCCD camera. Video was collected with a 100 ms integration time and a total length of 1200 frames. The fluorescence time trace videos were used to analyze SM behavior and localization microscopy super-resolution analysis.

3.3 Discussion

3.3.1 Design and Fabrication of GLAD Gratings

GLAD is a technique that is often utilized to produce unique surface structures. In its most basic form, GLAD is the deposition of metallic atoms at an oblique angle with respect to the substrate. Since little or no lithographic process is needed, it has a substantial commercial advantage over other column growth methods as it can be performed rapidly on large-scale substrates. Nano-protrusions and nanogaps can be formed by modifying the surface energy of a regularly spaced grating substrate and by controlling the vapor incident angle and the deposition rate. During the deposition, 2 nm thick chromium and 40 nm thick silver films were deposited sequentially at an angle, α , onto PMSSQ gratings. Due to the oblique angle, the metallic atoms primarily impinge on the ridges of the grating facing the evaporation source. The oblique deposition angle also causes the formation of a shadow region behind each ridge (**Figure 3-2**).

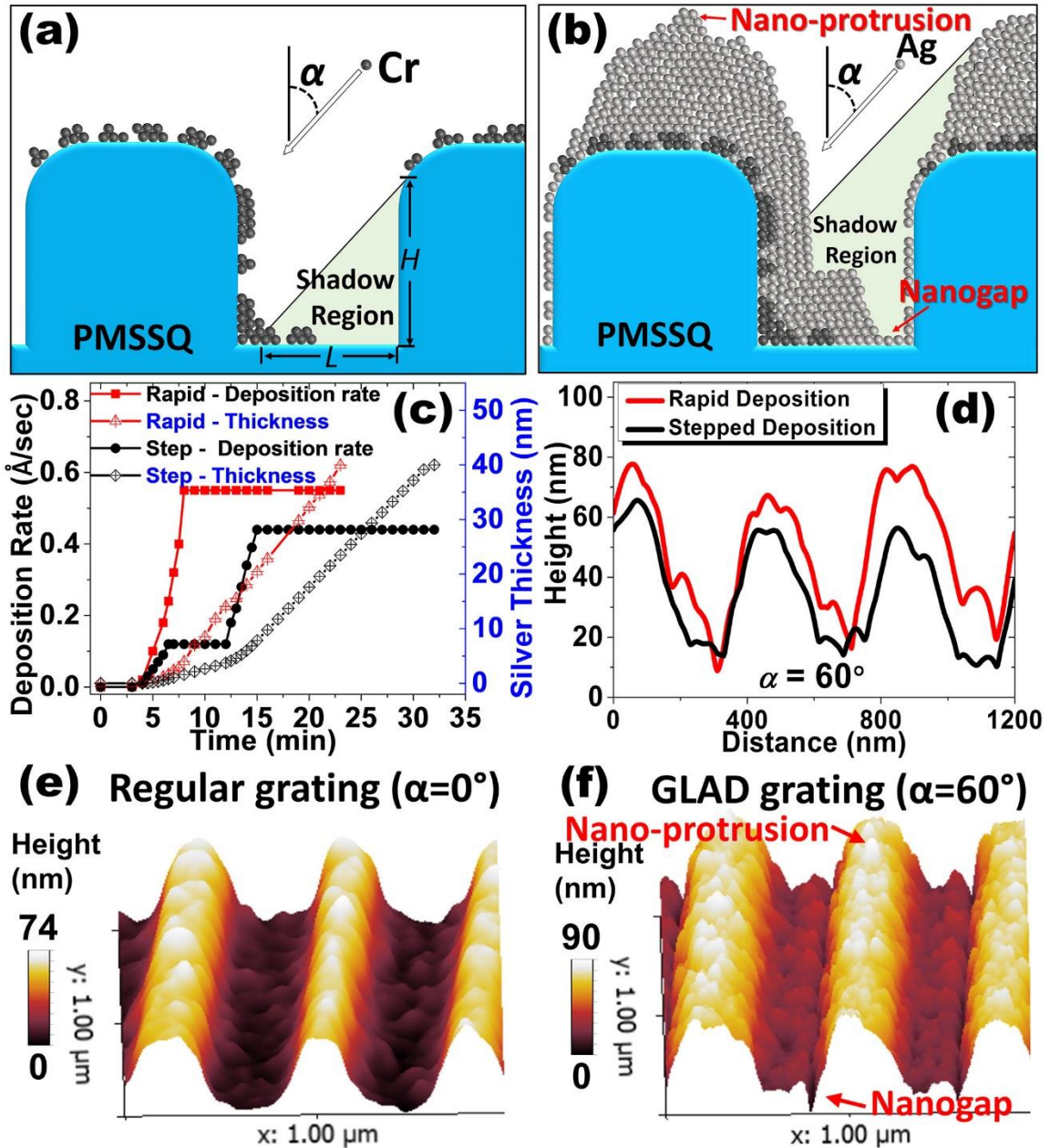


Figure 3-2 Illustration of the GLAD growth process showing the oblique arrival of silver vapor to the PMSSQ gratings: (a) step #1. Deposition of the thin chromium adhesion layer; (b) step #2. Rapid silver deposition encourages vertical growth that results in plenty of nano-protrusions, and clear nanogaps. Comparison between rapid and stepped-deposition: (c) deposition rates and silver thicknesses over time, (d) AFM 2D profiles. AFM 3D contour maps: (e) regular grating at a normal deposition angle ($\alpha = 0^\circ$) showing few typical

surface features; (f) GLAD grating with rapid silver deposition rates at an oblique deposition angle ($\alpha = 60^\circ$), showing controlled nanogaps, and nano-protrusions (hot spots).

The mobility of chromium and silver adatoms was also influenced by the low surface energy of the PMSSQ gratings (0.0236 J m^{-2}) resulting in the formation of metal seeds and islands (**Figure 3-2a**). Due to the higher dissociation energy of Ag-Ag vs. Ag-Cr, silver typically follows Stranski-Krastanov growth and forms metal islands when deposited on a chromium adhesion layer.[4], [96], [97] The deposition rate was increased rapidly to $0.55 \text{ \AA sec}^{-1}$ at the start of the silver deposition and maintained for the duration of the deposition. The rapid increase in deposition rate encourages vertical film growth by reducing adatom mobility (**Figure 3-2b**). [4] The metal atoms are preferentially deposited on the top and side of the grating ridges resulting in the formation of nano-protrusions on top of the ridges and a very thin film on the walls of the gratings in the nanogap shadow region. In contrast, increasing the deposition rate in steps from $0.12 \text{ \AA sec}^{-1}$ to $0.44 \text{ \AA sec}^{-1}$ with a lower final deposition rate increases adatom mobility and encourages lateral film growth, resulting in smoother films without nano-protrusions (**Figure 3-2c-d**). Typically, GLAD is performed with rotating substrates, but the samples used here were kept stationary to avoid disrupting the shadow region.[98] Care was taken to ensure that the direction of the grating ridges was perpendicular to the incoming flux such that each grating unit contains a single shadow region, the initial width of which, was determined based on **Equation 3-1**.

$$L = H \times \tan \alpha \quad (3.1)$$

Where L is the width of the shadow region, H is the height of the barriers, α is the GLAD angle in degrees (**Figure 3-2a**). H is close to the grating height at the beginning of

the deposition and increases over time. H and L change during the metal deposition process, which is also a factor resulting in different levels of nanostructures. Characterization of the gratings was performed to find the exact set of surface morphologies. We observed that the formation of a nanogap in the shadow region was largely dependent on α and only formed nanogaps with well-defined dimensions over a specific angle range, $\alpha = 60^\circ - 70^\circ$ (See **Figure 3-3** and **Table 1** for AFM profiles at different deposition angles $\alpha = 0^\circ, 30^\circ, 60^\circ, 70^\circ$). When lower GLAD angles were used, $\alpha \leq 50^\circ$, the nanogaps were too narrow and shallow as a result of the diminishing shadow width; further, the nano-protrusions were too sparse and blunt to provide enough probes. GLAD silver gratings deposited at $\alpha = 60^\circ$ were selected for the following experiments due to the high density of nano-protrusions found on those gratings as well as the well-defined, narrow and deep nanogaps (**Figure 3-2e-f**, **Figure 3-4**, **Figure 3-5**). Each of these hierarchical nanoscale surface structures will concentrate the surrounding field to produce the desired hot spots. The resulting fluorescence enhancement for Cy5 on the silver GLAD grating ($\alpha = 60^\circ$) was demonstrated to be highest amongst all deposition angles we investigated (**Figure 3-6**).

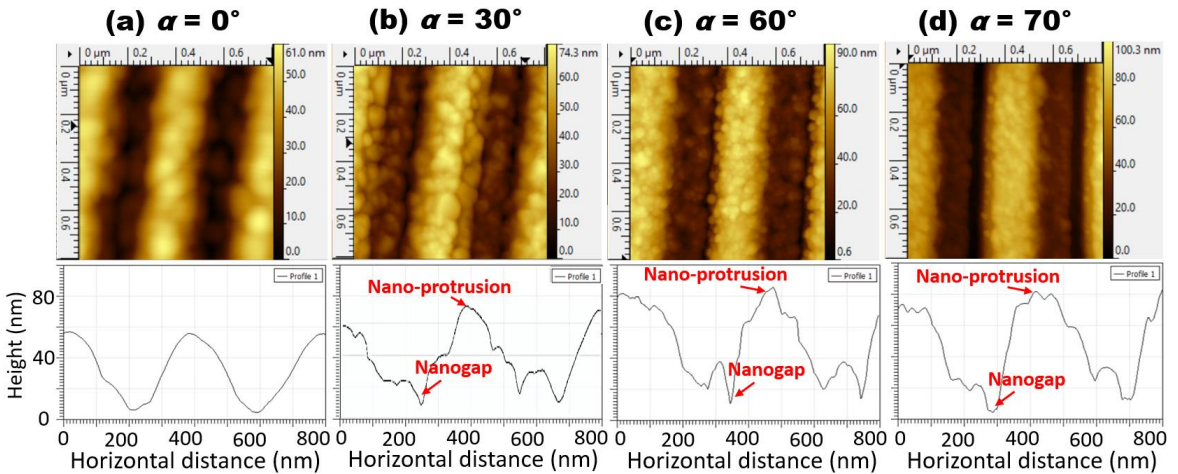


Figure 3-3 2D AFM images and profiles of silver GLAD gratings with rapid silver

deposition rates at different deposition angles (a) $\alpha = 0^\circ$, (b) $\alpha = 30^\circ$, (c) $\alpha = 60^\circ$, (d) $\alpha = 70^\circ$.

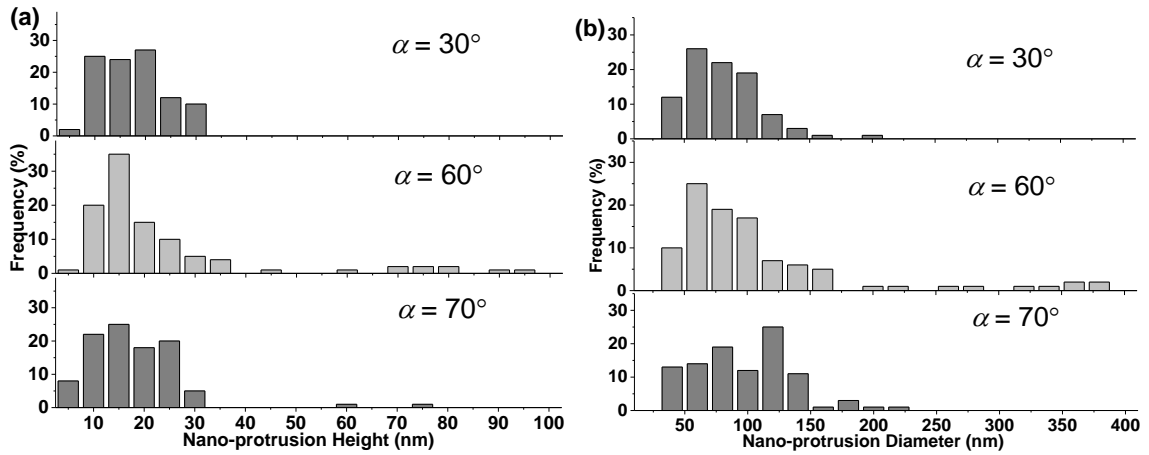
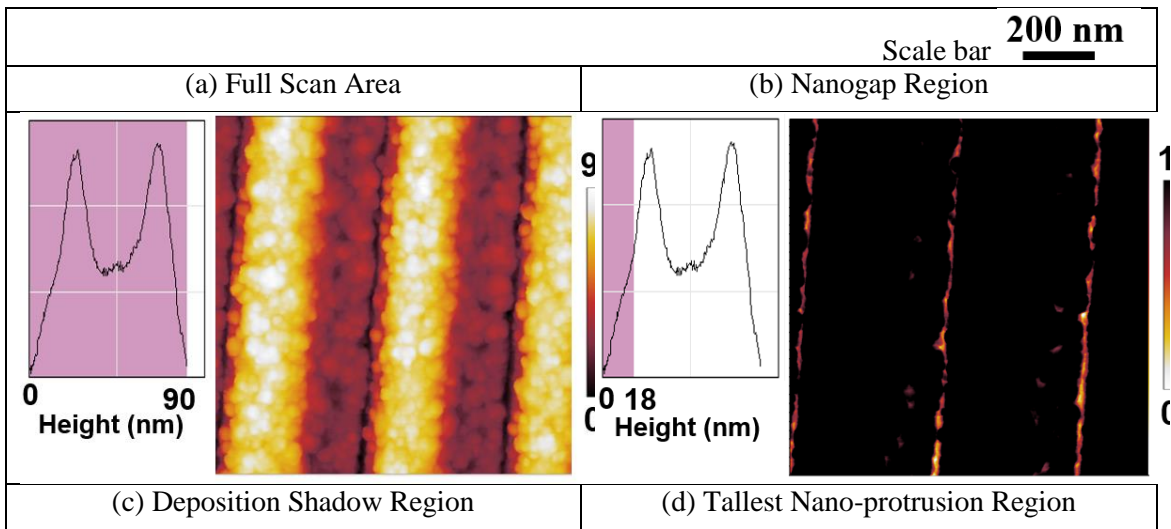


Figure 3-4 (a) Nano-protrusion height above the grating ridge histograms and (b) nano-protrusion base diameter histograms at $\alpha = 30^\circ$, $\alpha = 60^\circ$, and $\alpha = 70^\circ$ deposition angles. Histograms obtained from a sample of 100 nano-protrusions from AFM topography scan with a ~ 1 nm radius tip. GLAD samples were deposited over an 8 month period and found to be very consistent in surface structure and reflectance.



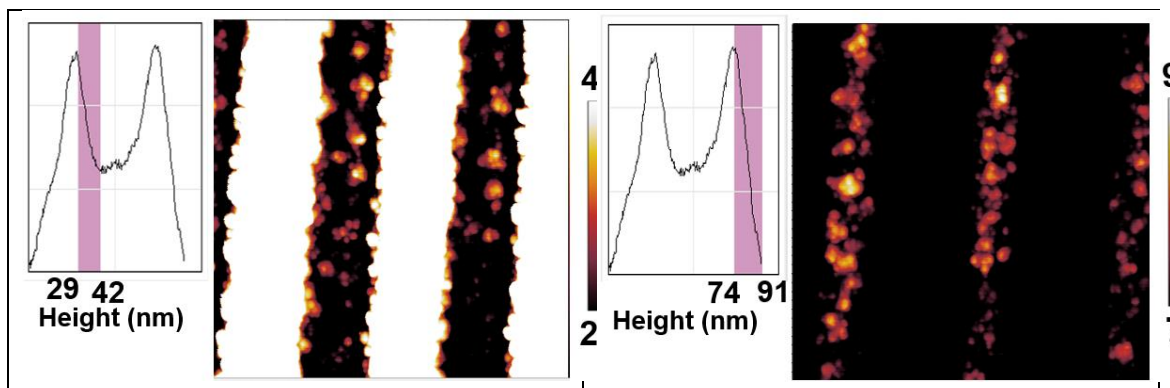


Figure 3-5 $1 \times 1 \mu\text{m}$ AFM scans and height histograms of silver GLAD gratings ($\alpha = 60^\circ$) with the (a) entire scan or (b,c,d) regions of interest highlighted. Highlighted portion of the GLAD grating containing the (b) nanogap region, (c) nano-protrusions in the deposition shadow region, and (d) Nano-protrusion region on top of the grating ridge.

Table 3-1 Average grating pitch, height, and nano-protrusion height above the ridge and nanogap width obtained by AFM.

	Grating Pitch (nm)	Grating Height (nm)	Nano-protrusion height (nm)	Nanogap width (nm)
PMSSQ Grating	401.8 ± 4.1	51.3 ± 0.3	-	-
GLAD $\alpha=0^\circ$	402.7 ± 3.9	57.7 ± 1.1	8.6 ± 3.1	-
GLAD	398.8 ± 4.5	39.6 ± 5.8	17.9 ± 6.8	15.4 ± 6.3

$\alpha=30^\circ$				
GLAD	399.2 ± 6.8	46.4 ± 6.6	20.7 ± 18.4	18.9 ± 4.0
$\alpha=60^\circ$				
GLAD	401.5 ± 5.6	50.3 ± 2.5	18.2 ± 9.5	34.4 ± 6.6
$\alpha=70^\circ$				

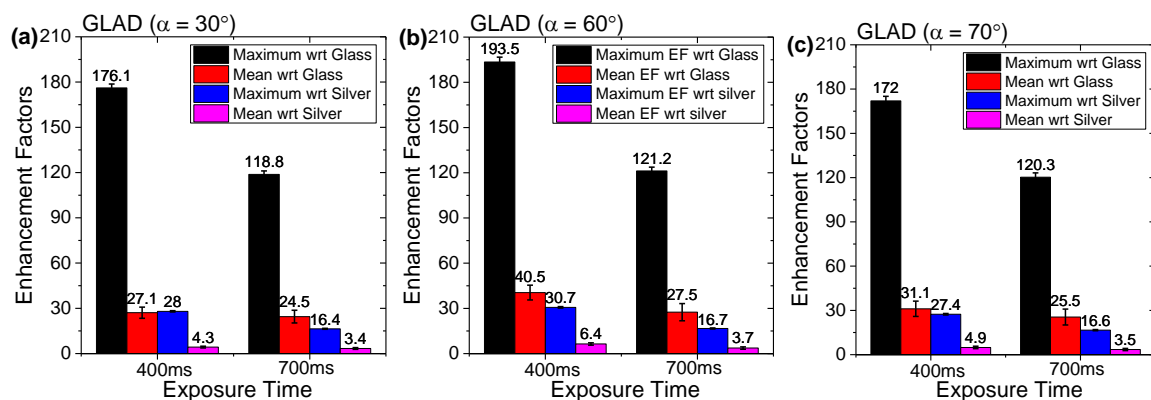


Figure 3-6 Enhancement factors (with respect to glass and flat silver) with spun-coated Cy5 (in PMSSQ + ethanol solution) on 40 nm silver HDDVD GLAD gratings at different deposition angles (a) $\alpha = 30^\circ$, (b) $\alpha = 60^\circ$, (c) $\alpha = 70^\circ$. The images were taken with $60\times$ water-immersion objective and with 400 ms and 700 ms exposure times. The samples were illuminated by Xenon light source with broad spectra filtered by Cy5 filter cubes.

3.3.2 Experimental and Simulated Optical Properties

GLAD gratings achieve their unique properties through the combination of a periodic surface corrugation and the field concentrating effect of localized nanostructures including nano- protrusions, and nanogaps. Due to the growing interest in plasmonic biosensors, the field has obtained a much better understanding of the fundamental science

behind SPR on nanostructures, such as plasmonic gratings. In the case of gratings, light can be diffracted off of metallic gratings at several orders and, as a result, the diffracted light can gain momentum.[4], [15] Surface plasmons can only be generated by a transverse-magnetic (TM) polarized electric field because the electron oscillations in the incident plane exhibit the discontinuity at the metal-dielectric interface. SPR formation only occurs if the incoming wave vector matches that of a surface plasmon polariton (SPP), which can be achieved in part by utilizing the additional momentum and re-direction supplied by grating diffraction.[99] The grating itself must also be coated with a negative permittivity material, such as silver or gold, at the desired frequencies to form SPR. Silver can be used to form higher intensity EM fields due to its inherently low dielectric losses at optical frequencies; however, it is very susceptible to corrosion, unlike gold.[100] The wave vector matching conditions for a particular metal grating and the dielectric interface was seen in **Equation 3-2** [4], [15], and experimental data from a silver GLAD grating was shown in **Figure 3-7**.

$$k_{\text{SPP}} = \frac{\omega}{c} \sqrt{\frac{\epsilon_m \epsilon_d}{\epsilon_m + \epsilon_d}} = k_{ph}^x \pm mG \quad (m = \pm 1, 2, 3, \dots) \quad (3.2)$$

By introducing metallic nano-protrusions into this grating structure, we create a unique light coupling situation. Unlike the SPR characteristics of a regular metallic grating (**Figure 3-1a** and **Figure 3-2e**), metallic nano-protrusions can couple propagating photons and, due to the small size, the resulting localized SPP is confined to the structure (**Figure 3-1b** and **Figure 3-2f**).[101] The confinement of light into such nanostructures is one of the underlying principles that increases the spatial resolution of NSOM.[101] If, instead of using a single probe as in NSOM, many probes in the form of nano-protrusions are placed on the surface, we can obtain an increase in spatial resolution without many of the scanning

restrictions of NSOM. The shape and size of these nano-protrusions can have an enormous influence on optical microscopy spatial resolution and electric field strength in much the same way that the shape and size of probes can have on the spatial resolution of NSOM.[102]

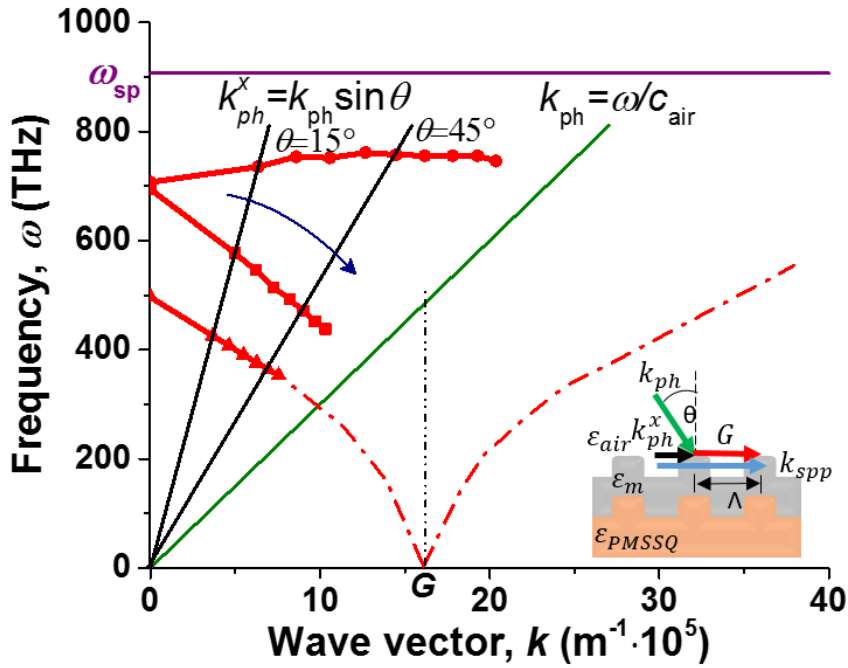


Figure 3-7 Experimental frequency vs. wave vector plot for a silver GLAD grating in air calculated by the SPR peak location from the reflectance. Inset: Illustration of the wave vector matching between incident EM radiation (transverse-magnetic (TM) light) on a grating and a propagating surface plasmon polariton.

While not as uniform as individual NSOM tips, the presence of the nano-protrusions greatly enhances the signal-to-noise ratio, which is more critical than uniformity in spatial resolution when studying individual molecule behavior. The distribution of the nano-protrusions grown by this technique is still much narrower than

the growth of silver on non-patterned substrates, such as the structures on the glass regions outside of the grating (**Figure 3-8**). This is due to the fine control over the surface energy, deposition rate, deposition angle, and the growth barriers provided by the grating structure itself. To fully understand the effect of nanostructure-mediated plasmonic electric field (E-field) strength on fluorescence enhancement, the field strength associated to the nanostructure must be quantified. Fluorescence enhancement is proportional to the local E-field intensity and is a product of both enhancements of the excitation and emission of the fluorescent molecule.[6] This suggests that the fluorophore should be placed in the location with the highest E-field strengths, typically found very close to the metal film, to obtain the highest enhancement. However, the proximity of the fluorophore can also reduce the fluorescent emission due to quenching and thus it must also be considered to obtain the highest enhancements.[103] FDTD simulations using FullWAVE software (RSoft, Inc.) were conducted to determine the E-field strength at different locations on the GLAD gratings and to aid in quantifying fluorescence enhancement.

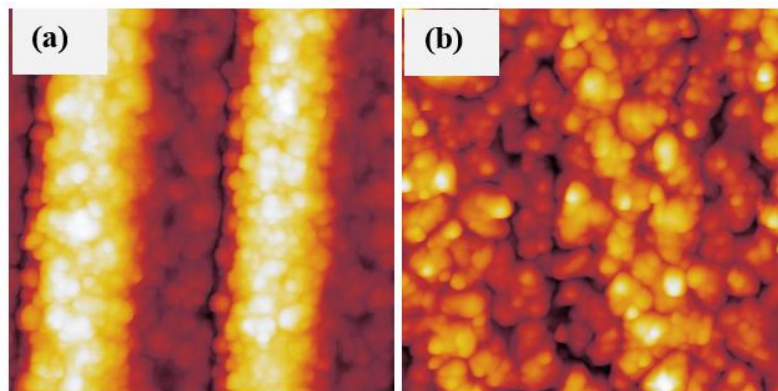


Figure 3-8 800×800 nm AFM scans of (a) 60 °GLAD Grating and (b) silver grown on flat glass deposited at 60 °GLAD with the same height scale as Fig. S2 (0 – 90 nm). Scanned with a ~1 nm AFM tip. The roughness of the flat silver film and its granular structure provides a substantial increase in surface area as compared to, for example, glass surfaces.

The calculated surface area via Gwiddyon © AFM analysis software of (a) is $782.475 * 10^{-15}m^2$ with a projected flat area of $640.0 * 10^{-15}m^2$. (b) has a calculated surface area via via Gwiddyon © of $782.173 * 10^{-15}m^2$ and a projected flat area of flat area of $640.0 * 10^{-15}m^2$.

The optical properties of GLAD gratings were investigated in the air with variable angle ellipsometry before their usage as platforms for biological imaging. Based on the AFM profile as shown in **Figure 3-2f**, we built a 2D model structure for GLAD grating (**Figure 3-10**). The resulting simulated reflection matches well with the experimentally obtained reflection. **Figure 3-9a** shows that the simulated reflection measured at 15° incidence of light for GLAD gratings follows the same baseline and similar SPR coupling peak at silver/air interface located at approximately 520 nm, compared with experimental reflection data. Other peaks at longer wavelengths correspond to the interaction at PMSSQ/silver interface after light has passed through the silver grating layer. These sharp peaks appear only for GLAD gratings (**Figure 3-10** and **Figure 3-11**) because the thinner layers of silver on the grating walls in the shadowed nanogap region, as well as periodic nanogaps, make it easier for light to transmit through the silver. The modeled E-field distribution at the cross-section of GLAD gratings demonstrates that the light is primarily coupled to the thin wall of nanogap at these additional peaks (**Figure 3-10**). Unlike the regular gratings ($\alpha = 0^\circ$), GLAD gratings can couple light in both visible and IR regions, which is demonstrated by experimental and simulated reflectance spectra (**Figure 3-10**). It was also observed that E-fields were highly localized at nanogaps in the IR spectrum, this demonstrates that these platforms could have additional applications in research topics such

as heating and IR sensors.

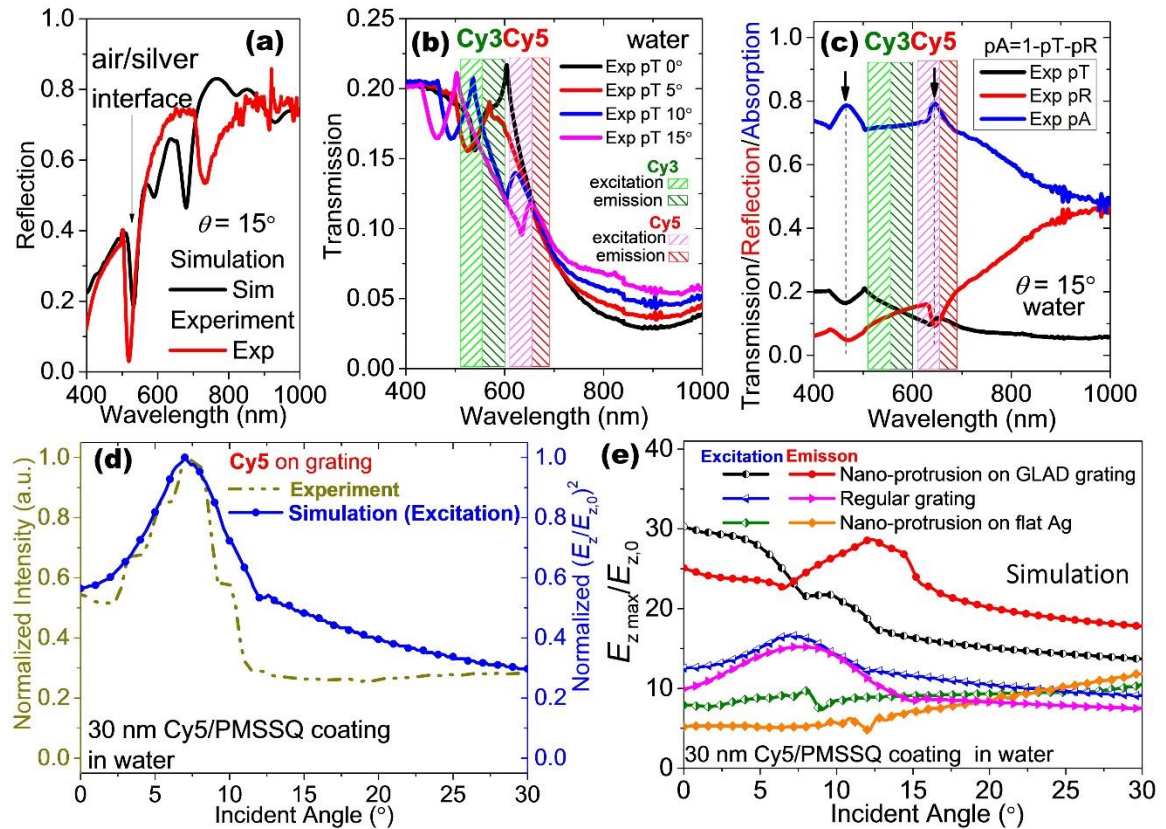


Figure 3-9 Optical properties of 40 nm Ag GLAD gratings (deposited at $\alpha = 60^\circ$): (a) experimental and simulated TM-polarized light reflection spectra taken at 15° incidence of light in air; (b) experimental transmission taken at $0 - 15^\circ$ incidence of light in water; (c) experimental transmission, reflection, and absorption taken at 15° incidence of light in water, where absorption (pA) = 1-transmission (pT)-reflection (pR). The color bars in (b-c) indicate the excitation and emission wavelengths range for Cy3 and Cy5; the arrows point out the upper and lower resonance mode at 15° incidence for GLAD gratings. (d) Normalized fluorescence intensities vs excitation angle for different Cy5 spin-coated on the surface of Ag GLAD gratings (10 μM concentration, and thickness of 30 nm in a PMSSQ matrix using a $60\times$ water-immersion objective by epifluorescence microscope; the power of 642 nm laser for Cy5 is 50 mW) and simulated normalized E-field intensity

$(E_z/E_{z,0})^2$) under Cy5 excitation wavelength (642 nm). (e) Simulated maximum $E_z/E_{z,0}$ at nano-protrusion vs. incident angle for 40 nm Ag GLAD gratings coated with 30 nm PMSSQ in water environment at excitation and emission wavelength of Cy5; maximum $E_z/E_{z,0}$ at regular grating and nano-protrusion on 40 nm flat Ag under the same condition as comparisons.

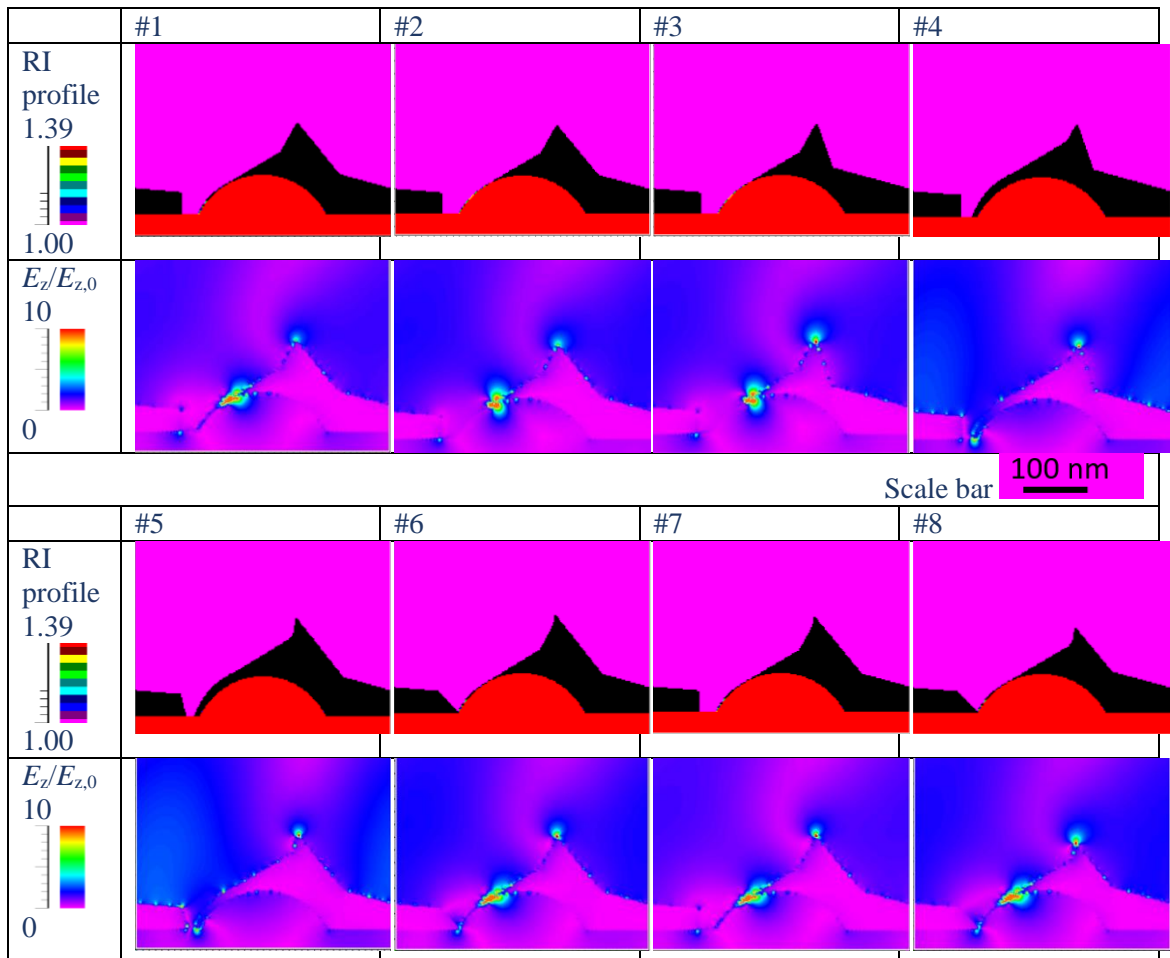


Figure 3-10 Design of simulated geometry for 40 nm Ag HD-DVD GLAD gratings: refractive index (RI) profile and E-field ($E_z/E_{z,0}$) at 40° incident angle at resonance wavelength in air; intensity bar is 0-10, and scale bar is 100 nm.

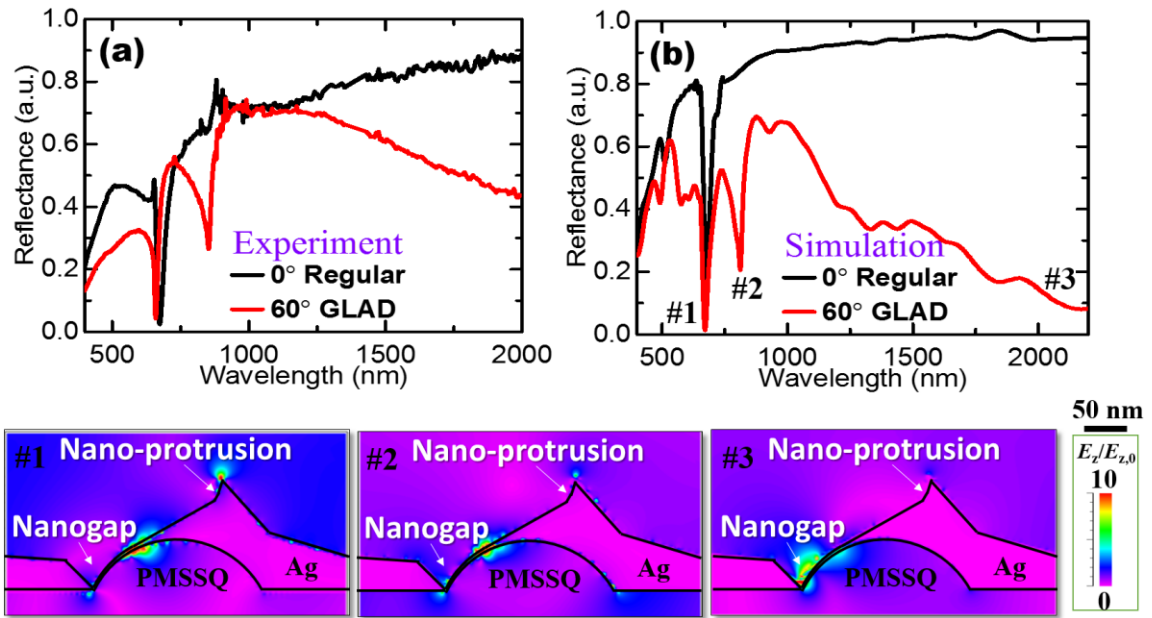


Figure 3-11 Experimental and simulated p-polarized light reflectance spectra taken at 40° incidence of 40 nm Ag gratings deposited at $\alpha = 0^\circ$ (regular) and $\alpha = 60^\circ$ (GLAD) in air; (#1-#3) FDTD-simulated E-field ($E_z/E_{z,0}$) for one period of GLAD structure showing E-field concentration at hot spots for different incident wavelengths; intensity bar is 0-10, and scale bar is 50 nm.

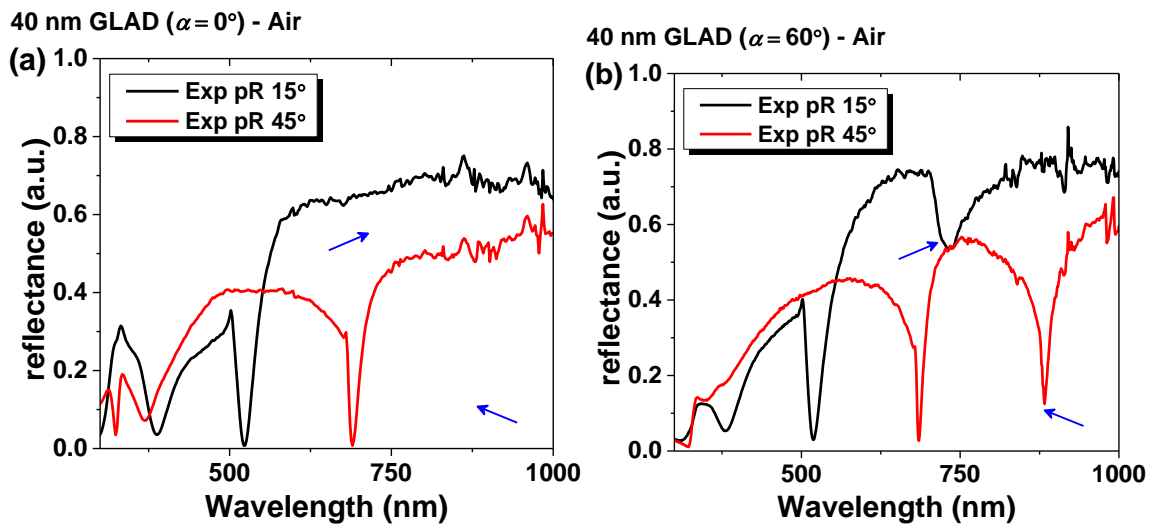


Figure 3-12 Experimental reflectance taken by ellipsometry for 40 nm silver HDDVD gratings: (a) regular grating ($\alpha = 0^\circ$) in the air, (b) GLAD grating ($\alpha = 60^\circ$) in the air. The blue arrows point out the additional peak from GLAD gratings compared with regular gratings.

As the imaging of biological samples requires submersion in water (or buffer), the optical properties of GLAD gratings ($\alpha = 60^\circ$) were studied under an aqueous conditions both experimentally and with simulations. The coupling of light to plasmonic gratings is highly angle dependent and can extend over a wide range of wavelengths.[6] In order to obtain the highest fluorescent enhancement using regular plasmonic gratings and a microscope objective for imaging, the selected fluorophores must possess excitation and emission spectra that overlap with the low angle coupling range of our platforms.[4] The transmission spectra at $0 - 15^\circ$ incidence of light taken by ellipsometry (**Figure 3-9b**) indicates that Cy3 excitation and emission wavelengths are coupled to the gratings from $0 - 5^\circ$ of incidence, whereas Cy5 excitation and emission wavelengths exhibit SPR coupling at higher angles ($10 - 15^\circ$). For plasmonic gratings, matching the angular excitation range with imaging equipment capabilities is critical for optimal illumination and signal capture.[4], [6], [94] However, GLAD gratings are less sensitive to angular illumination due to the combination of SPR coupling and LSPR by nanosingularities, which is further discussed in the following sections.

To rule out the effect of high reflection being the cause for sharp declines in transmission intensity, the platforms were investigated based on the peaks of absorption ($=1 - \text{transmission} - \text{reflection}$). The “absorption” value includes not only the coupling on

the water/silver grating interface, but also scattering and loss inside materials as well as interfaces. However, those factors are not highly sensitive to incident angles and wavelengths. We can thus study the absorption peak for SPR coupling. The transmission, reflection, and absorption spectra taken at 15 ° incidence of light in a water environment can be found in **Figure 3-9c** (reflection measurements are limited to $\geq 15^\circ$ due to equipment limitations). The absorption peaks (black arrows) overlap with the transmission and reflection dips, which confirms that the light is being absorbed into the grating.

Cy5 fluorophores spin-coated within a 30 nm PMSSQ matrix over the GLAD silver gratings were measured in a water environment for fluorescence studies. **Figure 3-9d** shows the experimental normalized fluorescence intensity of Cy5 fluorophores on the overall area of silver gratings as a function of excitation angle and simulated normalized E-field intensity for grating. As constant power is used for every incident angle, variations in E-field intensity should be the result of changes in coupling efficiency.[104], [105] The simulated E-field intensity vs. incident angle under an excitation wavelength (642 nm) of Cy5 on regular gratings exhibits peaks similar to that observed in the experimental intensity for the overall area of GLAD grating at $7^\circ \sim 8^\circ$ incident angle (**Figure 3-9d**), indicating that GLAD gratings retain the SPR coupling properties observed from regular gratings. To compare the value of E-field strength and angle dependency of Cy5 excitation on different substrates, simulations for GLAD grating with nano-protrusions, regular grating, and nano-protrusions on flat silver film were investigated (**Figure 3-9e**). The E-field strength for nano-protrusion on flat silver film changes slightly with incident angle, while that for regular grating has angle dependency for SPR coupling as discussed above. The E-fields at hot spots in GLAD gratings are the combination of SPR from the periodic metallic

grating structure and LSPR from nano-protrusions created by GLAD deposition, resulting in the E-fields at hot spots on GLAD gratings are higher than both regular gratings and nano-protrusion on flat silver under all angle excitations. Although the coupling of grating platforms have angle dependency, the broad coupling range eases the use of these platforms in many of optical systems with less angular control.

The simulated E-field distribution at the incident angles resulting in the maximum E-field values for excitation and emission shown in **Figure 3-9e** are displayed in **Figure 3-13** and **Figure 3-14** for Cy5 and Cy3, respectively. E-field is not uniformly distributed on the grating surface with different coupling pattern as shown in **Figure 3-9**, and hence, the E-field on nano-protrusion changes with its position on the grating. This results in the angles for maximum E-field for nano-protrusions on GLAD grating showing shift compared with the coupling peaks for regular grating as seen in **Figure 3-9e**, although it is still within the broad coupling region of the grating. When Cy5 is illuminated with a 642 nm laser, the highest E-field on nano-protrusions is obtained at $\theta = 0^\circ$, with hot spots located on both nano-protrusion and nanogap regions (**Figure 3-13b**). **Figure 3-13a** is the corresponding E-field distribution for regular grating under the same condition. From the E-field pattern on regular grating showing “bunny ears” shape, SPR is coupled to a higher frequency resonance mode.[2], [106] The nano-protrusion is located on one of the “bunny ears”, resulting in very high E-field intensity. In the case of Cy5 emission at a peak wavelength of 670 nm, the E-field reaches the maximal value from hot spots at $\theta = 12.2^\circ$ (**Figure 3-13d**). From the coupling pattern on regular grating under this condition (**Figure 3-13c**), SPR is coupled to a lower frequency resonance mode.[2], [106] The evanescent wave formed by SPR coupling is further concentrated at nano singularities including nano-

protrusion and nanogap regions for GLAD gratings. Extremely high E-field intensities at hot spots are obtained due to the sudden field discontinuity leading to “extreme crowding” of the surface charges.[15]

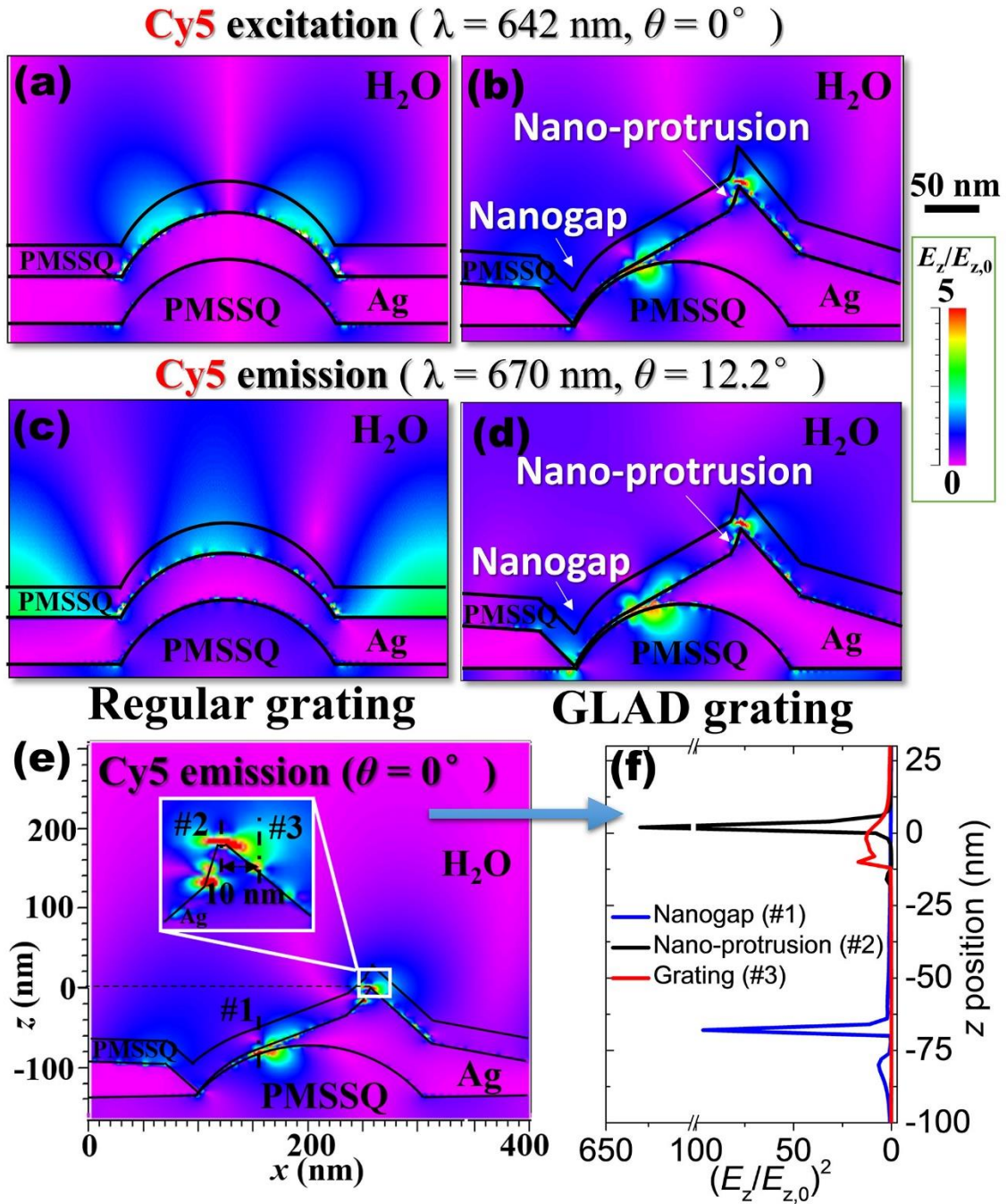


Figure 3-13 Simulated E-field ($|E_z/E_{z,0}|$) distribution for 40 nm Ag regular (left) and
69

GLAD (right) gratings coated with 30 nm PMSSQ in water environment at excitation and emission wavelength of Cy5: (a, b) Cy5 excitation ($\lambda = 642$ nm, $\theta = 0^\circ$); (c, d) Cy5 emission ($\lambda = 670$ nm, $\theta = 12.2^\circ$). (e) E-field distribution for Cy5 emission ($\lambda = 670$ nm, $\theta = 0^\circ$) and (f) corresponding E-field profile in the z-direction at nano-protrusion and nanogap region, and grating (10 nm apart from nano-protrusion). Intensity bar is 0-5, and scale bar is 50 nm.

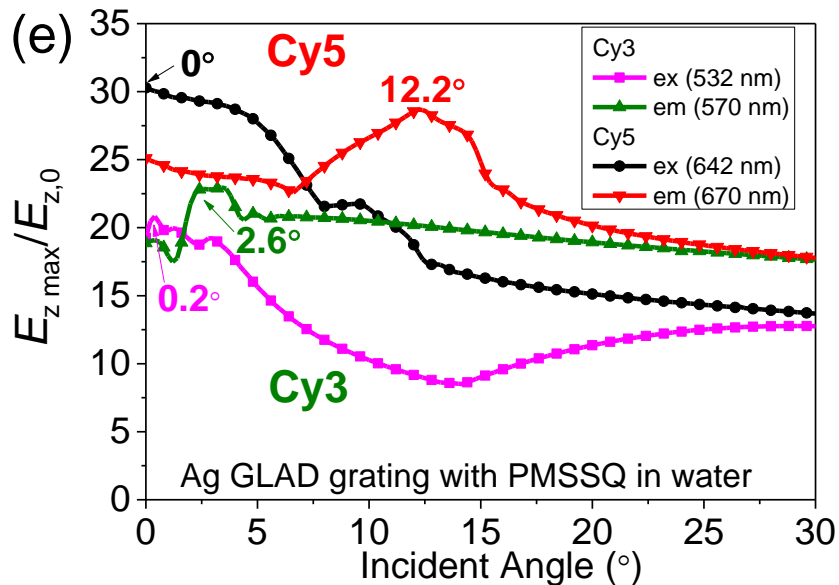
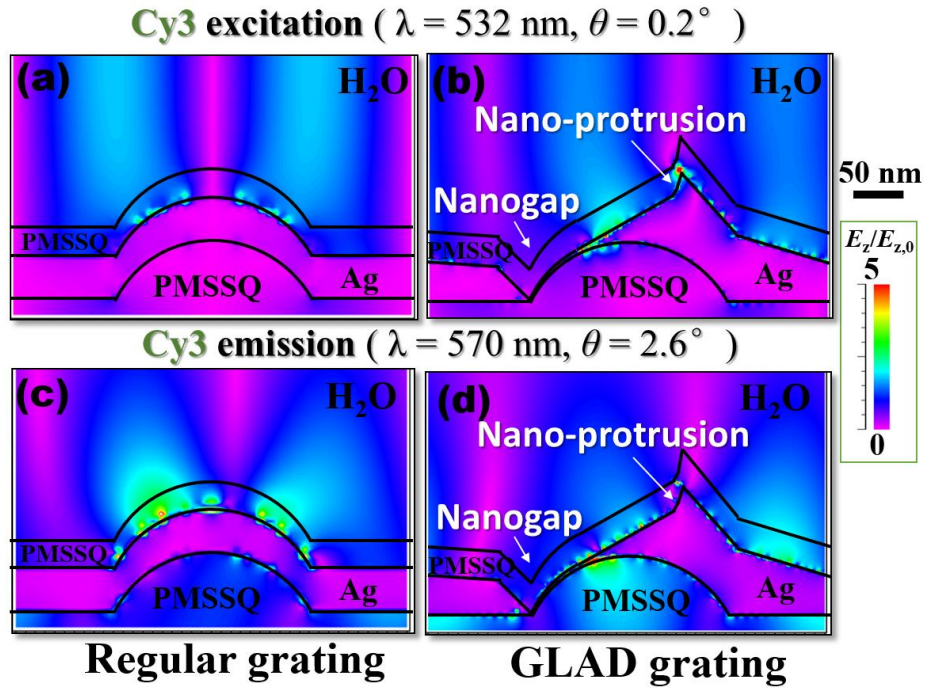


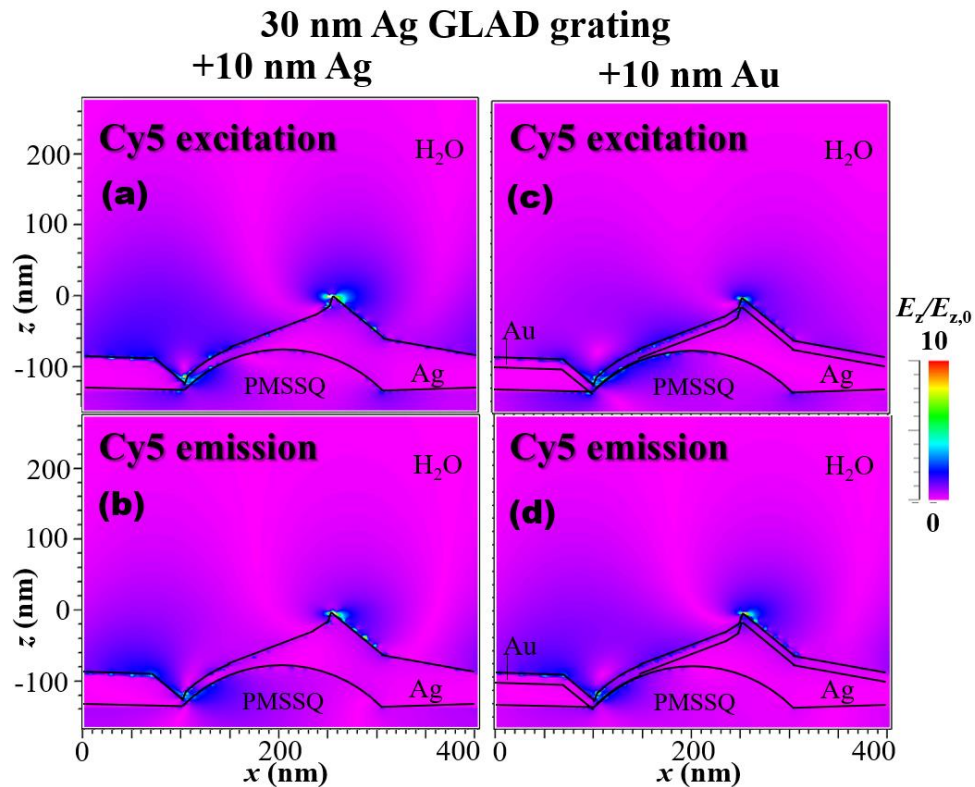
Figure 3-14 Simulated E-field ($|E_z/E_{z,0}|$) distribution for 40 nm Ag regular (left) and GLAD (right) gratings coated with 30 nm PMSSQ in water environment at excitation and emission wavelength of Cy3: (a, b) Cy3 excitation ($\lambda = 532$ nm, $\theta = 0.2^\circ$); (c, d) Cy3 emission ($\lambda = 570$ nm, $\theta = 2.6^\circ$). Intensity bar is 0-5, and the scale bar is 50 nm. (e) Simulated maximum $E_z/E_{z,0}$ at hot spots vs. incident angle for 40 nm Ag GLAD gratings coated with 30 nm PMSSQ in water environment at excitation and emission wavelength of Cy3 and Cy5. The angles with the maximum $E_z/E_{z,0}$ are as indicated.

Cy5 emission at $\theta = 0^\circ$ (due to easily being captured at this angle and still with high E-field) was used as an example to analyze how the E-field distribution changes in the vertical (z-axis) and horizontal (x-axis) directions (**Figure 3-13e**). **Figure 3-13f** shows the resulting E-field intensity vs. position. As one can see, there is a very high E-field intensity ($|E_z/E_{z,0}|^2$ is more than 600) at the nano-protrusion, and close to 100 at the thin film in the shadowed nanogap region. The intensities decay rapidly in the z-direction for hot spots and approaches similar E-fields as the grating at a z-position of about 10 nm from the nano-protrusion surface. The lateral resolution is of interest for SM studies, and hence, the E-field on the grating 10 nm away from the nano-protrusion in the x-direction was investigated. The E-field intensity (less than 25) on the grating region is much lower than the nano-protrusion, that is to say, the E-field is highly confined on the nano-protrusion. The E-field is highly concentrated at the hot spots in both axial and lateral directions while other areas on the grating surface show a very low E-field. This specific E-field distribution lowers grating noise, resulting in significant signal-to-noise (SNR) improvement, allowing imaging single molecules in a large range of concentration of fluorophores. Typically, for

low fluorophore concentration, hot spots enhanced the fluorescence intensity, enabling the visualization of the single fluorophore at an acceptable exposure time to reduce the high noise level created by long exposure time; for high fluorophore concentration, the localized E-field will be concentrated in a small volume without bulk averaging that is affected by surrounding large amount of fluorophores located in both axial and lateral direction. The volume of the confined light determines the spatial resolution in plasmon-related optical observations, which is comparable to the size of the nano singularities.[101] The broad coupling wavelengths and incident angles of this platform allow the usage of a simple epifluorescence microscope with a broad light source instead of high-demanded lasers for SM imaging.

Most, if not all, of DNA-based fluorescence experiments, require a gold surface on which to attach the thiol anchor of the DNA. Unfortunately, gold-based plasmonic platforms suffer from low enhancement due to the higher losses associated with gold films. However, the addition of a gold thin film over a silver grating can provide a good attachment layer to DNA and spacer with minimal loss in E-field strength compared with dielectric spacers. Simulations (**Figure 3-15a-d**) incorporating 10 nm gold coatings were found to decrease maximum E-field intensity ($|E_z/E_{z,0}|^2$) from 784 to 458 for Cy5 emission wavelength, indicating that the fluorescence enhancement of Cy5 dye should be reduced compared to silver gratings alone. The gratings imaged after the overnight period immersed in T50 buffer did not show any signs of silver oxidation/nanocluster formation or peeling (**Figure 3-16**). To examine the effect of the gold layer on fluorescence enhancement with respect to glass substrates, GLAD gratings were spin-coated with a 30 nm layer of PMSSQ with 10 μ M Cy5 dye. As seen in **Figure 3-15e-g**, the addition of the 10 nm gold coating

reduced the bulk grating enhancement from $27\times$ to $7\times$ due to the lossy nature of the gold film and the corresponding lower E-field strengths than gratings without gold. However, hot spots on 10 nm gold capped GLAD grating exhibited almost the same fluorescence enhancement ($\sim 120\times$) as silver GLAD gratings with respect to glass substrates. This is believed to be the result of the strong E-fields at these nanostructures, as well as, the thinner gold film deposited on nano-protrusions compared with the overall grating, which reduces the loss of E-field at nano-protrusions. As the bulk grating enhancement is reduced with little effect on the hot spot enhancement, there is much higher intensity contrast between the two and should increase the SNR significantly (**Figure 3-15f**).



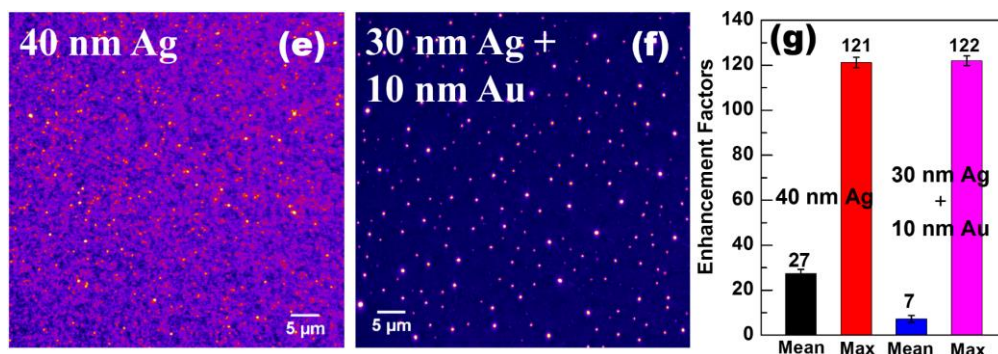


Figure 3-15 Effect of Au coating on E-field and fluorescence. Simulated E-field distribution for 30 nm Ag GLAD grating with additional (a, b) 10 nm Ag and (c, d) 10 nm Au coating at excitation and emission wavelength of Cy5 taken at 0° incidence in water. E-field strength is plotted from 0 to 10. Note: Cy5 excitation wavelength = 642 nm, Cy5 emission wavelength = 670 nm. Fluorescence images (false-color) for (e) 40 nm Ag and (f) 30 nm Ag + 10 nm Au GLAD grating ($\alpha = 60^\circ$) with $10 \mu\text{M}$ Cy5 in 30 nm PMSSQ coating; (g) corresponding mean and maximum enhancement factors with respect to the glass with 700 ms exposure time.

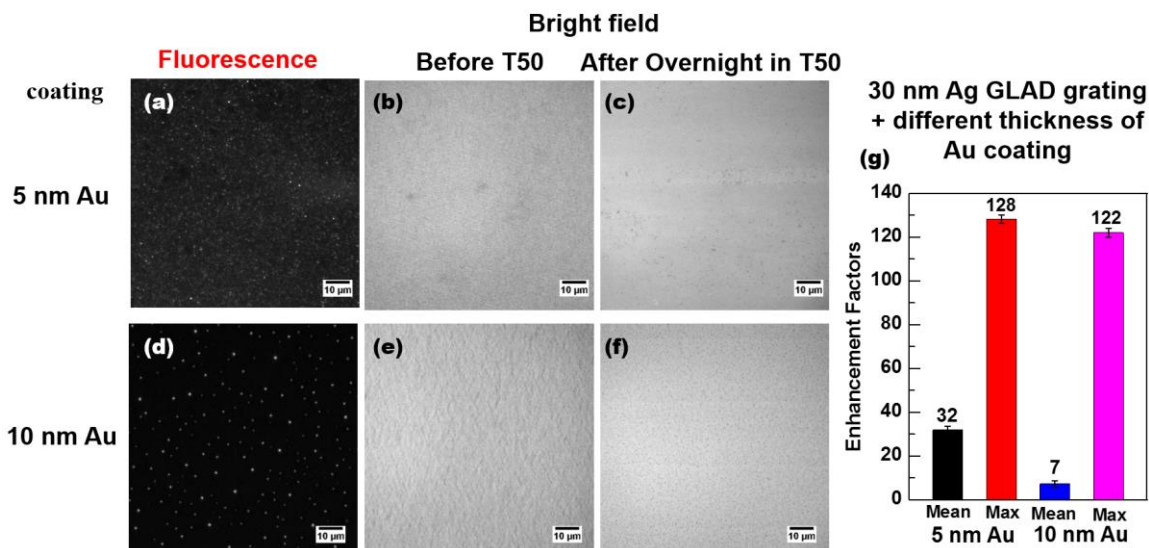


Figure 3-16 Fluorescence and bright field images for 30 nm Ag GLAD grating ($\alpha = 60^\circ$) capped with different thickness of gold (a-c) 5 nm and (d-g) 10 nm, with $10 \mu\text{M}$ Cy5 in 30

nm PMSSQ coating. Bright field images: (b, e) before and (c, f) after T50 buffer solution overnight test. The scale bar for all images is 10 μm . (g) Corresponding mean and maximum enhancement factors with respect to the glass with 700 ms exposure time.

3.3.3 *Single-molecule Imaging*

It was previously observed that dye molecules near nano-protrusions and nanogaps exhibit substantially higher emission intensity than fluorophores exposed to only the bulk grating enhancement. This contrast in intensity between the nanostructures enables users to image fluorophores at the different focal planes where each nanostructure exists, *i.e.* the user can focus on the nano-protrusions followed by the thin film in the shadowed nanogap region, and then the bottom of nanogaps as the focal plane is lowered through the sample. As demonstrated in the simulation section, E-field is highly confined at the hot spots in all directions. This feature can give better axial and lateral resolution for SM imaging. To test the detectable dye concentration range for SM fluorescence images, we investigated a Cy3/Cy5 labeled DNA/RNA duplex (**Figure 3-17a**) with low concentration (50 pM and 100 pM) which was frequently used concentration for SM biological research[6], [94], and a Cy5 dye film immobilized in a 30 nm thick PMSSQ matrix with high concentration (1 μM and 10 μM) to avoid the influence of duplex and other fluorophores. GLAD gratings make it possible to image SM fluorescence over a much wider fluorophore concentration than other systems, as demonstrated by using a sensitive electron multiplying charge-coupled device (EMCCD) (**Figure 3-17b-d**) with quantum efficiency larger than 90%, and a much less sensitive complementary metal-oxide semiconductor (CMOS) camera with quantum efficiency no more than 67% (**Figure 3-17e**). It should also be noticed that the

ORCA-flash 2.8 CMOS camera provides more pixel resolution (2.8 megapixels) compared with iXon⁺ EMCCD (0.3 megapixels), which allows us to map smaller features directly if the system can beat the diffraction limit.

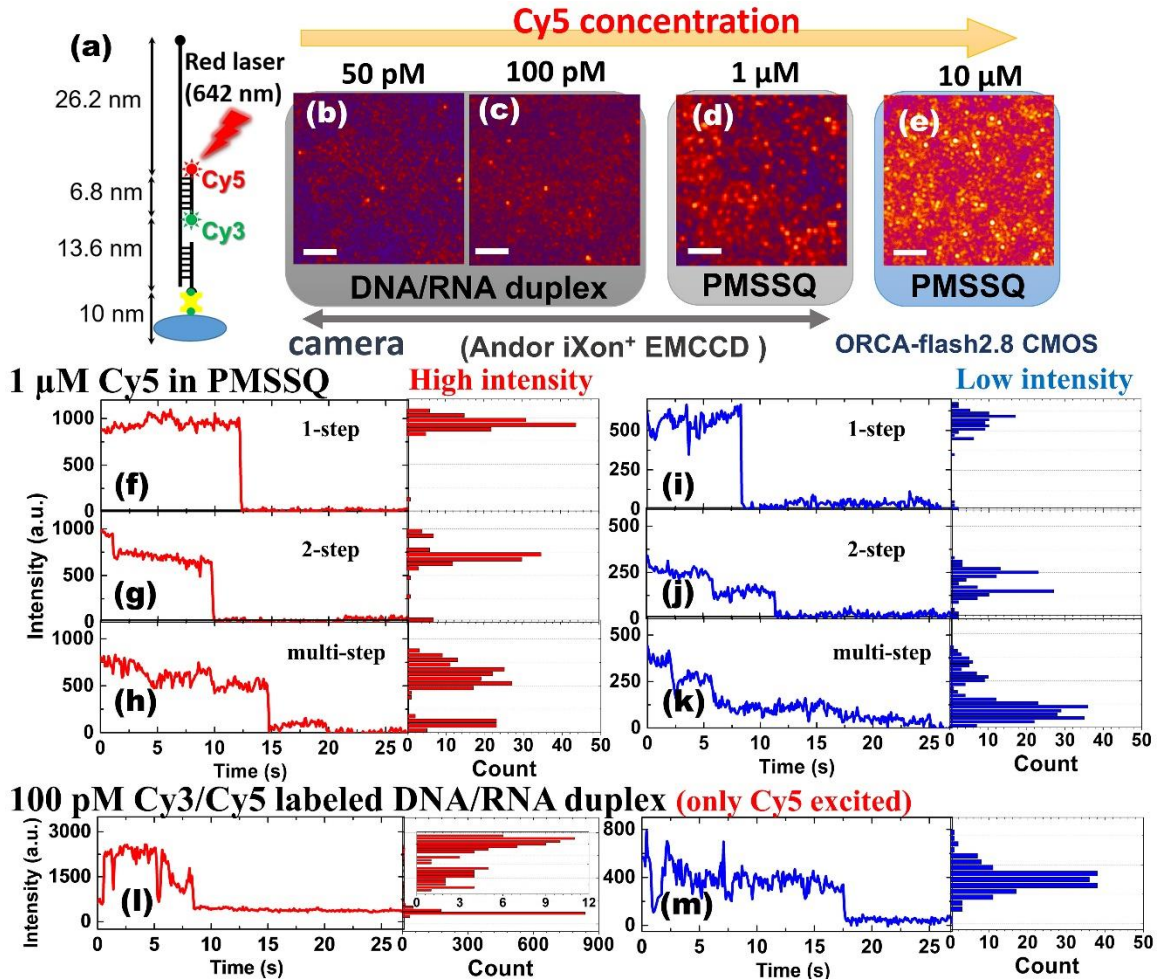


Figure 3-17 (a-e) A wide range of dye concentration for SM imaging on silver GLAD gratings ($\alpha = 60^\circ$): (a) the structure of Cy3/Cy5-labeled DNA-RNA duplex (excited Cy5 only with 642 nm red laser); (b) 50 pM and (c) 100 pM DNA/RNA duplex labelled with Cy3/Cy5, (d) 1 μ M and (e) 10 μ M Cy5 in PMSSQ matrix. Scale bar is 5 μ m for all images. Representative time traces for 1 μ M Cy5 at hot spots with single/double/multiple step bleaching behavior: (f-h) high-intensity levels (i-k) low-intensity levels, using 550 μ W 642 nm laser taken with 60 \times objective in epifluorescence mode. (l-m) Representative time

traces for 100 pM Cy3/Cy5-labeled DNA/RNA duplex at hot spots: (l) high-intensity levels (m) low-intensity levels.

When the trace intensity of single dye molecules located at each of the nanostructures is examined over time, we find that the dye molecules exhibit single/double/multiple step bleaching behaviors (**Figure 3-17f-k**). Since each Cy5 molecule exhibits quantized photobleaching and exhibits one on- and off-state, the number of dyes on a hot spot can easily be determined by counting the number of photobleaching steps in each time trace. [107]–[109] The fluorescence intensity of a single dye molecule also depends on the orientation of its electronic transition dipole moment relative to the direction of observation and (linearly) polarized laser excitation.[107] We assume that the molecules are randomly orientated resulting in a broad distribution of intensities for the single fluorophores with a higher intensity at an optimal orientation. The single-step photobleaching traces seen in **Figure 3-17f** and **Figure 3-17i** demonstrates that the visualization of single dye molecule bleaching at high dye concentration (1 μ M) is possible using a simple epifluorescence microscope and GLAD gratings. Imaging SM in high concentration without bulk averaging requires extremely confined E-field at hot spots. It can also be observed that there are high and low-intensity levels in the corresponding fluorescence image (**Figure 3-17d**), which may be the result of randomly immobilized molecules located within the proximity of a nano-protrusion or the range of sizes and locations of the nano-protrusions. Further, we used a red (642 nm) laser only to excite Cy5 molecules labeled to DNA/RNA duplex with low concentration (100 pM) (**Figure 3-17l-m**). The fluorescence intensity of fluorophore is high enough for detection even in low

concentration, due to high E-field intensity located at hot spots.

3.3.4 Beating the Diffraction Limit

In the fluorescence image of the GLAD gratings taken by ORCA-flash2.8 CMOS camera, it was also observed that the images matched well with AFM scans of the GLAD surface. By masking the grating grooves in an AFM image (**Figure 3-18a**), we can see conical grating peaks that are believed to be representative of the fluorescence hot spots after background subtraction, such as that shown in **Figure 3-18b**. Typically, there are many of dispersed brighter spots with larger and sharper nano-protrusions compared with other smaller nano-protrusions as shown in the AFM image, which leads to hot spots with higher fluorescence intensity compared with other dimmer ones, resulting in high- and low-intensity levels of SM traces as discussed above.[110] This indicates that the GLAD grating enables users to image and distinguish different nanostructures to analyze the morphology of a large area by simply capturing one shot of fluorescence imaging by an epifluorescence microscope, as opposed to time-consuming scanning methods.

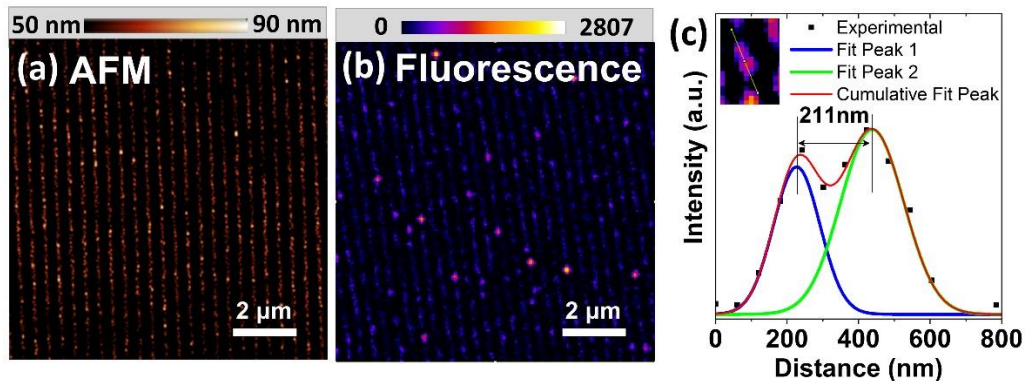


Figure 3-18 Comparison of hot spot density between (a) AFM image using masking regions to expose protruding grains and (b) fluorescence image (false-color) of 10 μM Rhodamine 6G dye in a PMSSQ matrix using 60 \times water-immersive objective (NA=1.2)

after background subtraction; (c) intensity vs. distance plot from fluorescence image; the inset image shows two analyzed hot spots and the cutting curve for profile analysis. The fluorescence images were taken by ORCA-Flash 2.8 CMOS camera.

The fluorescence image for GLAD gratings using 60× water-immersive objective (NA=1.2) can distinguish two hot spots with distance of ~211 nm (**Figure 3-18c**), indicating that this plasmonic platform can beat the diffraction limit (**Equation 3-3** and **Table 3-2**). Sub-diffraction limit imaging using silver plasmonic gratings as a far field superlens (FSL) has been previously performed using brightfield illumination.[39] However, this technique required the use of silver windows to block the 0 order diffracted light that carries diffraction limited information and to collect the ±1 order diffraction that carried the sub-diffraction-limited information.[34] It is important to suppress 0 order diffraction and enhance ±1 order diffraction to retrieve the original evanescent information. In the far-field fluorescence imaging, the enhanced emission from the fluorophores within 100 nm of the plasmonic gratings is re-coupled to the grating and emitted at the corresponding surface plasmon wavevector (**Equation 3-2**) in a phenomenon known as surface plasmon coupled emission (SPCE).[111] In this work, we filter out the 0 order diffracted excitation light with fluorescence filter cubes in order to retrieve the SPCE emission that contains sub-diffraction limit information. As a result, fluorescence images taken of this GLAD grating will contain the projected near-field information.

The observation of sub-wavelength structures with microscopes is limited by diffraction limit for general system:

$$d = 0.61 \frac{\lambda}{NA} \quad (3.3)$$

Where d is the Rayleigh diffraction limit, λ is the wavelength of light, NA is the numerical aperture of the objective lens.

Table 3-2 The Rayleigh diffraction limit (in nanometers) given different wavelengths and different objective lenses.

Wavelength (nm) / Objective Lens	Cy3 excitation 530	R6G emission 550	Cy3 emission 570	Cy5 excitation 642	Cy5 emission 670
60× water (NA = 1.2)	270	279	290	327	340

Note: R6G is rhodamine 6G dye.

However, as seen in **Figure 3-18**, the fluorescence image taken by an epifluorescence microscope is not able to provide the exact size of nanostructures less than ~210 nm, due in part to the pixel size of the CMOS sensor. Therefore, we employed localization microscopy super-resolution techniques, to further improve the resolution of fluorescence image based on GLAD platforms.

3.3.5 Localization Microscopy for Super-resolution Imaging

Super-resolution fluorescence microscopy techniques can achieve sub-diffraction-limit resolution by SM localization microscopy. For example, STORM and PALM or FPALM can map the localization coordinates of the temporally separated fluorophores by fitting an isolated point-spread-function (PSF). Calculating the fluorophore positions based on their corresponding fluorescence images is critical to these

localization super-resolution techniques. However, methods like STORM depend on few dyes blinking on each time frame, requiring long stacks (thousands of images), which limits the efficiency of obtaining data.[112] In our case, high dye concentrations (e.g. 1 μM Cy5) usually give high spatial densities of activated molecules when imaging. This situation can create a “crowded field problem”, and hence single molecules generally can not be resolved adequately. The GLAD grating with incorporated nano-protrusions can confine E-field to resolve a certain amount of SM behavior by beating the diffraction limit, allowing to map and identify the higher density of fluorophores in each time frame, which can reduce the “crowded field” effect. However, double/multiple step photobleaching with several fluorophores located at very close hot spots is still detected but cannot be resolved by the camera sensor. Most of the current super-resolution reconstruction techniques have the limitation of the PSF models designed to fit only a single molecule. Therefore, we used a multiple-emitter fitting analysis (MFA) approach to solving this problem as it is capable of processing a much higher density of emitters than single emitter analysis. In a two-dimensional single-frame fitting sub-region, MFA approach utilizes the maximum likelihood estimator in order to localize multiple emitters simultaneously, which provides an order of magnitude improvement in the tolerance of the analysis routine with regards to the single-frame active emitter density.[113] ThunderSTORM software[114] using Monte Carlo simulations was employed to reconstruct the super-resolution images from a fluorescence blinking movie. In addition, the highly confined E-field at hot spots of a GLAD grating results in an enhancement in the total number of detected photons (N), which is beneficial to decrease the uncertainty of the localization since it is equal to the diffraction limit divided by \sqrt{N} .[115]

A pointillism of the coordinates of all SM localizations was utilized to obtain super-resolution images of nano-protrusions. A 642 nm laser was used to excite 1 μM Cy5 immobilized in PMSSQ matrix, and we can observe blinking of Cy5 on hot spots from the fluorescence movie taken by EMCCD using epifluorescence microscope. We can precisely determine the position of individual fluorophores at each image frame by fitting MFA. Finally, a super-resolution image can be reconstructed by collecting a tremendous amount of fluorophore positions from fluorescence stacks with respect to time. **Figure 3-19** is a representation of the different separation of closely located nanostructures. After super-resolution analysis, the resolution of fluorescence images is significantly improved compared with the original fluorescence data with FWHM of approximately 500 nm (due to the large pixel size), and the details of nanostructure less than 100 nm started to be resolved. In **Figure 3-19a-e**, the fluorescence image shows the separation is ~ 65 nm and FWHM of approximately 40 nm, which is consistent with nano-protrusion separation and size measured in representative AFM scans (**Figure 3-19f**). From the time traces (**Figure 3-19d**), nanostructures at different positions can be resolved separately by dividing the fluorescence blinking movie into two halves for reconstruction when the blinking time for fluorophores located in different positions does not overlap. Therefore, we can identify the sources of fluorescence by analyzing the signals of interest separately.

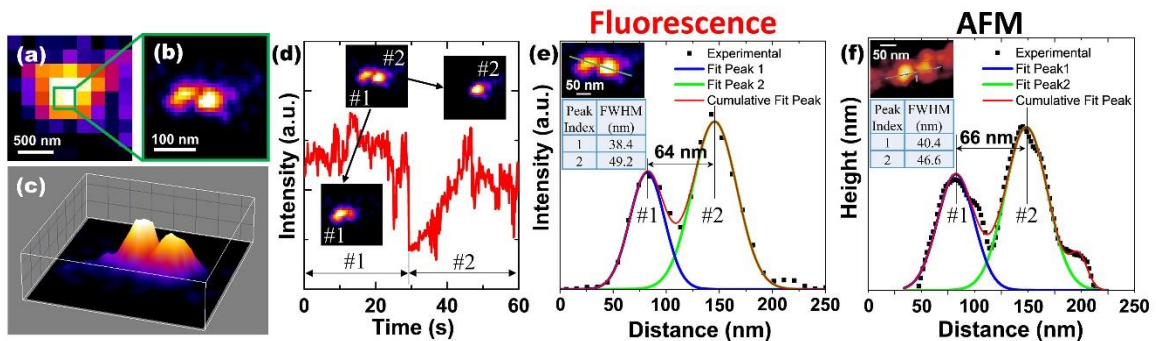


Figure 3-19 Single molecules images to show the size and separation of nanostructures: Representative fluorescence image (a) one time frame fluorescence raw image before super-resolution analysis and (b) super-resolution image after localization microscopy analysis (zoom in), and (c) corresponding 3D intensity map of nano-protrusions and (d) corresponding time trace to resolve nanostructures at different positions; (e) intensity vs. distance plot to show the size obtained from super-resolution fluorescence image; (f) height vs. distance plot of AFM image to show the size of nano-protrusions. Insets are corresponding fluorescence and AFM images with the cutting curve for profile analysis, and full width at half maximum (FWHM) for each fitting peaks. The fluorescence movies were taken by Andor iXon⁺ EMCCD camera.

To study the relationship between the fluorescence image and the actual morphology measured by AFM, statistical analysis was performed on AFM scans over large grating areas (**Figure 3-20a-d**) as well as the super-resolution fluorescence image (**Figure 3-20e-g**). By vertically cutting the grating at a specific height (**Figure 3-20a**), we can get the mean grain size and density (number of grains per unit area) at different height levels. When the height value is large (e.g. 80 nm), that is to say, close to the top of large nano-protrusions on gratings, the sharpest and tallest nano-protrusions are selected. Due to the low population and width of such nano-protrusions, the mean grain size and density are low. With decreasing cutting height, more and more grains are selected which results in an increasing mean grain size and density. When the cutting height decreases further, nano-protrusions in close proximity appear to be merged into one grain, resulting in a continued increase in mean grain size but a decrease in grain density. Similarly, the fluorescence

image is analyzed by cutting at different intensities (**Figure 3-20e**). Since the super-resolution fluorescence only shows hot spots without an effect of the bulk of gratings, the mean grain size would not become very large when intensity is very small. Using this analysis, the fluorescence image (**Figure 3-20f**) exhibits a similar mean grain size of approximately 40 nm as measured by AFM (**Figure 3-20c**). The trend for mean grain size and density changing with height for AFM is analogous to varying the intensity of the fluorescence images, indicating that we can identify nanostructure sizes using the fluorescence intensity alone. Besides the comparison of the lateral size of nanostructures, the relationship between the nano-protrusion height (**Figure 3-20h**) and fluorescence intensity of hot spots (**Figure 3-20i**) was also investigated. The histogram calculated from fluorescence image before localization microscopy analysis (**Figure 3-20c**) was analyzed using this method. The nano-protrusions with height less than 20 nm corresponded to fluorescence intensities less than 400, while the nano-protrusion with heights greater than 50 nm corresponded to fluorescence intensities higher than 900. This is in agreement with (**Figure 3-20h, i**) and confirms the relationship between the distribution of nano-protrusion heights and the fluorescence intensity distribution.

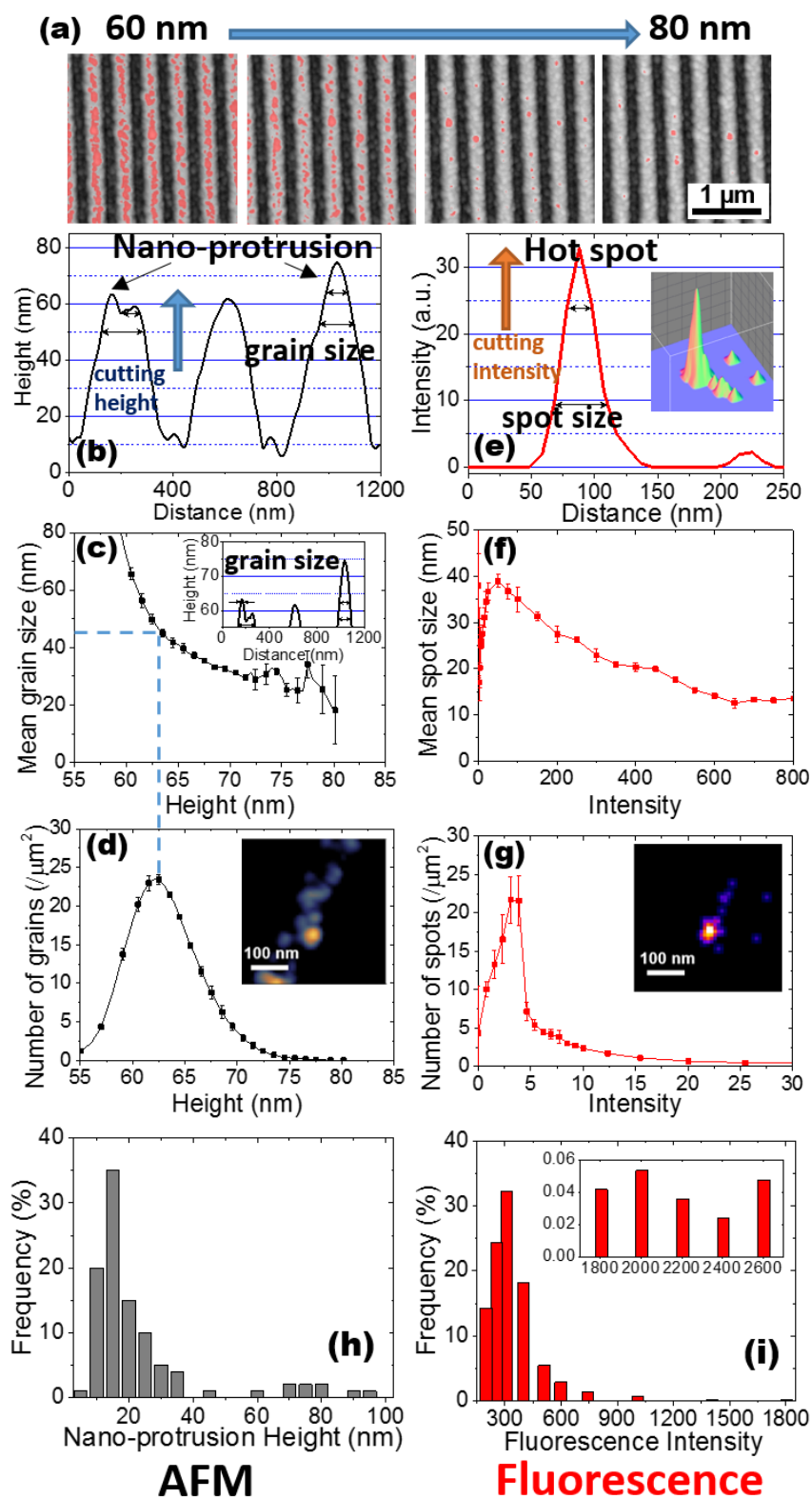


Figure 3-20 Statistical analysis for (a-d) AFM scan over large areas ($30 \mu\text{m} \times 30 \mu\text{m}$) of GLAD gratings and (e-g) super-resolution fluorescence image for GLAD grating coated

with 1 μM Cy5: (a) AFM 2D profile to show how the nano-protrusion size, distribution and density changes with height (vertically cutting), and the red regions are selected for analysis; (b) representative AFM height *vs.* distance profile to show grain sizes by increasing the cutting height; (c) mean grain size and (d) grain density for AFM image (inset: masking the structures below height of 58 nm to show the nano-protrusion distribution); (e) representative intensity *vs.* distance profile to show spot sizes by increasing the cutting intensity, and the inset is corresponding 3D fluorescence profile; (f) mean spot size and (g) spot density for super-resolution fluorescence image (inset: showing hot spots distribution in a small area). Histogram of (h) nano-protrusion height obtained from AFM image and (i) fluorescence intensity of hot spots obtained from fluorescence image before localization microscopy analysis (Fig. 6c).

3.4 Future Work

In conclusion, we designed and fabricated plasmonic GLAD gratings for the purpose of imaging SM dye behavior over a large dye concentration range, 50 pM to 10 μM . GLAD gratings with incorporated nano-protrusions enable SM imaging over a wide concentration range by enhancing the fluorescence such that the required exposure time is much lower for lower concentrations and the single molecules located near nano-protrusions are enhanced well above the bulk fluorescence signal at higher concentrations. The presence of a large number of nano-protrusions enabled the use of multiple-emitter fitting analysis instead of single emitter analysis to solve the “crowded field problem” created by the high concentration of fluorophores. It was demonstrated that a thin gold coating has a minimal effect on enhancement and increases SNR. The presence of this film

enables the attachment of DNA to the GLAD gratings. Also, the reported GLAD gratings revealed the ability to determine the scalable nanostructure topography with the use of a simple epifluorescence microscope with the use of much more expensive systems, such as confocal microscopy. The super-resolution approach of localization microscopy was applied to further improve the resolution of fluorescence images down to 65 nm. The GLAD grating fabricated in this article represents a promising platform that can be used to easily obtain super-resolution images for cost-effective, high-speed and large-concentration-range biomedical imaging.

Chapter 4. Super-resolution Imaging on Nanostructures on Plasmonic Grating Superlens

4.1 Introduction

Metal nanostructures are of interest in many researches due to various applications such as temperature sensing[20], chemical sensing[16], [116], [117], and electronics[118]–[122]. However, the small size of nanostructures cannot be imaged by optical microscope due to the limitation of diffraction limit. Overcoming the optical resolution limit, advanced super-resolution techniques rely on costly, sophisticated, and demanding approaches. Here, we demonstrated a cost-effective silver plasmonic grating as superlens for super-resolution imaging in both bright field and fluorescence mode. We imaged various shapes of silver nanoparticles using a less complex and less expensive epi-fluorescence microscope. Different super-resolution approaches including ground state depletion (GSD) microscopy, Airyscanning Microscopy and localization microscopy under epi-fluorescence mode, were compared to obtained super-resolution image to reveal the actual size of nanoparticles. The single-molecule blinking and super-resolution images can be observed by smartphone, which can be popularized to more poor areas and people from different background.

4.2 Experiment

The silver plasmonic gratings were fabricated using nano-imprint lithography from commercially available HDDVDs. [4], [9], [15]–[17] A 5 nm chromium adhesion layer and a 100 nm silver layer was deposited on poly-(methylsilsesquioxane) (PMSSQ) gratings by thermal evaporator, followed by a 10 nm alumina capping layer by atomic layer

deposition (ALD). The nanoparticles were synthesized in DI water or methanol using polyvinyl pyrrolidone (PVP) as stabilizer/coating to prevent aggregation. [123] Silver nanoparticles were deposited onto silver gratings to investigate the images by an epifluorescence microscope (Olympus BX51W1). Silver nanoparticles in methanol with 1 nM R6G were drop-casted on the silver grating substrate. Fluorescence images were taken with 100 \times oil-immersion objective.

4.3 Discussion

In this work, we studied super-resolution imaging on nanostructures on plasmonic grating superlens and the combination with different advanced super-resolution techniques. The silver nanoparticles were coated with 1 nM R6G and then deposited onto silver plasmonic grating platforms (**Figure 4-1a**) or plain glass slides as a control. The silver plasmonic gratings were fabricated by using a simple and inexpensive nano-imprint lithography from commercially available molds HDDVDs as described previously (see **Methods**). [4], [9], [15]–[17] **Figure 4-2a** shows atomic force microscope (AFM) image for silver gratings with 400 nm grating period. The large area TEM images show that silver nanoparticles (see **Methods**) contain ~50% yield of nanoprisms or pyramids mixed with cubic particles (**Figure 4-1b, Figure 4-2b**) in the size of approximately 45 nm (**Figure 4-1c, Figure 4-2c**). **Figure 4-1d** shows the corresponding super-resolution fluorescence image of triangle structure obtained by blinking localization microscopy.

4.3.1 *Ground state depletion (GSD) microscopy*

In order to confirm the structure of silver nanoparticles on the plasmonic grating superlens, we first combined with the current advanced super-resolution method, ground state depletion (GSD) microscopy. GSD fluorescence microscopy uses repeated light excitation with high power lasers to force the probe transition to a long-lived ‘off’ triplet state, so that a subset of fluorophores are activated at a sufficiently low density to enable isolated spots of each fluorophore in all captured images. For localization of single molecules in GSD fluorescence microscopy, point spread function (PSF) of each molecule is recorded and a fit by finding the centroid of each spot is performed to determine the position of each fluorophore. After localizing and pinpointing a sufficient number of fluorophores, a super-resolution fluorescence image was constructed by plotting all the positions of the fluorophores.

If imaging in a regular fluorescence microscope, the regular PSF can determine the lateral position of the fluorophore. To acquire additional axial information of fluorophore for 3D mapping, a cylindrical lens is positioned into the emission beam path to obtain a different PSF (astigmatism). The z position of the probe can be determined by the elongated direction and the size of elliptical deformation of the fluorescence spot on a camera, thereby enabling 3D reconstruction of each detected molecules. Due to the high power laser excitation, a short exposure time of 6.6 ms was required to capture enough fluorescence intensity. **Figure 4-1e** shows that the fluorescence hot spots on nanoparticle were blinking very fast, which enables isolation of fluorophores in each image as well as the capture of enough locations for reconstruction in a short imaging time. After recording more than

30000 frames of the blinking molecules (**Figure 4-3**), a 3D nanoprism/nanopyramid structures with size approximately 50 nm were reconstructed by GSD (**Figure 4-1f**).

4.3.2 Localization Microscopy using Plasmonic Grating under epi-fluorescence microscope

Since an epi-fluorescence microscope is common and available in most of the bio-labs, it would be meaningful to popularize super-resolution techniques to more areas and different ages if we can obtain super-resolution imaging with such a cheap and easy system. We first compared the bright field images of silver nanoparticles on a plasmonic grating superlens platform and a glass slide taken under an epi-fluorescence microscope. The shapes of silver nanoparticles can be visualized as dark triangular or rectangular spots on plasmonic grating superlens (**Figure 4-1g**), while all different structures of the nanoparticles were scattered as only bright circular dots on glass (**Figure 4-1h**). The silver nanoparticles appear as lower intensity compared to the grating platform, due to the strong absorption from nanoparticles and the non-radiative dissipation of energy within the metal. The far-field super-resolution bright field image is achieved by transferring the evanescent wave around silver nanoparticles to propagation wave via the plasmonic grating superlens. Although it carries the higher spatial frequency information, it also includes diffraction-limited information not well coupled to the plasmonic gratings due to the broad wavelength ranges of Xenon lamp (**Figure 2-7**) as well as large illumination angles of the objectives (**Figure 2-7g**). Therefore, despite visualization of the shape roughly, the bright field image still shows blurring edges of nanoparticles and larger sizes than that obtained by TEM image, due to the scattering of some un-coupled wavelengths around nanoparticles. In addition, the

observable range in Fourier space can be further extended by reducing the grating periods for future study to improve spatial resolution.

Considering that the bright field image cannot completely resolve the size of the nanoparticles less than 50 nm, we utilized blinking localization microscopy for these samples with the same imaging system by incorporating additional fluorescence filter sets. The super-resolution images are possible to achieve in this simple epi-fluorescence mode without high power laser, and not necessary using TIRFM with highly enhanced and confined evanescent wave, as mentioned previously. This is because the localization precision can be improved by the fluorescence enhancement as well as the better resolution of original fluorescence images due to the plasmonic grating superlens. Figure 4-1i-j shows a representation bright field image of one nanoprism on the grating and its corresponding super-resolution fluorescence image after processed by localization microscopy. The 2D reconstructed super-resolution image (Figure 4-1d, j, Figure 4-3) shows a nanoparticles size of around 50 nm.

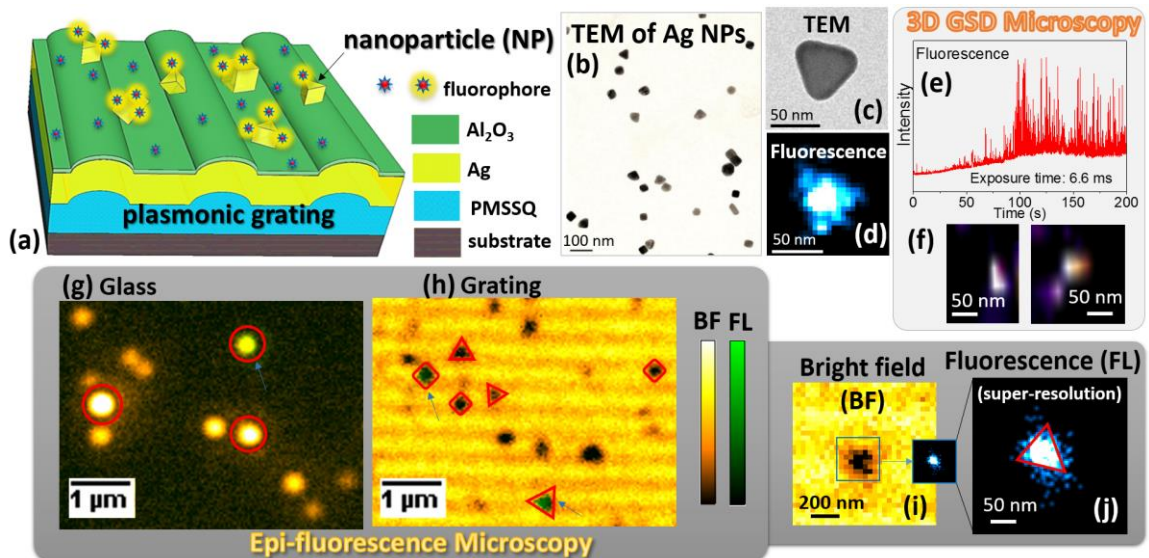


Figure 4-1 (a) Schematic of nanoparticles (nanoprisms/nanopyramids and cubical nanocages) on silver plasmonic gratings platform with dye coating, the brighter color of fluorophores indicates that the fluorescence is enhanced by nanoparticles. (b-c) TEM images of silver nanoparticles: (b) large area image shows 50% yield of triangle structures, (c) higher resolution TEM image to show the triangle structure and (d) corresponding super-resolution fluorescence image by blinking localization microscopy. (e-f) 3D ground state depletion (GSD) microscopy on silver nanoparticles coated with 1 nM R6G on the grating platform: (e) fluorescence blinking time trace; (f) 3D reconstructed structures show nanoprism/nanopyramid structures. (g-j) Epi-fluorescence microscopy images: super-impose bright field (BF, false-color of orange hot) and fluorescence (FL, false-color of green) images for nanoparticles on (g) glass and (h) grating, the arrows point out the fluorescence showing up and enhanced by nanoparticle at this fluorescence time frame, and the triangle and circle shows the shape of nanoparticles seen from bright field; (i) representation bright field and fluorescence image (false-color: cyan hot) after localization blinking super-resolution microscope for one nanoprism on grating.

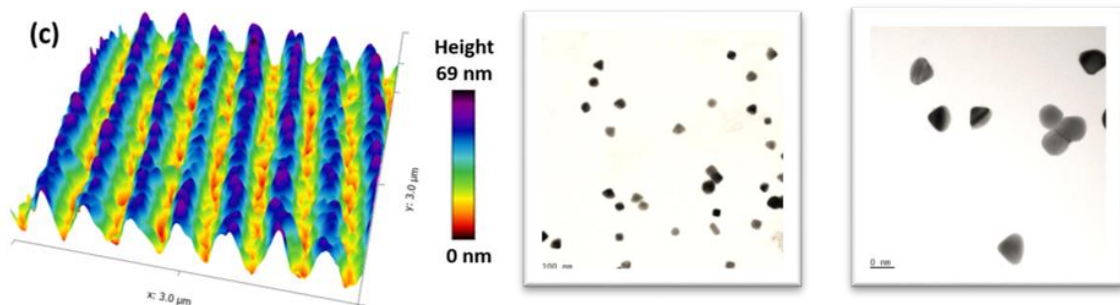


Figure 4-2 (a) AFM 3D profile for thermally deposited silver gratings with 10 nm capping layer, the length and width are 3 μm . TEM of Nanoparticles with different scale bars (b) 100 nm and (c) 50 nm.

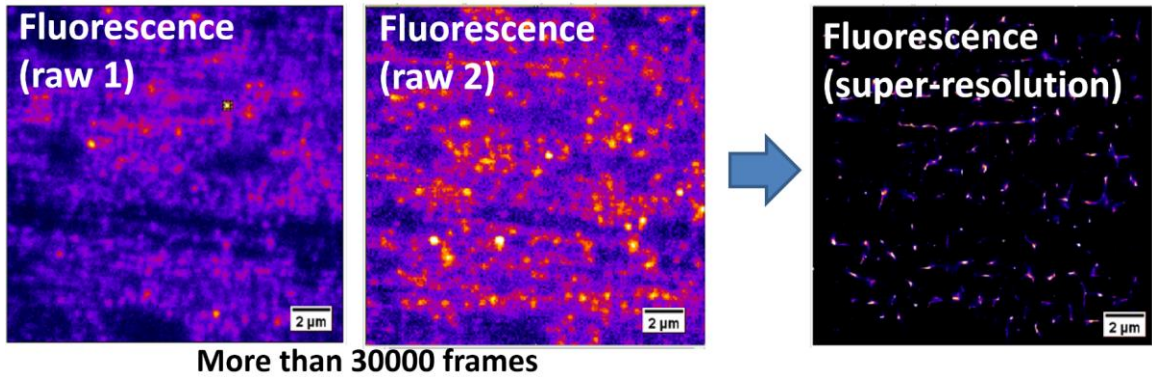


Figure 4-3 (a) AFM 3D profile for thermally deposited silver gratings with 10 nm capping layer, the length and width are 3 μm . TEM of Nanoparticles with different scale bars (b) 100 nm and (c) 50 nm.

4.3.3 Airyscanning Microscopy Combining with Plasmonic Grating

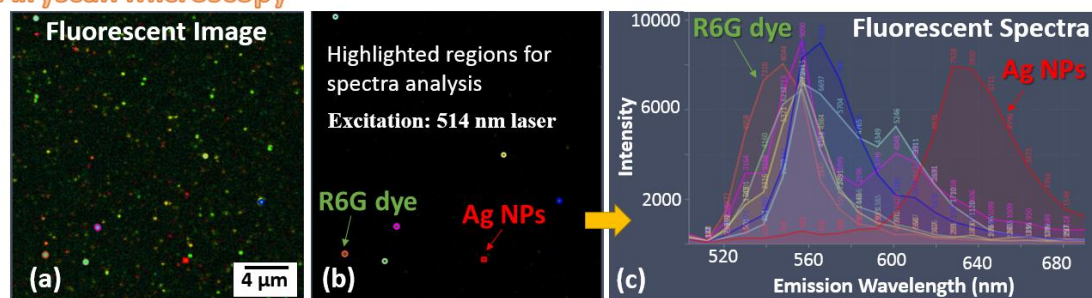
Other than obtaining the super-resolution images, we utilized Airyscanning to achieve local spectra analysis on super-resolution map as well. Airyscan microscopy is a new super-resolution technique developing from confocal laser scanning microscopy (CLSM), but the signal of Airyscanning is drastically improved by making use of the light rejected by the confocal pinhole, utilizing the concept of pixel reassignment. The increased SNR can be utilized to retrieve high-resolution information as shown in **Figure 4-4a-b**. Airyscan microscope consists an array of 32 GaAsP detector elements with excellent quantum efficiency in a compound eye fashion, equipped with emission filters in front of the detector for the selection of the emission wavelengths spectrally. According to the emission spectra

(**Figure 4-4c**), one can distinguish the fluorescence originated from R6G dye or silver nanoparticle, or even the scattering from nanoparticles.

4.3.4 Combining Plasmonic Grating with Smartphone Imaging

Since the change of emission spectra results in the difference of color in images, the enhanced intensity and improved resolution due to plasmonic grating superlens make it possible to distinguish the fluorescence sources by simply using a CMOS camera of a smartphone. We utilized a smartphone to image through the eyepiece of an epi-fluorescence microscope under 10 \times , 40 \times and 100 \times objectives. **Figure 4-4d** shows a smartphone image of the interface between the silver grating and flat silver with silver NPs on both surfaces. A larger amount of NPs was visualized with defined color on grating compared with flat silver. We can record single-molecule blinking from silver NPs even with low magnification (10 \times) and low numerical aperture (NA) objective when combining the plasmonic grating superlens (**Figure 4-4e**). Single nanoparticles and nanoclusters can be visualized under 100 \times objectives by smart phone (**Figure 4-5**).

Airyscan Microscopy



Smartphone



Figure 4-4 (a-c) Airyscan microscopy: (a) fluorescence image for silver nanoparticles coated with 1 nM R6G on grating platform, (b) change the contrast of the fluorescence image to highlight the regions selected for spectra analysis, and (c) corresponding emission spectra for nanoparticles, the arrows point out the fluorescence from R6G dye or silver nanoparticle based on the spectra. (d-g) Smartphone imaging for the silver nanoparticles samples through the eyepiece of epi-fluorescence microscope: (d) a demo to show the smartphone imaging platform; fluorescence images were taken by (e) 10×, (f) 40× and (g) 100× objectives.

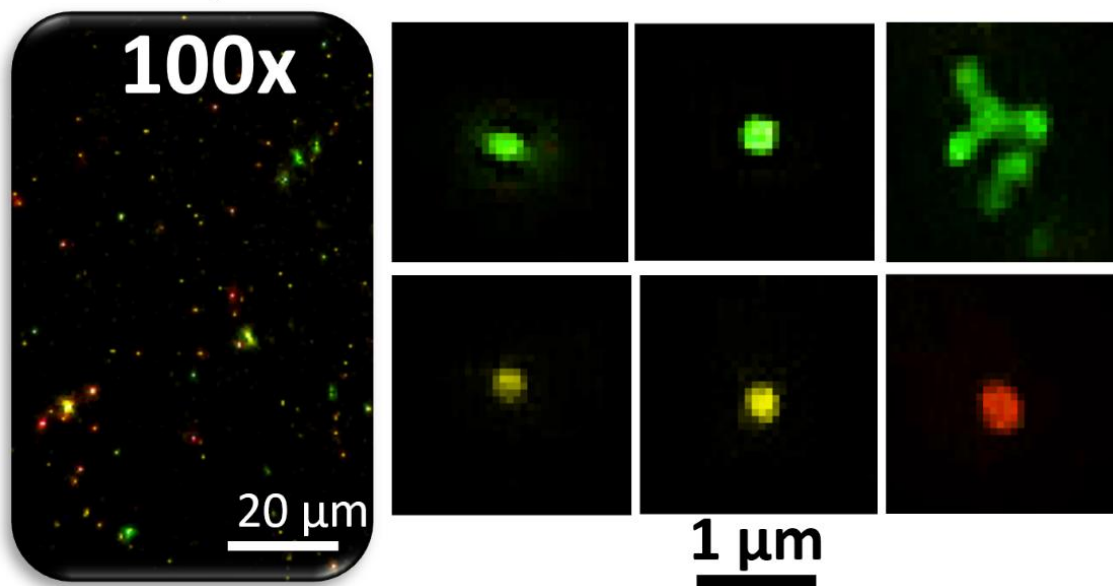


Figure 4-5 smartphone imaging platform: fluorescence images taken by 100× objectives.

4.4 Future Work

We will add the analysis for different nanostructure including gold nanorods, aluminum nanoparticles, and the application on biological materials including collagen and cells. In addition, we will add the data with polarizer and analyzer used to improve the fluorescence images. More analysis for matching the coupling and suplensing imaging mechanism of the grating as mentioned in **Chapter 2** will be added to explain the data.

Chapter 5. Theory for Photothermal Heating

5.1 Design of Plasmonic Gratings

5.1.1 FDTD simulation for grating microchips with Al nanoparticles

To simulate grating microchips with Al nanoparticles, we employed three-dimensional (3D) FDTD simulation instead of a 2D simulation, because of the symmetry for the spherical shapes of Al nanoparticles is different from the 1D periodic grating structure. The model setup requires the graphical input of the substrate geometry and material composition. The selected 3D grid size for this computational domain was $\Delta x = \Delta y = \Delta z = 5$ nm. Different laser wavelengths were chosen to be incident upon this 3D nanostructure. As the photothermal heating characteristics of the Al-polymer nanoenergetics deposited on grating microchips are highly related to E-field intensity enhancement ($|E_z/E_{z,0}|^2$), we investigated the effect of different substrates, Al nanoparticles size, loading and positioning on E-field strength enhancement ($E_z/E_{z,0}$) of the Al nanoparticles/nitrocellulose films on the grating microchips. We used lasers with different wavelengths and powers for photothermal excitation of Al-polymer nanoenergetics on the grating microchips and employed red (650 nm), green (532 nm) and blue (408 nm) lasers as light sources in the current simulation setup.

We simulated FDTD simulated E-field distribution of Al nanoparticles on different substrates including flat silver, silver gratings, plain glass and aluminum gratings for comparison of substrate selection as shown in **Figure 5-1**. Different laser wavelengths including 408 nm, 532 nm and 650 nm under normal incidence (0°) of light were used in

oil (or nitrocellulose) environment. For silver HD-DVD gratings in oil environment, based on the dispersion curve (**Figure 2-4(b)**), the simulated reflectance minimum is achieved at 638 nm at 0° incidence. Nevertheless, the broad coupling peak (**Figure 2-5(b)**) allows red laser at 650 nm to achieve resonance properties. As shown in **Figure 5-1(d-f)** for E-field distribution of Al nanoparticles on silver grating microchip illuminated with different laser wavelengths, the maximum E-field enhancement was achieved at red laser compared with the blue and green laser, which matches the dispersion curve as expected. The E-field is highly localized around Al nanoparticles at all three wavelengths due to localized surface plasmon resonance (LSPR), and E-field is further enhanced when combining with SPR generated from silver gratings. Compared with the flat silver substrate, silver grating microchip shows higher E-field around Al nanoparticles with all lasers. Typically, blue and red lasers give significant E-field enhancement of Al nanoparticles on the silver grating with respect to flat silver, while E-field enhancement with a green laser (532 nm) is not as obvious as the other two lasers. We also compared glass and aluminum gratings with silver grating and flat silver under 650 nm laser illuminations. The silver grating shows highest E-field compared with the other substrates (silver grating > flat silver > aluminum grating > plain glass). Although aluminum gratings also show resonance properties under 650 nm, the E-field strength is still low due to the high loss of Al materials. We are also interested in the E-field penetrating inside Al nanoparticles which would benefit the photothermal heating of Al nanoparticles. As seen on the silver grating substrates, blue laser shows more light penetrates inside the metal compared with the green and red lasers.

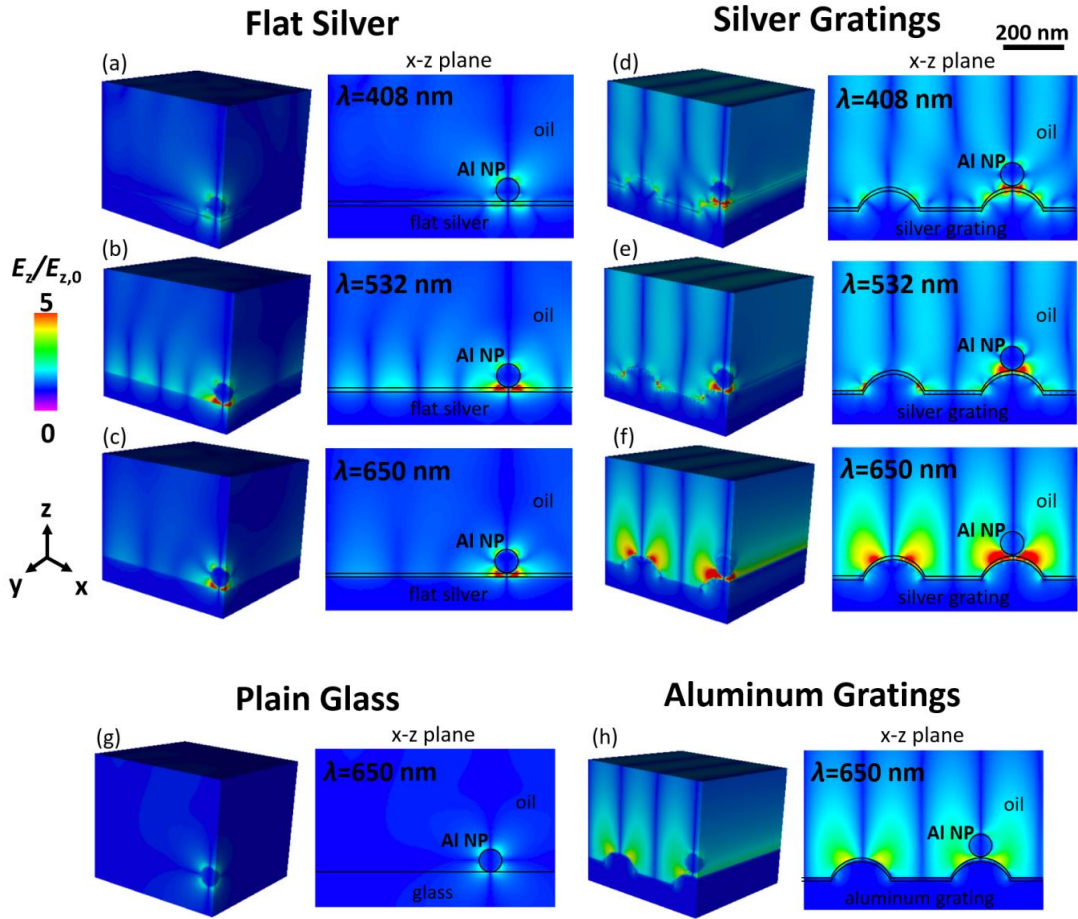


Figure 5-1 FDTD simulated E-field distribution of 80 nm Al nanoparticles (NPs) on different substrates: (a-c) flat silver, (d-f) silver gratings, (d) plain glass and (h) aluminum gratings, with different laser wavelengths including 408 nm, 532 nm and 650 nm under normal incidence (0°) of light in oil (or nitrocellulose) environment. The E-field ($E_z/E_{z,0}$) scale is normalized to 0~5. Each condition shows a 3D view of E-field distribution (left) and the corresponding 2D view of the x-z plane (right). The scale bar in x-z plane is 200 nm.

In addition, we simulated different size of Al nanoparticles to investigate the effect of the coupling. Due to surface plasmons and interband adsorption, metallic nanoparticles

scatter and absorb light strongly at certain wavelengths. Generally, Al nanoparticles feature plasmonic absorption in the UV range and interband absorption in red to infrared range. The surface plasmon resonance for Al nanoparticles is size-dependent. With increasing particle size, the plasmonic peaks shift to the red, and the extinction spectra broaden because the plasmonic and interband absorption properties of Al nanoparticles begin to merge. The red-shifted absorption of large Al nanoparticles is beneficial to use the plasmonic absorption of gratings and interband absorption of Al instead of using a plasmonic absorption in UV region for small Al nanoparticles. We simulated Al nanoparticles with 50 nm, 80 nm, and 120 nm average diameters with a laser wavelength of 650 nm under normal incidence of light in oil (or nitrocellulose) environment. As shown in **Figure 5-2**, the E-field strength increases with increasing Al nanoparticle from 50 nm to 120 nm. The largest Al nanoparticle (120 nm) shows very intense localized E-field around Al nanoparticle, exhibiting a large hot spot (high E-field region shown in red color on gratings). This large hot spot influences the surrounding E-field, which leads to the distortion of the E-field on grating nearby. For example, the E-field distribution next to the grating ridge, where Al nanoparticle sits, becomes asymmetric and distorted towards the nanoparticles.

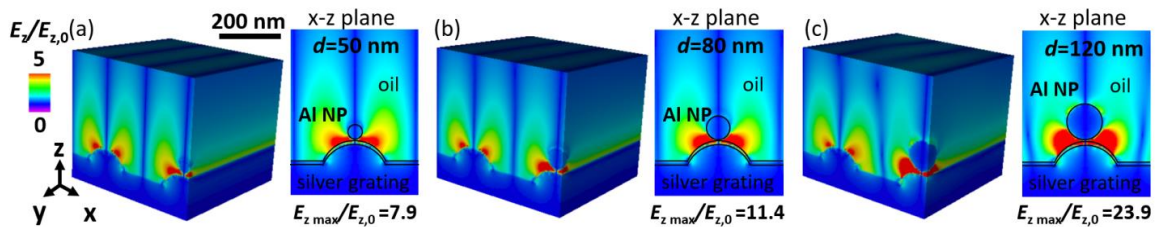


Figure 5-2 FDTD simulated E-field distribution of Al nanoparticles with different sizes: (a) 50 nm, (b) 80 nm, (c) 120 nm, with 650 nm laser under normal incidence (0°) of light

in oil (or nitrocellulose) environment. The E-field ($E_z/E_{z,0}$) scale is normalized to 0~5. Each condition shows a 3D view of E-field distribution (left) and the corresponding 2D view of the x-z plane (right). The scale bar in x-z plane is 200 nm.

The Al nanoparticles loading is important for our study since we are interested in the fundamental properties of single Al nanoparticle and Al aggregates/clusters in real experimental condition. Further, the Al aggregation can be considered as an increase of the overall Al nanoparticle size to some extent, without changing the nanoscale properties, which is helpful for light coupling in the red region. We simulated Al nanoclusters consisting of two adjacent 80 nm Al nanoparticles with different configurations using the same simulation parameters as the previous simulation for comparison. As shown in **Figure 5-3**, E-field is localized around Al nanoparticles, but the distribution is different due to the different positions of Al nanoparticles aligned to the gratings. In the case of two adjacent Al nanoparticles aligned vertical to grating lines, Al nanoparticles are sitting on the two resonance hot spots, resulting in the hot spots beginning to propagate to the top of Al nanoparticles, generating extremely tense and localized E-field on both top and bottom of Al nanoparticles as shown in x-z plane and y-z plane in **Figure 5-3** (a). It is also interesting to see that E-field starts to penetrate inside Al nanoparticle with this configuration (see the x-z plane), which is helpful in plasmonic photothermal heating. However, in the case of two adjacent Al nanoparticles aligned parallel to grating lines, E-field distribution in x-z plane (**Figure 5-3** (b)) is close to a single Al nanoparticle (**Figure 5-3** (f)). Therefore, the position of Al nanoparticles on the grating is a very important parameter for E-field enhancement.

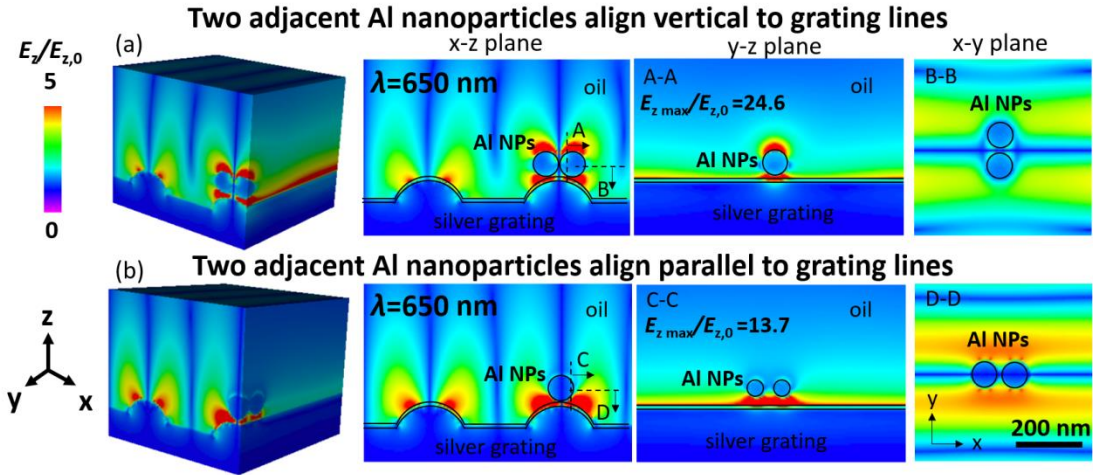


Figure 5-3 FDTD simulated E-field distribution of two adjacent 80 nm Al nanoparticles with different arrangement on silver gratings: (a) align vertically to grating lines and (b) align parallel to grating lines, with laser wavelength of 650 nm under normal incidence (0°) of light in oil (or nitrocellulose) environment. The E-field ($E_z/E_{z,0}$) scale is normalized to 0~5. Each condition shows a 3D view of E-field distribution (left) and the corresponding 2D view of the x-z plane, y-z plane and x-y plane (right). The scale bar in 2D view is 200 nm. The y-z plane view is a cross section with maximum E-field strength ($E_{z\text{ max}}/E_{z,0}$).

5.2 COMSOL modeling absorption and electric field of Al-polymer nanoenergetic systems

In order to investigate the mechanism of photothermal heating on the Al-polymer energetic systems on a plasmonic grating microchip under laser excitation, we modeled photon to phonon conversion and thermal characteristics of the systems. In the first step, we simulated the scattering and absorption of single Al nanoparticle (NP) by COMSOL software to understand the intrinsic properties of Al NP. We investigated the effects of wavelengths, the refractive index of oxidizers, Al NP sizes on scattering and absorption. We distinguished the plasmonic peaks and dielectric loss peak for further laser heating

study. The transient thermal response and the temperature variations as a function of time and space were determined. For future study, we will couple COMSOL Multiphysics with both the RF Module and Heat Transfer Module to simulate the plasmonic photothermal heating and phase change of nanothermites on a plasmonic grating microchip with lasers and flash.

5.2.1 Scattering and absorption of Al nanoparticle in different oxidizers

Model Definition and Results

We coupled COMSOL Multiphysics with the RF Module to simulate the scattering and absorption of single Al nanoparticle (NP) in a different medium including air, fluoropolymer oxidizer THV and another polymer oxidizer nitrocellulose (NC). The COMSOL model demonstrates the calculation of the absorption and scattering of a plane wave of light for an Al nanosphere. We used the Electromagnetic Waves, Frequency Domain in RF Module to solve the problem. To set up the physics in COMSOL, we solve the model for the scattered field, and we need to provide the background plane wave that travels in the positive z-direction with the electric field polarized along the x-axis. The background electric field (E-field) \mathbf{E}_b is specified as:

$$E_{b,x} = E_0 e^{-j2\pi/\lambda_0 z} \text{ (V/m)}, E_{b,y} = E_{b,z} = 0 \text{ (V/m)} \quad (5.1)$$

where λ_0 is the wavelength in free space that corresponds to the laser wavelength, E_0 is the input electric field that is related to laser intensity used for photothermal heating or laser ignition for nanoenergetic systems. Maxwell's wave equation is solved with respect to scattered electric field \mathbf{E} :

$$\nabla \times \mu_r^{-1}(\nabla \times \mathbf{E}) - k_0^2 \left(\varepsilon_r - \frac{j\sigma}{\omega\varepsilon_0} \right) \mathbf{E} = 0 \quad (5.2)$$

$$\mathbf{n} \times (\nabla \times (\mathbf{E} + \mathbf{E}_b)) - jk\mathbf{n} \times (\mathbf{E} \times \mathbf{n}) = 0 \quad (5.3)$$

where $k_0 (= \frac{2\pi}{\lambda_0})$ is the wave vector, \mathbf{n} is the normal vector, ε_r and μ_r is the relative permittivity and relative permeability of materials, respectively. For the electric displacement field model, $\varepsilon_r = (n - ik)^2$, $\sigma = 0$, $\mu_r = 1$, and n and k is the real part and imaginary part of materials, respectively. In the input parameters, the real part of refractive indices (n) of the mediums increase: 1 for air, 1.36 for THV (since the refractive index of Teflon is 1.33, close to 1.36, we simulated THV as of now), 1.5 for NC. We studied the Al NP core sizes of 50 nm ($r=25$ nm), 80 nm ($r=40$ nm), 120 nm ($r=60$ nm), with Al_2O_3 shell thickness of 2 nm for all simulations. We investigated incident wavelengths in the range from 250 nm to 1000 nm.

The cross-section (σ) is an effective area that quantifies the probability of a certain particle-particle interaction, such as scattering or absorption, when an incident beam strikes a target object, for example, individual Al nanoparticle or Al aggregates. The cross-section can be obtained by calculating scattered fields in COMSOL. Subsequently, we can calculate absorption energy (W_{abs}) by integrating the energy loss over the volume of nanoparticle, as well as scattering energy (W_{sca}) by integrating Poynting vector over an imaginary sphere around the particle. The cross section can be defined as the net rate at which electromagnetic energy (W) crosses the surface of an imaginary sphere centered at the particle divided by the incident irradiation (\mathcal{P}_b) that is laser energy flux [W/m^2]. In order to quantify the energy rate absorbed (W_{abs}) and scattered (W_{sca}) by the Al nanoparticle, the absorption (σ_{abs}) and scattering (σ_{sca}) cross section can be defined[124]:

$$\sigma_{abs} = \frac{W_{abs}}{\mathcal{P}_b}, \sigma_{sca} = \frac{W_{sca}}{\mathcal{P}_b} \quad (5.4)$$

Typically, the optical absorption and scattering of one single homogeneous metal nanosphere with radius of r embedded in an optically homogeneous matrix was modelled by Mie theory, so σ_{abs} and σ_{sca} can be expressed as:

$$\sigma_{abs} = \frac{8\pi^2 r^3}{\lambda} \text{Im} \left| \frac{\varepsilon_{particle} - \varepsilon_{medium}}{\varepsilon_{particle} + 2\varepsilon_{medium}} \right| \quad (5.5)$$

$$\sigma_{sca} = \frac{128\pi^5 r^6}{3\lambda^4} \left| \frac{\varepsilon_{particle} - \varepsilon_{medium}}{\varepsilon_{particle} + 2\varepsilon_{medium}} \right|^2 \quad (5.6)$$

where $\varepsilon_{particle}$ and ε_{medium} is the relative permittivity of the metallic sphere and dielectric mediums, respectively. Plasmons are the coherent collective oscillations of free electrons due to the light waves. The confinement of the electromagnetic field results in localized surface plasmon resonance (LSPR) of metallic nanoparticle, which enhances the nanosphere absorption and scattering at the resonant wavelength λ_R . The resonance conditions are achieved by minimizing the denominator $|\varepsilon_{particle} + 2\varepsilon_{medium}|$ close to zero, in order to obtain the maximized cross-sections. The LSPR wavelength λ_R of one single nanosphere is determined by both the metallic particle properties ($\varepsilon_{particle}$) and the surrounding mediums (ε_{medium}).

Equation 5-6 indicates that increasing the Al NP radius leads to higher absorption and scattering cross section at the same wavelengths, since larger Al NP can interact with more photons. **Figure 5-4** shows that Al NP radius of 60 nm exhibits the highest absorption and scattering cross section among all three simulated Al NP sizes. The geometrical size of the nanoparticle (cross-section area, $A=\pi r^2$) is 1963 nm², 5027 nm², and 11310 nm² for Al NP core radius of 25 nm, 40 nm, and 60 nm, respectively. Under most of the wavelengths, the size of the effective absorption cross-section of Al NP is smaller than its

geometrical size; while the size of the effective scattering cross-section of Al NP is larger than its geometrical size at wavelengths close to LSPR peaks.

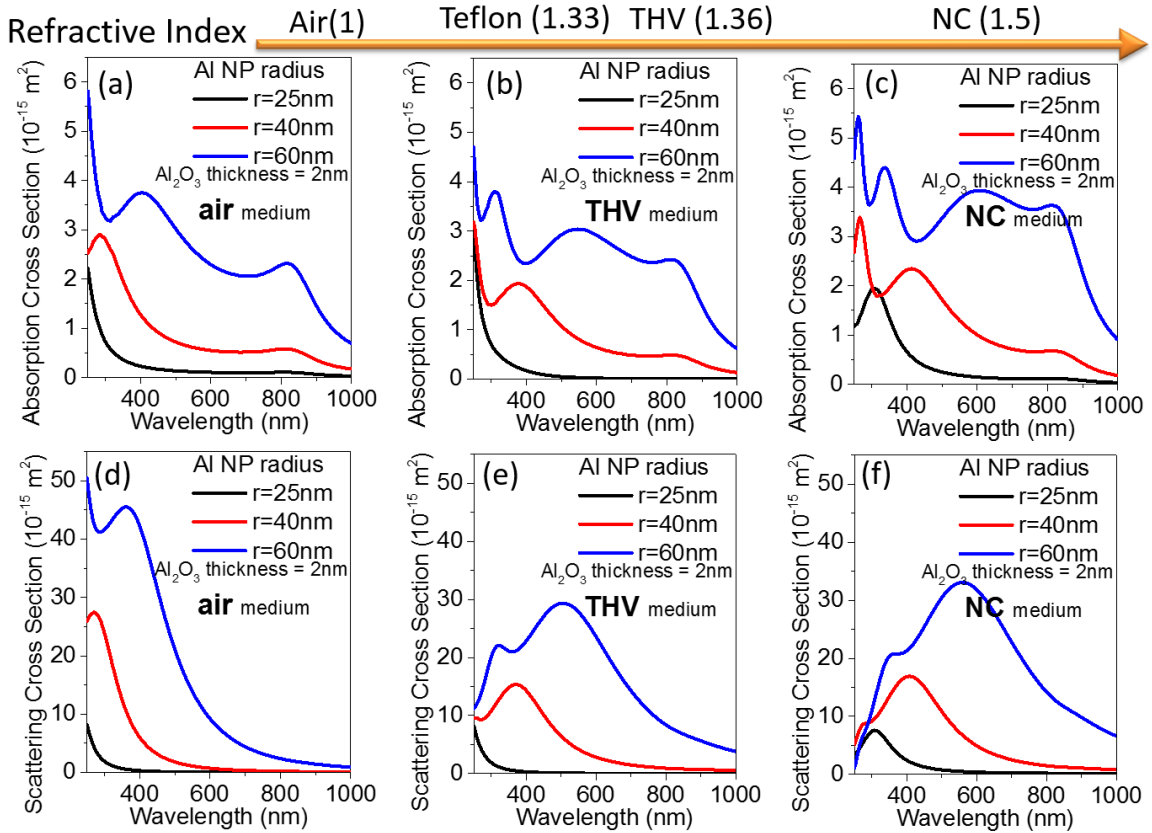


Figure 5-4 (a-c) Absorption and (d-f) scattering cross section of a single sphere aluminum nanoparticle with different aluminum radius ($r=25 \text{ nm}$, 40 nm , 60 nm) in different medium: (a) air, (b) THV, (c) Nitrocellulose (NC). The thickness of the alumina shell is 2 nm for all models.

The absorption and scattering efficiency Q [dimensionless] is the proportionality constant between σ and A , which follows the relationship of $\sigma = QA$. When the thickness of alumina shell is the same (2 nm), a smaller size of Al core results in higher absorption and scattering efficiency at LSPR peaks due to better E-field confinement effect per area (**Figure 5-5**). The absorption peak located around 810 nm is due to the dielectric losses of Al (independent with Al size), and the absorption peak at lower wavelength region is due

to the plasmonic absorption (related to the Al size). Increasing the size of Al NP red-shifts and broadens the plasmonic peaks. The LSPR peaks shift to longer wavelengths with the increase of refractive index of the mediums from the air, THV to NC.

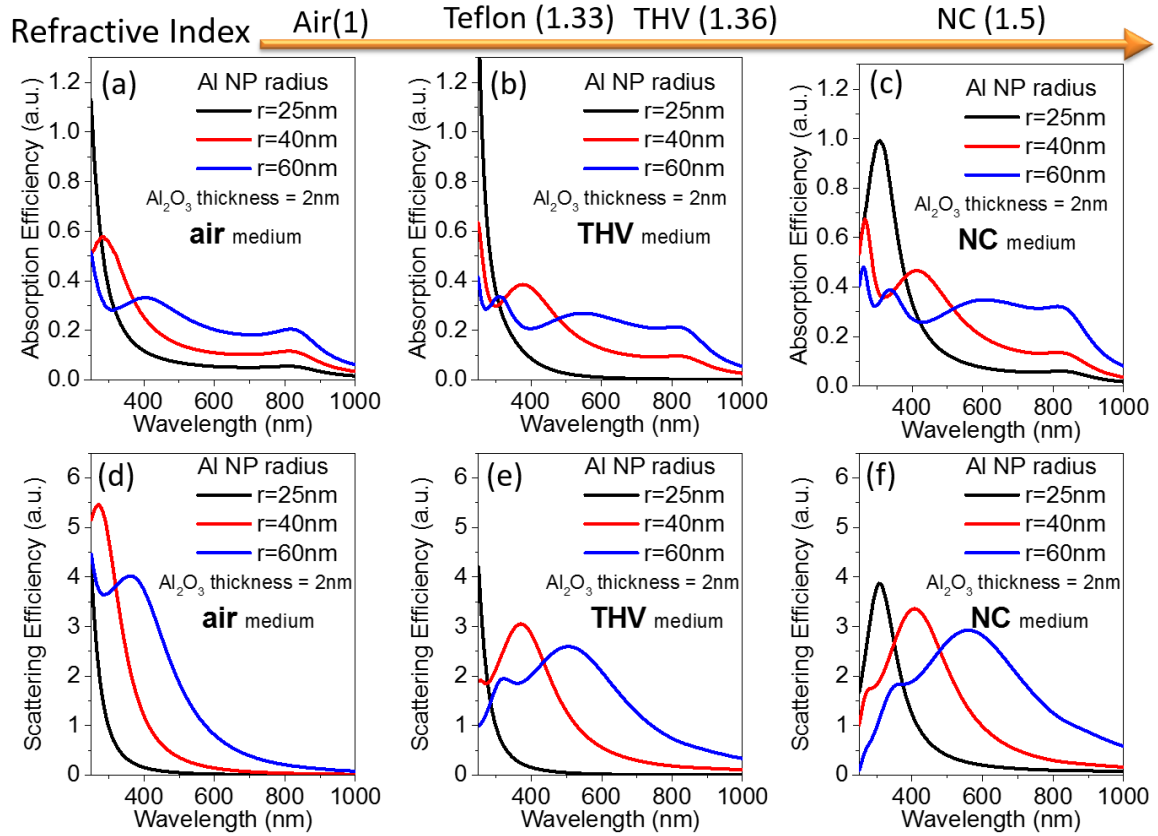


Figure 5-5 (a-c) Absorption and (d-f) scattering efficiency of a single sphere aluminum nanoparticle with different aluminum radius ($r=25$ nm, 40 nm, 60 nm) in different medium: (a) air, (b) THV, (c) Nitrocellulose (NC). The thickness of the alumina shell is 2 nm for all models.

5.2.2 Electric field of Al nanoparticle in different oxidizers

We took the analysis of electric field strength distribution for an 80 nm Al NP ($r=40$ nm) embedded in THV and NC as examples. When Al NP is surrounded by THV (**Figure**

5-6), the two LSPR peaks located at 378 nm and less than 250 nm are attributed to the dipolar and quadrupolar plasmon modes, respectively. [125], [126] The resonant E-field is highly confined in x-direction as the incident light polarized in this direction. The better confinement of light at quadrupolar plasmon modes than that at dipolar plasmon modes leads to higher absorption; while the dielectric loss peak due to the intraband absorption from Al located at 810 nm shows lower E-field than the plasmonic peaks. When we switch the polymer oxidizer NC with higher refractive index compared with THV, both the dipolar and quadrupolar plasmon modes red-shift to 414 nm and 266 nm, respectively (Figure 5-7). The trend of E-field patterns in NC are similar to those in THV at the peak wavelengths.

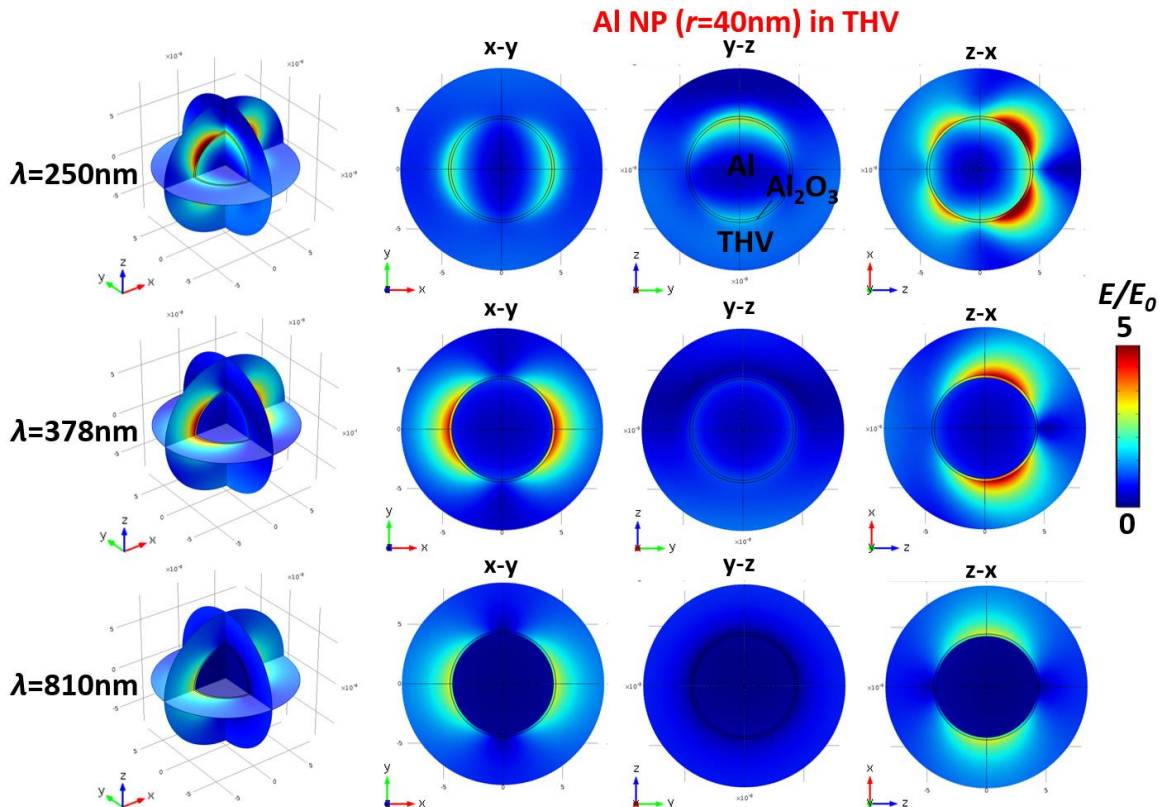


Figure 5-6 Electric field strength (E/E_0) distribution of a single sphere aluminum nanoparticle with aluminum radius ($r=40\text{ nm}$) in THV at different peak wavelengths of 250

nm (quadrupole), 378 nm (dipole) and 810 nm. The thickness of the alumina shell is 2 nm for all models.

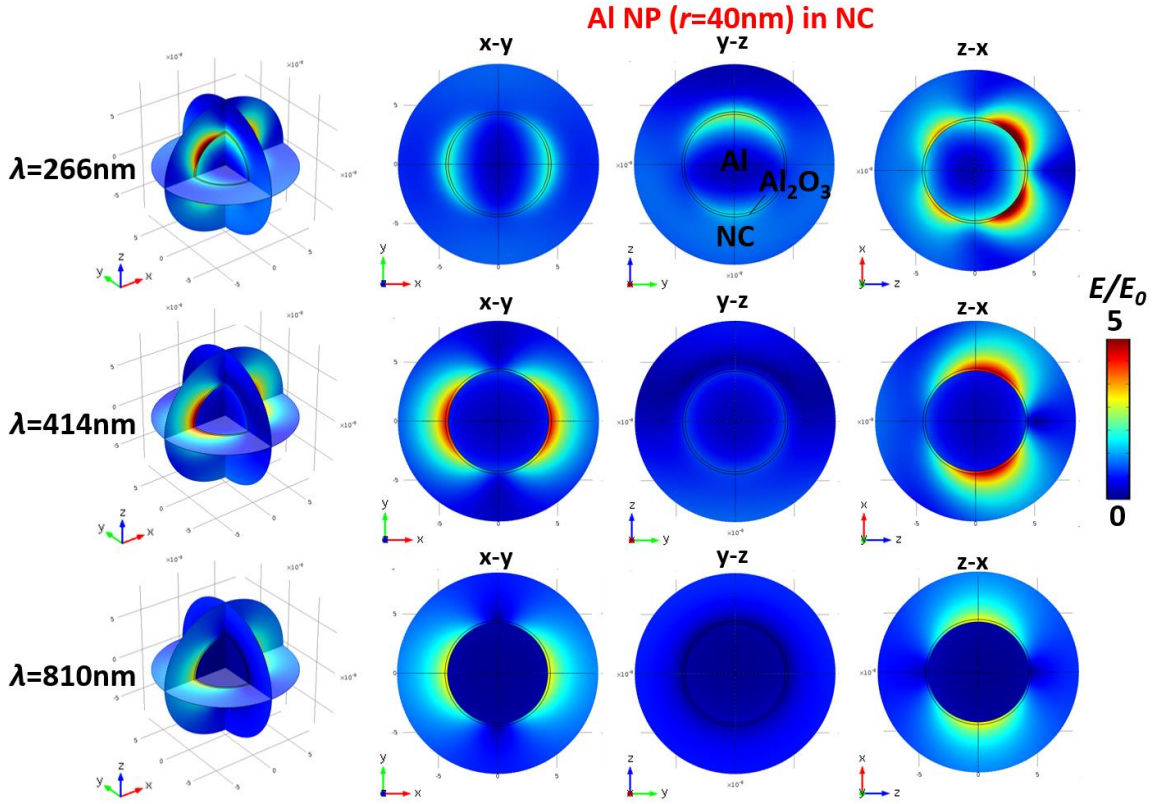


Figure 5-7 Electric field strength (E/E_0) distribution of a single sphere aluminum nanoparticle with aluminum radius ($r=40\text{ nm}$) in nitrocellulose (NC) at different peak wavelengths of 266 nm (quadrupole), 414 nm (dipole) and 810 nm. The thickness of the alumina shell is 2 nm for all models.

5.2.3 Temperature of Al nanoparticles by photothermal heating

For the photothermal heating problems, the COMSOL model needs to solve two governing equations including Maxwell's equations that describe the electromagnetic fields, and the heat transfer equation that describes the temperature. The objective of the analysis is to determine the change in temperature due to the particle sizes, aggregates, and

wavelength dependency. Photothermal heating is a process by which photons excite free electrons, and then convert into phonon to generate heat loss. Generally, the electrons migrate in the metal to restore its initial state; however, the oscillation of light waves result in a constant shift in the dipole that forces the electrons to oscillate at the same frequency as the light. Assuming the light is turned on, the light intensity (light flux, [W/m²]) is calculated by[127]:

$$I_0 = \frac{cn\epsilon_0}{2} |E_0|^2 \quad (5.7)$$

The total amount of heat generated in the Al nanoparticles embedded in polymer oxidizers was estimated from the total light absorption rate [127]. This is highly related to the absorption we calculated above, which shows the effects of laser wavelengths, Al nanoparticle sizes, and the polymer oxidizers on the heat generation for the nanoenergetic systems. In order to quantify energy flow from Al nanoparticle to the polymer or the substrate, the maximum temperature on the surface was calculated. If we assume that the wavelength of incident light is much longer than the nanoparticle radius ($\lambda \gg r$), the photothermal energy of a single, spherical Al nanoparticle can be simplified with an expression as [127]:

$$Q = \frac{\omega}{8\pi} E_0^2 \left| \frac{3\epsilon_{medium}}{2\epsilon_{medium} + \epsilon_{particle}} \right|^2 \text{Im}\epsilon_{particle} \quad (5.8)$$

Since Al nanoparticles act as a heat source, the temperature decreases as the distance increases from the Al nanoparticle. Therefore, the maximum temperature occurs at the surface of Al nanoparticle. The maximum nanoparticle temperature gain ΔT_{max} is calculated using the following equation [127]:

$$\Delta T_{max}(I_0) = \frac{r^2}{3k_0} \frac{\omega}{8\pi} \left| \frac{3\epsilon_{medium}}{2\epsilon_{medium} + \epsilon_{particle}} \right|^2 \text{Im}\epsilon_{particle} \frac{8\pi \cdot I_0}{c\sqrt{\epsilon_{medium}}} \quad (5.9)$$

Heat and differential temperature strongly depend on the physical properties and imaginary permittivity of the Al nanoparticle [128]. The light intensity inside the matrix is enhanced by surface plasmon resonance of microchip grating to increase and control photothermal response. Additionally, our Al-polymer films contain many configurations of Al nanoparticles including single nanoparticle, small nanoclusters, and large aggregates, and therefore the total power conversion rate is much larger than the case of only one single isolated Al nanoparticle. The temperature inside Al aggregates with arbitrary dimensionality m , can be estimated in the limit $N_{particle} \gg 1$ [127]:

$$\Delta T_{total}(\mathbf{r}) \approx \Delta T_{max,0} \frac{r}{d} N_{particle}^{\frac{m-1}{m}} \quad (m=2 \text{ and } 3) \quad (5.10)$$

$$\Delta T_{total}(\mathbf{r}) \approx \Delta T_{max,0} \frac{r}{d} \ln[N_{particle}] \quad (m=1) \quad (5.11)$$

where $\Delta T_{max,0}$ is the temperature increase at the surface of nanoparticle when $N_{particle} = 1$ (one single particle); this temperature is calculated by **Equation 5.10**. d and $N_{particle}$ are the average distance between nanoparticles and the total number of nanoparticles in the nanoenergetic system. The index m is 1, 2, and 3 for the 1D, 2D, and 3D superstructures, correspondingly. A cumulative photothermal effect from multiple particles and Coulomb interaction among the particles are two additional mechanisms that impacts the photothermal heating process [127], [129]. Based on the above estimated equation, the total temperature of nanothermite grows with the number of Al nanoparticles. According to the scanning electron microscopy (SEM) and high-resolution microscopic images obtained in the following tasks, Al nanoparticles closely contact with each other in the aggregates, so we can assume that the distance between nanoparticles d is equal to twice of the radius of Al nanoparticle. Also, there also exist some nanoparticles with distance about 500 nm, 1 μm or even more, and the total temperature decreases as

increasing the distance. Therefore, we started with the *in-situ* imaging study of the laser heating and ignition on Al aggregates, which requires lower energy to heat up and initiate the reaction compared with single Al nanoparticle.

5.3 Combining FDTD simulation and COMSOL modeling for thermal characteristics of Al-polymer nanoenergetic systems under laser excitation

In order to simulate the temperature of Al-polymer nanoenergetic systems on gratings induced by laser heating, we combined the electric field simulated by FDTD simulation and heat transfer model by COMSOL. The details of simulation setups are described in these sections. And the results of the temperature under different conditions will be discussed in **Chapter 6** and **Chapter 7**.

5.3.1 FDTD simulations of electric field on gratings

FDTD analysis was performed to simulate the theoretical electromagnetic (EM) field distribution, and EM field enhancement resulting from the light interaction of plasmonic grating microchip. Graphical input of the geometry and material composition was required to setup the model. The silver gratings following the HDDVD template exhibited 400 nm peak-to-peak pitch, 200 nm grating width, and 60 nm grating height. The surface of silver gratings was coated with 10 nm Al₂O₃ conformal layer. The Al NPs were 80 nm in diameter with 2 nm Al₂O₃ shell. The number of particles, location, and arrangement of Al NPs was investigated.

The boundaries in both the x- and y-directions are periodic boundary conditions for simulating the periodic structures of gratings. The boundary condition on the top of z-

direction is a perfectly matched layer (PML) for the dielectric layer of THV, which is a reflectionless boundary that absorbs electromagnetic waves incident upon them. The boundary condition on the bottom of z-direction is a perfect electric conductor (PEC) for the metal layer of silver, which is a perfectly reflecting boundary that allows no energy to escape the simulation volume along that boundary. When simulating grating substrates, the incident light was polarized orthogonal to the direction of the grating lines to stimulate plasmonic resonance, because the resonance of plasmonic gratings occurs only under p-polarized light. The selected 3D grid size for this computational domain was $\Delta x = \Delta y = \Delta z = 5 \text{ nm}$. The FDTD stop time was set to $40 \mu\text{m}$ (in units of cT) and a 446 nm of the laser was chosen to be incident upon this 3D nanostructure.

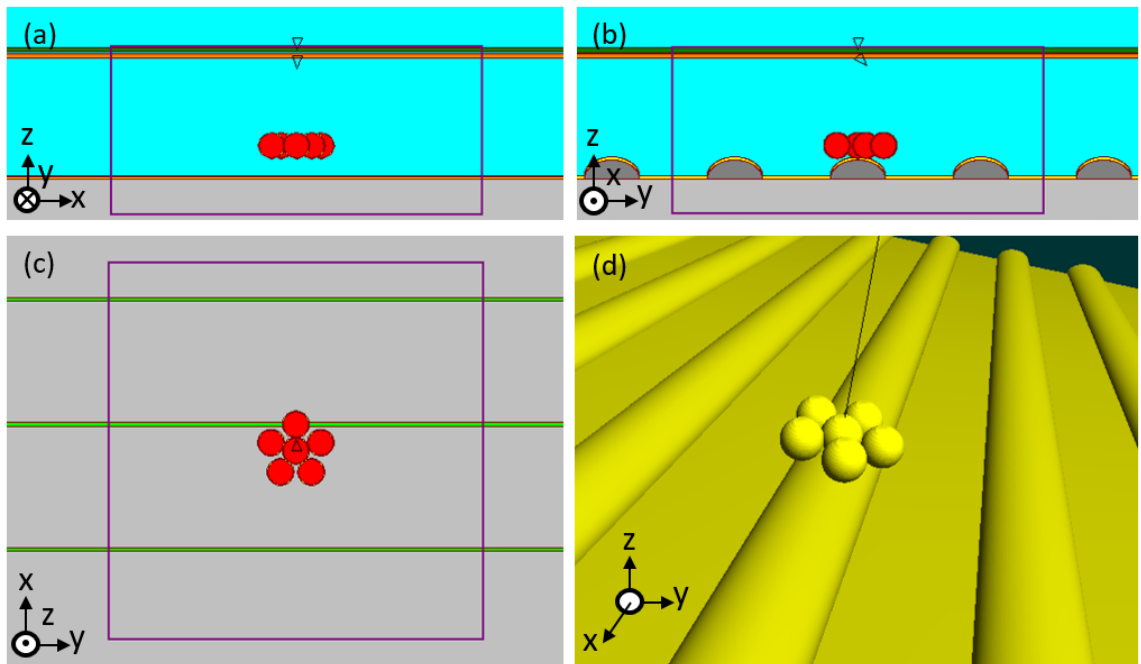


Figure 5-8 Schematic diagrams of 3D FDTD simulated silver plasmonic gratings with Al NPs. (a) x-z plane (side) and (b) y-z plane (front) and (c) x-y plane (top-down) views with color code: red = aluminum, yellow = Al_2O_3 , gray = silver, and turquoise = THV. The orange horizontal bar represents the angled light source and the green one represents the

photodetector, and the open purple box represents the simulation window. The open triangle indicates angle with respect to the axis view. The incident angle is calculated based on Snell's law, 70° incident from the air ($n=1$) corresponds to 43.7° in THV ($n=1.36$). (d) 3D schematic of six Al NPs on silver plasmonic gratings showing the arrangement of Al NPs.

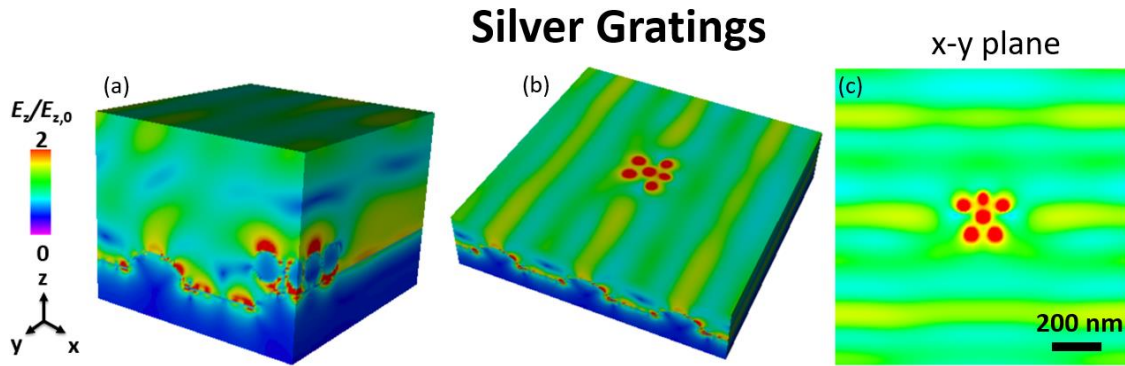


Figure 5-9 FDTD simulated E-field distribution of six 80 nm Al NPs on plasmonic silver gratings under laser wavelengths of 446 nm in THV matrix: (a) 3D side view and (b) 3D top view of E-field distribution and (c) the corresponding 2D view of the x-y plane. The scale bar in x-z plane is 200 nm. The relative z-component of E-field ($E_z/E_{z,0}$) scale is normalized to 0~2. The incident angle is calculated based on Snell's law, 70° incident from the air ($n=1$) corresponds to 43.7° in THV ($n=1.36$).

5.3.2 COMSOL modeling for temperature of Al/THV under laser excitation

The COMSOL program allows us to evaluate 80 nm diameter Al NPs being photothermally heated on a plasmonic grating microchip using the COMSOL Multiphysics package and heat transfer model for joule heating. Since the model requires large domains when evaluating the thermal map of the model during simulation, it is important to use

anisotropic properties. Due to the materials in the system being directional with respect to semi-infinite transient boundary conditions, it is useful to use these anisotropic properties for the simulation. With respect to the boundary conditions, the z-directions of the model are thermally insulated, while the x- and y-direction the faces are at a constant temperature bound of 20°C. Considering these boundary conditions, the front, back, left, and right faces of the model are joined with altered “effective” properties. These altered properties are in a sense that they will be scaled. Doing so would allow the model to be simulated at a large-scale simulation using a smaller domain. The convenience provides a reduction in numerical calculation time as well as providing accurate results.

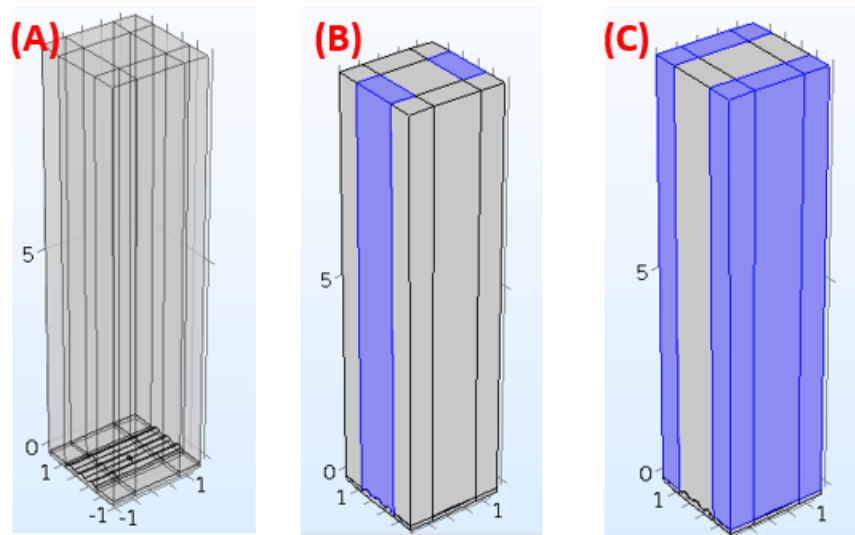


Figure 5-10 (A) Geometric Model. Anisotropic properties in (B) X direction (C) Y direction. The faces indicated in blue were joined with altered “effective” properties.

To calculate the modified values for thermal conductivity and density, we consider equivalent the thermal resistance and thermal capacitance. Assuming the thermal resistance is pure conduction, we equate the actual resistance with a simulated resistance. The actual resistance in the model is 100 μm in length and our simulated

resistance is 1 μm in length. The derivation for the simulated thermal conductivity value is shown below:

$$Res_{actual} = Res_{sim} \quad (5.12)$$

$$\left(\frac{L}{kA}\right)_{actual} = \left(\frac{L}{kA}\right)_{sim} \quad (5.13)$$

$$k_{sim} = k_{actual} \left(\frac{L_{sim}}{L_{actual}}\right) \quad (5.14)$$

Where Res_{actual} is the actual resistance, Res_{sim} is the simulated resistance, L is the length, k is the thermal conductivity, and A is the cross-sectional area. After considering the equivalent resistance, we also consider the equivalent capacitance to find the equivalent density for this simulation. The derivation is given as follows:

$$Cap_{actual} = Cap_{sim} \quad (5.15)$$

$$(c\rho V)_{actual} = (c\rho V)_{sim} \quad (5.16)$$

$$\rho_{sim} = \rho_{actual} \left(\frac{L_{actual}}{L_{sim}}\right) \quad (5.17)$$

Where Cap_{actual} is the actual capacitance, Cap_{sim} is the simulated capacitance, L is the length, V is the volume, and ρ is the density.

The temperature of Al NPs on plasmonic grating microchip due to photothermal heating was simulated by importing an electric field map already simulated in the RSoft program into COMSOL. The electric field was imprinted onto a fixed geometry made in COMSOL. Different geometries including a single, double, and six particles were simulated. Laser powers of 0, 255 mW (0.32 mW/ μm^2 peak), 1080 mW (1.35 mW/ μm^2 peak), 1150 mW (1.44 mW/ μm^2 peak) and 1500 mW (1.88 mW/ μm^2 peak) were examined. For the simulation, it ran from 0 to 250 μs with increments of 5 μs . It is apparent that temperature increases with power density and temperature increases with the number of

particles, which follows a square root type trend.

5.4 Future Work

Based on the current FDTD simulation results, we will continue to optimize the plasmonic grating configuration by simulating different grating height, grating width, grating shape, metallic thickness, metallic or dielectric coating, etc. We will explore the best grating configuration for top and bottom illumination. Meanwhile, we will simulate more conditions of Al nanoparticles on the grating in the future study to understand the fundamental science for Al nanoenergetic system incorporated with plasmonic grating microchip and optimize the experimental conditions to get best energetic performance.

We will employ COMSOL software coupling RF Module and Heat Transfer Module for modeling the photothermal heating as well as a phase change of Al nanoparticles/polymer on a plasmonic grating microchip using lasers. We will adjust the laser power and wavelength, pulse duration, and nanothermite configuration on a grating microchip to study the transient thermal response, the temperature variations with time and space, and then compare with experimental results. The heat flow from the Al nanoparticles to the adjacent nanoparticles, surrounding oxidizer medium, and substrates will be studied to understand the reaction kinetics.

Chapter 6. Plasmonic Grating Enhanced Fluorescence-Based Temperature Sensor for *In-Situ* Imaging Local Temperature of Aluminum Nanoparticles

6.1 Abstract

A fluorescence-based temperature sensor enhanced by a plasmonic grating platform was developed for *in-situ* dynamic mapping of temperature at the nanoscale induced by photothermal heating of aluminum nanoparticles (Al NPs). Al/fluoropolymer nanoenergetics films with temperature sensitive dyes (Rhodamine 6G) were prepared and calibrated to obtain a linear correlation between temperature and fluorescence intensity. The temperature-dependent emission spectra were reversible in the calibrated temperature range. The *in-situ* temperature response shows a maximum heating rate of 1.2×10^4 °C/s achieved at 6 ms and 20 ms to reach a stable heating rate. The spatial temperature gradient between Al NP and surrounding polymer indicates the nanoscale heat transfer. Under irradiation of high power laser, both *in-situ* and *ex-situ* movements of Al NPs caused by the thermal expansion or melting of polymer were resolved. Al NPs play an important role in laser heating due to the plasmonic, interband and intraband absorption characteristics of Al NPs. Plasmonic grating platforms were proved experimentally and theoretically to significantly improve both fluorescence intensity and the photothermal heating of Al compared with glass platforms due to the enhanced electric field, opening a new path for fast *in-situ* high-resolution temperature mapping.

6.2 Introduction

Nanoenergetic composites represent a class of materials that undergo a large exothermic combustion reaction at temperatures in excess of 3000K and consist of nanoscale fuel particles a solid state oxidizer. Nanoscale fuel particles offer performance advantages over conventional energetic materials [63], [65], [67]. Aluminum nanoparticle (Al NP) fuel embedded in thin reactive polymer films may be activated on demand and may be integrated into MEMS-type devices. The temperature evolution of a nanoenergetic systems is key to understanding the ignition behavior and reaction kinetics and for designing nanoenergetic systems with custom responses. Photothermal heating of Al NPs [66], [67], [69], [71]–[73] is of particular interest in nanoenergetic systems as it facilitates thermal energy generation by the Al NPs themselves, resulting in rapid heating rates with minimal external energy application. *In situ* temperature characterization of nanoscale systems is of significant importance in diverse applications including chemical propellant thrusters[54]–[57], nanoscale catalysis, photothermal therapeutic medicine for biology [58], [59], [61], nanofluidics [62], and nanoelectronics. A variety of techniques have been developed to obtain high-resolution temperature mapping or fast temperature acquisition. For example, Scanning Thermal Microscopy (SThM) enables a spatial resolution less than 100 nm utilizing a sharp composite tip to directly probe the surface temperature of a sample; however, this scanning method is invasive to the sample and relatively slow, and it cannot measure the subsurface temperature inside the sample.[130] Non-invasive and in-depth temperature measurements can make use of optical-based approaches due to the temperature dependence of fluorescence intensity[131], photoluminescence spectra or lifetime[132], infrared spectra, and Raman spectra[133].

Temperature-sensitive fluorescent dyes offer real-time *in-situ* temperature mapping and ease of incorporation in different matrices. Among candidate materials, nanoscale lanthanide-doped oxide precursors [132], [134], [135] are very promising dyes for high-temperature mapping in nanoenergetics. For example, Dy³⁺-doped oxide precursors can be calcined at temperatures ranging from 440 K to 1256 K for the calibration. [132] These dyes undergo a phase transformation during heating leads to different crystal fields. [132] However, the temperature sensing is irreversible and the size of oxide precursors range from 300 nm to several tens of micrometers. Rhodamine 6G (R6G) molecular dye, by contrast, exhibits reversible temperature-sensitive fluorescence behavior up to 250 °C and may be molecularly coated to nanoparticles or homogeneously dispersed in solution [109], [136]. Traditionally, however, fluorescence techniques for *in-situ* temperature mapping have been hindered by the low quantum yield of dyes. The accumulated fluorescence intensity is not sufficient for fast dynamic processes, and the signal to noise ratio is insufficient for adequate resolution at elevated temperatures. To overcome this shortcoming, surface plasmon resonance (SPR) may be used to enhance the fluorescence intensity by a factor of 100. SPR enhancement may be realized using a plasmonic grating substrate to couple to both the excitation and emission wavelengths of the fluorophores. Moreover, utilizing of a plasmonic grating is less expensive than prism-based SPR systems [4], [9], [12] and can serve as super-resolution imaging platform to visualize nanostructures and localized heating at the nanoscale [9].

Here we report an innovative *in-situ* temperature imaging and sensing platform for Al NP/polymer nanoenergetic systems, using a common epifluorescence microscope and a plasmonic grating substrate, as shown in **Figure 6-1**. Al/THV nanoenergetics films with

temperature-sensitive R6G dye were dispersed on plasmonic gratings fabricated by inexpensive nano-imprint lithography based on HDDVDs. [4], [5], [9], [12]–[17] Energetic films were then photothermally heated using a tunable laser while *in-situ* thermal mapping and particle imaging were recorded by a black and white CMOS camera.

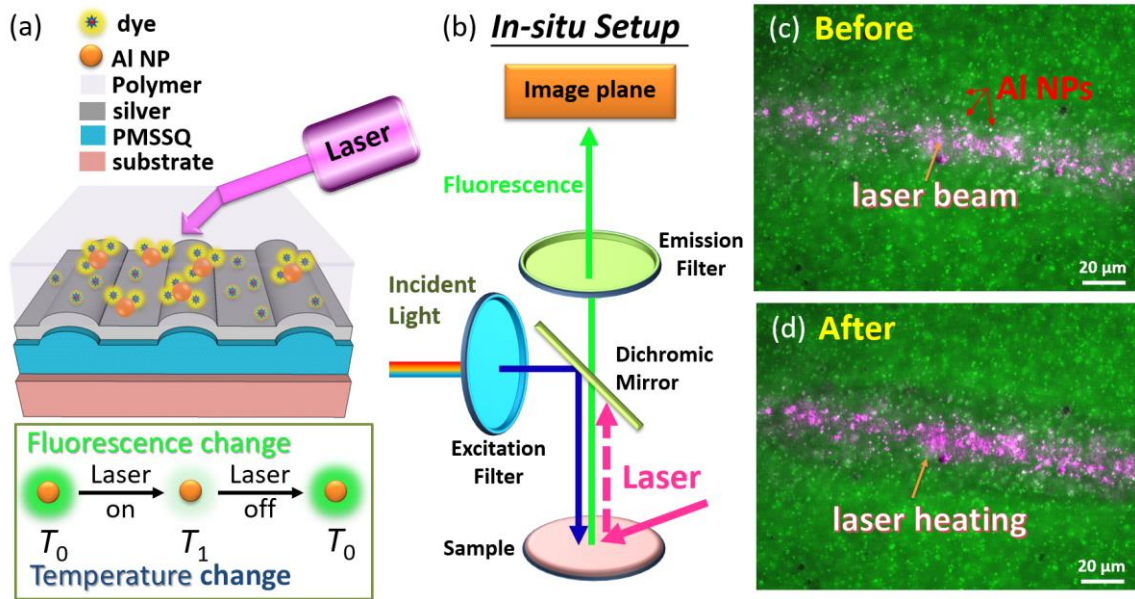


Figure 6-1 (a) A schematic of the *in situ* fluorescence imaging platform to study photothermal heating of nanoenergetic thin film. The system consists of a plasmonic grating, microscope objective, fast camera, and external laser. (b) A schematic of the imaging setup for *in-situ* in fluorescence mode with a band-pass emission filter to block the excitation light and the laser. (c-d) Fluorescence images for Al/THV/R6G films on gratings (c) before and (d) after 808 nm laser heating (200 mW, 4 s continuous wave (CW) exposure) with magenta laser spot superimposed.

6.3 Experiment

6.3.1 Fabrication of Plasmonic Gratings

Polymethylsilsesquioxane (PMSSQ) gratings were fabricated by a nano-lithography process using HD DVD grating templates in a similar manner as described previously.[6], [15]–[17], [94], [137] PMSSQ gratings were formed using a 3 wt% PMSSQ in 100% ethanol and (3-aminopropyl)triethoxysilane (APTES) vapor treatment. Following stamping, gratings were heated at 60 °C for 3 min to crosslink further the PMSSQ/APTES gratings. The silver was deposited on to PMSSQ using sputtering to make a smooth metal film.

6.3.2 Prepare Al/THV nanoenergetics films with temperature sensitive dyes

Aluminum NPs (80 nm in average diameter with 2.2 nm alumina shell) were purchased from Novacentrix (Austin, TX, USA) and were used as received. THV is a fluoropolymer consisting of tetrafluoroethylene (TFE), hexafluoropropylene (HFP), and vinylidene fluoride (VDF). THV 220A as an oxidizer was purchased from 3M (St. Paul, MN, USA). Temperature sensitive fluorescent dyes R6G were purchased from Exciton (Dayton, OH, USA). R6G is selected due to its high thermal stability (~250 °C) with a temperature-sensitive fluorescence quenching behavior. Additionally, the plasmonic coupling angles of the excitation and emission wavelengths of R6G in THV were within the illumination angle and captured angle of the microscope. Four different sample/substrate combinations were prepared for testing. These include 10 μm thick THV/R6G (1 μM) films with and without Al NPs drop-casted on plasmonic gratings and on the

glass. A low Al to THV ratio (0.1wt %) was used to study the behavior of individual Al NPs. Additional acetone treatment process was used to improve the smoothness of the film by creating a saturated vapor environment that can slow down the solvent evaporation process. After acetone treatment, all films became transparent due to so the reduction of the scattering on the film surface.

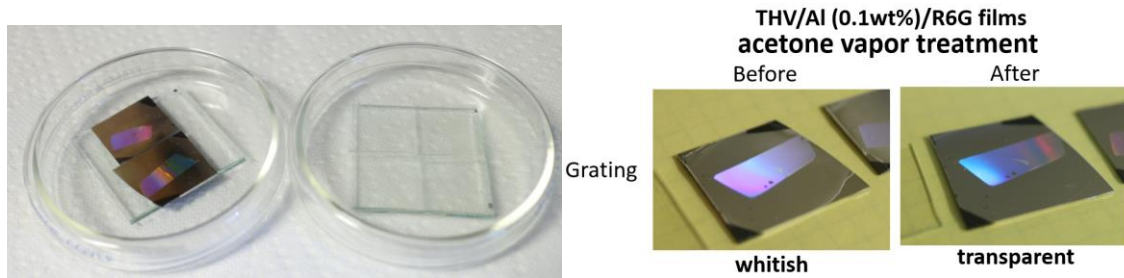


Figure 6-2 Al/THV/R6G film preparation on plasmonic grating and glass substrate.

6.3.3 Temperature-fluorescence calibration curve for Al/THV/R6G systems

6.3.3.1 Excitation and emission spectra characterization by microplate

reader with built-in temperature control

The temperature dependency of excitation and emission spectra was characterized using a microplate reader with built-in temperature control. A wavelength of 580 nm with 9.0 nm bandwidth was chosen for the excitation measurements, while a 480 nm wavelength with a bandwidth of 9.0 nm was selected as an excitation light source for all emission measurements. All films were heated from 30 °C to 65 °C and then cooled to 30 °C at 5 °C steps. Note that the maximum temperature that can be achieved by microplate reader is 65 °C. For each measured temperature, a 15 min dwell time was implemented to ensure

temperature uniformity and steady state.

6.3.3.2 *Temperature-fluorescence characterization by microscope equipped with heat stage*

The Al/THV/R6G films on gratings were imaged with an Olympus BX51WI epifluorescence microscope equipped with an ORCAflash 2.8 CMOS camera, 40× air objective, and illuminated with a xenon broadband light source. Fluorescence images were taken under excitation ($475 \text{ nm} \pm 15 \text{ nm}$) and emission ($518 \text{ nm} \pm 10 \text{ nm}$) band-pass filters (**Figure 6-1b**). The temperature was calibrated from room temperature to $80 \text{ }^\circ\text{C}$ with a step increment of $10 \text{ }^\circ\text{C}$ using a home-built heating stage (**Figure 6-3**) equipped with the epifluorescence microscope and acquired the fluorescence images at each temperature setting. The temperature is controlled by a thermocouple and measured by infrared thermometer (AR228).

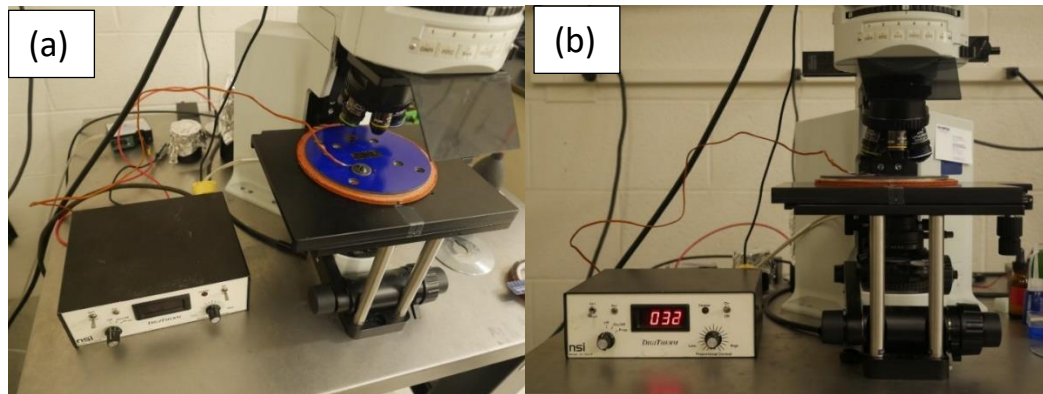


Figure 6-3 Setup for microscope equipped with a heating stage for temperature calibration.

6.3.4 Develop and characterize tunable laser heating setup in microscope for *in-situ* heating and imaging

The laser control setup consisted of an 808 nm laser diode, a focus lens, a goniometer, a micro-positioner and a laser driver for adjusting laser power. A near-infrared (NIR) laser at 808 nm was selected because this wavelength is located at the intraband absorption band of Al, resulting in an efficient photothermal heating. The laser beam area was $13.8 \mu\text{m} \times 103 \mu\text{m}$ measured by CMOS camera with vertical illumination. The laser was incident at an angle of 70° for laser heating experiments. The laser beam is distributed as an ellipse, with the fluence in the central region, J_c , represented by:

$$J_c(\text{J/m}^2) = 1.19 \times 10^5 \cdot P(\text{mW}) \cdot t(\text{s}) \quad (6.1)$$

where P is the power of a laser, and t is a pulse time.

Fluorescence images for laser heating experiment were taken with the same epi-fluorescence microscope used for the temperature calibration. All samples were imaged in both fluorescence and bright field modes by ORCAflash 2.8 CMOS camera under $40\times$ air objective. The time-resolved *in-situ* fluorescence images and *ex-situ* fluorescence images were taken using the same fluorescence filter sets without neutral density (ND) filters with 2 ms exposure time, while the *ex-situ* bright field images were taken using bright field filter sets. The fluorescence intensities of these Al/THV/R6G films were enhanced by the plasmonic gratings, only requiring a short exposure time (2 ms), which can facilitate the *in-situ* measurement with high temporal resolution (500 fps). For photobleaching test, the

ND filters are 25% and 6%, and the combination of both ND filters provides 1.5% of the illumination intensity without ND filters.

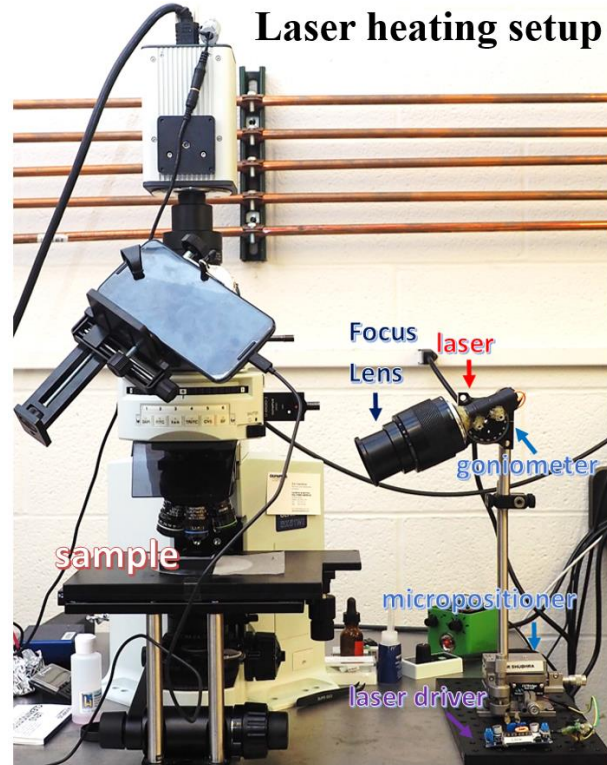


Figure 6-4 Schematic of the laser heating setup.

The laser beam area was $13.8 \mu\text{m} \times 103 \mu\text{m}$ measured by CMOS camera with vertical illumination (90° with respect to the sample surface), and hence the area of the laser beam is about $4465 \mu\text{m}^2$. The projected area for 20° incident angle w.r.t. the sample surface (or 70° degree incident angle w.r.t. the normal to the sample surface) that was used in this experiment, should be $13056 \mu\text{m}^2$.



Figure 6-5 The 808 nm laser beam calibrated by CMOS camera with 20° illumination (incident angle w.r.t. the sample surface). It shows a Gaussian distribution of laser power density over the area.

6.4 Results and Discussion

6.4.1 Temperature-dependent spectra and reversible response

To calibrate the temperature dependency of resultant fluorescence images, excitation and emission spectra of all samples at different temperatures from 30 °C to 65 °C were investigated. **Figure 6-6a** shows that the RG6 excitation peak wavelength (514 nm) and intensity change minimally with temperature. The emission peak wavelength red-shifts when temperature increases from 30 °C to 65 °C, and the emission peak intensity decreases with elevated temperature due to the thermal activation of nonradiative de-excitation pathways[138] (**Figure 6-6b**). The excitation and emission spectra and intensity repeatability were studied to reduce the influence of irreversible photobleaching or heat damage. Both excitation and emission spectra completely overlap at 30 °C before and after one heating and cooling cycle (from 30 °C to 65 °C then back to 30 °C) in a microplate reader, indicating that the emission intensity is reversible and repeatable (**Figure 6-6c**).

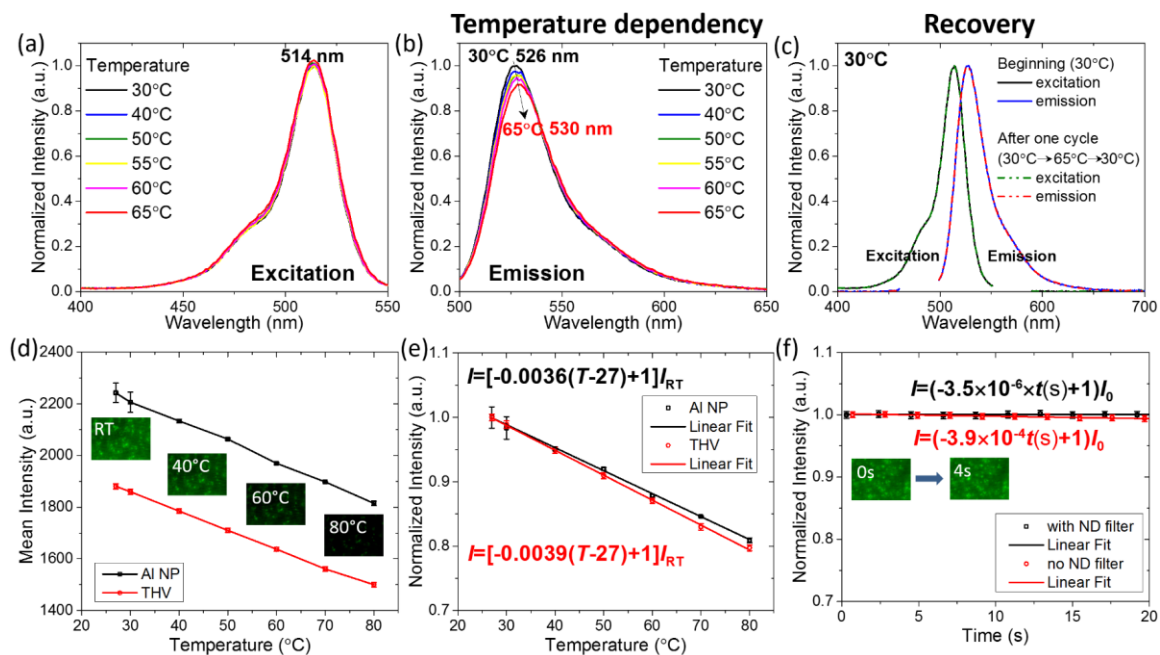


Figure 6-6 Temperature dependency of R6G spectra: (a) excitation and (b) emission spectra of the sample of THV-220V/R6G (1 μ M)/Al films on grating heated from 30 $^{\circ}$ C to 65 $^{\circ}$ C in a microplate reader. Spectra recovery: excitation and emission spectra at 30 $^{\circ}$ C before and after one heating cycle on the sample (heated from 30 $^{\circ}$ C to 65 $^{\circ}$ C, and then cooled back to 30 $^{\circ}$ C). Data (a-c) were taken by microplate reader with built-in temperature control and normalized to maximum intensity at 30 $^{\circ}$ C. Fluorescence-temperature curve for THV-220V/R6G (1 μ M)/Al films on gratings: (d) mean intensity and (e) normalized mean intensity with respect to the room temperature (RT), for analysis of Al and THV regions. (f) Photobleaching measurement by the background excitation light over time with and without 25% and 6% neutral density (ND) filters. Data (d-f) are taken by 40 \times air objective in an epi-fluorescence microscope equipped with a heating stage.

6.4.2 Temperature calibration curve and effects of photobleaching

The temperature was calibrated from room temperature to 80 °C with a step increment of 10 °C using a heating stage equipped to the epi-fluorescence microscope and acquired the fluorescence images at each temperature setting. The fluorescence response of R6G on Al NPs and THV were measured separately, as fluorescence intensity of Al NPs is significantly greater than that of THV. The slopes of mean fluorescence intensity vs. temperature for THV and Al NPs are similar (**Figure 6-6d**), indicating temperature stability and a uniform response of R6G for both THV and Al NP. Using room temperature (T_{RT}) and the corresponding fluorescence (I_{RT}) as a reference (**Figure 6-6e**), the following calibration curves were obtained:

$$I = [-0.0039(T-T_{RT}) + 1] I_{RT} \quad \text{for THV} \quad (6.2)$$

$$I = [-0.0036(T-T_{RT}) + 1] I_{RT} \quad \text{for Al NP} \quad (6.3)$$

The effect of photobleaching of R6G under background excitation over time was examined with and without neutral density filters (**Figure 6-6f**). In the first 20 ms determining the heating rate as discussed in the following sections, the intensity decrease is $7.8 \times 10^{-6} I_0$ under a strong background light without neutral density filters, but the intensity decreases $4.0 \times 10^{-3} I_0$ when the temperature increases only 1 °C, and hence the photobleaching of R6G due to the excitation light is negligible. If the temperature increases more than 100 °C, the intensity decrease due to laser heating is more than $0.4 I_0$, which is over 5000 times of photobleaching intensity in the first 20 ms. Even after 4 s laser irradiation, the intensity only decreases $1.6 \times 10^{-3} I_0$, which is also much lower than the intensity reduction due to laser heating. The illumination intensity with neutral density

(ND) filters is 1.5% of that without ND filters, and the photobleaching speed without ND filter ($3.5 \times 10^{-6}/s$) is also about 100 times of that with ND filter ($3.9 \times 10^{-4}/s$), indicating that the photobleaching speed is linear with the excitation intensity.

6.4.3 Enhancement of Plasmonic Gratings and Al Nanoparticles on Laser

Heating

THV/R6G(1 μ M) on Plasmonic Grating

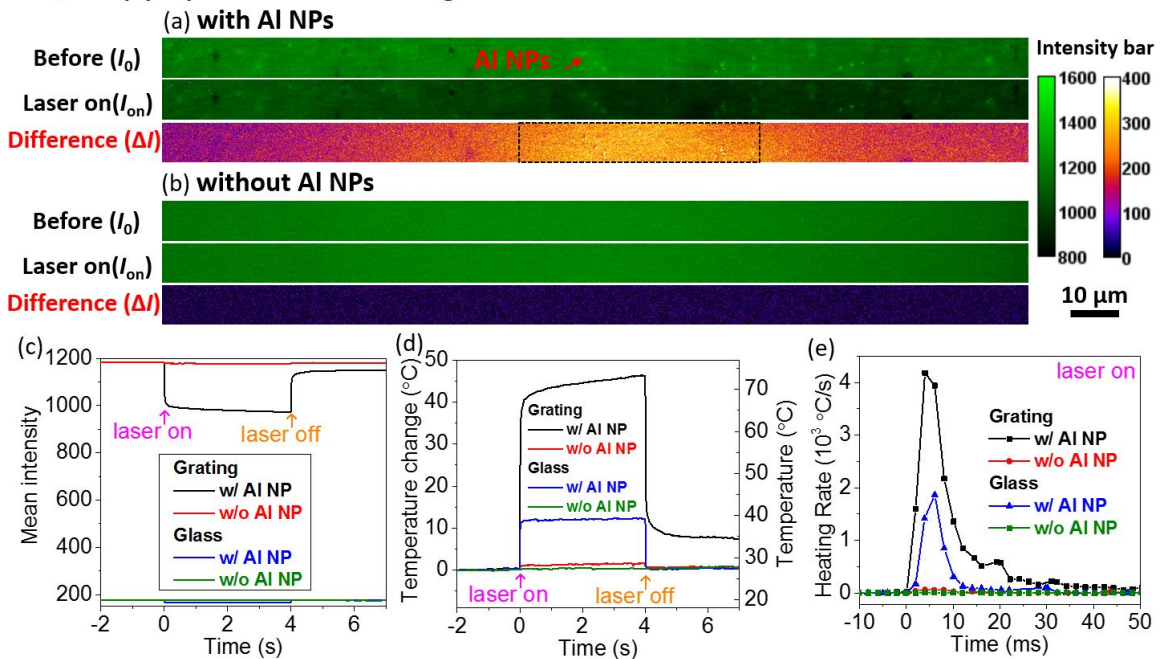


Figure 6-7 Effect of plasmonic gratings and Al NPs on laser heating. Fluorescence images for THV/R6G films (a) with and (b) without Al NPs on gratings, before and after 808 nm laser heating (60 mW, 4 s exposure) and the corresponding fluorescence difference. (c) Mean intensity, (d) temperature change and temperature, (e) heating rate under 808 nm laser heating (60 mW, 4 s exposure). All data were taken by $40\times$ air objective in the epi-fluorescence microscope. The mean value is obtained by analysis in the large area indicated

as a black rectangular box in a.

Figure 6-7a-b shows spatial fluorescence intensity maps for THV/R6G films with and without Al NPs on plasmonic gratings, before (I_0) and during laser irradiation (I_{on}). Localized regions of high intensity indicate fluorescence enhancement of the dye near Al NPs resulting from electric field enhancement near the metallic nanoparticle. Aggregated Al nanoparticles appear as dark regions, as the fluorescent dyes are unable to diffuse between the Al NPs. The intensity difference between a given frame and the initial intensity ($\Delta I = I_{on} - I_0$) is used to distinguish temperature change during irradiation. Fluorescence intensities decreased dramatically in the irradiated regions (60 mW) for THV/R6G films with Al NPs on gratings (**Figure 6-7a**), indicating a large temperature difference, while the sample without Al NPs undergoes a minimal fluorescence change (**Figure 6-7b**). Similarly, the fluorescence decrease for the film with Al NP on the glass is also much higher than the one without Al NP on the same substrate. These results confirm that Al NPs act as sites of energy absorption while THV is optically transparent with very low absorption at 808 nm.

An $8 \mu\text{m} \times 48 \mu\text{m}$ area in the center of laser marked as a rectangular box in **Figure 6-7a** was used for analysis of the mean fluorescence intensity in **Figure 6-7c**. Note that the average fluorescence intensity on plasmonic gratings (~ 1184) was 7 times greater than that on glass (~ 176) at ambient temperature. Because increased temperature decreases fluorescence intensity, enhancing the native fluorescence intensity is imperative to accurately distinguish temperature increases. In addition, capturing high-speed imagery requires high fluorescence intensity to compensate for the short camera exposure time. After capturing *in-situ* spatial fluorescence data, the temperature was obtained using the

calibration curves. Overall, THV/R6G with Al NP on grating shows the highest fluorescence intensity, the most significant temperature increase, and the highest heating rate among all four samples (**Figure 6-7c-e**). The intensity decreased rapidly during initial laser irradiation indicating a rapid heating and increased immediately after irradiating, consistent with rapid cooling.

Plasmonic gratings can enhance both fluorescence intensity and photothermal heating. Al/THV/R6G film on plasmonic grating reaches 67 °C at 100 ms and shows the maximum temperature of 73 °C after 4 seconds of 60 mW laser irradiation, while the same film on glass substrate only shows maximum temperature of 39 °C (**Figure 6-7d**), indicating that approximately 4-fold enhancement on the temperature change by plasmonic gratings (46 °C) to the glass (12 °C). No matter on grating or glass, the temperature increase for the samples without Al NPs is negligible. The maximum heating rates by 60 mW 808nm laser were 4.2×10^3 °C/s and 1.7×10^3 °C/s for plasmonic gratings and the glass substrate, respectively (**Figure 6-7e**).

The laser heating mechanism of Al/THV nanoenergetic system on plasmonic grating platform is: (1) plasmonic gratings couple the incident light to Al NPs and enhance the E-field that leads to the improvement of absorption of Al NPs; (2) Al NPs absorb photons that would excite electrons, which generate phonons through relaxation to the ground state, resulting in increased temperature; (3) the heat is transferred from Al NPs to surrounding THV and heats up a larger region; (4) the heat distributed in Al NP and THV is transferred to temperature-sensitive dye R6G, and finally the increasing temperature decreases the corresponding fluorescence intensity.

It should be noted that the fluorescence intensity for the grating sample without Al NPs after laser off shows only $1.6 \times 10^{-3} I_0$ reduction (**Figure 6-7c**), which matches very well with the photobleaching induced by the background excitation (**Figure 6-6f**). This indicates that the 808 nm laser would not bring any additional photobleaching to the measurement because NIR is not in the range of excitation wavelengths of R6G. Therefore, the additional intensity reduction after laser off is only due to the photothermal heating effects on the samples. There is no temperature change after laser off for all samples except for the gratings with Al NPs (**Figure 6-7d**). A temperature change of 7 °C remains at 3 s after laser off, but it shows a trend of temperature slowly goes down due to the slow cooling process. A slight thermal expansion of the THV polymer film is also possible to result in a small variation of fluorescence intensity.

6.4.4 Effects of laser power on heating

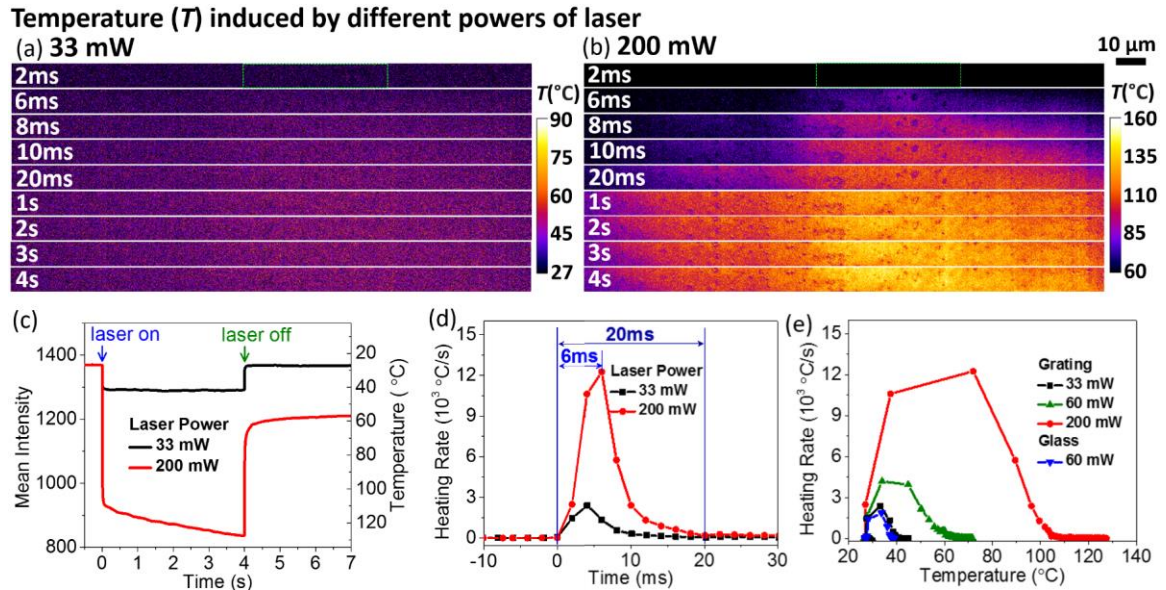


Figure 6-8 Comparison between the low power (33 mW) and high power (200 mW) of

laser input for *in-situ* fluorescence and temperature monitoring for Al/THV/R6G films on gratings with exposure to 808 nm laser for 4 s. Dynamic temperature map for different laser input power (a) 33 mW and (b) 200 mW over time. All images are false-color images. (c) Mean fluorescence intensity and corresponding temperature over time; (d) Heating rate calculated by the first derivative of temperature change over time; (e) Heating rate vs. The temperature for different powers and substrates. All data are taken by 40× air objective in the epi-fluorescence microscope. The mean value is obtained by analysis in the large area indicated as a green rectangular box in a-b.

The temperature response induced by photothermal heating with low laser power (33 mW) and high laser power (200 mW) were compared. Dynamic temperature maps (**Figure 6-8a-b**) were constructed using ImageJ software to convert the fluorescence intensity to temperature by the calibration curve. The mean temperature responses (**Figure 6-8c-e**) as a function of time for all samples were recorded in the central region of the laser ($8\ \mu\text{m} \times 48\ \mu\text{m}$). **Figure 6-8c** shows that 33 mW reaches 42 °C and 200 mW reaches 110 °C at 100 ms of irradiation, and the maximum temperature after 4 seconds of irradiation is 128 °C at 200 mW and still 42 °C for 33 mW. Note that steady state is achieved for the 33mW case, but not for the 200mW case. The fluorescence intensity is fully recovered within 50 ms after laser off for 33 mW but not for 200 mW, but there is a trend of slow fluorescence recovery for 200 mW. After an extended high-temperature heating, the deformation of THV and degradation of the dye probably occurs and results in an artificially higher temperature reading. It is also difficult to determine how much the deterioration of the dye is responsible for the unsteady response. Furthermore, the temperature-fluorescence correlation may not be linear at a high temperature out of the

calibrated range, especially close to the decomposition temperature of the dye.

Figure 6-8d indicates a maximum heating rate is achieved after between 4-6 ms and 20 ms to reach a stable heating rate, which is also indicated in the dynamic temperature maps (**Figure 6-8a-b**). The maximum heating rates observed were 1.2×10^4 °C/s and 2.4×10^3 °C/s for 200mW and 33mW, respectively. The heating rate vs. temperature plot is shown in **Figure 6-8e**. The maximum heating rate achieved at ~34 °C under most of the conditions, while the maximum heating rate is achieved at 72 °C for 200 mW laser. All of these temperatures are within the calibrated temperature region, so it should be safe to process temperature conversion. The heating rate above 1×10^3 °C/s is reached at less than 100 °C that is below the melting point of THV and the degradation temperature of R6G, the calculated heating rate should be accurate for all these conditions in this study.

6.4.5 Nanoscale local temperature comparison between Al NPs and THV

Upon 200mW laser heating, a fluorescence intensity gradient is established, with maximum intensity decrease near the laser line. **Figure 6-9** shows laser scattering on the sample and spatial fluorescence intensity maps before, during, and after the 200 mW laser irradiation. The intensity difference map is used to select Al NPs with substantial temperature change for further analysis. Note that the laser power intensity is spatially distributed (**Figure 6-9a**), so a spatially uniform temperature response is not anticipated. To obtain the temperature response as a function of time for the Al NPs and THV polymer independently, four Al NPs (two Al NPs in low and high power density regions, respectively), and one THV region next to an Al NP as well as an entire large area (**Figure 6-9e**). All Al NPs and THV regions were selected as a circle with a diameter of 550 nm,

i.e., the area is $0.237 \mu\text{m}^2$, and the large area is an $8 \mu\text{m} \times 48 \mu\text{m}$ rectangular region.

The fluorescence intensities and the reconstructed temperature were seen in **Figure 6-9f**. The mean fluorescence intensity of R6G on Al NPs in low power density region showed constant value, while those in high power density region kept decreasing as the laser continued to illuminate during the entire laser heating period of 4 s. Therefore, the converted temperature was constant for low power density region, while the temperature continued increasing for high power density region (**Figure 6-9f**). The maximum temperature achieved was $135 \text{ }^\circ\text{C}$ in the low power density region and $157 \text{ }^\circ\text{C}$ in the high power density region. It should be noted that the relative temperature can be compared, but the actual temperature reading can only be treated as approximate in the regions where the dyes decompose due to excessive temperature and do not return to baseline intensities at room temperature. **Figure 6-9g** shows that the THV close to a hot Al NP ($157 \text{ }^\circ\text{C}$) can reach the maximum temperature of $133 \text{ }^\circ\text{C}$, while the maximum value of the average temperature in a large area is $127 \text{ }^\circ\text{C}$. The gradient of temperature between Al NP and THV indicates that the heat transfer from Al NP to THV in nanoscale.

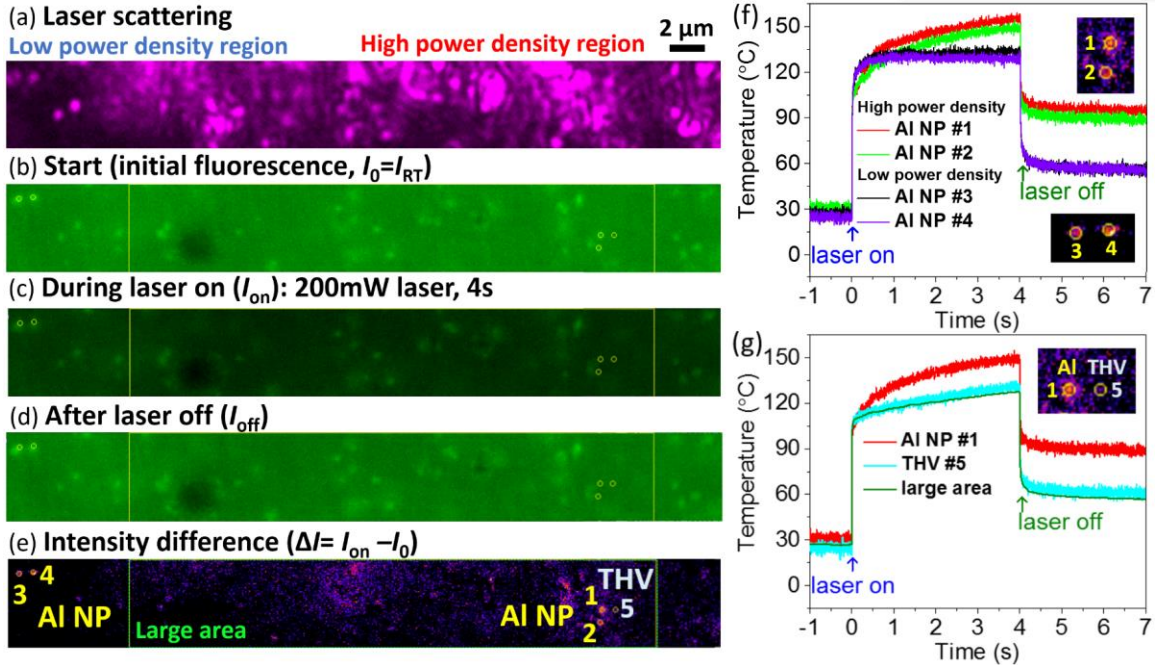


Figure 6-9 *In-situ* fluorescence and temperature monitoring for Al/THV/R6G films on gratings with exposure to 200 mW 808 nm laser for 4 s: (a) Laser scattering to show the laser power intensity distribution; (b) Start (initial fluorescence, $I_0=I_{RT}$); (c) During laser on (I_{on}): the frame shown is right at 4 s radiation before laser off; (d) After laser off (I_{off}): after exposure to 808 nm laser for 4 s; (d) Intensity difference ($=$ initial fluorescence – fluorescence during laser on, i.e. $\Delta I= I_{on} - I_0$). All images are false-color images, taken by 40 \times air objective in the epi-fluorescence microscope. The circles point out the Al NPs and THV, and the rectangle points out the large area with laser heating. Temperature monitoring over time: (f) Comparison among Al NPs in the high and low power density regions; (g) Comparison among Al NP, THV and a large area in the high power density region.

6.4.6 Movement of Al NPs

At high laser power (200mW), the local temperatures approach and exceed the THV melting temperature, resulting in THV softening and melting. Consequently, at high temperatures, the movement of Al NPs is observed. As shown in **Figure 6-10**, the Al NPs located in the high power density region exhibit clear movement during irradiation. As monitoring the *in-situ* movement of Al NPs, some Al NPs disappeared or appeared in the focused optical plane. For example, Al NPs (#1) shows the presence of several Al NPs at 20 ms, and then they became one intense Al NP at 0.44 s and disappeared at 0.88 s, and later appeared again at 1.13 s. Similarly, Al NPs (#2) shows the active local movement of Al NP due to the localized melting of THV. However, in the low power density regions, the position of Al NPs (#3) almost did not change, indicating that THV melting did not occur.

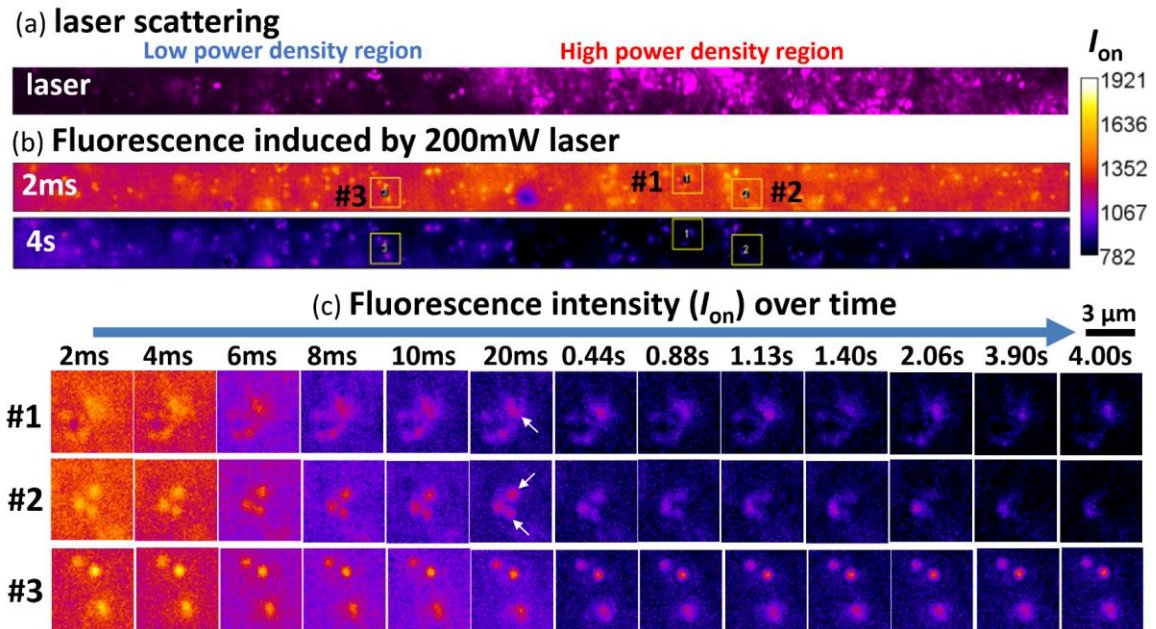


Figure 6-10 Al NPs *in-situ* movement monitored by fluorescence images of Al/THV/R6G

films on gratings with exposure to 200 mW 808 nm laser for 4 s. (a) Laser scattering to show the laser power intensity distribution; (b) fluorescence induced by the laser; (c) fluorescence intensity change over time. All images are false-color images, taken by 40 \times air objective in the epi-fluorescence microscope.

In order to statistically analyze and figure out the law of Al NP movement, the *ex-situ* fluorescence and bright field images with a larger field of view at different states were investigated. The bright field images can assist the visualization of Al NPs in addition to the fluorescence because their intensities were almost not affected by the temperature and the difference of dye coating inside the Al aggregates. **Figure 6-11a** shows the movement patterns of a few representative Al NPs located at different positions along the laser beam before and after 200 mW laser irradiation. All Al aggregates show similar movement direction outward from the laser center, probably due in part to the thermal expansion and softening of THV induced by laser heating. For example, Al aggregates labeled as (#2) move 182 nm and 273 nm away from the original positions, Al aggregates (#5) and Al aggregates (#4) move 546 nm and 728 nm away, respectively. The thermal expansion of THV can be compared with the Al NPs movement. The linear thermal expansion coefficient of fluoroplastics is in the range of $4\sim 15\times 10^{-5}/^{\circ}\text{C}$, so $15\times 10^{-5}/^{\circ}\text{C}$ is taken as the thermal expansion coefficient of THV. Assuming the temperature is heated up to the melting point of THV (120°C) from room temperature (27°C), it requires heating lengths of 13 μm , 20 μm , 40 μm , and 52 μm to achieve thermal expansion of 182 nm, 273 nm, 546 nm and 728 nm. This distance matches well with the location of the particles to the center of the laser beam.

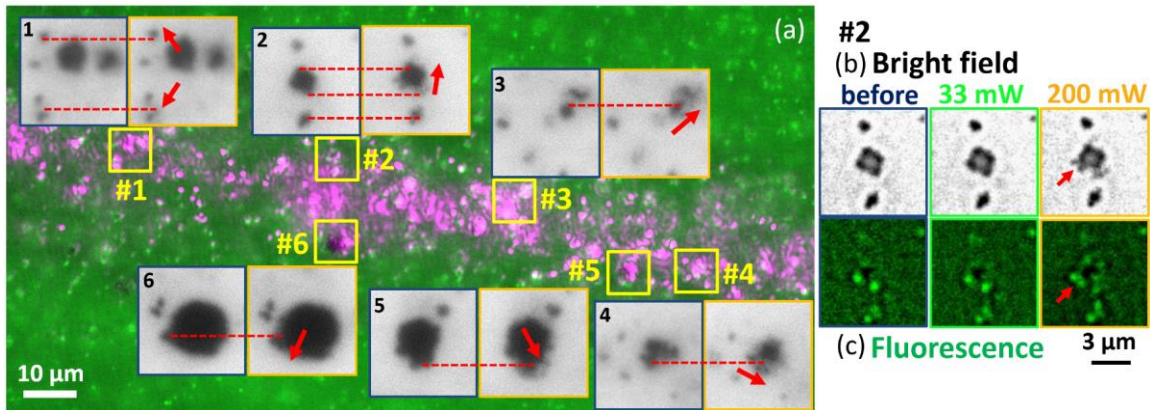


Figure 6-11 Al NPs *ex-situ* movement monitored by bright field and fluorescence images of Al/THV/R6G films on gratings after exposure to 200 mW 808 nm laser for 4 s. (a) Bright field images (gray color) before and after 200 mW laser irradiation to show the movement direction for Al NPs at different locations indicated by red arrows. The image at the back superimposes fluorescence (green) after 200 mW laser irradiation and laser spot (magenta). The yellow rectangular boxes mark down important interesting areas (#1-#6). (b-c) Comparison between the bright field (gray color) and fluorescence image (green color) before laser heating, and after exposure to 33 mW and 200 mW lasers for 4 s for the data of #2 Al aggregates. Deconvolution imaging processing was applied to increase the contrast of the image. The scale bar for b-c is 5 μm . All images are false-color images, taken by 40 \times air objective in the epi-fluorescence microscope. All bright field and fluorescence images before, after exposure to 33 mW and 200 mW lasers were outlined by dark blue, green, and orange, respectively.

It is noted that the movement of Al NPs can only be observed after high-laser power (200 mW). After exposure to low laser power of 33 mW for 4 s, both fluorescence and bright field images almost did not change (**Figure 6-11b** and **Figure 6-13** for #1-6), due to

the average rising temperature up to only 42 °C in the central laser region (**Figure 6-11c**). However, some Al NPs appear to be separating from Al aggregates after 200 mW laser irradiation. Al aggregates (#2) were attached perhaps due to weak van der Waals interactions before exposure to high-power laser, and then several small Al NPs break apart from the large aggregates due to the laser heating and softening/melting of THV. Another evidence of the morphology change of THV is that the fluorescence intensity around the perimeter of the irradiation zone increases after 200 mW laser heating as shown in **Figure 6-1d** and **Figure 6-12**, indicating an accumulation of R6G due to THV softening and particle migration during heating.

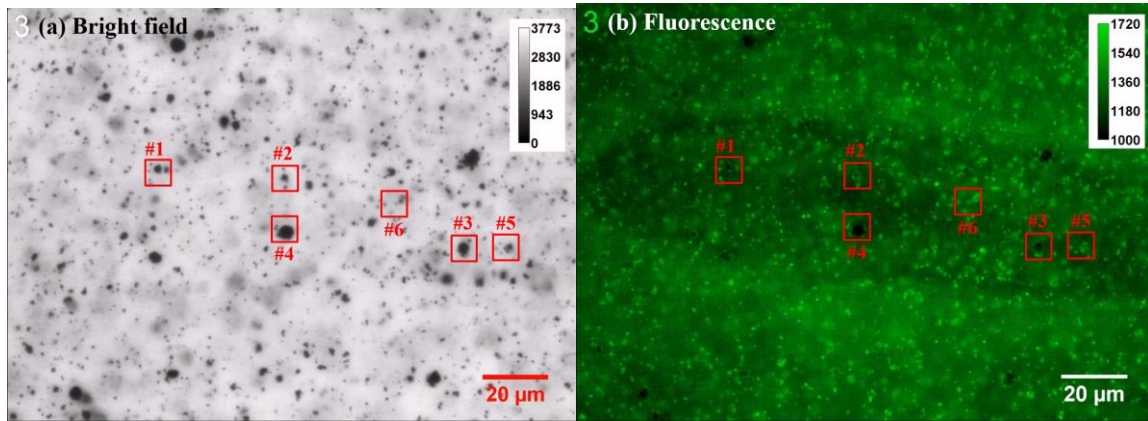


Figure 6-12 Comparison between (a) bright field and (b) fluorescence image for Al/THV/R6G films on gratings after exposure to 808 nm laser heating (200 mW, 20° incidence with respect to the horizontal line) for 4 s. All images are false-color images, taken by 40× air objective in the epi-fluorescence microscope. The scale bar is 20 μm. The red rectangular boxes mark down important interesting areas for further analysis.

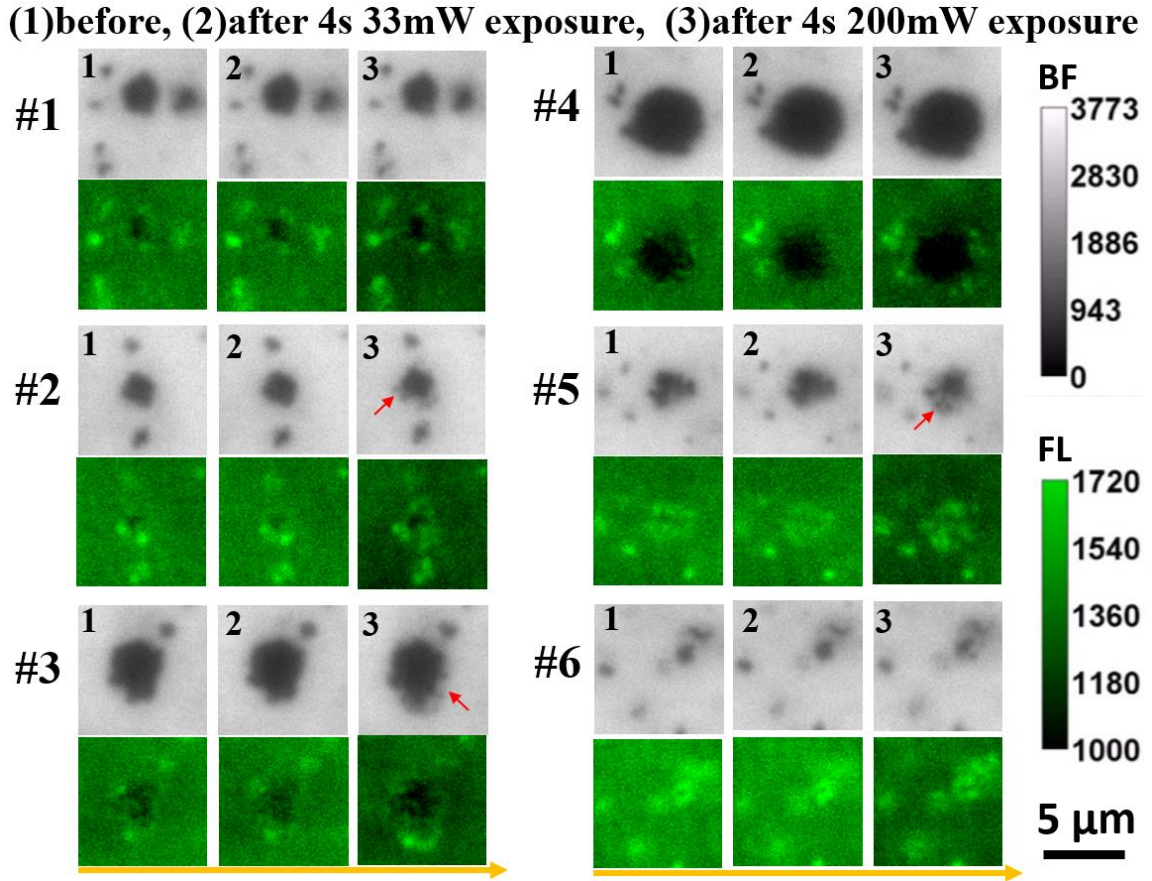


Figure 6-13 Comparison between bright field (gray color) and fluorescence image (green color) for Al/THV/R6G films on gratings (1) before laser heating, and after exposure to 808 nm laser heating (20° incidence with respect to horizontal line) for 4 s with different powers (2) 33 mW and (3) 200 mW. All images are false-color images, taken by $40\times$ air objective in the epi-fluorescence microscope. The scale bar is $5\ \mu\text{m}$. The interesting areas #1-6 in this analysis are marked as the red rectangular boxes in **Figure 6-12**.

6.4.7 Simulation for electric field enhancement and temperature change

The electric field (E-field) enhancement and distribution of Al NPs on plasmonic gratings were simulated by a finite-difference time-domain (FDTD) method using the

FullWAVE software. An 80 nm Al NP embedded in THV was located above the groove of silver gratings and a plain glass substrate as a control, under irradiation of 808 nm laser.

Figure 6-14a-b shows that the E-field strength ($E_z/E_{z,0}$) in the Al/THV film on the grating is higher than that on the glass, and especially, the E-field around Al NP is significantly enhanced by the plasmonic gratings. The light intensity enhancement of Al NP on the grating is $|E_{grating}/E_{glass}|^2 = 10$ times greater than that on a glass substrate. This E-field enhancement results in the enhancement of both fluorescence and photothermal heating of Al NPs as discussed above.

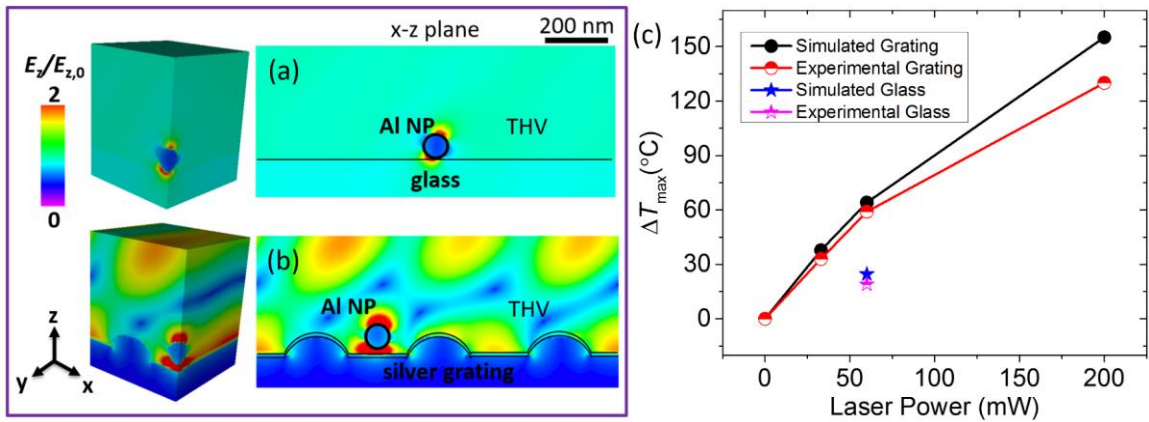


Figure 6-14 (a-b) FDTD simulated E-field distribution of 80 nm Al NP on different substrates: (a) plain glass (b) silver gratings under laser wavelengths of 808 nm in THV matrix. The relative z-component of E-field ($E_z/E_{z,0}$) scale is normalized to 0~2. Each condition shows a 3D view of E-field distribution (left) and the corresponding 2D view of the x-z plane (right). The scale bar in x-z plane is 200 nm. The incident angle is calculated based on Snell's law, 70° incident from the air ($n=1$) corresponds to 43.7° in THV ($n=1.36$). (c) Comparison of the maximum temperature change (ΔT_{max}) vs. laser power between the

COMSOL simulated value and experimental value on the plasmonic silver grating and the glass substrate.

The temperature response of Al NPs embedded in THV was numerical simulated using COMSOL Multiphysics package utilizing both heat transfer modulus for the phase change and RF modulus for EM simulation. Heating was implemented using the FDTD electric field data as an input. An isolated 80 nm Al NP was simulated as occupying a THV volume consistent with the inverse of the Al NP number density (716 nm in width, length, and height). The domains along the x-coordinate faces were periodic, as identical unit cells were assumed to reside to the left and right of the particle in the simulated domain. The top z-coordinate face was insulated for a similar reason. The domain boundaries in the y-coordinate were mated with an additional 10 μm of THV to simulate semi-infinite boundaries through which diffusive conduction may occur. The simulated time was 100 ms, with power inputs of 33, 60 and 200 mW. Temperature increase was nearly linearly for laser powers less than 60 mW and then the rate of temperature increase is diminished (**Figure 6-14**). Note that the particle temperature in simulation and experiment exceed the melting temperature of THV, and particle temperature is expected to be a strong function of particle physical arrangement, as significant energy is absorbed during the phase change process. Note that the simulation results are in excellent agreement with the experimental measurements, indicating that the simplifications and assumptions used in the model are appropriate. The photothermal heating of an Al/THV composite on a glass substrate was also simulated with FDTD and COMSOL and compared to experimental measurements. Here too, simulation and experiment are in excellent agreement.

6.5 Effect of Laser Wavelengths on Heating (Blue vs IR Laser)

As we already studied the laser heating on THV/R6G (1 μM)/Al films on grating by 808 nm IR laser matching the dielectric loss peak, we would like to study the effect of 446 nm blue laser located at the plasmonic peak of the Al NP, as well as, enhanced coupling with the plasmonic grating compared to the 808 nm IR laser. In order to investigate the effect close to the grating without averaging from a thick film, thinner THV/R6G (10 μM dye concentration) films of 500 nm with and without Al NP (0.1wt% Al to THV) were prepared by spin-coating on gratings (100 nm Ag HDDVD gratings by sputtering) and glass. The R6G concentration was increased from 1 μM for the thick film to 10 μM for a thin film to ensure enhanced fluorescence intensity and shorter exposure time for fluorescence measurement.

For the *in-situ* measurement of 446 nm blue laser heating, the Al/THV/R6G films on gratings were imaged with an Olympus BX51WI epifluorescence microscope equipped an ORCAflash 2.8 CMOS camera (excitation (475 nm \pm 15 nm) and emission (518 nm \pm 10 nm) band-pass filters), 40 \times air objective with 2.5 \times adaptor (with pixel size of 36 nm). The exposure time is 0.5 ms (due to strong blue laser illumination), and the frame rate for laser exposure was 500 fps (2 ms, limited by the CMOS sub-array). The blue laser acts as both excitation and heat source, so the fluorescence distribution at the beginning can indicate the laser power distribution. As the laser exposure continues on, the fluorescence intensity reduces due to heating and photobleaching of dyes. For the blue laser heating, we should consider the facts that (1) the heat is generated by the absorption from both Al NP and R6G, and (2) the irreversible fluorescence intensity reduction is due to photobleaching or the decomposition of the dyes. As we can see, even without Al NP, the fluorescence

reduction is very severe, indicating the photobleaching and photodecomposition of R6G dye are dominant when exposed to the blue laser. So the R6G dye is not a very good temperature indicator for the laser wavelengths located in the excitation spectra of the dye. In future, we plan to use inorganic molecular crystals with high temperature and photobleaching stability.

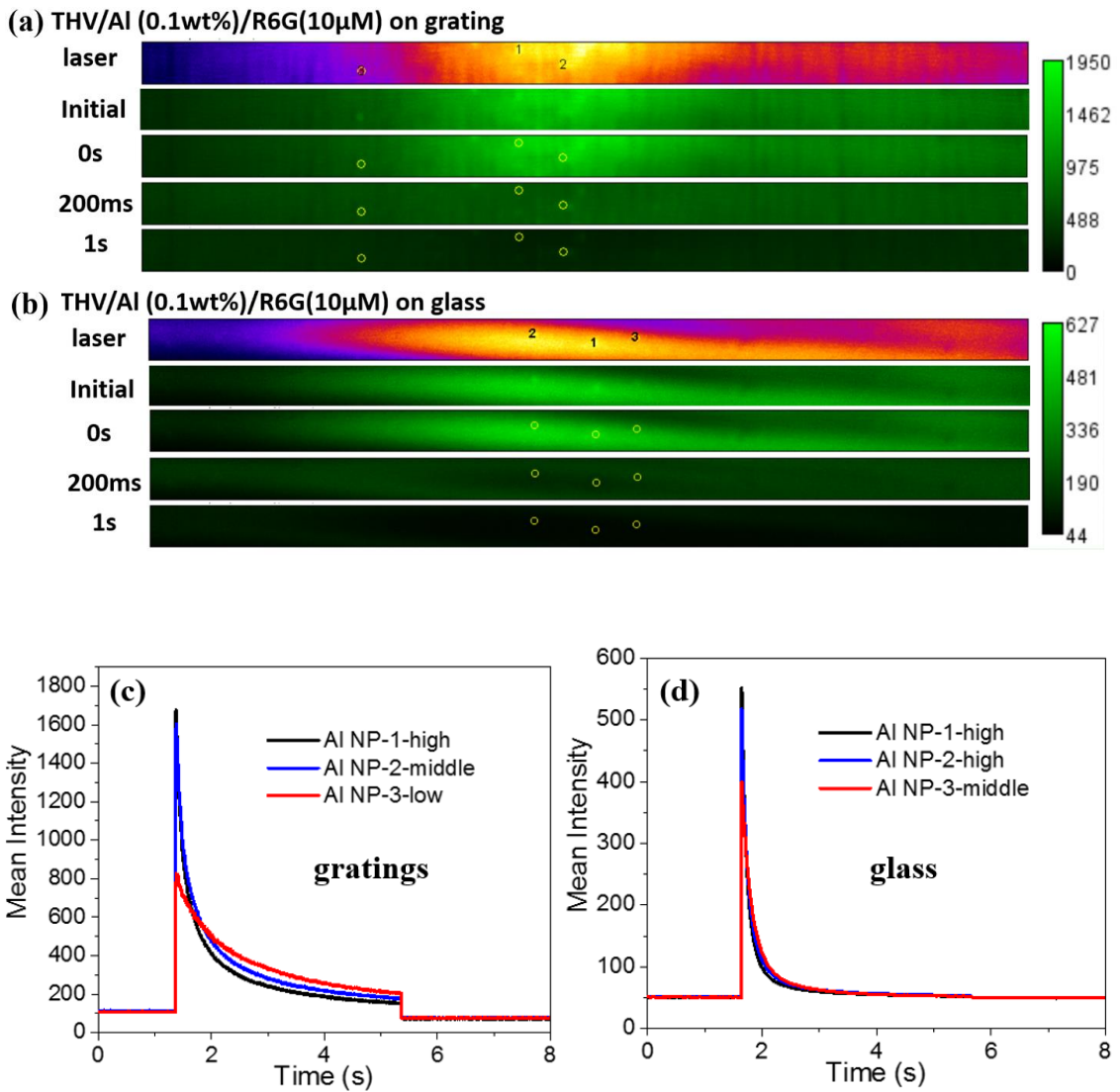
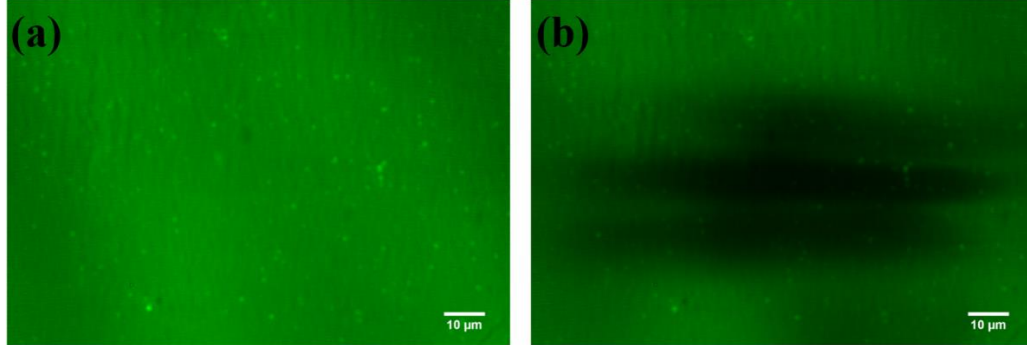


Figure 6-15 *In-situ* measurement of 446 nm blue laser heating of the Al/THV/R6G films on (a,c) gratings and (b,d) glass. All data were taken by 40 \times air objective with the 2.5 \times

adaptor in epi-fluorescence microscope.

THV/Al (0.1wt%)/R6G(10 μ M) on grating



THV/R6G(10 μ M) on grating

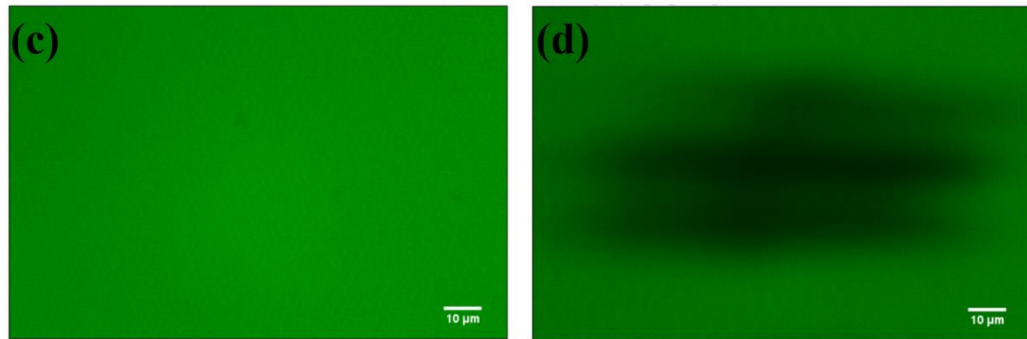


Figure 6-16 Fluorescence of the THV/R6G films (a,b) with and (c,d) without Al NPs on gratings (a,c) before and (b,d) after blue laser heating. All data were taken by 20 \times air objective with the 2.5 \times adaptor in the epi-fluorescence microscope.

6.6 Conclusion

A plasmonic grating platform was developed to enhance a fluorescence-based temperature sensor for *in-situ* mapping temperature in nanoscale for Al/THV nanoenergetic films. Both excitation and emission spectra of the temperature-dependent dye (R6G) were completely reversible and repeatable at heating and cooling cycle from 30 $^{\circ}$ C to 65 $^{\circ}$ C tested in a microplate reader. A linear calibration curve between temperature

and fluorescence intensity was established from room temperature to 80 °C in an epi-fluorescence microscope. Al NPs are vital in laser photothermal heating due to the intraband absorption at 808 nm. The reconstructed *in-situ* spatial temperature responses indicate that Al/THV/R6G on plasmonic grating exhibits highest fluorescence, greatest temperature change and fastest heating among all testing conditions. Taking the advantages of the enhanced electric field, the combination of Al NPs and plasmonic grating platforms significantly enhance the fluorescence intensity and photothermal effect on the nanoenergetic systems when compared with the glass substrate, which was proved by experiment and FDTD and COMSOL simulation. The *in-situ* and *ex-situ* movements of Al NPs only occur under high power laser (200 mW) instead of low power laser (33 mW), which should be ascribed to the thermal expansion or melting of THV. This study provides a novel methodology by introducing plasmonic gratings to enhance the spatial and temporal sensitivity of a temperature sensor, and simultaneously improve the photothermal heating of nanoenergetics. This idea can be extended to the application with high-temperature molecular dyes, which should be very promising to reconstruct the *in-situ* response for the study of the combustion evolution of nanoenergetics.

6.7 Future Work

We will optimize the fluorescence-temperature dependency system to work at high temperature by calculating the actual fluorescence reference due to the decomposition of dyes so that we can obtain accurate temperature response at high temperature. Moreover, we will extend the fluorescence-temperature calibration into other nanoenergetic systems with other oxidizers, such as nitrocellulose and Teflon. We will study the thermal behavior

and dynamic mechanism induced by laser heating on the nanoenergetic systems. Finally, we will develop the temperature dependence of the plasmon absorption and scattering due to photothermal effect in high-temperature regimes (>250 °C). We will also use nanoscale pyrometry to study local temperatures of the flame generated from nano and micro scale combustion processes in nanoenergetic Al/polymer systems.

Chapter 7. *In-Situ* Characterization of Photothermal Nanoenergetic Combustion on a Plasmonic Microchip

7.1 Abstract

Plasmonic gratings facilitate a robust *in-situ* diagnostic platform for photothermal combustion of nanoenergetic composite thin films using an optical microscope and high-speed camera. Aluminum nanoparticles (Al NPs) embedded in THV fluoropolymer oxidizer are cast onto a plasmonic grating microchip and ignited using a low-power laser. The plasmonic grating enhances both spatial resolution and sufficient photothermal coupling to combust small Al NP clusters, initiating localized flames as small as 600 nm in size. Two-color pyrometry obtained from a fast color camera indicates an average flame temperature of 3,900K. Scattering measurements using polarized light microscopy enabled precise identification of individual Al NPs over a large field of view, leading to 3D reconstruction of combustion events.

7.2 Introduction

As we already studied the laser heating of Al NPs in **Chapter 6**, we investigated the *in-situ* imaging of laser ignition of Al/THV nanothermites in this section. Since organic fluorescent dye R6G is not suitable as a high-temperature sensor, instead, we obtained scattering images of Al NPs before and after the laser ignition to assist us with the analysis of the chemical reaction of Al NPS with THV. Plasmonic structures couple incident electromagnetic irradiation to the resonant oscillation of free electrons in metals, known as SPR. [1]–[3] The plasmonic photothermal heating effect of Al NPs represents an

unexplored opportunity for light-induced nanoenergetic heating and combustion. When Al NPs are exposed to laser pulses within the wavelengths of surface plasmon resonances, electrons are excited and subsequently relax to ground states with effective electron-phonon conversion to generate volumetric heating[125], [139], [140].

Here we report a new *in-situ* characterization platform to study photothermal ignition of nanoenergetic materials (**Figure 7-1a**). The system utilizes conventional optical microscopy with plasmonic grating microchips to significantly enhance the electric field on the surface of gratings when satisfying the wave vector matching condition[4], [9], [12], which is utilized to enhance the photothermal heating of Al NPs on the plasmonic microchip. Moreover, it can serve as a super-resolution imaging platform to visualize nanostructures[9], which enables imaging localized heating and combustion of individual Al NPs at the nanoscale. Our previous study shows that the plasmonic grating platform can achieve 60 nm spatial resolution when combining with localization microscopy for fluorescence super-resolution imaging.[9] The setup facilitates sub-wavelength resolution while allowing an observation field width of up to hundreds of microns. Images can be obtained at a rate up to 222,222 frames per second (fps) by a fast speed camera for high temporal resolution of reactions. Further, concurrent dual-wavelength pyrometry is readily supported to provide combustion flame temperature.

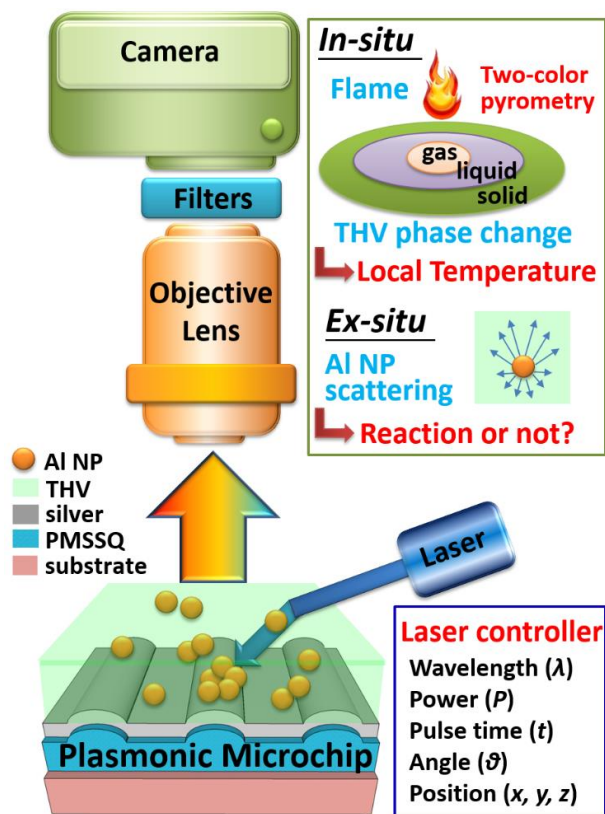


Figure 7-1 A schematic of the *in situ* analysis platform to study nanoenergetic thin film morphology and combustion. The system consists of a plasmonic grating microchip, microscope objective, fast camera, and external laser.

7.3 Materials and Methods

7.3.1 Plasmonic Grating Fabrication

The fabrication of plasmonic microchips was based on nano-imprint lithography using commercially available HDDVDs as a master mold.[4], [9], [15]–[17] Briefly, polymethylsilsesquioxane (PMSSQ) gratings were fabricated by a microcontact stamping process, followed by a vapor treatment of a crosslinker, 3-aminopropyltriethoxysilane (APTES). A 5 nm Germanium adhesion layer and 100 nm silver layer was deposited on

the PMSSQ grating by RF sputtering. Finally, a 10 nm alumina capping layer was deposited to the exposed silver by atomic layer deposition (ALD). The pitch between grating ridges is 400 nm, while the height of grating ridges is approximately 60 nm.

7.3.2 Preparation of Al/THV Nanoenergetic Films

Nanoenergetic composite thin films consisted of 80 nm Al NPs fuel and THV 220A fluoropolymer oxidizer. Al NPs (80 nm Avg. dia., 80 % active Al, 2.2 nm alumina (Al₂O₃) passivation shell, specific surface area of 25 m²/gm) were purchased and used as received from Novacentrix (Austin, TX, USA). THV 220A is a fluoropolymer purchased from 3M Company (St. Paul, MN, USA). THV is a terpolymer composed of tetrafluoroethylene (TFE), hexafluoropropylene (HFP), and vinylidene fluoride (VDF), with a very high fluorine content of 70.5%. The 80 nm Al NPs were dispersed in acetone by sonication for 4 hours, and THV was dissolved in acetone by sonication for 3 hours. The well-dispersed Al NPs were mixed with the dissolved THV solution by vortex mixing for 15min and sonication for 2 hours to form an Al (0.05 mg/ml) / THV (50 mg/ml) solution. Subsequently, a 10 μm thick Al/THV films were drop-cast on silver grating microchips and flat silver substrates. The Al NP density in the THV films was sufficiently low (0.1wt%) to mitigate NP aggregation and photon absorption and scattering from Al NPs. The films were prepared in a saturated acetone vapor environment to decrease the rate of solvent evaporation resulting in smooth and transparent films.

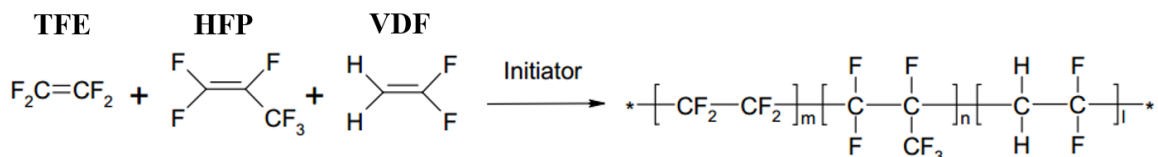


Figure 7-2 The preparation of THV, namely, poly(TFE-co-HFP-co-VDF).

Aluminum is capable of supporting surface plasmons in the visible and UV region depending on the geometry and size of Al nanostructures.[140]–[143] The Al NPs have a 2.2 nm self-terminated oxide layer, and they were stored in an inert environment (glove box) after purchase to prevent further oxidation before use. After mixing with THV, Al NPs were embedded in solid fluoropolymer THV, so the oxygen in the environment was hard to diffuse into Al NPs. The energetic films were very stable in ambient atmosphere, which can still be ignited even after half a year.

7.3.3 Characterization

Simultaneous differential scanning calorimetry and thermogravimetric analysis (DSC/TGA) (TA Instruments Q600) was carried out to study the thermal properties and combustion behavior. The heating rate was 5 °C/min under an argon environment. The number of Al NPs on grating microchips was identified by scanning electron microscopy (SEM) using Hitachi S-4700 Field Emission scanning electron microscope.

7.3.4 Laser Control

The laser control setup includes 1) laser; 2) focus lens; 3) goniometer to control the incident angle; 4) micro-positioner to align a laser to focus a point on a sample; 5) laser driver to change the laser power. The projected area of 8992 μm^2 was produced on the sample at a 70 ° incident angle. The nominal diameter of the laser is 11 μm . The laser duty cycle consisted of 1 ms irradiation followed by a 30 ms rest period to provide thermal cycling. Each test consisted of 20 pulses.

7.4 Results and Discussion

The diagnostic metrology, shown schematically in **Figure 7-1** (a), incorporates a plasmonic grating microchip to enhance the photothermal heating and *in-situ* imaging capability of conventional epi-fluorescence microscopy. During the laser exposure, the sample response was continuously monitored using a high-speed color camera calibrated to provide two-color pyrometry temperature data during combustion. Optical scattering images of Al NPs before and after the laser ignition obtained by polarized light microscopy provided the number of Al NPs and potential agglomeration morphology. DSC/TGA provided the phase transition and a reaction temperature of Al/THV nanothermite to provide insight into possible reaction pathways.

7.4.1 Imaging Methodologies

Sample imaging was performed in two modes including bright field imaging during *in-situ* observation and polarized scattering imaging performed before and after combustion. A schematic of these optical imaging setups is depicted in **Figure 7-3**. An Olympus BX51WI epi-fluorescence microscope enables laser illumination from the top side of the grating to obtain highest E-field enhancement. For *in-situ* testing, a Phantom v7.3 digital high-speed camera (Vision Research) was set to 512×128 pixel resolution to obtain both a large field of view (113 μm×28 μm) and frame rate of 20,000 fps (50 μs resolution). Imaging was obtained using a 40× air objective, with a modified FITC filter set (517 nm long-pass emission filter and 502 nm dichromic mirror without any excitation band-pass filter) and an exposure time of 48 μs. Because the FITC long-pass filter blocked the laser illumination wavelength, image capturing was performed in bright field reflection

mode (**Figure 7-3a**) with background lighting. Al NPs appeared as black spots due to absorption and THV appears as green due to the reflection of the filtered light (**Figure 7-3d**).

Polarized light microscopy in scattering mode was used to obtain a detailed 3-dimensional profile of Al NPs within the thin film before and after reactions (**Figure 7-3g**). These analyses used a $100\times$ oil-immersive objective (NA=1.49) for enhanced details. Because the scattering cross section of the Al NPs is greatly amplified relative to the native NP cross section, scattering analysis provides a means to resolve individual NPs. To illustrate the imaging resolution of the grating system, **Figure 7-3h-j** shows an example of a single 80 nm diameter Al NP imaged using SEM, optical scattering, and optical bright field on plasmonic gratings taken by ORCA flash 2.8 CMOS camera. Comparison of images clearly demonstrates the resolution ability of the grating-enabled platform to distinguish individual NPs.

Laser irradiation was enabled by a programmable controller that facilitated variation in power (P), pulse time (t), angle (θ), and position (x, y, z) of the laser, as listed in **Figure 7-1a**. A 446 nm laser (single 5.6mm Osram PLTB450B 1.6W 450nm LD Diode) served as an irradiation source and was programmed to have a pulse duration of 1 ms. The incident angle required to couple with the grating was 70° relative to the substrate normal, resulting in a beam profile of $11\ \mu\text{m}$ (width) \times $89\ \mu\text{m}$ (length) on the substrate. The incident laser was p-polarized to couple to the plasmonic grating microchip. **Figure 7-3b** shows the profile of laser beam directly measured by CMOS for calculation of fluence distribution. **Figure 7-3e** shows the superimposed image of laser and bright field to match laser location and Al NPs. The grating lines with 400 nm in pitch and 200 nm in width are readily

observed under 40 \times objective (**Figure 7-3f**).

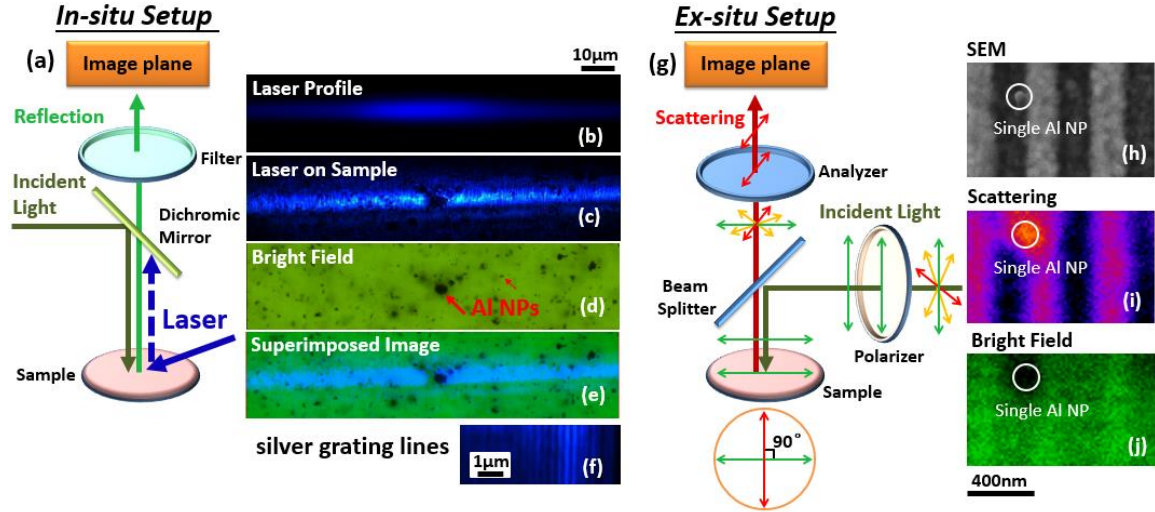


Figure 7-3 A schematic of the imaging setup for *in-situ* and *ex-situ* imaging. (a) *In-situ* imaging setup using the bright field in reflection mode with background light, and with a long-pass filter to block the laser. (b) Profile of laser beam directly measured by CMOS at an incident angle of 70°, (c) laser scattering from the sample after aligning and focusing on the Al NPs of interest, (d) bright field image of Al/THV film on plasmonic grating, (e) superimposed image of laser and bright field to match laser location and Al NPs, (f) the grating lines imaged under 40 \times objective by blue laser. All images were taken by the fast color camera. (g) *Ex-situ* imaging setup using polarization microscopy for scattering imaging by blocking the incident light with a combination of polarizer and analyzer. Images of single Al NP on a plasmonic grating microchip: (h) SEM, (i) scattering, (j) bright field. The scattering and bright field images were taken under 100 \times oil-immersive objective by the black and white camera; both images were false color images.

7.4.2 Photothermal Heating Experiments

Laser heating was provided at powers ranging from 200 mW to 1500 mW (corresponding to a peak energy flux of 0.25 – 1.88 mW/ μm^2) and was supplied to the sample via 20 consecutive pulses, each with a 1ms duration and 30 ms rest between pulses. To reiterate, the laser excitation wavelength of 446 nm was selected because it both resides within the broad plasmon peak of 80 nm diameter Al NPs and because it simultaneously couples to the lower resonance mode of plasmonic gratings. During laser irradiation, the energetic film response was recorded by the fast camera with 50 μs resolution (i.e. at a frame rate of 20,000 frames per second). The film response to photothermal heating ranged from no observable change, to localized Al NP motion, to localized Al NP ignition.

Figure 7-4a summarizes the characteristic responses of photothermally heated Al/THV films for both silver grating microchip and flat silver substrates as a function of laser heating power and flux. Data represented in the graphic were obtained by positioning a 3 μm diameter Al NP agglomeration in the region of highest laser fluence. The Al NP motion observed during irradiation (**Figure 7-4b**) is likely due to the softening and local melting of THV due to Al NP heating, while a lack of motion indicates that the particle temperature remained below the melting temperature of THV. As an illustrative example, slight Al NP motion is observed on the silver grating microchip at 200 mW, as denoted by red ovals in **Figure 7-4b**. A similar Al NP cluster residing on a flat silver substrate (**Figure 7-4d**) exhibits no motion at the same power, indicating less efficient photothermal heating. Increasing the laser power to 255 mW (0.29 mW/ μm^2) is sufficient to ignite the Al NP agglomerate (previously observed in **Figure 7-4b**) during the first 50 μs of the first pulse (**Figure 7-4c**). The combustion event is clearly visible in the form of micron-size orange

and red flames. On the flat silver substrate, 510 mW ($0.64 \text{ mW}/\mu\text{m}^2$) is the minimum power required to ignite the agglomerate first shown in **Figure 7-4d**. This combustion event is shown in **Figure 7-4e**. The 2-fold reduction in ignition power threshold when using the silver grating matches well with the simulated light intensity enhancement of 1.8, as will be discussed later. It is also noteworthy that the Al aggregates located at $10 \mu\text{m}$ above the grating surface were not ignited at 510 mW, indicating that coupling was confined near the grating surface, as expected.

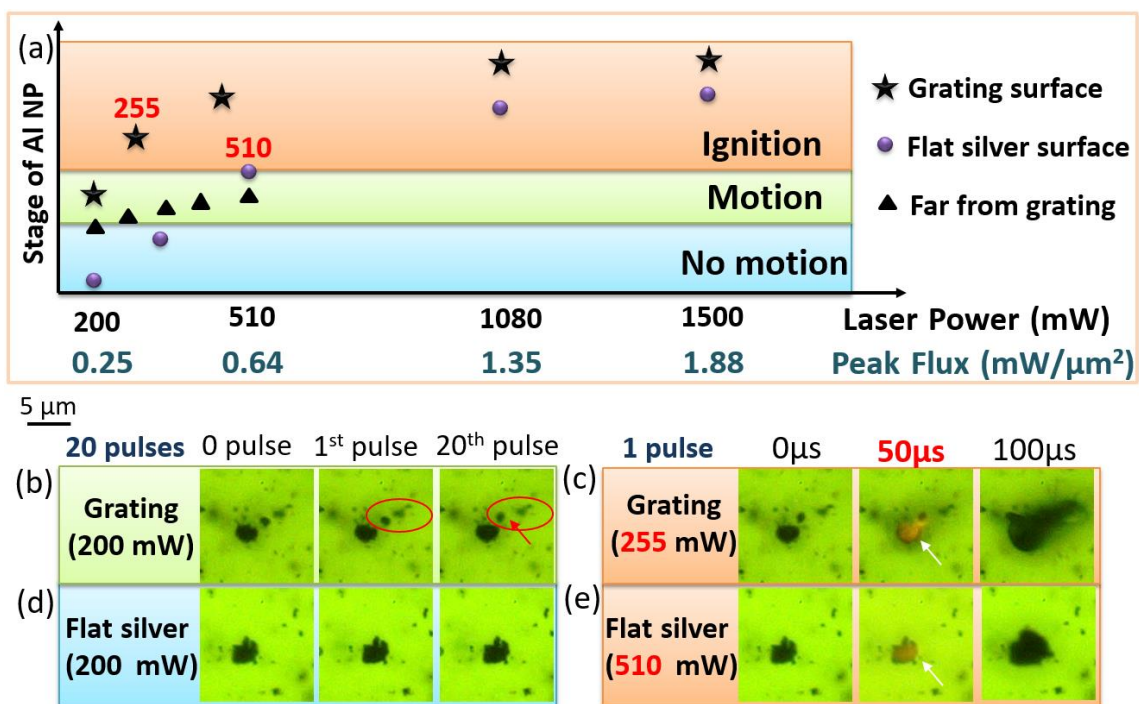


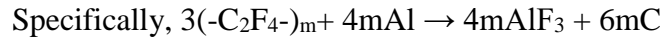
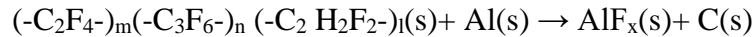
Figure 7-4 (a) Summary of the relationship between power (and peak energy flux) and phenomena for both silver grating microchip and flat silver platform. Comparison between (b-c) silver gratings and (d-e) flat silver for laser ignition. All data were taken by a fast camera in an epi-fluorescence microscope equipped with a $40\times$ air objective with the $2.5\times$ adaptor under modified FITC filter.

The energetic properties of neat THV and THV with embedded Al NPs were

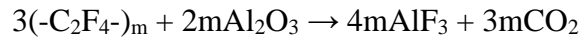
studied using DSC/TGA in flowing Ar. As shown in **Figure 7-5a**, the melting temperature of THV produced an endothermic peak at 120.5 °C. Furthermore, a 100% weight loss indicated the complete decomposition of THV into gaseous products, with an onset decomposition temperature at 463 °C and an endothermic peak at 508 °C indicating complete decomposition. The decomposition products of THV are similar to those of Teflon (PTFE) due to similar chemical structures, including tetrafluoroethylene (C₂F₄), hexafluoroethane (C₂F₆), carbonyl fluoride (CF₂O). These products remain gaseous phase even after cooling down to room temperature after the THV decomposition or Al-THV reaction.

Reactions between Al NP fuel and THV oxidizer, including fluorination of the Al core and the Al₂O₃ shell may occur by the following reactions.

The reaction between THV and Al:



The reaction between THV and Al₂O₃:



DSC/TGA (**Figure 7-5b**) analysis of a 30 wt % Al NP loading in THV was performed, consistent with a previous study[61]. The onset temperature of the exothermic Al-THV reaction, shown in **Figure 7-5b**, was 476 °C, This temperature exceeds the decomposition temperature of THV, indicating that THV first decomposed into gaseous products before reacting with Al NPs. Gas phase THV products diffuse much more rapidly than solid or liquid THV, which may explain why the onset reaction temperature of Al-THV is only slightly greater than the onset decomposition temperature of THV (463 °C).

The products of the fluorination reaction between THV and Al are aluminum fluoride (AlF_3) and carbon. The peak of the exothermic reaction of Al/THV occurred at 534 °C while the decomposition of neat THV was complete at 525 °C. The total heat of reaction for the Al/THV composite was 1,302 J/g. The small endothermic peak observed at 663 °C corresponds to the melting of unreacted Al. The small amplitude of the melting peak indicates that most Al had reacted prior to melting. Although the DSC/TGA measurements are obtained during a slow heating process (5 °C/min), the data provides an insight into possible reaction pathways, phase-change temperatures, reaction temperatures, and heat of reaction for the Al/THV system during rapid laser heating.

Figure 7-5 indicates that Al NP ignition occurred within the first 50 μs of laser irradiation. Assuming a reaction onset temperature of 476 °C obtained from DSC/TGA analysis, then an Al NP heating rate of 10^7 °C/s may be estimated. Localized melting of the surrounding THV matrix is first observed as a concentric ring at 50 μs which then expands with time. Although obstructed by the large combustion flame, we hypothesize that gaseous THV products are also present in the immediate vicinity of the Al NP. These fluorinated species likely assist in reacting and removing the alumina shell of surrounding NPs.

The Al NP heating rate is an important parameter in ignition mechanisms. The leading combustion initiation theories for Al NP fast heating include: (1) perforation of the oxide shell, observed by multimillion atom simulations for flash-heated Al/ Al_2O_3 core-shell nanoparticles at temperatures exceeding 3,000K [77]–[79]; (2) mechanically-induced spallation of core-shell nanoparticles, known as the melt dispersion mechanism (MDM), requiring heating rates in excess of 10^6 K/s [80]–[82]; (3) rapid melting of the

Al₂O₃ shell during laser flash-heating[83]; (4) the fluorination of Al₂O₃ shell to expose the Al core, an effect that is only significant in nanoscale Al fuel particles[84]. Based on our observations, we suggest that either the MDM or fluorination of the Al₂O₃ shell is responsible for the rapid ignition depicted in **Figure 7-5**, as the temperature range required for the other mechanisms exceeds those likely observed for our system. The relatively large flame size produced during combustion relative to the original Al NPs observed in **Figure 7-4c**, in particular, seems to indicate a rapid expulsion of reactive Al content from the protective alumina shell, potentially pointing to the MDM mechanism for this reaction.

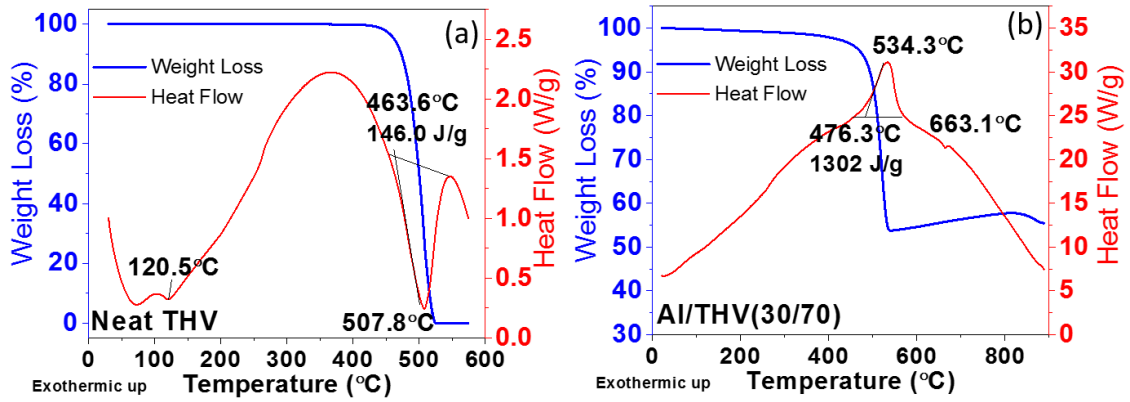


Figure 7-5 DSC/TGA measurement for (a) THV and (b) Al/THV(30/70) composites.

7.4.3 Time-evolving Combustion Behavior

Figure 7-6 depicts time sequences of the first 400 ms of laser irradiation for films supported on silver-coated gratings at various irradiation powers. A threshold ignition power of 255 mW (0.32 mW/ μm^2) was required to ignite large (3 μm) Al NP aggregates on plasmonic gratings, but this relatively low power is insufficient to ignite individual Al NPs or small sub-micron clusters. Figure 5a shows localized combustion on the 3 μm NP agglomerate at 50 μs , followed by the appearance of an elongated black zone near the

combustion event at 100 μs , indicative of carbonaceous combustion byproducts.

THV melting ($T_m = 120\text{ }^\circ\text{C}$), observed as a dark ring, is present near the combustion site at 50 μs and grows throughout the irradiation period. This ring is not associated with shock propagation, as the speed of a shock wave would be orders of magnitude faster than the propagation of the ring. Assuming a shock wave speed of 1,000 m/s, the shock wave would have propagated 5 cm after 50 μs , far outside of the field of view on the current experiments. The radial growth of the melting front is expected to expand at the same speed as or slower than the thermal diffusion length, defined as $2\sqrt{Dt}$, where $D = 0.95 \times 10^{-7}\text{ m}^2/\text{s}$ is the thermal diffusivity of THV. The boundary of this thermally affected region is outlined as a white dashed line in **Figure 7-6**. Although the plotted curve assumes only a single heat source located in the middle of the melt zone, the melting zone is well contained within the predicted envelope. The melting front manifests itself as a thin dark line from 50-200 μs in **Figure 7-6a** and then increases in thickness thereafter. We hypothesize that some increased distortion occurs near the melting front may be due to a change in refractive index between melted and solid THV. In the vicinity of the melt zone, imaging occurs through a hemispherical melted region with an increasing radius. A time of approximately 260 μs is required for a thermal diffusion length of 10 μm , the THV film thickness for the current study. This time scale is consistent with the appearance of an extended dark ring near the melting front. Material outside of the combustion and melt zones appears relatively unaffected by the laser at 255 mW, and THV melting away from the large central particle is not observed.

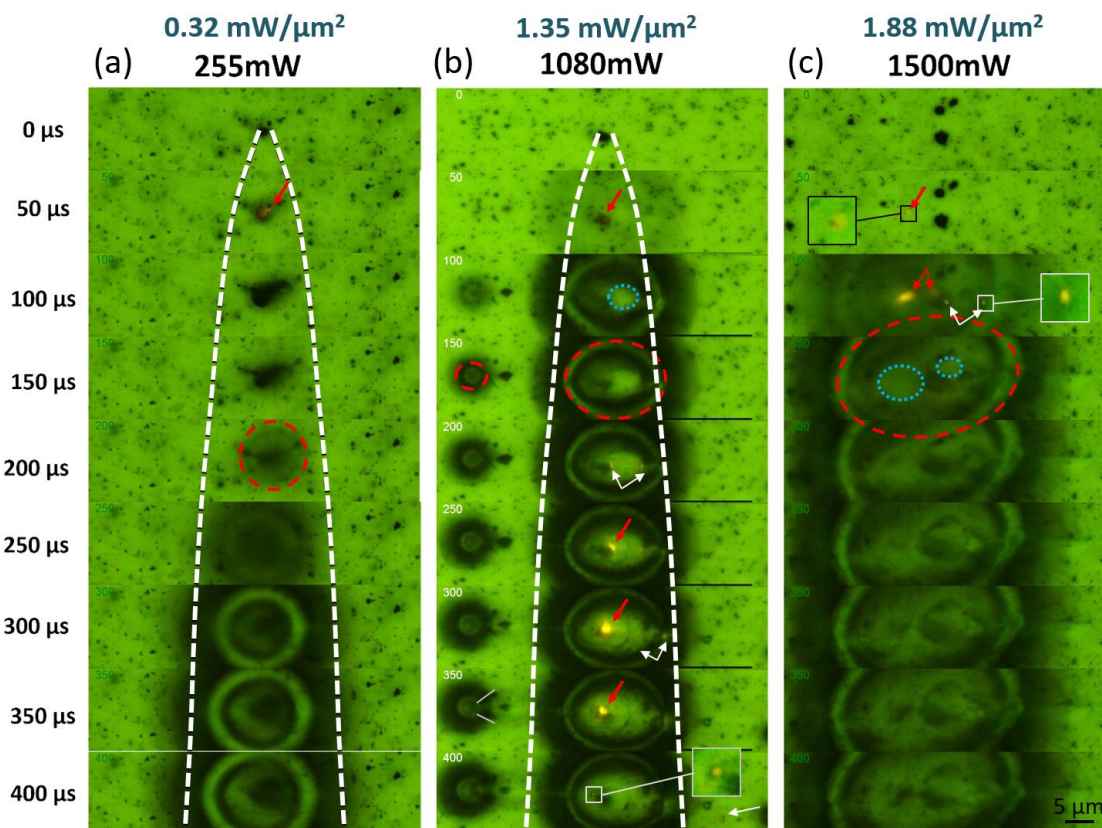


Figure 7-6 *In-situ* imaging (0-400 μs) of 446 nm blue laser ignition for Al/THV film on plasmonic silver gratings with different laser powers of (a) 255 mW ($0.32 \text{ mW}/\mu\text{m}^2$ peak), (b) 1080 mW ($1.35 \text{ mW}/\mu\text{m}^2$ peak), and (c) 1500 mW ($1.88 \text{ mW}/\mu\text{m}^2$ peak). All data were taken by a fast speed camera in an epi-fluorescence microscope equipped with a $40\times$ air objective with the $2.5\times$ adaptor under modified FITC filter. Red arrows indicate flames in excess of $1 \mu\text{m}$ in size, while white arrows indicate sub-micron nano-flames. The red dashed circles indicate the solid to the liquid melting front, and the blue dotted circles indicate the location of vapor-liquid boundaries. The extended dashed profile in (a-b) indicates the location of vapor-liquid boundaries. The extended dashed profile in (a-b) indicates the spatial envelope of thermal diffusion with time. Solid lines at $350 \mu\text{s}$ in (b) indicate aligned mobile Al NPs being carried by merging melting fronts.

At a laser power of 1080 mW ($1.35 \text{ mW}/\mu\text{m}^2$), shown in **Figure 7-6b**, combustion

is observed at 50 μs . THV melting is observed in two regions to the left of the main combustion region beginning at 50 μs . The growth rate of the melting fronts associated with these two small regions is significantly less than the rate of thermal diffusion, and Al NP combustion is not observed in these regions. Both particle aggregates residing in the center of the melting zone appear to be surrounded by small vapor regions beginning at 100 μs , indicating temperatures nearing the anticipated combustion temperature. A lack of combustion may indicate that particles sintered to form larger aggregates. These larger aggregates, in turn, would experience reduced E-field enhancement, slowing their heating rates. This possible mechanism would also explain the slow advancement of the melting zone, as heat generation within the region is abated. The melting fronts between these two regions begin to merge at 300 μs , resulting in alignment of mobile Al particles at the boundary of the melting zones. The aligned particles are represented as solid lines in Figure 5b.

Increasing the laser power to 1500 mW ($1.88 \text{ mW}/\mu\text{m}^2$), shown in **Figure 7-6c**, initiates the combustion of smaller (1 μm) Al NP aggregates within the first 50 μs . More widespread combustion events occur at 100 μs . These early combustion events produce both small nano-flames and larger aggregate combustion events that rapidly generate the largest observed THV melt zones. After 100 μs , no obvious additional combustion events are observed, although numerous vapor regions are observed within the central melt region where combustion previously occurred. We hypothesize that particle motion inside of the melt zone acted to disperse particles away from the laser irradiation region and the grating, ceasing combustion.

Note that in these experiments combustion events were only initiated on Al NP

aggregates, although individual Al NPs within the aggregates may produce the nano-flames that propagate between adjacent particles, observed in **Figure 7-6**. Note that Al NP aggregates generate greater heat than an isolated particle, but the generation will likely not scale linearly with aggregate volume because of complex E-field coupling between neighboring Al NPs and the grating. Combustion of individual Al NPs and smaller aggregates requires greater laser fluence. Further, because THV may not fully penetrate an aggregate, combustion events likely initiate preferentially at the cluster surface.

The phase change response during the laser on and after laser off can be monitored over time as shown in **Figure 7-7a**. The time mapping was reconstructed for investigating the change along a fixed x-axis (distance). The phase change regions over time and the wavefront moving speed can be calculated. The analysis for 1-3 pulses in the first set was listed as an example in **Figure 7-7b**. The phase change speed increases from the 1st to 3rd pulse, probably due to more reactions happen which generate more heat per time. The melting zone keeps extending even though there is no reaction, so the melting zone is not only due to combustion, but also due to the photothermal heating of all Al NPs in the laser region. Where there is a big combustion, there is an oscillation of phase change because a large amount of additional heat is generated. The phase recovery rate (see the slop of the changing zone) at different pulses is very similar, due to the naturally cooling down of the system.

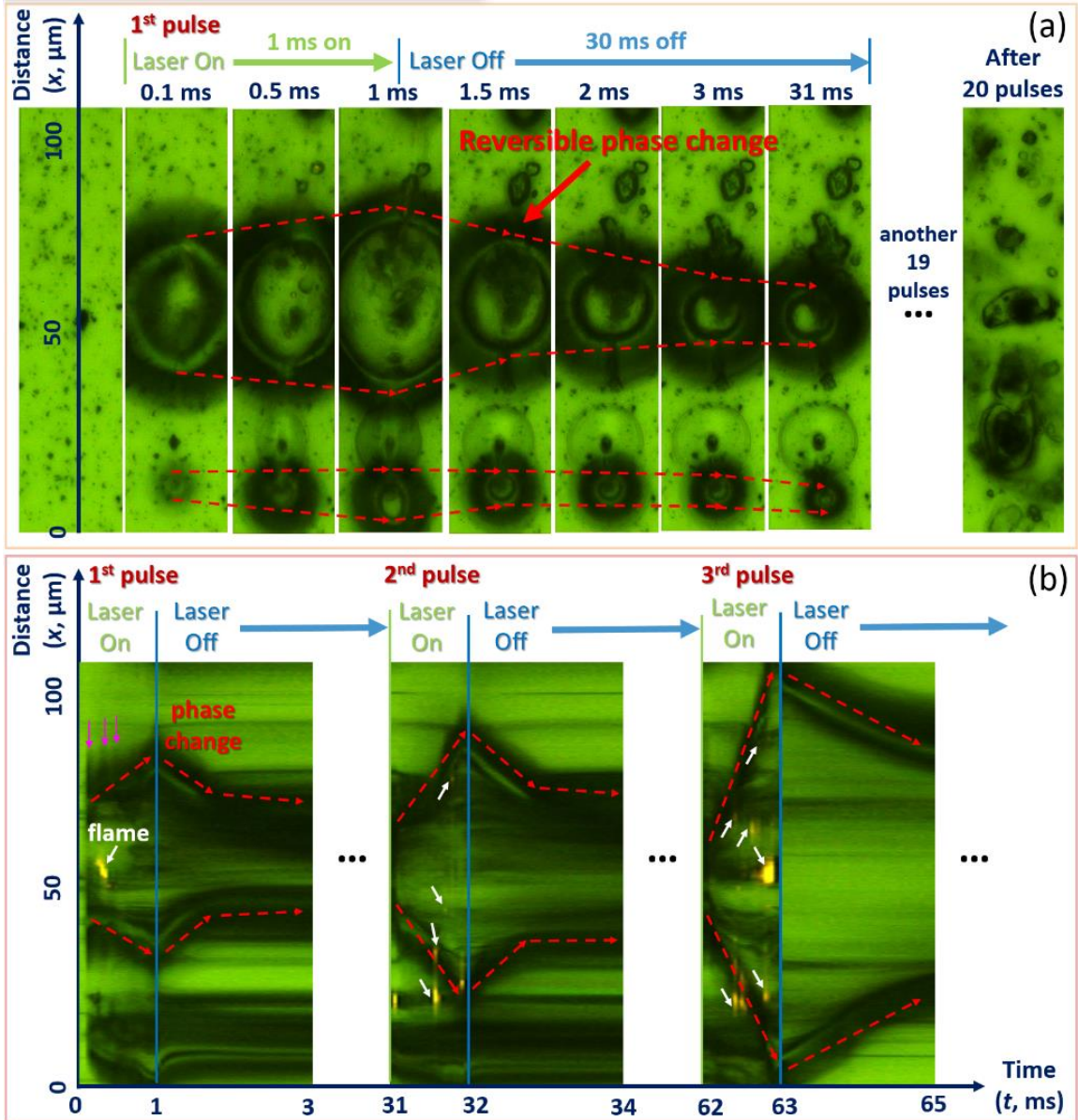


Figure 7-7 Phase change of THV before, during and after 446 nm blue laser ignition for Al/THV film on plasmonic silver gratings with a laser power of 1080 mW. (a) 2D x-y image sequences for the first pulse with 1 ms laser on and 30 ms laser off, and the image with THV re-solidification by removing the laser after 20 pulses. (b) Time (t , μs) vs distance (x , μm) plot by reconstructing the x-axis in the middle of the whole image sequences for the first three pulses out of 20 pulses. The red dashed curves indicate the trend of phase change region when the laser was on and off; the white arrows indicate some

of the flames during laser exposure; the pink arrows indicate the fluctuation of phase change. All data were taken by a fast speed camera in an epi-fluorescence microscope equipped with a 40× air objective with the 2.5× adaptor under modified FITC filter.

7.4.4 *In-Situ Optical Pyrometry*

The *in-situ* optical platform is uniquely suited for observation of nanoenergetic combustion within a polymer film. Electron microscopy methods are incapable of viewing these reactions because of the embedded depth of Al NPs within the polymer. Two-color pyrometry using the red and green channels of the fast camera was utilized to construct dynamic temperature mapping. Background lighting was extinguished for these tests such that all light received by the camera was from combustion events. Pre-combustion images and subsequent combustion evolution of a typical sample at 1080 mW laser power are shown in **Figure 7-8(a-b)**. By comparing the position of Al NPs in the bright field image before combustion (**Figure 7-8a**) and the location of flame during the first 650 μs of combustion (**Figure 7-8b**), the corresponding reacted nanoparticles can be readily identified. Large-scale images of four representative combustion events are shown in **Figure 7-8c** with the comparison of bright field image, *in-situ* flame image, and the corresponding temperature maps reconstructed by two-color pyrometry. The location and geometry of nano-flames match very well with that of Al NPs in bright field image, indicating that the Al/THV reaction is confined to the positions where Al NPs were embedded in THV. A Gaussian fit of the flame profile for a single nano-flame shows a full-width-half-maximum (FWHM) of 600 nm. The capability of two-color pyrometry to reconstruct the dynamic temperature mapping of single flame in nanoscale using our

system is important for the study of localized reactions for applications such as targeted cancer treatment or nano-thrusters.

A histogram of the measured flame temperature in all frames of a 1 ms pulse is shown in **Figure 7-8d**, accompanied by the states of the reactants (Al with Al₂O₃ shell, THV) and products (AlF₃ and carbon) within the corresponding temperature range. Combustion temperature ranges from 2400K to 5000K, with a mean temperature of approximately 3900K. This value matches well with published aluminum flame temperature values of 4000K obtained by others.[144] For an Al/Teflon energetic system, the combustion temperature was reported above 3273K, and the adiabatic flame temperature due to Al combustion is generally higher than the Al boiling temperature of 2743K [144]. The melting temperature of Al₂O₃ is 2345 K, considerably less than the observed flame temperatures. The phase of constituent materials relative to the observed flame temperature may be found in **Figure 7-8e**.

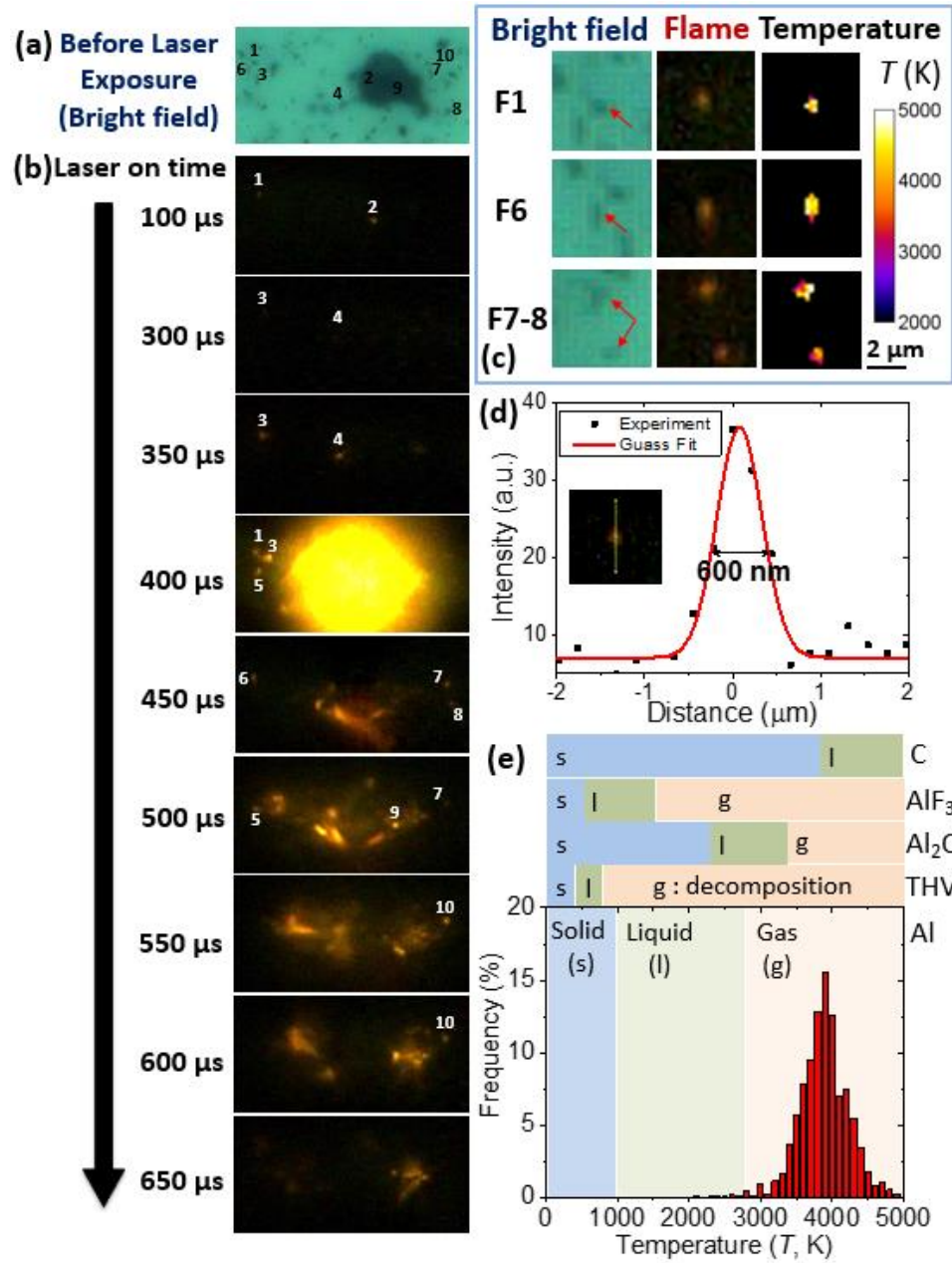


Figure 7-8 Two-color pyrometry analysis. (a) Before and (b) *In-situ* ignition imaging of Al/THV film on plasmonic silver gratings with laser powers of 1080 mW. *In-situ* images were taken by a high-speed camera in an epi-fluorescence microscope equipped with a 40× air objective with the 2.5× adaptor under modified FTIR filter without background light. The white numbers indicate isolated combustion events. (c) Comparison of bright field, *in-situ* flame image, and corresponding temperature maps. (d) The temperature profile of

single nano-flame from position F1, with FWHM of 600 nm. (e) Histogram of all flame temperatures observed in 1 ms pulse.

7.4.5 Electromagnetic Simulation

COMSOL software was utilized prior to experimentation to determine the optimum coupling between Al NP diameter and radiation wavelength. Al NPs having diameters of 50 nm, 80 nm, and 120 nm were numerically examined, each with an Al₂O₃ shell thickness of 2 nm. **Figure 7-9a** shows the absorption efficiency of a single Al NP in THV, defined as the absorption cross-section divided by the geometric cross-section. Overall, 80 nm diameter Al NPs show the highest absorption efficiency in the visible spectrum, with a peak absorption efficiency of 0.38 near 378 nm. Lower-intensity peaks near 810 nm, associated with the dielectric loss of Al, were present for all NPs, indicating that photothermal heating near the plasmonic resonance is significantly enhanced relative to heating using IR irradiation near 810 nm.

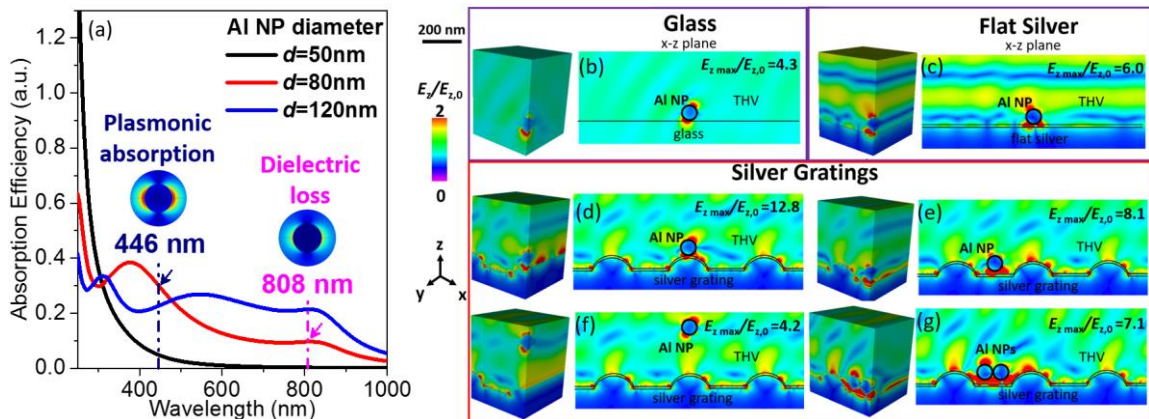


Figure 7-9 (a) Simulated absorption efficiency of a single Al NP embedded in fluoropolymer oxidizer THV; the inset is the E-field distribution at 446 nm and 808 nm for 80 nm Al NP with normalized E-field scale of 0-5. FDTD simulated E-field distribution of

80 nm Al NPs on different substrates: (b) plain glass (c) flat silver, (d-g) silver gratings under laser wavelengths of 446 nm in THV matrix. The relative z-component of E-field ($E_z/E_{z,0}$) scale is normalized to 0~2. Each condition shows a 3D view of E-field distribution (left) and the corresponding 2D view of the x-z plane (right). The scale bar in x-z plane is 200 nm. The incident angle is calculated based on Snell's law, 70° incident from the air ($n=1$) corresponds to 43.7° in THV ($n=1.36$).

The grating substrate further enhances the local electric field and resultant photothermal heating of nanoenergetic systems by activating surface plasmon resonance (SPR). FullWAVE Finite-difference Time-domain (FDTD) software was utilized to simulate the 3D E-field distribution of Al NPs embedded in THV while interacting with various solid substrates. The enhancement of SPR coupling generates an evanescent E-field perpendicular to the grating surface. As shown in **Figure 7-9(b-g)**, the grating provides the greatest E-field enhancement ($E_{z\max}/E_{z,0}$) when compared to glass and flat silver. The light intensity enhancement of a particle residing on the crest of the grating is $|E_{grating}/E_{flat}|^2 = (12.8/6.0)^2 = 4.6$ times greater than that produced by an Al NP residing on a flat silver substrate and a factor of 8.9 compared to a flat glass substrate. When the Al NP is located in the grating trough, the light intensity enhancement is 1.8 compared to flat silver, which matches with the 2-fold reduction in the threshold ignition power for the plasmonic grating as discussed previously. An Al NP located 300 nm above the silver grating produces an E-field value similar to that of glass, which is itself similar to an isolated Al NP suspended in THV (**Figure 7-9b**). **Figure 7-9g** shows the overall high E-field hot spot (red color region) for two adjacent NPs is larger than that produced by a single Al NP.

7.4.6 Thermal Model

The laser beam in these experiments is distributed as an ellipse, with the peak energy flux (I_p) and maximum fluence (J_c) in the central region, represented by:

$$I_p(\text{mW}/\mu\text{m}^2) = 1.25 \times 10^{-3} \cdot P(\text{mW}) \quad (7.1)$$

$$J_c(\text{J}/\text{m}^2) = 1.25 \times 10^6 \cdot P(\text{mW}) \cdot t(\text{s}) \quad (7.2)$$

where P is the power of a laser, and t is a pulse time. The absorbed energy absorbed by a nanoparticle (E_{np}) may then be expressed as:

$$E_{np} = J_c \sigma_{abs} \quad (7.3)$$

where σ_{abs} is the absorption cross-section of Al NP. For an 80 nm diameter Al NP in THV under 446 nm irradiation, $\sigma_{abs} = 1.51 \times 10^{-15} \text{m}^2$ based on COMSOL simulation.

A transient heat transfer model can be considered to understand the behavior between threshold fluence (J_{th}) to initiate combustion from an embedded particle and the duration of a laser pulse (t_p). The model considers diffusive conduction in the THV polymer and the glass substrate while neglecting phase change. Note that the plasmonic microchip used in this study is made of a 100 nm silver thin film (with 10 nm Al_2O_3 capping layer) deposited on a 200 nm PMSSQ grating structure which resides on a 1 mm thick glass slide. Since the thermal diffusivity of the thin silver layer ($D = 1.66 \times 10^{-4} \text{m}^2/\text{s}$) is approximately 3-order larger than that of glass ($D = 3.4 \times 10^{-7} \text{m}^2/\text{s}$) and THV ($D = 0.95 \times 10^{-7} \text{m}^2/\text{s}$), the diffusion through the alumina and silver films is neglected. Because thermal diffusion is dominated by contributions from the glass substrate and THV, a composite average diffusivity of ($D = 1.5 \times 10^{-7} \text{m}^2/\text{s}$) representing the combined

response of glass and THV is considered for simplicity. If we assume a continuously heated Al NP (represented as a point particle) embedded in an infinite conductive media, the temperature response may be found using a Green's Function approach as

$$T(r, t) - T_o = \frac{q}{4\pi kr} \operatorname{erfc}\left(\frac{r}{\sqrt{4Dt}}\right) \quad (7.4)$$

where T_o is the initial temperature of the system, q is the constant heat absorption rate experienced by the particle (Watts), k is the thermal conductivity of THV, r is the distance away from the Al NP center, erfc is the complimentary error function, and D is the average thermal diffusivity between the glass and THV.

The absorption efficiency $\alpha = 0.301$ for 80 nm Al NP embedded in THV under illumination of 446 nm laser. The fraction of light absorbed by an isolated particle would be enhanced by the plasmonic gratings by E-field enhancement. Thus, for a constant heating rate the total energy absorbed by a single NP, Q , can be expressed as

$$Q = qt \quad (7.5)$$

$$Q = \alpha J(\pi r_o^2) E^2 \quad (7.6)$$

$$E^2 = |E_{grating}/E_{background}|^2 \quad (7.7)$$

where t is time, J is the laser fluence, r_o is the radius of the NP, and E represents the electric field enhancement. The relationship between critical fluence to initiate combustion as a function of time may be found by substituting equations 7.5-7.7 into equation 4 and evaluating at the outer radius of the Al NP

$$J_{th} = \frac{4k(T_{reaction} - T_o) t_p}{\alpha r_o E^2} \frac{1}{\operatorname{erfc}\left(\frac{r_o}{\sqrt{4Dt_p}}\right)} \quad (7.8)$$

where J_{th} is the threshold laser fluence, $T_{reaction}$ is the temperature at which combustion occurs, t_p is the pulse time required to initiate the reaction, and r_o is the outer

radius of the Al NP.

The relationship between J_{th} , pulse time, and E-field enhancement is shown in **Figure 7-10(a-b)**. The plot is generated for a single Al NP and a ring of six Al NPs in contact. The fluence provided by various laser powers is also plotted. Note that the threshold fluence increases nearly linearly with t_p , within the time range considered. Although the E-field enhancement provided by the grating significantly reduces the threshold fluence, a single Al NP will not reach the threshold ignition temperature even with an enhancement factor of 9. When a cluster of six particles is considered, however, ignition may be observed for laser powers in excess of 1080 mW, consistent with experiments. Each Al NP in the cluster is assumed to experience the same enhancement factor in the model. Note that the nominal diameter of a disk of six Al NPs is approximately 240 nm. Three-dimensional configurations of 6 particles would have a decreased effective cluster diameter. The conduction is most applicable for short time scales before significant heat loss from conduction and THV melting occurs. Nevertheless, the model output provides guidance relative to the necessity of the plasmonic grating to ignite Al NPs and predicts the minimum Al NP cluster size required for ignition that is consistent with experimental observations.

The transient temperature of Al NPs on plasmonic gratings was simulated by COMSOL *via* combining the heat transfer model with the E-field obtained by FDTD simulation. **Figure 7-10c** shows the effects of different laser powers and different numbers of Al NPs (single, double, and six particle system). One and two Al NPs cannot reach the reaction temperature of Al-THV (476 °C) within 1500 mW laser irradiation, however, an Al NP cluster containing six Al NPs can be ignited and laser power in excess of 1080mW.

The simulated results match well with experimental observations and the theoretical prediction by the transient heat transfer model using a Green's Function approach.

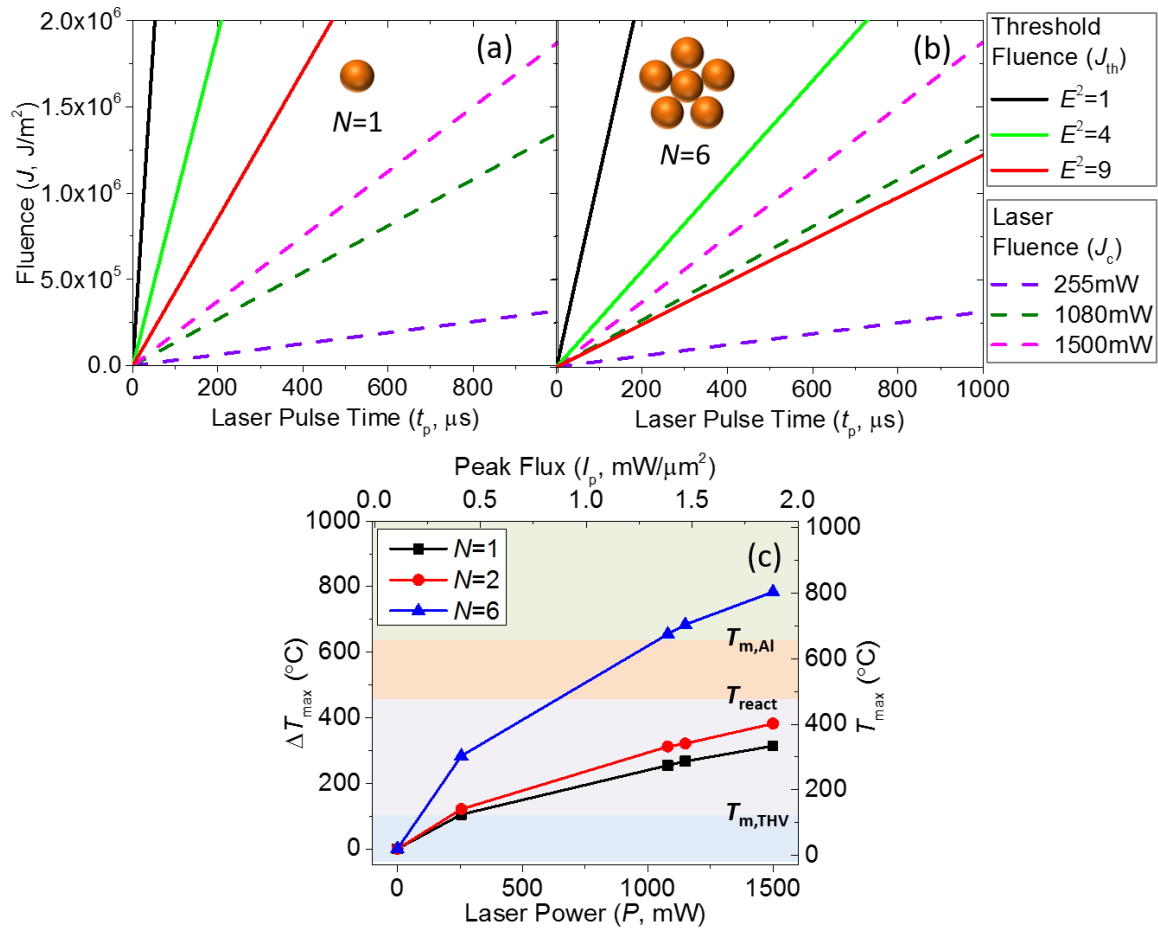


Figure 7-10 (a-b) Comparison of theoretical threshold fluence (J_{th}) for Al/THV energetic system (solid lines) and experimental laser fluence (J_c) with laser powers of 255 mW, 1080 mW and 1500 mW (dashed lines). (c) Maximum Al NP temperature at the end of the laser pulse as a function of laser power for different numbers (N) of Al NPs.

7.4.7 Optical Scattering

The greatly enhanced scattering cross section of 80 nm diameter Al NPs enables precise location and counting of Al NPs before and after combustion experiments.

Scattering measurements were obtained in the epi-fluorescence microscope using both polarizer and analyzer. Images were obtained using either a 40 \times objective and a low pixel resolution color fast camera (**Figure 7-11c-d**), or a 100 \times oil objective and a high pixel resolution black and white camera (ORCA flash 2.8, **Figure 7-11e-f, h**). While Al NPs presented high imaging contrast, the carbon byproducts formed during combustion appeared as dark areas (**Figure 7-11c-d**), as they do not preferentially scatter light. By contrast, unreacted Al NPs, reacted Al, and carbon products all appeared as dark spots in bright field imaging (**Figure 7-11a-b**), hindering compositional differentiation. Gas phase products can leave large indelible voids in the final state of the sample in the post-reaction images, an example of which can be seen in **Figure 7-11f**.

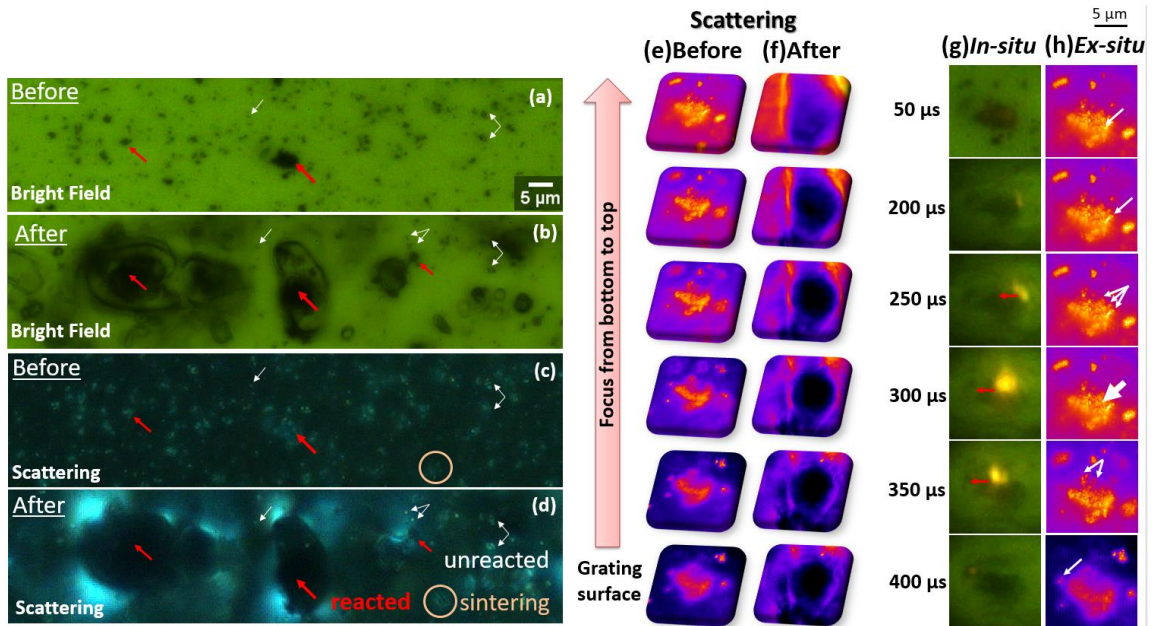


Figure 7-11 Optical scattering before and after laser ignition for Al/THV films on plasmonic silver gratings. Low-resolution images: bright field (a) before and (b) after laser ignition; scattering (c) before and (d) after laser ignition. The data were taken by 40 \times air objective with the 2.5 \times adaptor in the epi-fluorescence microscope by the fast camera. The

red and white arrows indicate the reacted and unreacted spots, respectively. High-resolution images: scattering (e) before and (f) after laser ignition. The data were taken by 100 \times oil objective with the 2.5 \times adaptor in the epi-fluorescence microscope by the black and white camera. (g) *In-situ* imaging of 446 nm laser ignition for Al/THV film on silver gratings and the red arrows show the flame propagation. (h) *Ex-situ* imaging of scattering before ignition for identification of the combustion sites.

Note that individual NPs may be distinguished within larger Al NP clusters before combustion. After combustion, bright areas were observed around the perimeter of reaction centers (**Figure 7-11c-d**) and at varying heights above the plasmonic grating, as shown in **Figure 7-11e-f**. Prior to reaction, individual NPs are observed at all heights within the film, whereas ill-resolved bright streaks are observed after the reaction, indicating that most of the Al NPs sintered into large agglomerates during the reaction. The aligned nature of the agglomerates seems to form on the exterior surface of a gaseous void, indicating that mechanical forces likely acted to bring the particles together.

Optical scattering images obtained before combustion can also elucidate the 3D pathway of combustion propagation. **Figure 7-11g-h** shows 100 \times *ex-situ* scattering images. **Figure 7-11g** shows an isolated flame on the top surface of an Al aggregate at 50 μ s of laser irradiation. At 200 μ s, combustion re-ignites at the right side of the aggregate, and propagates from right to left until 400 μ s following the direction of laser irradiation. Comparing the *in-situ* combustion images to the 3D optical scattering images enables ready identification of combusted Al NPs and the combustion pathway. Arrows in **Figure 7-11h** indicate the likely particles combusted in the corresponding frame in **Figure 7-11g**. All combustion events occur on the top surface of the aggregate from 50-300 μ s, whereas the

flame propagates toward the grating thereafter. Note that the scattering images confirm that combusted particles reside at the agglomerate surface, indicating that THV availability likely contributes to the reaction. At 400 μs , reaction propagates to a small neighboring agglomerate located near the grating surface.

7.4.8 *Effects of Temperature on Properties and Coupling*

In our application, the spherical nature of our nanoparticles and the relatively rigid alumina coating likely mitigate the influence of shape change. That said, for the current material system, the interaction between the heated plasmonic particle and its environment is encouraged. Some possible factors that would cause plasmon transmutation effect at high temperature [145], [146] were discussed as follows. A quick estimation of deformation due to thermal expansion is found below, but found to be negligible at the reaction temperature.

First, let us consider the size effect on plasmonic coupling at high temperature. It is true that there may be some deformation of plasmonic nanostructures even before reaction, but the deformation is negligible. The following is the calculation to estimate the thermal expansion of Al and Al_2O_3 up to the reaction temperature.

$$dl = \alpha l_0(t_1 - t_0) \quad (7.9)$$

where dl is the change in object length (thermal expansion), α is the linear thermal expansion coefficient, l_0 is the initial length of the object, t_0 is the initial temperature, t_1 is the final temperature.

The linear thermal expansion coefficient of Al and Al_2O_3 is $2.1 \times 10^{-5} \text{ m}/(\text{m } ^\circ\text{C})$ and $8.1 \times 10^{-6} \text{ m}/(\text{m } ^\circ\text{C})$, respectively. When the temperature of Al NP is heated from room temperature ($25 \text{ } ^\circ\text{C}$) to the reaction onset temperature ($476 \text{ } ^\circ\text{C}$), the thermal expansion of

80 nm Al core and 2 nm Al₂O₃ shell is less than 1 nm, which is a negligible size effect on the plasmonic coupling.

Table 7-1 Thermal expansion of Al and Al₂O₃

Material	α	l_0	t_0	t_1	dl
Unit	$10^{-6} \text{ m/(m } ^\circ\text{C)}$	nm	$^\circ\text{C}$	$^\circ\text{C}$	nm
Aluminum (Al)	21	80	25	476	0.758
Alumina (Al ₂ O ₃)	8.1	2	25	476	0.007

Second, let us consider the change of the dielectric function at high temperature. In general, the increase in temperature results in increasing the overall Drude absorption but broadening and lowering absorption peak for the interband absorption. The absorption peak would red-shift with increasing temperature. However, the effects of the dielectric function on the changes of absorption are small when compared with the effects of structure factor (such as lattice parameters) and thermal expansion.[147] Since the thermal expansion is minor, the change of dielectric function is negligible.

Finally, let us consider that Al may rapidly transform to the molten and gaseous state before reaction. This mechanical reaction is known as the melt dispersion model of Al ignition. Such a reaction requires heating rates on the order of 10^6 K/s. The melt dispersion mechanism postulates that the fast melting of the Al core of the nanoparticles creates high internal pressure inside the Al₂O₃ shells, due to the volume expansion until dynamic spallation occurs when the hoop stresses exceed the ultimate strength of Al₂O₃.[68] The spallation generated by such a high pressure releases a radial dispersion of molten Al at high velocities. We are interested in the enhanced coupling (prior to structural changes) that results in melt-dispersion, instead of the changes of coupling due to this extensive change of entire structures after melt-dispersion.

7.4.9 Melt and Vaporize Al

The heating rate of Al NPs and Al phase is critical to understanding the combustion reaction pathways. The energy required to heat Al from room temperature (25 °C) to melting temperature (663 °C) 1.55 kJ/cm³, while the latent heat of melting Al is 0.87 kJ/cm³, and hence the total energy required to melt Al is around 2.42 kJ/cm³. Similarly, the energy required to vaporize solid Al is 31 kJ/cm³. [73] For Al/THV system, the actual energy release due to exothermic chemistry is less than the theoretical heat of combustion of Al/Teflon (21 kJ/cm³). In the absence of energy losses during the heating process, the minimum pulse time required to melt and vaporize solid Al was calculated. The light intensity enhancement provided by the grating substrate enhances photothermal heating and reduces the time required to melt or vaporize the Al NPs. Enhancement factors of 1, 4, and 9 are to approximate the Al NP residing on a glass substrate, the trough of the grating, and the crest of the grating, as previously discussed. The time to melt and to vaporize Al within the Al NP assuming adiabatic boundaries, is less than 25 μs even for no field amplification and 200 mW of laser power. The minimum time to vapor Al can reach less than 500 ns when using 1500 mW laser with E-field enhancement of 9.

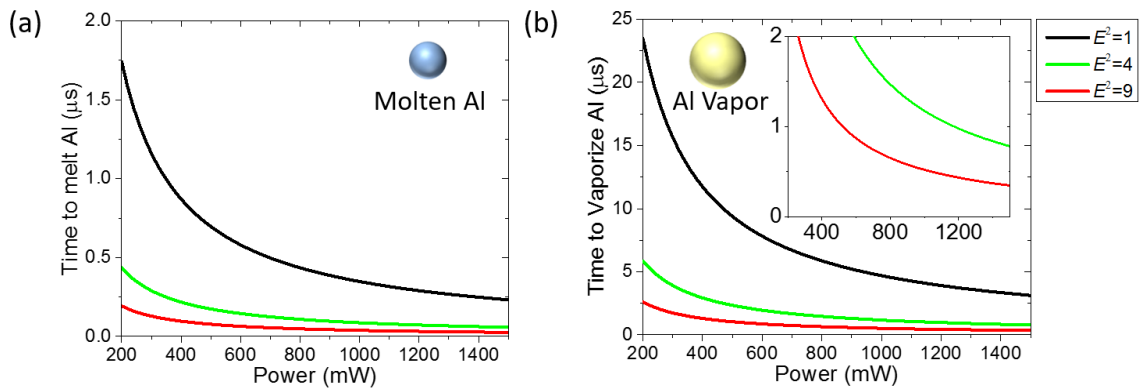


Figure 7-12 The minimum laser pulse time required to (a) melt solid Al and (b) vaporize

solid Al with different E-field enhancement.

7.5 Two-Color Pyrometry

7.5.1 Theory

According to black-body emission and Planck's radiation law, the monochromatic exitance of a black-body object emitted in energy per unit area per unit time ($\text{W}/\text{m}^2/\mu\text{m}$) is

$$M(\lambda, T) = \epsilon_\lambda \cdot \frac{C_1}{\lambda^5} \cdot \left(e^{\frac{C_2}{\lambda T}} - 1 \right)^{-1} \quad (7.10)$$

For the case when $C_2/\lambda T \gg 1$, the Planck's law can be simplified to Wien's radiation law, which gives

$$M(\lambda, T) = \epsilon_\lambda \cdot \frac{C_1}{\lambda^5} \cdot e^{-C_2/\lambda T} \quad (7.11)$$

where ϵ_λ stands for the monochromatic emissivity, $C_1 = 2\pi hc^2$ is the first radiation constant, and $C_2 = hc/k_B$ is the second radiation constant. It can be proven that the grey level output of an imaging system depends on:

$$G(\lambda, T) = R \cdot S_\lambda \cdot M(\lambda, T) = R \cdot S_\lambda \cdot \epsilon_\lambda \cdot \frac{C_1}{\lambda^5} \cdot e^{-C_2/\lambda T} \quad (7.12)$$

For a two color system, the ratio of grey level between two different color channel at wavelength of λ_1 and λ_2 can be expressed as

$$\frac{G(\lambda_1, T)}{G(\lambda_2, T)} = \frac{S_{\lambda_1} \cdot M(\lambda_1, T)}{S_{\lambda_2} \cdot M(\lambda_2, T)} = \frac{S_{\lambda_1}}{S_{\lambda_2}} \cdot \frac{\epsilon_{\lambda_1}}{\epsilon_{\lambda_2}} \cdot \frac{\lambda_2^5}{\lambda_1^5} \cdot \exp\left[\frac{C_2}{T} \cdot \left(\frac{1}{\lambda_2} - \frac{1}{\lambda_1}\right)\right] \quad (7.13)$$

which yields the temperature

$$T = C_2 \cdot \left(\frac{1}{\lambda_2} - \frac{1}{\lambda_1}\right) / \left[\ln \frac{G(\lambda_1, T)}{G(\lambda_2, T)} + \ln \frac{S_{\lambda_2}}{S_{\lambda_1}} + \ln \frac{\epsilon_{\lambda_2}}{\epsilon_{\lambda_1}} + \ln \frac{\lambda_1^5}{\lambda_2^5} \right] \quad (7.14)$$

When the wavelengths are very close, grey-body behavior for the detected object is assumed which gives $\epsilon_{\lambda_2}/\epsilon_{\lambda_1} = 1$. For gaseous flames, the size of the soot particles ranges from 5 nm to 100 nm, which is much smaller than the wavelengths used. If these particles are homogeneous, optically thin and isothermal along a horizontal line through the flame, one may assume $\epsilon_{\lambda_2}/\epsilon_{\lambda_1} = \lambda_1/\lambda_2$, which gives

$$T = C_2 \cdot \left(\frac{1}{\lambda_2} - \frac{1}{\lambda_1}\right) / \left[\ln \frac{G(\lambda_1, T)}{G(\lambda_2, T)} + \ln \frac{S_{\lambda_2}}{S_{\lambda_1}} + \ln \frac{\lambda_1^6}{\lambda_2^6} \right] \quad (7.15)$$

The instrument factor can be derived from the above equations as,

$$S = \frac{S_{\lambda_2}}{S_{\lambda_1}} = \exp\left(\frac{k_1}{T}\right) / \left(GR + \frac{\epsilon_{\lambda_2}}{\epsilon_{\lambda_1}} + k_2 \right) \quad (7.16)$$

Which can be obtained by calibrating the imaging system with a standard black-body temperature source with the following equation:

$$k_1 = C_2 \cdot \left(\frac{1}{\lambda_2} - \frac{1}{\lambda_1}\right), k_2 = \frac{\lambda_1^5}{\lambda_2^5}, GR = \frac{G(\lambda_1, T)}{G(\lambda_2, T)} \quad (7.17)$$

Differentiating the spectral radiation emittance with respect to λ and solving for the maximum emittance gives rise to Wein's displacement law as expressed:

$$\lambda_m = \frac{a}{T} \quad (7.18)$$

Where λ_m is the wavelength of maximum emittance, a is a constant (= 2898 μmK), and T is the black body radiator temperature. The above gives the fundamental theory of two-color pyrometry for measuring the flame temperature using an imaging system with two color channels, and the necessary calibration steps for our system.

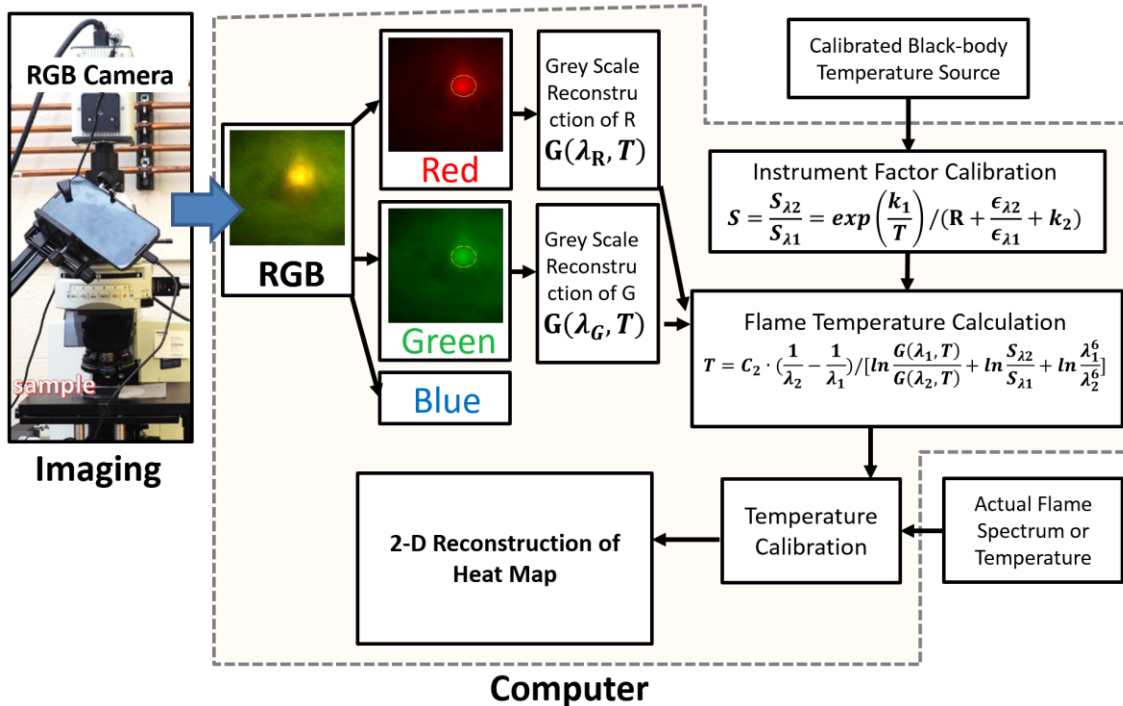


Figure 7-13 Schematics showing the heat map reconstruction using Two-color Pyrometry

7.5.2 Temperature calibration by both fast camera and spectrometer

To enable simultaneous measurement of both the flame spectrum and flame imaging, we utilized the two eyepiece ports, which contain identical optical image information. Both the fast camera to eyepiece port adaptor (1), and the spectrometer to eyepiece adaptor (2) are designed using OpenSCAD and 3-D printed using PLA as material. Below shows the design of Adaptor 1 as an example.

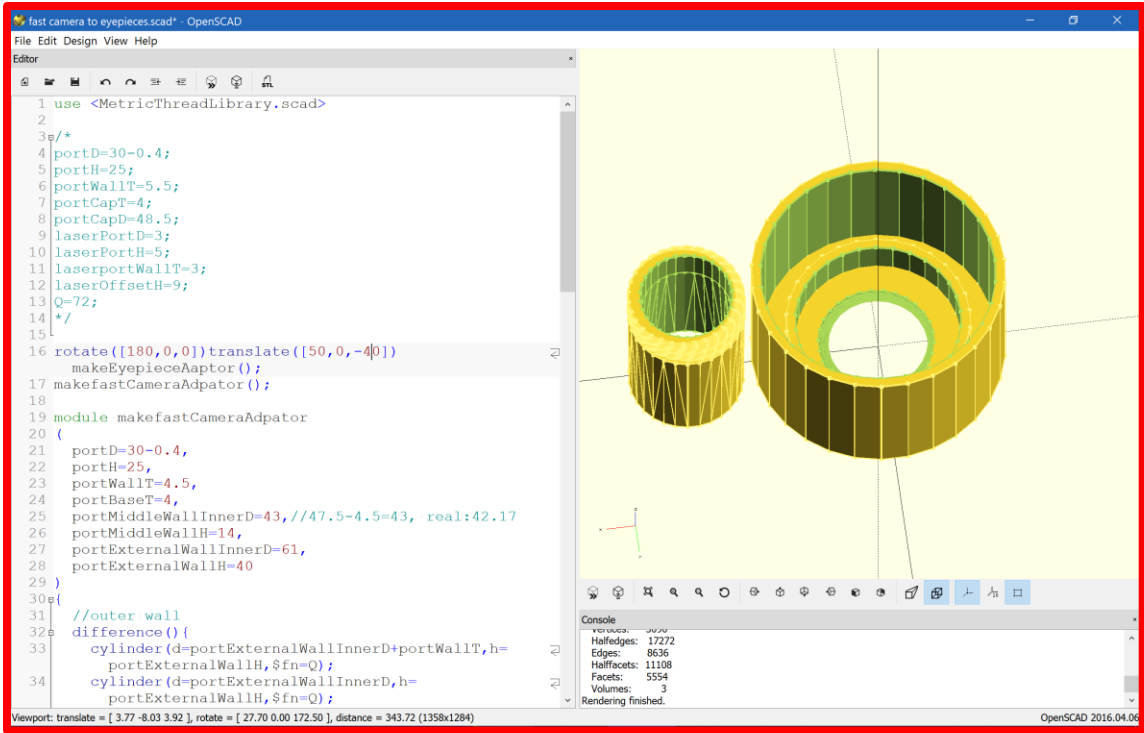


Figure 7-14 Designing of adaptor using OpenSCAD

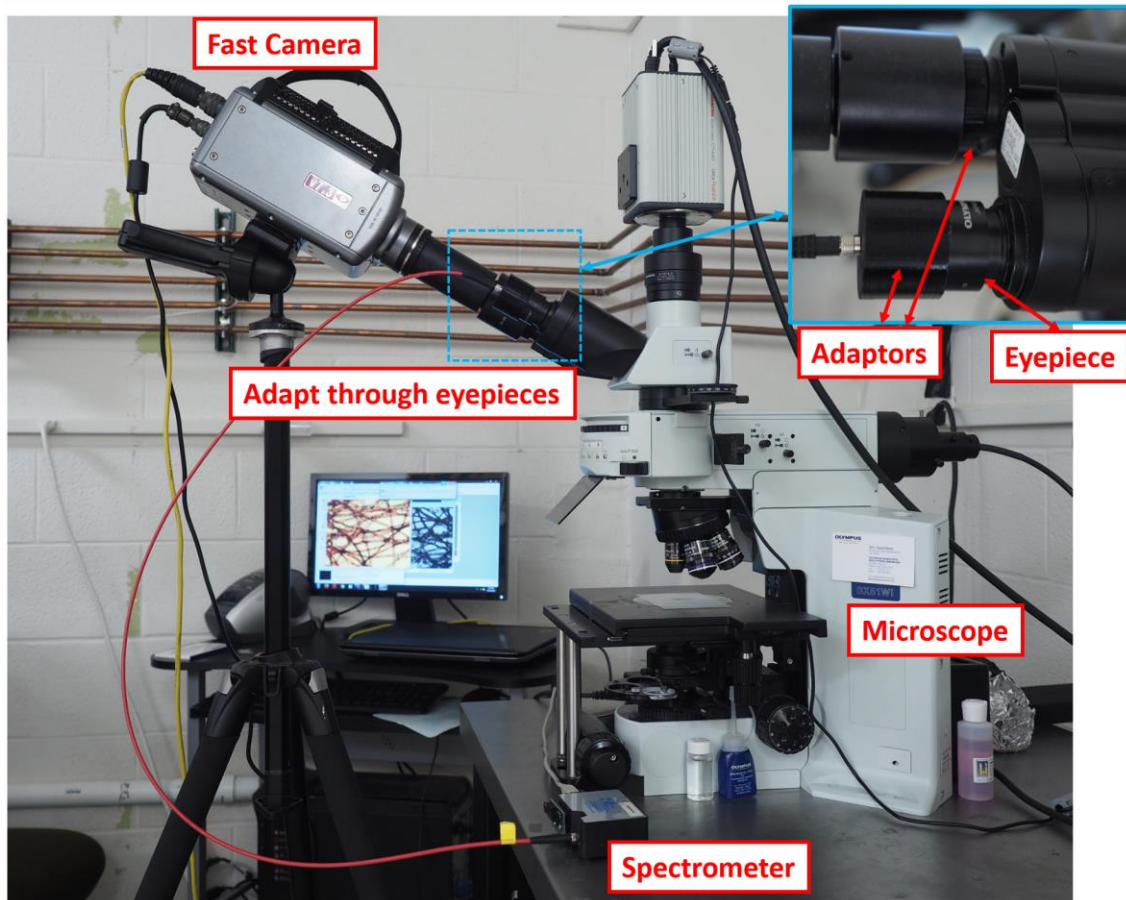


Figure 7-15 Illustration showing the optical setup for taking the flame spectrum using a USB-4000 spectrometer and flame imaging using the Phantom V7.3 fast camera simultaneously.

7.5.3 Calibration Curves for New Setup through Eyepiece Port

We calibrated the improved tungsten filament at a different temperature, using our RGB camera (V7.3 Phantom fast camera) with the exact optical setup used for laser ignition experiment. One important note for this calibration is that we keep the gray intensity around 187 in red channel for all voltages by adjusting the exposure time, so that it avoids the problem that different intensity affects the G/R ratio. After imaging the

tungsten filament, we obtained the intensity per millisecond vs. the lamp voltage for different channel, and calculate the G/R grey intensity vs. lamp voltage. A temperature (T , K) vs. G/R channels grey intensity ratio ($I_{G/R}$) relation is then obtained. Without further calculation of the instrument factor, the temperature curve can be used directly for reconstruction of temperature map for blackbody system. The linear fitted curves can be expressed as follows:

$$\text{Through camera port: } T = 5889.3 * I_{G/R} - 178.0$$

$$\text{Through eyepiece port: } T = 6955.4 * I_{G/R} - 429.4$$

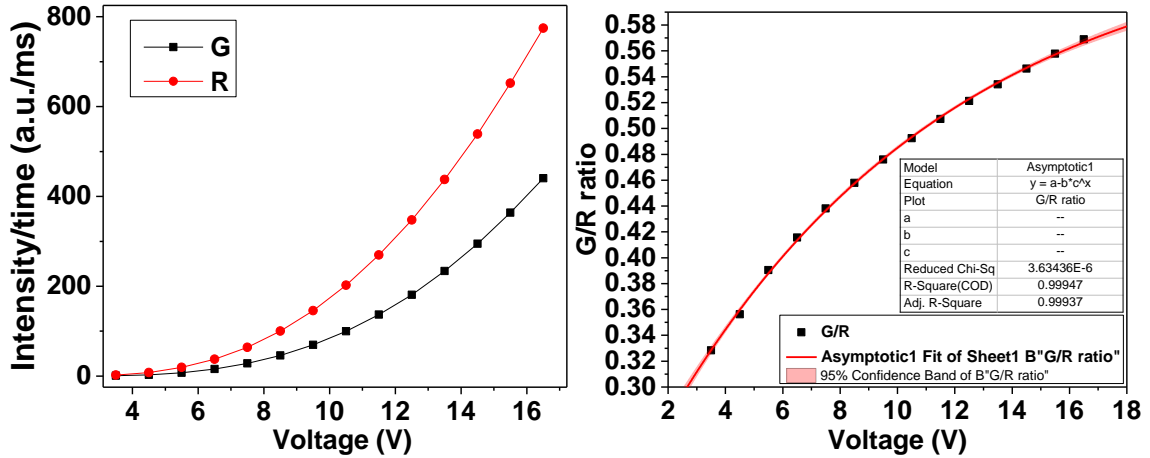


Figure 7-16 Temperature vs. G/R channels gray intensity ratio of our optical system with the V7.3 Phantom fast camera through camera port.

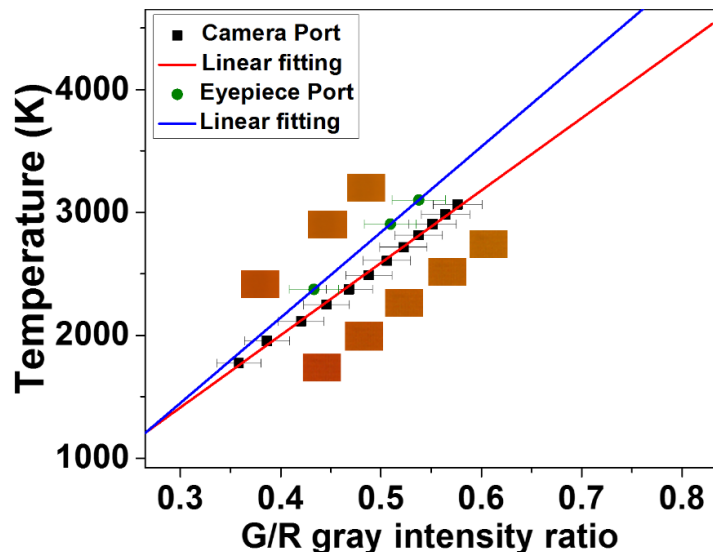


Figure 7-17 Temperature vs. G/R channels gray intensity ratio of our optical system with the V7.3 Phantom fast camera. The curves were calibrated through camera port and eyepiece port, respectively.

7.5.4 *Spectrum Measurement and Fitting for Laser Ignition Study*

We synchronized flame spectrum measurement of the laser burned THV/Al NPs together with the two-color pyrometry (using the fast camera) through the dual eyepiece ports of the microscope. The laser background (>510 nm) is due to the scattering of the laser peak tail (longer wavelength) not being cut by the filter, instead of the peak of the laser. In the figure below, the filter can cut the laser peak very well (<510 nm). The figure for comparing with and without the filter was measured by the scattering of the laser on the Al/THV film on flat silver under the 90mW blue laser. We did not measure very high power without the filter in order to protect the detectors. In the grating region, for big flame, this small background is negligible; but for small local flame, the background has some effects. One idea to resolve this issue is to add bandpass for the laser in the incident path.

This method can at least remove the elastic scattering (the same wavelength as the incident laser) of laser peak tail.

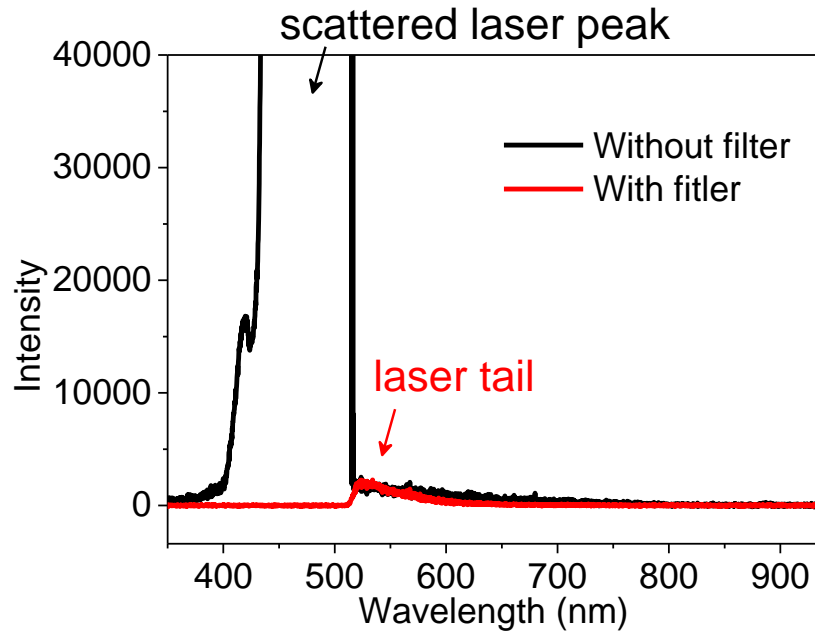


Figure 7-18 Spectrum of the laser with and without filtering the main laser peak. Al/THV on gratings exposed to 90 mW 466nm pulse laser (10 ms on) without background light. With filter was measured under FTIC, and without the filter was measured under DAPI.

Since the spectrometer has sampling rate resolution around 50 ms per spectrum, so we chose 50 ms as integration time as well as pulse duration to make sure it can resolve the signal from each pulse. We used 1 ms as a pulse on time in order to get enough signal for the big flame but not saturate the spectra, meanwhile, reduce the laser tail background. At the beginning, we tried to use 10 ms pulse on time, but the spectra were saturated, and the pulse background is also strong due to longer pulse on time compared with 1 ms.

The following results are for the measurements without background light from Xenon lamp for the grating regions. The sample was thick Al/THV film (~10 μm) on silver plasmonic gratings, which was exposed to 1080 mW 466nm pulse laser (1 ms on and 49

ms off, 30 pulses) without background light, under FITC emission filter.

For the spectra directly from the measurement, there are several broad peaks, especially at 827 nm. After comparing with the FITC filter, the peaks should come from the FITC emission path including the dichroic and emission filter. The spectra were calibrated by system response and the temperature was fitted at the range around 540 nm to 700 nm. The temperature of the big flame based on the measured spectrum fitted by blackbody emission is about 3700K. The chemical reaction sharp peaks did not appear in the spectra, probably due to the following reasons:

(1) For the big “flames”, there are enough signals to suppress the background to fit the blackbody model, however, the “hot spots” may not only come from the flames created by the Al and THV chemical reaction, instead, they also probably come from the laser heating of the reaction product of carbon. (Carbon has high melting point of 3825 K.) Different from the regular flame measure from the side view with the only flame, the microscope imaged from the top of the sample, so the top view image would include both flame and the color or emission from all the materials. In this case, the “hot carbon” very likely dominates the spectra than the chemical reaction peaks.

(2) For the small local flames, the Al and THV reaction just happened, and the product of carbon should be heated to high temperature at the very first few pulse. The chemical reaction peaks were still not visible under this condition probably due to the low intensity of flame and the non-ignorable laser background. We can improve the setup and optimize the conditions if we want to the chemical peaks from small flames.

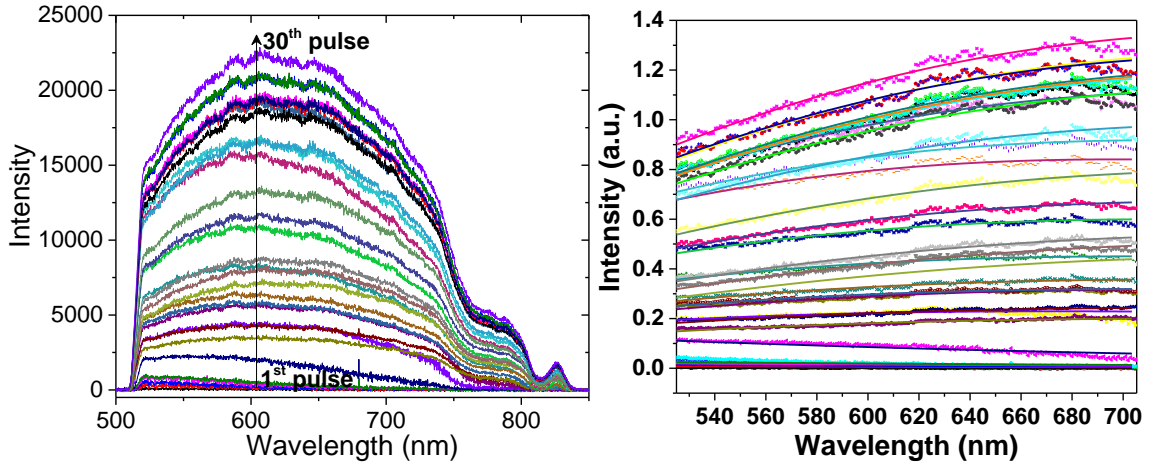


Figure 7-19 (left) Spectrum and (right) after system response calibration and fitted with the blackbody emission model for laser ignition study. Al/THV on gratings exposed to 1080 mW 466nm pulse laser (1 ms on and 49 ms off, 30 pulses) without background light, under FITC emission filter.

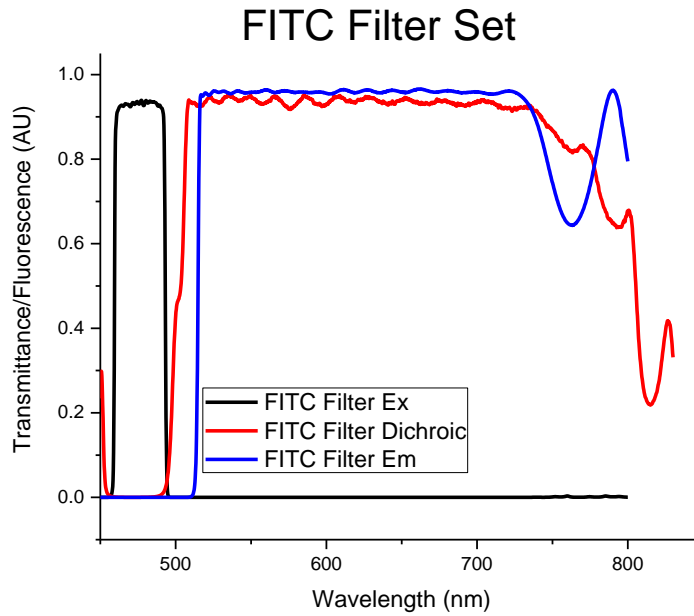


Figure 7-20 Spectra for FITC filter set including excitation, dichroic and emission filters.

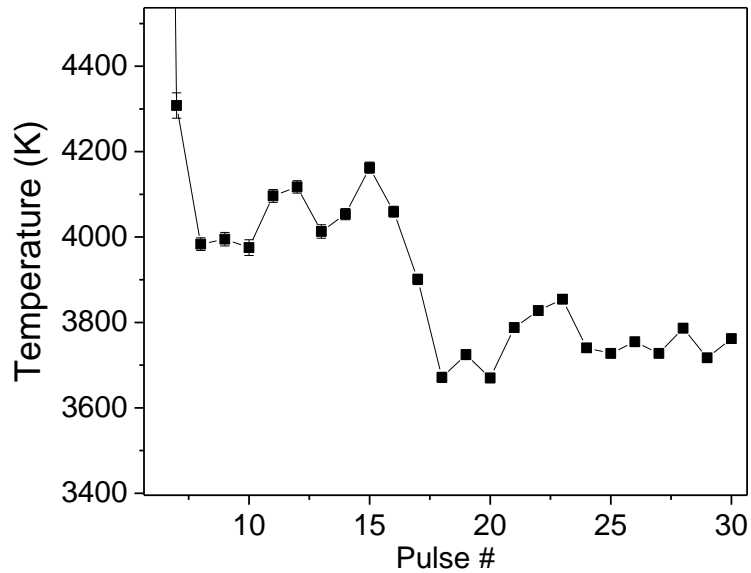


Figure 7-21 Fitted temperature (K) vs. pulse number (#). Al/THV on gratings exposed to 1080 mW 466nm pulse laser (1 ms on and 49 ms off, 30 pulses) without background light, under FITC emission filter.

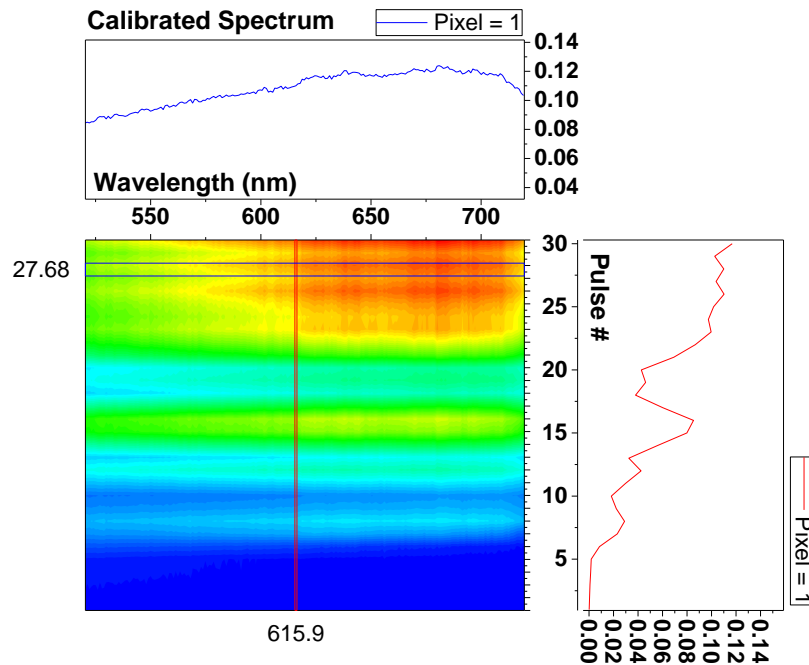


Figure 7-22 Calibrated and fitted spectra for laser ignition study over multiple pulses. Al/THV on gratings exposed to 1080 mW 466nm pulse laser (1 ms on and 49 ms off, 30 pulses) without background light, under FITC emission filter. The figure (top) shows the

calibrated spectrum at the 28th pulse, and the figure (right) shows the intensity dependency at 615.9nm over time.

7.5.5 Comparison between Grating and Flat Silver under Laser Ignition.

We compared the laser ignition spectra for the grating and flat silver regions. The samples were thick Al/THV films (~10 μm) on silver plasmonic gratings or flat silver, which was measured under the same condition, i.e. exposed to 1080 mW 466nm pulse laser (1 ms on and 49 ms off, 30 pulses) without background light, under FITC emission filter. As shown in the comparison below, the silver plasmonic grating can generate much stronger flames or “hot carbon” than the flat silver under the same condition, which proves that the plasmonic grating platforms can enhance the photo-thermal heating and ignition due to better coupling the laser. In order to make sure this is not a typical case for only one region, we tested at different areas of flat silver, which provides similar results.

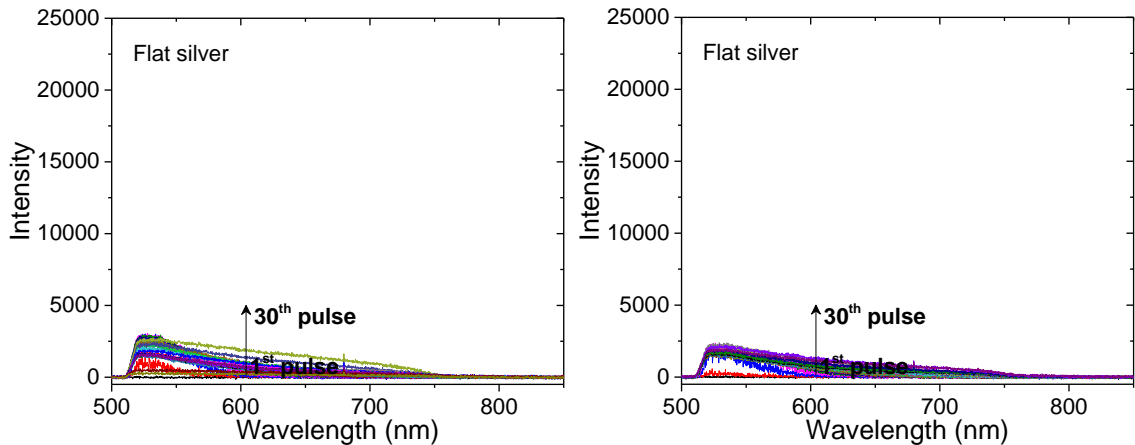


Figure 7-23 Spectrum for laser ignition study on the flat silver region (two different areas). Al/THV on flat silver exposed to 1080 mW 466nm pulse laser (1 ms on and 49 ms off, 30 pulses) without background light, under FITC emission filter.

7.5.6 Temperature Map Reconstruction for Grating under Laser Ignition.

In order to synchronize the flame spectrum measurement of the laser burned THV/Al NPs together with the two-color pyrometry (using the fast camera) through the dual eyepiece ports of the microscope, we also imaged the laser ignition process by fast camera simultaneously for the sample above during the spectra recording. The following results are from the thick Al/THV film (~10 μm) on silver plasmonic gratings, which was exposed to 1080 mW 466nm pulse laser (1 ms on and 49 ms off, 30 pulses) without background light, under FITC emission filter.

Since the spectra are the integration of all signals during 50 ms, we summed up all the frames in each pulse (50 ms pulse duration with 1 ms on) as a comparison. After summing up all frames for each channel (R, G and B), we reconstructed the temperature map using the same method as previously. We first analyzed images the 30th pulse in 30 pulses, since the big “flame” provides stronger SNR to fit the temperature in the spectra. There is a broad temperature range from 2000K to 4000K, and the most probable temperature is 3000K. For the temperature above 2743K, Al can be gasified, and Al₂O₃ can be melted. If the temperature is above 993.5K and below 2345K, that is to say, Al₂O₃ is still in a solid state while Al is in a liquid state, in that case, melt-dispersion would happen. For the last few pulses, there were lots of carbon generated besides the chemical reaction; it is meaningful to study the Al/THV reaction induced by “hot carbon” as well. For the small local flame, the analysis for the 350 μs in the 1st pulse of 30 pulses was shown below as an example. The local flame can also reach a temperature around 3000 K. We will analyze more data in the earlier pulses to more reaction process.

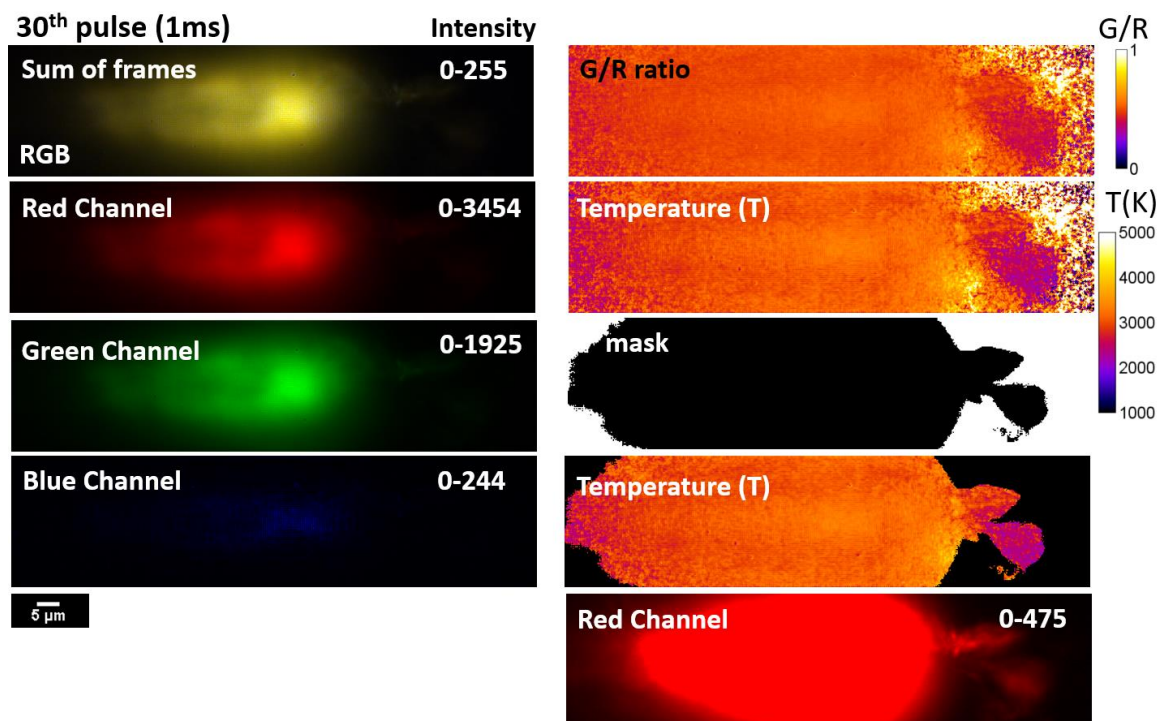


Figure 7-24 Temperature map reconstruction of the flame or “hot carbon”. Al/THV on gratings exposed to 1080 mW 466nm pulse laser (1 ms on and 49 ms off, the 30th pulse in 30 pulses) without background light, under FITC emission filter.

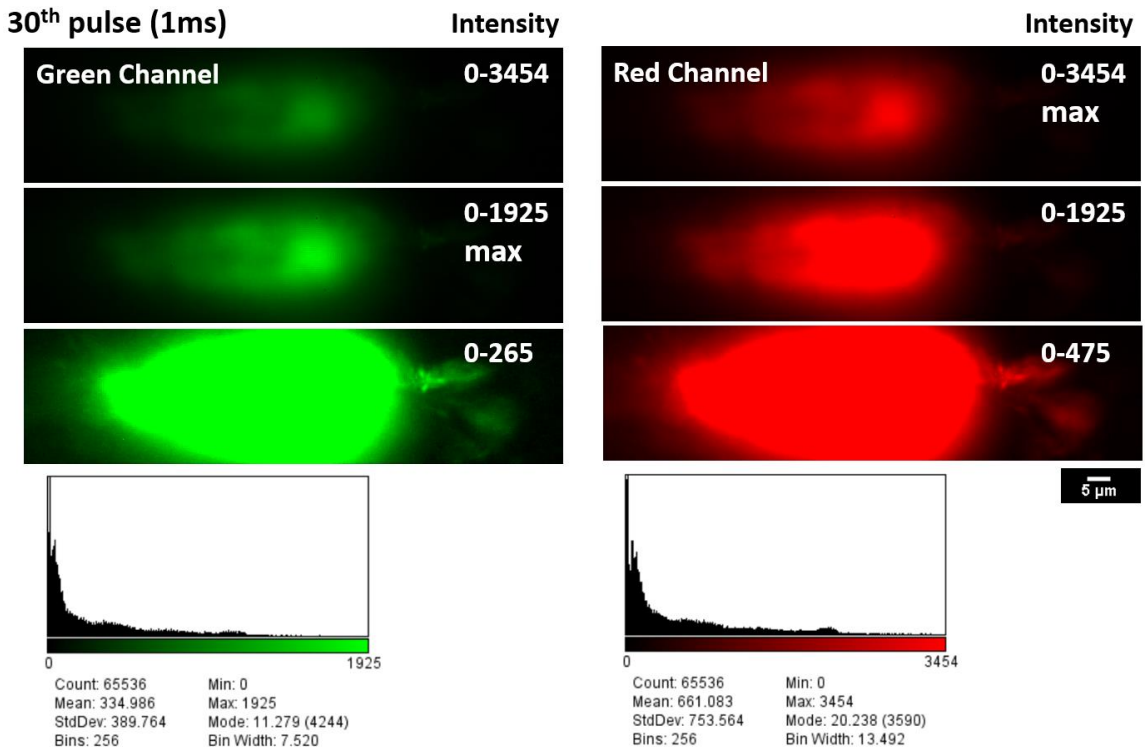


Figure 7-25 (Left) Green and (Right) red channel images with different intensity bar to show different visible structures. Al/THV on gratings exposed to 1080 mW 466nm pulse laser (1 ms on and 49 ms off, the 30th pulse in 30 pulses) without background light, under FITC emission filter.

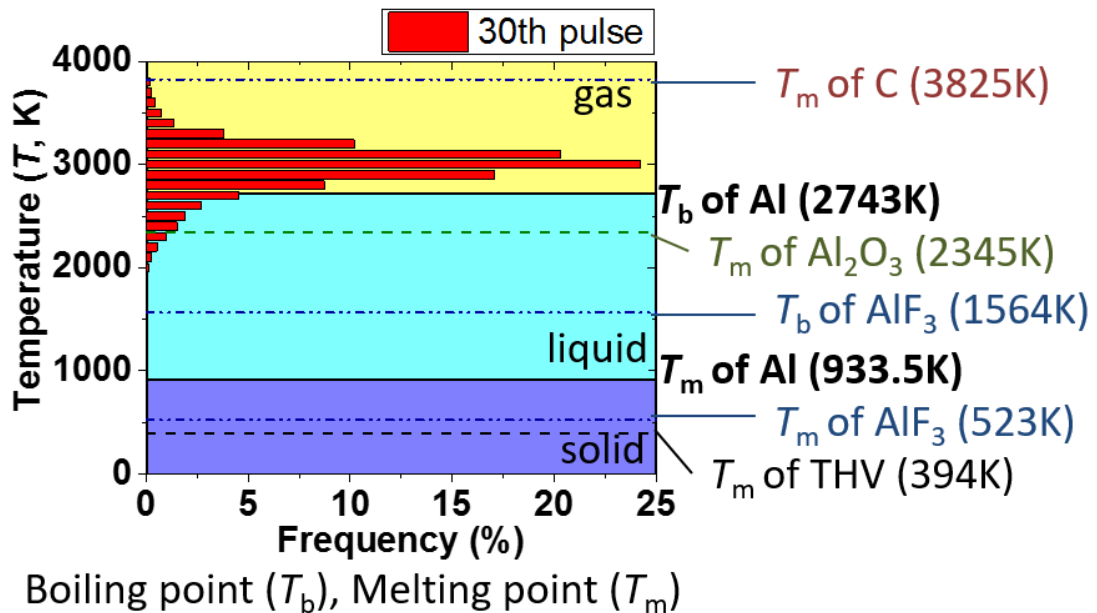


Figure 7-26 The statistical analysis for frequency vs. temperature (right) of the flame in all frames (0-1 ms). Al/THV on gratings exposed to 1080 mW 466nm pulse laser (1 ms on and 49 ms off, the 30th pulse in 30 pulses) without background light, under FITC emission filter.

1st pulse (350 μ s)

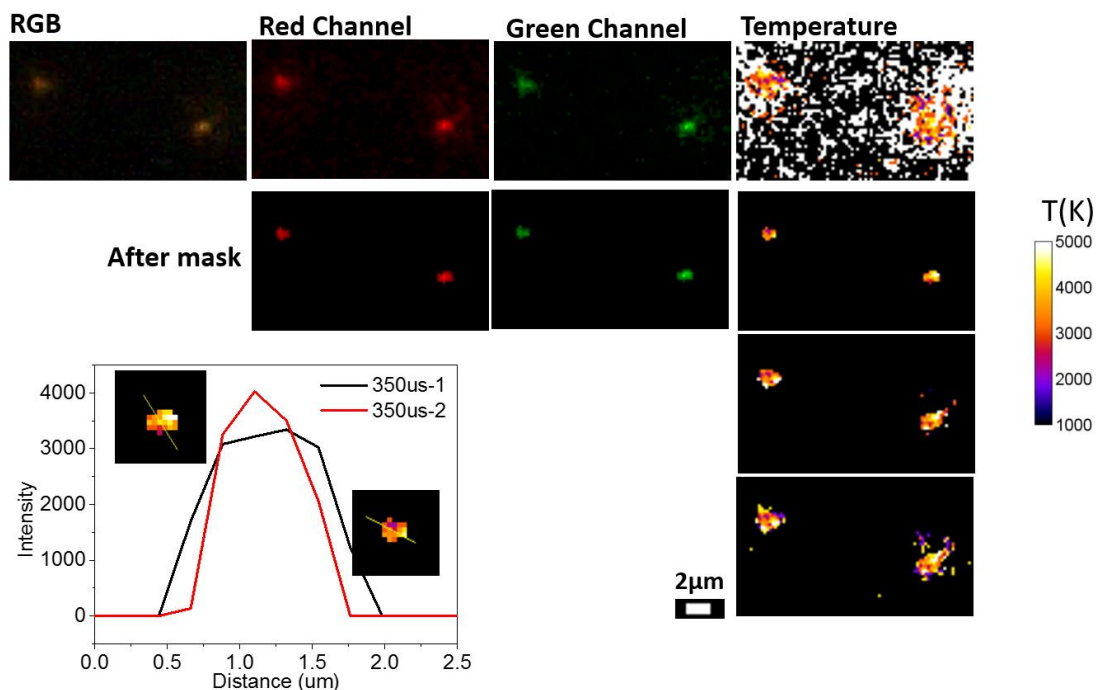


Figure 7-27 Temperature map reconstruction of the small local flame. Al/THV on gratings exposed to 1080 mW 466nm pulse laser (1 ms on and 49 ms off, 350 μ s in the 1st pulse of 30 pulses) without background light, under FITC emission filter.

7.6 Conclusion

A plasmonic grating facilitated detailed *in-situ* combustion characterization of reactive nanoenergetic films using a simple optical microscope while providing sufficient resolution to identify isolated Al NPs. The plasmonic grating microchip is critical to the characterization platform, as it enhances both the photothermal heating and spatial

resolution of the optical microscope. With this technique, combustion of Al NPs was observed within 50 μ s of irradiation, and nano-flames having an FWHM of 600 nm were identified. The combustion flame temperature was estimated to be 2,400K – 5,000K, with an average temperature of 3,900K, consistent with adiabatic flame temperature calculations. Polarized light microscopy performed before and after combustion provided a 3D representation of Al NP occupation before and after combustion. These images, coupled with *in-situ* images of combustion, provided a 3D reconstruction of flame propagation around the perimeter of Al NP agglomerates. A thermal model further clarifies the need for the plasmonic grating to ignite small Al NP clusters at low laser powers. This work represents a promising advance towards integrated nanoenergetic material and plasmonic microchip substrates for miniaturized defense, medical, and energy technologies. Further, the test platform allows the characterization of small quantities of nanoenergetic material, to improve handling safety and reduce testing costs.

7.7 Future Work

We will study the physical and chemical change of Al/THV nanothermites to reveal the reaction mechanism induced by laser. We will conduct measurements including *in-situ* imaging, *ex-situ* imaging before and after reaction by microscope, and postmortem characterization, such as SEM, TEM, energy dispersive X-ray spectroscopy (EDS), to confirm the reaction mechanism. We will study phase change, calibrate flame temperature, and analyze the reaction process and products. In addition to 446 nm laser, we will investigate other laser wavelengths to study the plasmonic effect for both LSPR of Al NPs and SPR of gratings. We will also study the effects of pulse duration and power on laser

ignition. For single Al NP *in-situ* imaging, it is better to use high-resolution (100× oil) objective, however, we cannot bring the laser due to short working distance (less than 200 μm from the sample surface) of the high-resolution objective. We will utilize a new inverted microscope with better tunability for laser input, especially we can take high-resolution *in-situ* imaging and control any laser incidence angles. Although we can ignite Al aggregates easily by current laser setup, we will purchase a very high power pulse laser for the study of single Al NP ignition in the future study. We will also extend study on another polymer oxidizer including nitrocellulose and Teflon.

Specifically, for flame temperature study, we will analyze more data in the earlier pulses to study more reaction process and calculate the theoretical flame temperature using Cheetah. We will check the temperature of tungsten lamp with an infrared thermometer (AR228) to further confirm the calibration source temperature. We will improve the setup to remove the background from laser completely by using a filter in the laser incident path. Finally, we will optimize the conditions (pulse on time, the position of the spectrometer, lens, etc) to study the chemical peaks from small flames.

REFERENCES

- [1] S. Hayashi and T. Okamoto, "Plasmonics: visit the past to know the future," *J. Phys. Appl. Phys.*, vol. 45, no. 43, p. 433001, 2012.
- [2] W. L. Barnes, A. Dereux, and T. W. Ebbesen, "Surface plasmon subwavelength optics," *Nature*, vol. 424, no. 6950, pp. 824–830, Aug. 2003.
- [3] M. Kauranen and A. V. Zayats, "Nonlinear plasmonics," *Nat. Photonics*, vol. 6, no. 11, pp. 737–748, Nov. 2012.
- [4] A. J. Wood *et al.*, "Influence of silver grain size, roughness, and profile on the extraordinary fluorescence enhancement capabilities of grating coupled surface plasmon resonance," *RSC Adv.*, vol. 5, no. 96, pp. 78534–78544, Sep. 2015.
- [5] S. Gangopadhyay *et al.*, "Nano-gap grating devices with enhanced optical properties and methods of fabrication," US20140226207 A1, 14-Aug-2014.
- [6] B. Chen, A. Pathak, K. Gangopadhyay, P. V. Cornish, and S. Gangopadhyay, "Single-molecule Detection in Nanogap-embedded Plasmonic Gratings," *Nanobiomedicine*, vol. 2, no. 8, p. 1, 2015.
- [7] S. Basuray *et al.*, "Plasmonic nano-protrusions: hierarchical nanostructures for single-molecule Raman spectroscopy," *Nanotechnology*, vol. 28, no. 2, p. 025302, 2017.
- [8] M. Li *et al.*, "Surface-Plasmon-Enhanced Raman and Photoluminescence of Few-Layers and Bulk MoS₂ on Silver Grating," 2016, p. JW2A.111.
- [9] B. Chen *et al.*, "Plasmonic gratings with nano-protrusions made by glancing angle deposition for single-molecule super-resolution imaging," *Nanoscale*, vol. 8, no. 24, pp. 12189–12201, Jun. 2016.
- [10] W.-S. Chang *et al.*, "Low absorption losses of strongly coupled surface plasmons in nanoparticle assemblies," *Proc. Natl. Acad. Sci.*, vol. 108, no. 50, pp. 19879–19884, Dec. 2011.
- [11] B. Chen *et al.*, "In-Situ Characterization of Photothermal Nanoenergetic Combustion on a Plasmonic Microchip," *ACS Appl. Mater. Interfaces*, Dec. 2017.
- [12] B. Chen, A. Pathak, K. Gangopadhyay, P. V. Cornish, and S. Gangopadhyay, "Single-molecule Detection in Nanogap-embedded Plasmonic Gratings," *Nanobiomedicine*, p. 1, 2015.
- [13] S. Basuray *et al.*, "Single Molecule Oscillations of an RNA/DNA Duplex in a Plasmonic Nanocavity," *J. Nanomedicine Nanotechnol.*, vol. 2015, 2015.
- [14] S. Barizuddin, S. Bok, and S. Gangopadhyay, "Plasmonic Sensors for Disease Detection-A Review," *J Nanomed Nanotechnol*, vol. 7, no. 373, p. 2, 2016.
- [15] K. Bhatnagar, A. Pathak, D. Menke, P. V. Cornish, and K. Gangopadhyay, "Fluorescence enhancement from nano-gap embedded plasmonic gratings by a novel fabrication technique with HD-DVD," *Nanotechnology*, vol. 23, p. 495201, 2012.
- [16] C. M. Darr, V. Korampally, B. Chen, K. Gangopadhyay, and S. Gangopadhyay, "Plasmonic-enhanced conjugated polymer fluorescence chemosensor for trace nitroaromatic vapor," *Sens. Actuators B Chem.*, vol. 202, no. 2014, pp. 1088–1096, Oct. 2014.
- [17] B. Chen, C. J. Mathai, S. Mukherjee, and S. Gangopadhyay, "Indium Tin Oxide Photonic Crystal for Controllable Light Coupling in Solar Cells by an Inexpensive Soft Lithography with HD-DVD and Blu-ray," *ECS Trans.*, vol. 61, no. 18, pp. 69–82, 2014.
- [18] B. Chen *et al.*, "In-Situ Characterization of Photothermal Nanoenergetic Combustion on a Plasmonic Microchip," *ACS Appl. Mater. Interfaces*, Dec. 2017.

- [19] B. Chen *et al.*, “Super-resolution Imaging of Silver Nanostructures on Plasmonic Grating,” 2016, p. STh3H.1.
- [20] B. Chen *et al.*, “Fluorescence-based temperature sensor for in-situ imaging local temperature of aluminum nanoparticles on plasmonic gratings,” 2016, pp. 1–3.
- [21] B. Chen *et al.*, “In Situ Characterization of Photothermal Nanoenergetic Combustion on a Plasmonic Microchip,” *ACS Appl. Mater. Interfaces*, Dec. 2017.
- [22] A. Wood *et al.*, “Super-Resolution Light Microscopy Using Plasmonic Gratings,” *Microsc. Today*, vol. 25, no. 1, pp. 42–47, Jan. 2017.
- [23] A. Wood *et al.*, “Anti-corrosive films on silver plasmonic gratings for fluorescence imaging of single molecules and cancer cells,” in *2016 Conference on Lasers and Electro-Optics (CLEO)*, 2016, pp. 1–2.
- [24] B. Chen *et al.*, “Super-resolution Imaging of Silver Nanostructures on Plasmonic Grating,” in *Conference on Lasers and Electro-Optics (2016)*, paper STh3H.1, 2016, p. STh3H.1.
- [25] S. Bok *et al.*, “Highly sensitive plasmonic grating platform for the detection of a wide range of infectious diseases,” in *2015 Transducers - 2015 18th International Conference on Solid-State Sensors, Actuators and Microsystems (TRANSDUCERS)*, 2015, pp. 1573–1576.
- [26] B. Chen *et al.*, “Fluorescence-based temperature sensor for in-situ imaging local temperature of aluminum nanoparticles on plasmonic gratings,” in *2016 IEEE SENSORS*, 2016, pp. 1–3.
- [27] A. Wood *et al.*, “Super Resolution Fluorescent Imaging and Biosensing Applications of Plasmonic Gratings with Nanoprotrusions,” in *Advanced Photonics 2017 (IPR, NOMA, Sensors, Networks, SPPCom, PS) (2017)*, paper SeTu1E.1, 2017, p. SeTu1E.1.
- [28] C. G. Galbraith and J. A. Galbraith, “Super-resolution microscopy at a glance,” *J. Cell Sci.*, vol. 124, no. Pt 10, pp. 1607–1611, 2011.
- [29] D. S. Kim, J. Heo, S. H. Ahn, S. W. Han, W. S. Yun, and Z. H. Kim, “Real-space mapping of the strongly coupled plasmons of nanoparticle dimers,” *Nano Lett.*, vol. 9, no. 10, pp. 3619–3625, 2009.
- [30] B. Y. T. D. Harris, R. D. Grober, J. K. Trautman, E. Betzig, T. B. Laboratories, and I. A. Room, “focal point Super-Resolution Imaging Spectroscopy,” 1994.
- [31] L. Schermelleh, R. Heintzmann, and H. Leonhardt, “A guide to super-resolution fluorescence microscopy,” *J. Cell Biol.*, vol. 190, no. 2, pp. 165–75, Jul. 2010.
- [32] G. Shtengel *et al.*, “Interferometric fluorescent super-resolution microscopy resolves 3D cellular ultrastructure,” *Proc. Natl. Acad. Sci. U. S. A.*, vol. 106, no. 9, pp. 3125–3130, 2009.
- [33] Y. Wang, G. Fruhwirth, E. Cai, T. Ng, and P. R. Selvin, “3D super-resolution imaging with blinking quantum dots,” *Nano Lett.*, vol. 13, no. 11, pp. 5233–5241, 2013.
- [34] Z. Liu *et al.*, “Far-Field Optical Superlens,” *Nano Lett.*, vol. 7, no. 2, pp. 403–408, Feb. 2007.
- [35] Y. Fu and X. Zhou, “Plasmonic Lenses: A Review,” *Plasmonics*, vol. 5, pp. 287–310, 2010.
- [36] Z. Xie *et al.*, “Plasmonic Nanolithography: A Review,” *Plasmonics*, vol. 6, no. 3, pp. 565–580, 2011.
- [37] X. Zhang and Z. Liu, “Superlenses to overcome the diffraction limit,” *Nat. Mater.*, vol. 7, no. 6, pp. 435–441, 2008.
- [38] Y. Xiong, Z. Liu, C. Sun, and X. Zhang, “Two-dimensional imaging by far-field superlens at visible wavelengths,” *Nano Lett.*, vol. 7, no. 11, pp. 3360–3365, 2007.
- [39] S. Kawata, Y. Inouye, and P. Verma, “Plasmonics for near-field nano-imaging and superlensing,” *Nat. Photonics*, vol. 3, no. 7, pp. 388–394, 2009.

- [40] J. B. Pendry, "Negative refraction makes a perfect lens," *Phys. Rev. Lett.*, vol. 85, no. 18, pp. 3966–3969, 2000.
- [41] S. T. Hess, T. J. Gould, M. Gunewardene, J. Bewersdorf, and M. D. Mason, "Ultra-high resolution imaging of biomolecules by fluorescence photoactivation localization microscopy.," *Methods Mol. Biol. Clifton NJ*, vol. 544, pp. 483–522, 2009.
- [42] E. Betzig *et al.*, "Imaging intracellular fluorescent proteins at nanometer resolution.," *Science*, vol. 313, no. 5793, pp. 1642–1645, 2006.
- [43] M. J. Rust, M. Bates, and X. Zhuang, "Sub-diffraction-limit imaging by stochastic optical reconstruction microscopy (STORM).," *Nat. Methods*, vol. 3, no. 10, pp. 793–795, 2006.
- [44] M. Bates, S. A. Jones, and X. Zhuang, "Stochastic optical reconstruction microscopy (STORM): A method for superresolution fluorescence imaging," *Cold Spring Harb. Protoc.*, vol. 8, no. 6, pp. 498–520, 2013.
- [45] S. W. Hell and J. Wichmann, "Breaking the diffraction resolution limit by stimulated emission: stimulated-emission-depletion fluorescence microscopy.," *Opt. Lett.*, vol. 19, no. 11, pp. 780–782, 1994.
- [46] Y. Wang, W. Srituravanich, C. Sun, and X. Zhang, "Plasmonic nearfield scanning probe with high transmission," *Nano Lett.*, vol. 8, no. 9, pp. 3041–3045, 2008.
- [47] V. I. Levitas and K. Samani, "Size and mechanics effects in surface-induced melting of nanoparticles," *Nat. Commun.*, vol. 2, p. 284, Apr. 2011.
- [48] Y. Chen *et al.*, "Ultra-fast self-assembly and stabilization of reactive nanoparticles in reduced graphene oxide films," *Nat. Commun.*, vol. 7, p. 12332, Aug. 2016.
- [49] R. Thiruvengadathan *et al.*, "Combustion Behavior of Nanoenergetic Material Systems," in *Energetic Materials*, 0 vols., CRC Press, 2010, pp. 221–262.
- [50] R. Thiruvengadathan *et al.*, "Combustion Characteristics of Silicon-Based Nanoenergetic Formulations with Reduced Electrostatic Discharge Sensitivity," *Propellants Explos. Pyrotech.*, vol. 37, no. 3, pp. 359–372, Jun. 2012.
- [51] C. R. Becker *et al.*, "Galvanic Porous Silicon Composites for High-Velocity Nanoenergetics," *Nano Lett.*, vol. 11, no. 2, pp. 803–807, Feb. 2011.
- [52] C. S. Staley, C. J. Morris, R. Thiruvengadathan, S. J. Apperson, K. Gangopadhyay, and S. Gangopadhyay, "Silicon-based bridge wire micro-chip initiators for bismuth oxide–aluminum nanothermite," *J. Micromechanics Microengineering*, vol. 21, no. 11, p. 115015, 2011.
- [53] R. Shende *et al.*, "Nanoenergetic Composites of CuO Nanorods, Nanowires, and Al-Nanoparticles," *Propellants Explos. Pyrotech.*, vol. 33, no. 2, pp. 122–130, Apr. 2008.
- [54] S. J. Apperson *et al.*, "Characterization of Nanothermite Material for Solid-Fuel Microthruster Applications," *J. Propuls. Power*, vol. 25, no. 5, pp. 1086–1091, Sep. 2009.
- [55] C. S. Staley *et al.*, "Fast-Impulse Nanothermite Solid-Propellant Miniaturized Thrusters," *J. Propuls. Power*, vol. 31, no. 1, pp. 483–483, 2015.
- [56] Y. Gan, Z. Chen, K. Gangopadhyay, A. Bezmelnitsyn, and S. Gangopadhyay, "An equation of state for the detonation product of copper oxide/aluminum nanothermite composites," *J. Nanoparticle Res.*, vol. 12, no. 3, pp. 719–726, Mar. 2010.
- [57] A. Bezmelnitsyn *et al.*, "Modified Nanoenergetic Composites with Tunable Combustion Characteristics for Propellant Applications," *Propellants Explos. Pyrotech.*, vol. 35, no. 4, pp. 384–394, Aug. 2010.
- [58] M. Korampally *et al.*, "Transient pressure mediated intranuclear delivery of FITC-Dextran into chicken cardiomyocytes by MEMS-based nanothermite reaction actuator," *Sens. Actuators B Chem.*, vol. 171–172, pp. 1292–1296, Aug. 2012.

- [59] S. Apperson, S. Gangopadhyay, L. Polo-Parada, A. Bezmelnitsyn, and K. Gangopadhyay, "Device for transfecting cells using shock waves generated by the ignition of nanoenergetic materials," US20090105738 A1, 23-Apr-2009.
- [60] "Nanothermite-Based Microsystem for Drug Delivery and Cell Transfection (PDF Download Available)," *ResearchGate*. [Online]. Available: https://www.researchgate.net/publication/235196096_Nanothermite-Based_Microsystem_for_Drug_Delivery_and_Cell_Transfection. [Accessed: 27-Mar-2017].
- [61] B.-D. Lee *et al.*, "Ultra-rapid elimination of biofilms via the combustion of a nanoenergetic coating," *BMC Biotechnol.*, vol. 13, p. 30, 2013.
- [62] G. A. A. Rodríguez *et al.*, "A microactuator based on the decomposition of an energetic material for disposable lab-on-chip applications: fabrication and test," *J. Micromechanics Microengineering*, vol. 19, no. 1, p. 015006, 2009.
- [63] S. Apperson *et al.*, "Generation of fast propagating combustion and shock waves with copper oxide/aluminum nanothermite composites," *Appl. Phys. Lett.*, vol. 91, no. 24, p. 243109, Dec. 2007.
- [64] R. W. Conner and D. D. Dlott, "Time-Resolved Spectroscopy of Initiation and Ignition of Flash-Heated Nanoparticle Energetic Materials," *J. Phys. Chem. C*, vol. 116, no. 28, pp. 14737–14747, Jul. 2012.
- [65] R. Thiruvengadathan *et al.*, "Combustion characteristics of novel hybrid nanoenergetic formulations," *Combust. Flame*, vol. 158, no. 5, pp. 964–978, 2011.
- [66] S. Wang, Y. Yang, Z. Sun, and D. D. Dlott, "Fast spectroscopy of energy release in nanometric explosives," *Chem. Phys. Lett.*, vol. 368, no. 1–2, pp. 189–194, Jan. 2003.
- [67] R. W. Conner and D. D. Dlott, "Ultrafast Condensed-Phase Emission from Energetic Composites of Teflon and Nanoaluminum," *J. Phys. Chem. A*, vol. 114, no. 25, pp. 6731–6741, Jul. 2010.
- [68] K. W. Watson, M. L. Pantoya, and V. I. Levitas, "Fast reactions with nano- and micrometer aluminum: A study on oxidation versus fluorination," *Combust. Flame*, vol. 155, no. 4, pp. 619–634, Dec. 2008.
- [69] Y. Yang, Z. Sun, S. Wang, and D. D. Dlott, "Fast Spectroscopy of Laser-Initiated Nanoenergetic Materials," *J. Phys. Chem. B*, vol. 107, no. 19, pp. 4485–4493, May 2003.
- [70] Y. Yang, S. Wang, Z. Sun, and D. D. Dlott, "Propagation of shock-induced chemistry in nanoenergetic materials: The first micrometer," *J. Appl. Phys.*, vol. 95, no. 7, pp. 3667–3676, Mar. 2004.
- [71] F. R. Kearney, H. Yu, and D. D. Dlott, "Time-Resolved Microscopy Analysis of Laser Photothermal Imaging Media," *J. Imaging Sci. Technol.*, vol. 50, no. 5, pp. 401–410, Sep. 2006.
- [72] "In situ imaging of ultra-fast loss of nanostructure in nanoparticle aggregates," *J. Appl. Phys.*, vol. 115, no. 8, p. 084903, Feb. 2014.
- [73] M. A. Zamkov, R. W. Conner, and D. D. Dlott, "Ultrafast Chemistry of Nanoenergetic Materials Studied by Time-Resolved Infrared Spectroscopy: Aluminum Nanoparticles in Teflon," *J. Phys. Chem. C*, vol. 111, no. 28, pp. 10278–10284, Jul. 2007.
- [74] J. E. Abboud *et al.*, "Photothermally activated motion and ignition using aluminum nanoparticles," *Appl. Phys. Lett.*, vol. 102, no. 2, p. 023905, Jan. 2013.
- [75] D. E. Hare, S. T. Rhea, D. D. Dlott, R. J. D'Amato, and T. E. Lewis, "Pulse Duration Dependence of Lithographic Printing Plate Imaging by Near-Infrared Lasers," *J. Imaging Sci. Technol.*, vol. 42, no. 2, pp. 187–193, Mar. 1998.

- [76] "Propagation of shock-induced chemistry in nanoenergetic materials: The first micrometer." [Online]. Available: <http://connection.ebscohost.com/c/articles/12556231/propagation-shock-induced-chemistry-nanoenergetic-materials-first-micrometer>. [Accessed: 11-Mar-2017].
- [77] P. Vashishta, R. K. Kalia, and A. Nakano, "Multimillion Atom Simulations of Dynamics of Oxidation of an Aluminum Nanoparticle and Nanoindentation on Ceramics," *J. Phys. Chem. B*, vol. 110, no. 8, pp. 3727–3733, Mar. 2006.
- [78] P. Vashishta, R. K. Kalia, A. Nakano, B. E. Homan, and K. L. McNesby, "Multimillion Atom Reactive Simulations of Nanostructured Energetic Materials," *J. Propuls. Power*, vol. 23, no. 4, pp. 688–692, Jul. 2007.
- [79] "Fast reaction mechanism of a core(Al)-shell (Al₂O₃) nanoparticle in oxygen."
- [80] V. Levitas, "Burn time of aluminum nanoparticles: Strong effect of the heating rate and melt-dispersion mechanism," *Combust. Flame*, vol. 156, no. 2, pp. 543–546.
- [81] V. I. Levitas, "Mechanochemical mechanism for reaction of aluminium nano- and micrometre-scale particles," *Philos. Trans. R. Soc. Lond. Math. Phys. Eng. Sci.*, vol. 371, no. 2003, p. 20120215, Nov. 2013.
- [82] V. I. Levitas, M. L. Pantoya, and S. Dean, "Melt dispersion mechanism for fast reaction of aluminum nano- and micron-scale particles: Flame propagation and SEM studies," *Combust. Flame*, vol. 161, no. 6, pp. 1668–1677, Jun. 2014.
- [83] R. W. Conner and D. D. Dlott, "Comparing Boron and Aluminum Nanoparticle Combustion in Teflon Using Ultrafast Emission Spectroscopy," *J. Phys. Chem. C*, vol. 116, no. 4, pp. 2751–2760, Feb. 2012.
- [84] M. L. Pantoya and S. W. Dean, "The influence of alumina passivation on nano-Al/Teflon reactions," *Thermochim. Acta*, vol. 493, no. 1–2, pp. 109–110, Sep. 2009.
- [85] C. A. Crouse, "Fluorinated Polymers as Oxidizers for Energetic Composites," in *Advances in Fluorine-Containing Polymers*, vol. 1106, 0 vols., American Chemical Society, 2012, pp. 127–140.
- [86] M.-V. Coulet, B. Rufino, P.-H. Esposito, T. Neisius, O. Isnard, and R. Denoyel, "Oxidation Mechanism of Aluminum Nanopowders," *J. Phys. Chem. C*, vol. 119, no. 44, pp. 25063–25070, Nov. 2015.
- [87] R. J. Jacob, G. Jian, P. M. Guerieri, and M. Zachariah, "Gas vs. Condensed Phase Reactions in Nano-Thermites," in *52nd Aerospace Sciences Meeting*, American Institute of Aeronautics and Astronautics.
- [88] "Point spread function," *Wikipedia*. 12-Oct-2016.
- [89] E. Wertz, B. P. Isaacoff, J. D. Flynn, and J. S. Biteen, "Single-Molecule Super-Resolution Microscopy Reveals How Light Couples to a Plasmonic Nanoantenna on the Nanometer Scale," *Nano Lett.*, p. 150326093550005, 2015.
- [90] K. a Willets, "Super-resolution imaging of interactions between molecules and plasmonic nanostructures.," *Phys. Chem. Chem. Phys. PCCP*, vol. 15, no. 15, pp. 5345–54, 2013.
- [91] S. M. Stranahan and K. a. Willets, "Super-resolution optical imaging of single-molecule SERS hot spots," *Nano Lett.*, vol. 10, no. 9, pp. 3777–3784, 2010.
- [92] P. Holzmeister, G. P. Acuna, D. Grohmann, and P. Tinnefeld, "Breaking the concentration limit of optical single-molecule detection.," *Chem. Soc. Rev.*, vol. 43, no. 4, pp. 1014–28, Feb. 2014.
- [93] D. Punj *et al.*, "A plasmonic 'antenna-in-box' platform for enhanced single-molecule analysis at micromolar concentrations.," *Nat. Nanotechnol.*, vol. 8, no. 7, pp. 512–6, 2013.

- [94] S. Basuray *et al.*, "Single Molecule Oscillations of an RNA/DNA Duplex in a Plasmonic Nanocavity," *J. Nanomedicine Nanotechnol.*, vol. 06, no. 03, p. 1, 2015.
- [95] S. Bok *et al.*, "Confeito-like Assembly of Organosilicate-caged Fluorophores: Ultrabright Suprananoparticles for Fluorescence Imaging," *Nanotechnology*, vol. 23, no. 17, p. 175601, May 2012.
- [96] J.E. Greene, *Handbook of Deposition Technologies for Films and Coatings*, 3rd ed. William Andrew Publishing, 2010.
- [97] W. M. Haynes, *CRC Handbook of Chemistry and Physics, 96th Edition*. CRC Press, 2015.
- [98] and M. J. B. M. T. Taschuk, M. M. Hawkeye, "Chapter 13 - Glancing Angle Deposition," in *Handbook of Deposition Technologies for Films and Coatings*, 3rd ed., Boston, Ed. William Andrew Publishing, 2010, pp. 621–678.
- [99] E. Kretschmann and H. Raether, "Radiative decay of non-radiative surface plasmons excited by light," *Z Naturforsch*, vol. 23, pp. 2135–2136, 1968.
- [100] P. R. West, S. Ishii, G. V. Naik, N. K. Emani, V. M. Shalaev, and a. Boltasseva, "Searching for better plasmonic materials," *Laser Photonics Rev.*, vol. 4, no. 6, pp. 795–808, Nov. 2010.
- [101] S. Kawata, Y. Inouye, and P. Verma, "Plasmonics for near-field nano-imaging and superlensing," *Nat. Photonics*, vol. 3, no. 7, pp. 388–394, 2009.
- [102] J. Kim, D.-C. Kim, N. Ken, T. Mitsui, and H. Aoki, "Determination of spatial resolution of aperture-type near-field scanning optical microscope using a standard sample of quantum-dot embedded polymer film," *J. Korean Phys. Soc.*, vol. 56, no. 6, p. 1748, Jun. 2010.
- [103] P. Anger, P. Bharadwaj, and L. Novotny, "Enhancement and quenching of single-molecule fluorescence," *Phys. Rev. Lett.*, vol. 96, 2006.
- [104] I. Gryczynski, J. Malicka, Z. Gryczynski, and J. Lakowicz, "Radiative decay engineering 4. Experimental studies of surface plasmon-coupled directional emission," *Anal. Biochem.*, vol. 324, no. 2, pp. 170–182, 2004.
- [105] J. Lakowicz, "Radiative decay engineering 3. Surface plasmon-coupled directional emission," *Anal. Biochem.*, vol. 324, no. 2, pp. 153–169, 2004.
- [106] W. L. Barnes, T. W. Preist, S. C. Kitson, and J. R. Sambles, "Physical origin of photonic energy gaps in the propagation of surface plasmons on gratings," *Phys. Rev. B*, vol. 54, no. 9, pp. 6227–6244, Sep. 1996.
- [107] P. Dedecker, B. Muls, J. Hofkens, J. Enderlein, and J. Hotta, "Orientational effects in the excitation and de-excitation of single molecules interacting with donut-mode laser beams," *Opt. Express*, vol. 15, no. 6, p. 3372, 2007.
- [108] R. Roy, S. Hohng, and T. Ha, "A practical guide to single-molecule FRET," *Nat. Methods*, vol. 5, no. 6, pp. 507–516, Jun. 2008.
- [109] Y. Chen, N. C. Deffenbaugh, C. T. Anderson, and W. O. Hancock, "Molecular counting by photobleaching in protein complexes with many subunits: best practices and application to the cellulose synthesis complex," *Mol. Biol. Cell*, vol. 25, no. 22, pp. 3630–3642, Nov. 2014.
- [110] G. Das, E. Battista, G. Manzo, F. Causa, P. A. Netti, and E. Di Fabrizio, "Large-Scale Plasmonic nanoCones Array For Spectroscopy Detection," *ACS Appl. Mater. Interfaces*, vol. 7, no. 42, pp. 23597–23604, Oct. 2015.
- [111] J. R. Lakowicz, J. Malicka, I. Gryczynski, and Z. Gryczynski, "Directional surface plasmon-coupled emission: A new method for high sensitivity detection," *Biochem. Biophys. Res. Commun.*, vol. 307, no. 3, pp. 435–439, Aug. 2003.

- [112] S. Lsq *et al.*, “correspondence rapid STORM : accurate , fast open-source software for localization microscopy ORCAE : online resource for community annotation of eukaryotes,” vol. 9, no. 11, pp. 1040–1042, 2012.
- [113] F. Huang, S. L. Schwartz, J. M. Byars, and K. A. Lidke, “Simultaneous multiple-emitter fitting for single molecule super-resolution imaging,” *Biomed. Opt. Express*, vol. 2, no. 5, p. 1377, May 2011.
- [114] M. Ovesný, P. Křížek, J. Borkovec, Z. Svindrych, and G. M. Hagen, “ThunderSTORM: a comprehensive ImageJ plug-in for PALM and STORM data analysis and super-resolution imaging,” *Bioinformatics*, vol. 30, no. 16, pp. 2389–2390, 2014.
- [115] P. Zhu and H. G. Craighead, “Zero-Mode Waveguides for Single-Molecule Analysis,” *Annu. Rev. Biophys.*, vol. 41, no. 1, pp. 269–293, 2012.
- [116] H. Zheng and S. Gangopadhyay, “Molecularly Imprinted Organic Transistor-Based Sensor For Selective Trace Chemical Vapor Detection,” 2015.
- [117] H. Zheng, B. Ramalingam, V. Korampally, and S. Gangopadhyay, “Large sensitivity enhancement in semiconducting organic field effect transistor sensors through incorporation of ultra-fine platinum nanoparticles,” *Appl. Phys. Lett.*, vol. 103, pp. 193305–193305, Nov. 2013.
- [118] H. Zheng *et al.*, “Room temperature Coulomb blockade effects in Au nanocluster/pentacene single electron transistors,” *Nanotechnology*, vol. 26, no. 35, p. 355204, Sep. 2015.
- [119] H. Zheng, Y. Zhou, and S. Gangopadhyay, “Size-dependent work function and single electron memory behavior of pentacene non-volatile memory with embedded sub-nanometer platinum nanoparticles,” *J. Appl. Phys.*, vol. 117, p. 024504, Jan. 2015.
- [120] H. Zheng, S. Mukherjee, K. Gangopadhyay, and S. Gangopadhyay, “Ultrafine Pt nanoparticle induced doping/strain of single layer graphene: experimental corroboration between conduction and Raman characteristics,” *J. Mater. Sci. Mater. Electron.*, vol. 26, no. 7, pp. 4746–4753, Apr. 2015.
- [121] H. Zheng *et al.*, “Room temperature Coulomb blockade effects in Au nanocluster/pentacene single electron transistors,” *Nanotechnology*, vol. 26, p. 355204, Sep. 2015.
- [122] H. Zheng, S. Mukherjee, and K. Gangopadhyay, “Effect of Sub 1-Nm Pt Nanoparticle on the Conduction Properties of Graphene Based Field Effect Transistor,” in *ECS Transactions*, 2014, vol. 61.
- [123] D. Suresh, A. Zambre, and N. Chanda, “Bombesin Peptide Conjugated Gold Nanocages Internalize via Clathrin Mediated Endocytosis,” *Bioconjug. Chem.*, vol. 25, pp. 1565–1579, 2014.
- [124] S. Yushmanov, J. Crompton, and K. Koppenhoefer, “Mie Scattering of Electromagnetic Waves,” in *Proceedings of 2013 COMSOL Conference*, Boston.
- [125] X. Chong, N. Jiang, Z. Zhang, S. Roy, and J. R. Gord, “Plasmonic resonance-enhanced local photothermal energy deposition by aluminum nanoparticles,” *J. Nanoparticle Res.*, vol. 15, no. 6, pp. 1–10, May 2013.
- [126] S. K. Jha, Z. Ahmed, M. Agio, Y. Ekinci, and J. F. Löffler, “Deep-UV Surface-Enhanced Resonance Raman Scattering of Adenine on Aluminum Nanoparticle Arrays,” *J. Am. Chem. Soc.*, vol. 134, no. 4, pp. 1966–1969, Feb. 2012.
- [127] A. Govorov and H. Richardson, “Generating heat with metal nanoparticles,” *Nano Today*, vol. 2, no. 1, pp. 30–38, 2007.
- [128] P. West, S. Ishii, and G. Naik, “Searching for better plasmonic materials,” *Laser Photonics Rev.*, pp. 1–13, 2010.

- [129] X. Chong, N. Jiang, Z. Zhang, S. Roy, and J. R. Gord, "Plasmonic resonance-enhanced local photothermal energy deposition by aluminum nanoparticles," *J Nanopart Res*, vol. 15, pp. 1678–1677, 2013.
- [130] H. M. Pollock and A. Hammiche, "Micro-thermal analysis: techniques and applications," *J. Phys. Appl. Phys.*, vol. 34, no. 9, p. R23, 2001.
- [131] G. Baffou, M. P. Kreuzer, F. Kulzer, and R. Quidant, "Temperature mapping near plasmonic nanostructures using fluorescence polarization anisotropy," *Opt. Express*, vol. 17, no. 5, pp. 3291–3298, Mar. 2009.
- [132] B. R. Anderson, R. Gunawidjaja, and H. Eilers, "Spectroscopic Signatures of Sub-Second Laser-Calcined Dy³⁺-Doped Oxide Precursors for Use in ex Situ Thermal Impulse Sensors," *J. Phys. Chem. C*, Aug. 2017.
- [133] J. W. Pomeroy *et al.*, "Thermal mapping of defects in AlGaN/GaN heterostructure field-effect transistors using micro-Raman spectroscopy," *Appl. Phys. Lett.*, vol. 87, no. 10, p. 103508, Sep. 2005.
- [134] B. R. Anderson, R. Gunawidjaja, P. Price, and H. Eilers, "Spectroscopic determination of thermal impulse in sub-second heating events using lanthanide-doped oxide precursors and phenomenological modeling," *J. Appl. Phys.*, vol. 120, no. 8, p. 083102, Aug. 2016.
- [135] R. Gunawidjaja, B. R. Anderson, P. Price, H. Diez-y-Riega, and H. Eilers, "Sub-second laser heating of thermal impulse sensors," *AIP Conf. Proc.*, vol. 1793, no. 1, p. 060014, Jan. 2017.
- [136] I. I. Vlasov *et al.*, "Molecular-sized fluorescent nanodiamonds," *Nat. Nanotechnol.*, vol. 9, no. 1, pp. 54–58, Jan. 2014.
- [137] S. Gangopadhyay and V. Korampally, "Nano-gap grating devices with enhanced optical properties and methods of fabrication," US 20140226207 A1, 2014.
- [138] C. Cao *et al.*, "A twisted-intramolecular-charge-transfer (TICT) based ratiometric fluorescent thermometer with a mega-Stokes shift and a positive temperature coefficient," *Chem. Commun.*, vol. 50, no. 99, pp. 15811–15814, 2014.
- [139] Y. Ekinci, H. H. Solak, and J. F. Löffler, "Plasmon resonances of aluminum nanoparticles and nanorods," *J. Appl. Phys.*, vol. 104, no. 8, p. 083107, Oct. 2008.
- [140] M. W. Knight, N. S. King, L. Liu, H. O. Everitt, P. Nordlander, and N. J. Halas, "Aluminum for Plasmonics," *ACS Nano*, vol. 8, no. 1, pp. 834–840, Jan. 2014.
- [141] M. W. Knight *et al.*, "Aluminum Plasmonic Nanoantennas," *Nano Lett.*, vol. 12, no. 11, pp. 6000–6004, Nov. 2012.
- [142] M. J. McClain *et al.*, "Aluminum Nanocrystals," *Nano Lett.*, vol. 15, no. 4, pp. 2751–2755, Apr. 2015.
- [143] G. H. Chan, J. Zhao, G. C. Schatz, and R. P. V. Duyne, "Localized Surface Plasmon Resonance Spectroscopy of Triangular Aluminum Nanoparticles," *J. Phys. Chem. C*, vol. 112, no. 36, pp. 13958–13963, Sep. 2008.
- [144] M. W. Beckstead, "A Summary of Aluminum Combustion," in *RTO/VKI Special Course on "Internal Aerodynamics in Solid Rocket Propulsion"; Rhode-Saint-Genese, Belgium, Volume RTO-EN-023*, 2002.
- [145] A. Ahmadvand, N. Pala, and D. Ö. Güney, "Enhancement of photothermal heat generation by metallodielectric nanoplasmonic clusters," *Opt. Express*, vol. 23, no. 11, pp. A682–A691, Jun. 2015.
- [146] S. Lepeshov *et al.*, "Fine-Tuning of the Magnetic Fano Resonance in Hybrid Oligomers via fs-Laser-Induced Reshaping," *ACS Photonics*, vol. 4, no. 3, pp. 536–543, Mar. 2017.
- [147] A. G. Mathewson and H. P. Myers, "Optical absorption in aluminium and the effect of temperature," *J. Phys. F Met. Phys.*, vol. 2, no. 2, p. 403, 1972.

LIST OF PUBLICATIONS

JOURNAL PUBLICATIONS

1. **B. Chen**, H. Zheng, M. Riehn, S. Bok, K. Gangopadhyay, M. R. Maschmann, and S. Gangopadhyay, “*In-Situ* Characterization of Photothermal Nanoenergetic Combustion on a Plasmonic Microchip”, *ACS Applied Materials & Interfaces*, DOI: 10.1021/acsami.7b13226, 2017.
2. **B. Chen**, A. Wood, A. Pathak, J. Mathai, S. Bok, H. Zheng, S. Hamm, S. Basuray, S. Grant, K. Gangopadhyay, P. V. Cornish, and S. Gangopadhyay, “Plasmonic gratings with nano-protrusions made by glancing angle deposition for single-molecule super-resolution imaging,” *Nanoscale*, vol. 8, no. 24, pp. 12189–12201, Jun. 2016.
3. A. Wood, **B. Chen**, J. Mathai, S. Bok, S. Grant, K. Gangopadhyay, P. V. Cornish, and S. Gangopadhyay, “Super-Resolution Light Microscopy Using Plasmonic Gratings,” *Microscopy Today*, vol. 25, no. 1, pp. 42-47, Jan. 2017.
*Our work “Plasmonic Grating Platform” was judged one of the ten best microscopy innovations in the 2017 Microscopy Today Innovation Award competition.
4. S. Basuray, A. Pathak, S. Bok, **B. Chen**, S. C. Hamm, C. J. Mathai, S. Guha, K. Gangopadhyay and S. Gangopadhyay, “Plasmonic nano-protrusions: hierarchical nanostructures for single-molecule Raman spectroscopy,” *Nanotechnology*, vol. 28, no. 2, pp. 025302, Jun. 2016.
5. **B. Chen**, A. Pathak, K. Gangopadhyay, P. V. Cornish, and S. Gangopadhyay, “Single-molecule Detection in Nanogap-embedded Plasmonic Gratings,” *Nanobiomedicine*, vol.2, no.8, pp. 1-9, 2015.
6. A. J. Wood, **B. Chen**, S. Pathan, S. Bok, C. J. Mathai, K. Gangopadhyay, S. A. Grant, and S. Gangopadhyay, “Influence of silver grain size, roughness, and profile on the extraordinary fluorescence enhancement capabilities of grating coupled surface plasmon resonance,” *RSC Advances*, vol. 5, no. 96, pp. 78534–78544, Sep. 2015.
7. S. Basuray, A. Pathak, **B. Chen**, D. Menke, C. M. Darr, K. Gangopadhyay, P. V. Cornish, and S. Gangopadhyay, “Single Molecule Oscillations of an RNA/DNA Duplex in a Plasmonic Nanocavity,” *Journal of Nanomedicine & Nanotechnology*, vol. 06, no. 03, pp. 1-6, 2015.
8. C. M. Darr, V. Korampally, **B. Chen**, K. Gangopadhyay, and S. Gangopadhyay, “Plasmonic-enhanced conjugated polymer fluorescence chemosensor for trace

- nitroaromatic vapor,” *Sensors and Actuators B: Chemical*, vol. 202, pp. 1088–1096, Oct. 2014.
9. **B. Chen**, C. J. Mathai, S. Mukherjee, S. Gangopadhyay, Indium Tin Oxide Photonic Crystal for Controllable Light Coupling in Solar Cells by an Inexpensive Soft Lithography with HD-DVD and Blu-ray. *ECS Transactions*, vol. 61, pp. 69-82, 2014.
 10. **B. Chen**, N. Ma, X. Bai, H. Zhang, and Y. Zhang, “Effects of graphene oxide on surface energy, mechanical, damping and thermal properties of ethylene-propylene-diene rubber/petroleum resin blends,” *RSC Advances*, vol. 2, no. 11, pp. 4683-4689, 2012.
 11. N. Ma, **B. Chen**, W. Ren, Y. Zhang. “Study on damping composite of rubber/resin blends”, *Special Purpose Rubber Products*, vol. 3, no. 33, pp. 1-4, 2012.
 12. Biyan Chen, Haisheng Zheng, Matthew E. Riehn, Sangho Bok, Keshab Gangopadhyay, Jacob McFarland, Matthew R. Maschmann, and Shubhra Gangopadhyay, “Fluorescence-Based Temperature Sensor for In-Situ Imaging Local Temperature of Aluminum Nanoparticles on Plasmonic Gratings”, manuscript in preparation.
 13. Biyan Chen, Syed Barizuddin, Sangho Bok, Cherian Mathai, Keshab Gangopadhyay, Shubhra Gangopadhyay, “Super-Resolution Imaging of Nanostructures with Assistance of Plasmonic Gratings”, manuscript in preparation.

CONFERENCE PROCEEDINGS

1. **B. Chen**, H. Zheng, J. Yoon, S. Bok, C. Mathai, M. R. Maschmann, K. Gangopadhyay, and S. Gangopadhyay, “Fluorescence-Based Temperature Sensor for In-Situ Imaging Local Temperature of Aluminum Nanoparticles on Plasmonic Gratings”, *IEEE sensor*, Orlando, October 2016.
2. **B. Chen**, D. Suresh, S. Bok, C. Mathai, A. Upendran, R. Kannan, K. Gangopadhyay, and S. Gangopadhyay, “Super-resolution Imaging of Silver Nanostructures on Plasmonic Grating”, *Conference on Lasers and Electro-Optics (CLEO)*, June 2016, San Jose, USA.
3. **B. Chen**, S. Bok, S. Pathan, D. Suresh, A. Upendran, R. Kannan, J. Mathai, K. Gangopadhyay, and S. Gangopadhyay, “Nanostructure Imaging on Plasmonic Gratings by Epi-fluorescence Microscopy,” *Frontiers of Characterization and Metrology for Nanoelectronics (FCMN) conference*, April 2015, Dresden, Germany.
4. **B. Chen**, S. Bok, S. Pathan, A. Wood, A. Pathak, J. Mathai, S. Grant, P. V. Cornish³, K. Gangopadhyay, and S. Gangopadhyay, “Multifunctional Plasmonic Platform For Bio-Sensing and Single-Molecule Super-Resolution Imaging,” *Napa Institute*, August 2015, Napa, USA.
5. **B. Chen**, C. J. Mathai, S. Mukherjee, and S. Gangopadhyay, “Inexpensive Nanoimprint Lithography with HD-DVD and Blu-ray as Plasmonic and Photonic Platform”, *ACS Midwest Regional Meeting (MWRM)*, Nov 2014, Columbia, USA.

6. H. Zheng, M. Li, **B. Chen**, B. Sangho, C. M. Joseph, K. Gangopadhyay, and S. Gangopadhyay, "Surface-Plasmon-Enhanced Raman and Photoluminescence of Few-Layers and Bulk MoS₂ on Silver Grating", *Conference on Lasers and Electro-Optics (CLEO)*, June 2016, San Jose, USA.
7. Wood, S. Bok, J. Mathai, **B. Chen**, D. Suresh, K. Gangopadhyay, S. Grant, A. Upendran, R. Kannan, and S. Gangopadhyay, "Super-resolution Imaging of Silver Nanostructures on Plasmonic Grating", *Conference on Lasers and Electro-Optics (CLEO)*, June 2016, San Jose, USA.
8. S. Bok, S. Pathan, A. J. Wood, **B. Chen**, C. J. Mathai, K. Gangopadhyay, S. Grant, C. McArthur, and S. Gangopadhyay, "Highly sensitive plasmonic grating platform for the detection of a wide range of infectious diseases," in *2015 Transducers - 2015 18th International Conference on Solid-State Sensors, Actuators and Microsystems (TRANSDUCERS)*, 2015, pp. 1573–1576.
9. **B. Chen**, C. Wang, Y. Zhang. Reinforcement of nitrile-butadiene rubber with octadecylamine functionalized graphene. *Proceedings of National Polymer Science and Engineering Conference*, 2012, Wuhan, China.
10. N. Ma, **B. Chen**, Y. Zhang. Damping properties of ethylene-propylene-diene rubber/petroleum resin/ acrylonitrile-butadiene rubber/phenolic resin blends. *Proceedings of National Polymer Symposia*, 2011, Dalian, China.
11. S. Gangopadhyay, **B. Chen**, N. G. Zakiyyan, C. Wolenski, A. Wood, S. Barizuddin, C. Mathai, S. Bok, R. Thiruvengadathan, M. Maschmann, K. Gangopadhyay, "In Situ Characterization of Nanoenergetics", *2017 Fall Material Research Society Meeting*, Boston, USA, November, 2017.
12. N. Zakiyyan, **B. Chen**, M. Riehn, A. Wood, S. Bok, R. Thiruvengadathan, C. Mathai, S. Barizuddin, K. Gangopadhyay, M. Maschmann, and S. Gangopadhyay, "Laser Ignition on Aluminum-Polymer Nanoenergetic Systems Using Plasmonic Gratings", *2017 Fall Material Research Society Meeting*, Boston, USA, November, 2017.
13. A. Wood, S. Barizuddin, **B. Chen**, C. J. Mathai, K. Gangopadhyay, S. Grant, and S. Gangopadhyay, "Super Resolution Fluorescent Imaging and Biosensing Applications of Plasmonic Gratings with Nanoprotrusions," in *Advanced Photonics 2017 (IPR, NOMA, Sensors, Networks, SPPCom, PS)*, OSA Technical Digest (online) (Optical Society of America), paper SeTu1E.1, July, 2017.

Patent

1. S. Gangopadhyay, S. Bok, J. C. Mathai, S. Pathan, S. Basuray, K. Gangopadhyay, **B. Chen**, S. Grant, A. Wood, Fabrication of multilayer nanograting structures, The Curators Of The University Of Missouri, United State, Patent No. WO2017142745.
2. **B. Chen**, Y. Zhang, Preparation of oxidized graphene nanoribbon/polar rubber composites, State Intellectual Property Office, China. Patent No. CN102634106A.

VITA

Biyan Chen

Biyan Chen was born in Guangzhou, Guangdong province, China in 1987. She attended South China University of Technology (Guangzhou, China) from 2006 to 2010 and received a Bachelor of Science degree in Poly-materials and Engineering. Her studies involved in functional thiol ionic liquids as interfacial modifiers in polymer/halloysite nanotubes composites, and all-printed colorful OLED displays. She got various scholarships during her undergraduate, such as the National Scholarship. In 2010, she got the privilege to enter graduate program on Polymer Science in Shanghai Jiao Tong University, waived of the mandatory admission examination. She got a Master of Science in Materials Science and Engineering in 2013. Her research focused on structure and properties of graphene/polymer composites, multi-component damping blends, *etc.* She was awarded as Outstanding Graduate of Shanghai Jiao Tong University.

She pursued a Doctor of Philosophy in Electrical and Electronics Engineering at the University of Missouri-Columbia from August 2013 to December 2017. She joined Dr. Shubhra Gangopadhyay's research group as a graduate research assistant. During her Ph.D. study, she has been working on several research projects incorporating the technology of plasmonic gratings and photonic crystals, including fundamentals of nanoparticle heating and combustion in nanoenergetic systems, super-resolution single-molecule imaging and organic/perovskite solar cells. All of this hard work was rewarded fruitfully with the publication of several papers in high quality journals, such as *Nanoscale*, *RSC Advances*, *etc.* The projects were funded by Army Research Office (ARO, Grant number W911NF-15-1-0136) and National Science Foundation (NSF, Grant number 1102070) and others.

Biyang Chen received a 1907 Women in Engineering Award for 2016. The work “Plasmonic Grating Platform” was judged one of the ten best microscopy innovations in the 2017 Microscopy Today Innovation Award competition.